

# **The energy dissipation of the sea urchin spine as biomimetic concept generator for cellular ceramics and load-bearing systems**

**Dissertation**

der Mathematisch-Naturwissenschaftlichen Fakultät  
der Eberhard Karls Universität Tübingen  
zur Erlangung des Grades eines  
Doktors der Naturwissenschaften  
(Dr. rer. nat.)

vorgelegt von  
M.Sc. Katharina Klang  
aus Ibbenbüren

Tübingen  
2020

Gedruckt mit Genehmigung der Mathematisch-Naturwissenschaftlichen Fakultät der Eberhard Karls Universität Tübingen.

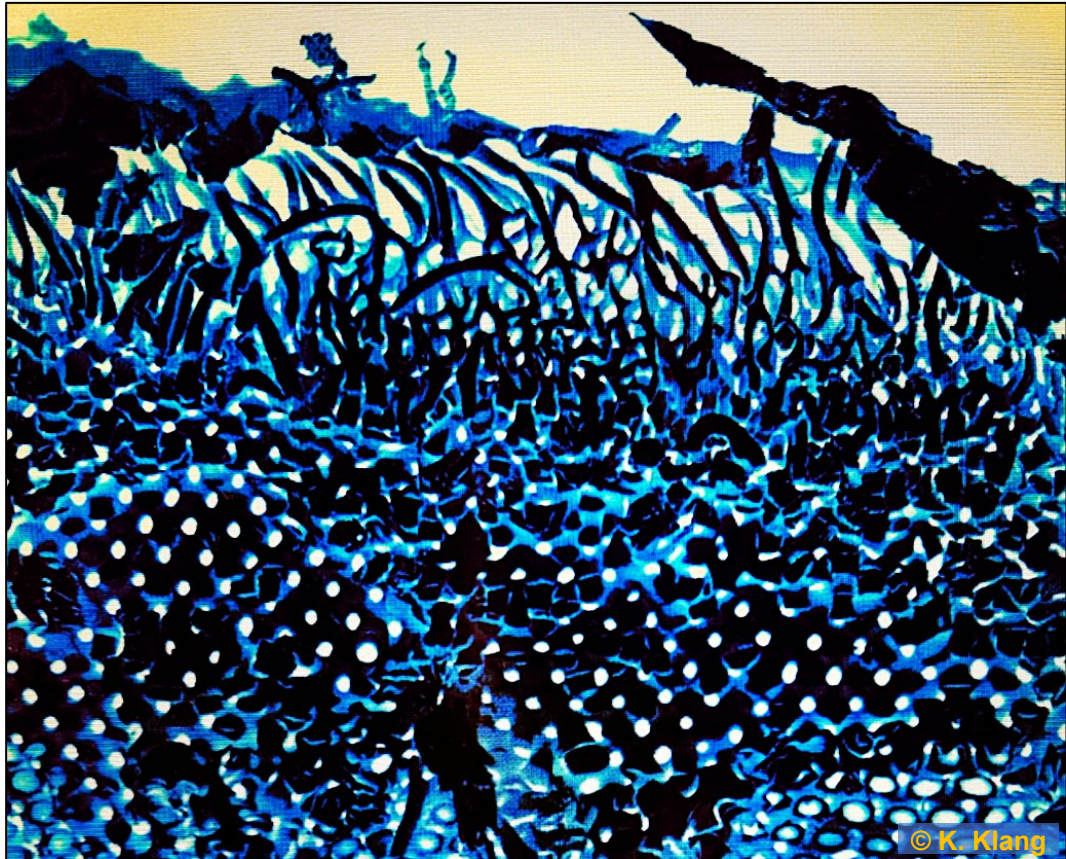
Tag der mündlichen Qualifikation:	07.08.2020
Dekan:	Prof. Dr. Wolfgang Rosenstiel
1. Berichterstatter:	Prof. Dr. Klaus G. Nickel
2. Berichterstatter:	Dr. Christoph Berthold





**THE CAPACITY TO BE PUZZLED IS THE PREMISE OF  
ALL CREATION, BE IT IN ART OR SCIENCE.**

Erich Fromm



“Robots do not rebel.”





This work was funded by the Deutsche Forschungsgemeinschaft (German Research Foundation) within the Collaborative Research Center (CRC) – Transregio (TRR) 141: Biological Design and Integrative Structures – Analysis, Simulation and Implementation in Architecture. The CRC – TRR 141 provided a network for interdisciplinary collaboration between biology, paleontology, engineering sciences and architecture. The idea behind the CRC – TRR is the identification of evolutionary optimized building principles, which can be implemented in engineered structures, architectural design and building materials.



# Thesis



## ABSTRACT

The sea urchin spine of *Phyllacanthus imperialis* is characterized by a lightweight construction undergoing energy dissipation by quasi-plastic deformation based on multiple fracturing, even though the constituting material is basically brittle magnesium calcite ( $\text{Ca}_x\text{Mg}_{1-x}\text{CO}_3$ ) with a very low content of organic matter and yet is organized in a hierarchical construction. The correlation between the structural and mechanical characteristics of the sea urchin spine of *Phyllacanthus imperialis* is analyzed in depth to discover the operating principle in order to transfer them into ceramic- and concrete-based materials.

High-resolved micro-computed tomography ( $\mu\text{CT}$ ) proved to be ideally suited to analyze the internal structures of the adult spine of *Phyllacanthus imperialis* non-invasively in regard of the strut arrangement, configuration and connectivity. Based on  $\mu\text{CT}$  reconstruction of the microstructural elements of the spine, the relationship of the varying structural elements was defined and summarized accurately in a two-dimensional map as abstracted, structural key elements. A comparative analysis of the microstructure of the adult and of a not fully grown spine shows that the growth process of the spine is characterized by an interplay of calcite resorption and precipitation caused by phagocytes and sclerocytes, respectively.

The type of mechanical behavior of adult spine segments of *Phyllacanthus imperialis* is dependent on the volumetric proportion of the outer layer, the cortex. Two main failure modes are identified: a) a high volumetric quantity of the cortex in the spine segment results in high initial strength and stiffness and b) when the volumetric quantity of the cortex is low, a comparable large energy dissipation capacity combined with a low initial strength and stiffness is given. A comparison between the spine interior (radiating layer and medulla) and the radiating layer in terms of the mechanical properties has revealed that the wedge-like enclosing of the radiating layer with the lateral side branches of the medulla provides a larger mechanical stability and is responsible for the controlled detachment of segments at advanced stages of compression.

A transfer of the highly interconnected and directional structures of the sea urchin spine in ceramic-based materials is feasible utilizing the freeze-casting method. Both agar and gelatin as additives in a water-based ceramic suspension are suitable to manufacture directional and cellular cell geometries in the ceramics. The concentration of gelatin in the ceramic suspension determines the degree of the connectivity of the cell walls, which dictates, in turn, the type of mechanical behavior. Two categories of failure modes are determined: a) a progressive interplay of flaking and crumbling and b) a segmental division of the ceramic into several lath-like segments.

The Zhang and Ashby (1992) honeycomb model prediction is not applicable for freeze-cast ceramics with a directional pore system, because it models an elastic/ plastic honeycomb foam behavior rather than brittle fracturing. Brittle fracturing can be covered by the pore model by Pabst and Gregorová (2014) and is a reasonable approach to cover the physical constraints for freeze-cast ceramics. Freeze-cast alumina ceramics characterized by prolate pore shape are associated with low Eshelby (1957)-Wu (1966) exponents and exhibit a high resilience in the light of strength and stiffness. Ceramics, which are comprising isolated cell walls have the lowest resilience. Their high values of the Eshelby (1957)-Wu (1966) exponents indicate an oblate pore shape. The relation of the elastic moduli and the pore shape by Pabst and Gregorová (2014) is applicable to freeze-cast alumina ceramics.

The operating principles of the sea urchin spine of *Phyllacanthus imperialis* have been revealed and are suitable as concept generator for biomimetic materials as well as for concrete-based constructions, which might be fabricated in pursuing research activities.

## ZUSAMMENFASSUNG

Das Seeigelstachelskelett von *Phyllacanthus imperialis* besitzt eine hierarchisch organisierte Leichtbauweise, die durch quasi-plastische Verformung basierend auf mehrfacher Risserzeugung und -ausbreitung in der Lage ist, Energie zu dissipieren, obwohl das Baumaterial aus sprödem Magnesiumcalcit ( $\text{Ca}_x\text{Mg}_{1-x}\text{CO}_3$ ) und mit sehr geringen Gehalten aus organischem Material besteht. Der Zusammenhang zwischen den strukturellen Skeletteigenschaften mit den mechanischen Charakteristika des Seeigelstachels von *Phyllacanthus imperialis* wird untersucht, um die grundlegenden Wirkprinzipien und ihre Funktionen aufzudecken, um diese auf keramische und zementbasierte Materialien zu übertragen.

Die hochaufgelöste Mikro-Computertomographie ( $\mu\text{CT}$ ) erwies sich als ideal für die nichtinvasive Analyse der inneren Strukturen von adulten Seeigelstacheln von *Phyllacanthus imperialis* in Bezug auf die Anordnung, Gestaltung und Konnektivität des Skelettnetzwerks. Basierend auf  $\mu\text{CT}$ -basierten Rekonstruktionen der mikrostrukturellen Elemente des Stachels wurde die Beziehung der verschiedenen Stereomstrukturelemente zueinander genauer definiert. Diese wurden in einer zweidimensionalen Karte als abstrahierte, strukturelle Schlüsselemente zusammengefasst. Eine vergleichende Analyse der Mikrostruktur des adulten und eines nicht vollständig ausgewachsenen Stachels hat ergeben, dass der Wachstumsprozess des Seeigelstachels von *Phyllacanthus imperialis* durch ein Zusammenspiel von Calcitresorption und -ausfällung gekennzeichnet ist, welcher durch intrazelluläre Phagozyten und Sklerozyten verursacht wird.

Die Art des mechanischen Verhaltens von adulten Stachelsegmenten von *Phyllacanthus imperialis* bei uniaxialer Kompression wird von dem Volumenanteil der äußeren Schicht, der Cortex, diktiert. Zwei grundsätzliche Versagensarten sind identifiziert worden: a) ein hoher volumetrischer Anteil der Cortex im Stachelsegment bewirkt eine hohe initiale Steifigkeit und Festigkeit und b) eine vergleichsweise hohe Energiedissipationsfähigkeit, aber geringere initiale Steifigkeit und Festigkeit ist gegeben bei einem geringen Volumenanteil der Cortex im Stachelsegment. Ein mechanischer Vergleich zwischen dem Stachelinneren (Medulla und radiierender Schicht) und der radiierenden Schicht hat ergeben, dass die keilartigen Überstrukturen zwischen radiierender Schicht und Medulla eine höhere mechanische Stabilität aufweisen und auch für das kontrollierte Ablösen von Segmenten bei fortgeschrittener Kompression verantwortlich sind. Eine Übertragung der stark vernetzten und gerichteten Skelettstruktur des Seeigelstachels in keramische Materialien ist durch die Gefriergussmethode möglich. Sowohl Agar als auch Gelatine sind als Additive in einer wasser-basierten Keramiksuspension geeignet, um gerichtete und zelluläre Zellgeometrien in den Keramiken herzustellen. Der Gehalt an Gelatine in der Keramiksuspension bestimmt den Grad der Verbundenheit der Zellwände, der wiederum

die Art des mechanischen Verhaltens diktiert. Zwei Kategorien an Versagensarten sind festgestellt worden: a) ein Zusammenspiel aus Abblättern und Zerbröseln und b) eine vertikale Segmentierung der Keramik.

Das Honigwabenmodell von Zhang und Ashby (1992) ist nicht für gefriergegossene Keramiken mit einem gerichteten Porensystem geeignet, da es nur die elastische/plastische Verformung eines Schaumes mit einer honigwabenförmigen Zellgeometrie beschreibt. Sprödes Bruchverhalten wird mit dem Porenmodell von Pabst und Gregorová (2014) abgedeckt und ist ein geeignetes mechanisches Modell für gefriergegossene Keramiken. Gefriergegossene Aluminiumoxidkeramiken, die sich durch längliche Porenkanäle auszeichnen, sind durch niedrige Eshelby (1957)-Wu (1966)-Exponenten charakterisiert und weisen eine hohe Widerstandsfähigkeit in Bezug auf Steifigkeit und Elastizität auf. Dagegen zeigen gefriergegossene Keramiken, die im Wesentlichen aus unzusammenhängenden Zellwänden bestehen, eine geringere Widerstandsfähigkeit aus. Ihre hohen Werte der Eshelby (1957)-Wu (1966)-Exponenten weisen auf eine abgeflachte Porenform hin. Die Beziehung zwischen den Elastizitätsmodulen und der Porenform von Pabst und Gregorová (2014) ist anwendbar auf gefriergegossene Aluminiumoxidkeramiken.

Die Wirkprinzipien des Seeigelstachels von *Phyllacanthus imperialis* sind entschlüsselt worden und eignen sich als Konzeptgeber für biomimetische Materialien und auch für zementbasierende Konstruktionen, die in weiterführenden Forschungstätigkeiten hergestellt werden könnten.

# Table of contents

ABSTRACT.....	II
ZUSAMMENFASSUNG.....	IV
List of abbreviations.....	4
<b>1. Introduction.....</b>	<b>6</b>
1.1 Natural materials and biomimetics.....	6
1.2 Motivation.....	7
1.3 Sea urchin spine of <i>Phyllacanthus imperialis</i> .....	7
1.4 Freeze-casting.....	12
1.5 Objectives.....	15
<b>2. Spines of <i>Phyllacanthus imperialis</i>.....</b>	<b>18</b>
2.1 Microstructure and morphology.....	18
2.1.1 Introductory remarks.....	18
2.1.2 Material and methods.....	19
2.1.2.1 Material.....	19
2.1.2.2 Scanning electron microscopy (SEM).....	19
2.1.2.3 Micro computed tomography ( $\mu$ CT) and data processing.....	19
2.1.3 Nomenclature.....	20
2.1.4 Results.....	24
2.1.4.1 Differentiation between the ‘medulla’ and ‘radiating layer’.....	24
2.1.4.1.1 Stereom types and strut arrangement.....	24
2.1.4.1.2 Calculated strut thickness.....	27
2.1.4.1.3 Definition of the ‘medulla and ‘radiating layer’.....	28
2.1.4.2 Numerical determination of the strut thickness and porosity.....	29
2.1.4.2.1 Step-wise analysis of the strut thickness.....	29
2.1.4.2.2 Porosity of the radiating layer and medulla.....	29
2.1.4.3 The ‘layered’ and ‘columnar’ stereom type.....	30
2.1.4.3.1 Numerical characterization of the ‘layered’ and ‘columnar’ stereom type.....	30
2.1.4.3.2 Numerical comparison with the galleried and laminar stereom type.....	32
2.1.4.4 Superstructures.....	33
2.1.4.5 Cortex.....	37
2.1.4.5.1 Inner structure.....	37
2.1.4.5.2 Outer structure.....	39
2.1.4.6 Proportion of the radiating layer, medulla and cortex.....	41
2.1.4.7 Microstructure of an oral spine and adolescent aboral spine.....	44
2.1.4.7.1 Oral spine.....	45
2.1.4.7.2 Adolescent aboral spine.....	47
2.1.5 Discussion.....	48
2.1.5.1 Growth mechanism.....	48
2.1.6 Conclusions.....	51
2.2 Mechanical characteristics.....	53
2.2.1 Introductory remarks.....	53
2.2.2 Sample characterization and methods.....	53

2.2.2.1 Sample preparation.....	53
2.2.2.2 Sample characterization.....	54
2.2.2.3 Mechanical testing.....	54
2.2.3 Results.....	55
2.2.3.1 Uniaxial compression of spine segments.....	55
2.2.3.1.1 Correlation of the microstructure with material properties.....	55
2.2.3.1.2 Failure mode I and II of the spine segments.....	58
2.2.3.1.3 Failure mode II: case ‘quasi bulging’ of the cortex.....	61
2.2.3.1.4 Energy capacity of failure mode I and II.....	62
2.2.3.2 Uniaxial compression of the structural elements of the spine.....	64
2.2.3.2.1 Correlation of the structural elements of the spine with the material properties.....	64
2.2.3.2.2 Failure mode of ‘medulla-cylinders’ and ‘radiating layer cylinders’.....	66
2.2.3.2.3 Energy capacity of the ‘medulla-cylinders’, ‘radiating layer cylinders’ and the core..	67
2.2.3.2.4 Crack propagation in the core.....	68
2.2.4 Discussion.....	69
2.2.4.1 Mechanical prediction by pore models.....	69
2.2.4.2 The strength – modulus chart.....	72
2.2.4.3 Implications of the function of the structural elements of the aboral spine.....	73
2.2.5 Conclusions.....	74
<b>3. Technical transfer into ceramics.....</b>	<b>77</b>
3.1 Freeze-casting.....	77
3.1.1 Introductory remarks.....	77
3.1.2 Material and methods.....	77
3.1.2.1 Gelatin as additive.....	77
3.1.2.2 Agar as additive.....	78
3.1.2.3 Mold designs, sublimation and sintering conditions.....	79
3.1.2.4 Microstructural characterization.....	80
3.1.2.5 Strut network.....	80
3.1.2.6 Mechanical characterization.....	81
3.1.3 Results.....	81
3.1.3.1 Microstructure of the gelatin series.....	81
3.1.3.1.1 Analysis of the strut network.....	85
3.1.3.2 Microstructure of the agar series.....	87
3.1.3.3 Uniaxial compression of the ceramics.....	90
3.1.3.3.1 Material properties.....	91
3.1.3.3.2 Ceramic type ‘circular cell shape’.....	92
3.1.3.3.3 Ceramic type ‘cellular oblate cell shape’.....	93
3.1.3.3.4 Ceramic type ‘disjointed cell walls’.....	94
3.1.3.3.5 Energy absorption capacity.....	96
3.1.3.4 Gradation and separate structural areas in one ceramic.....	97
3.1.4 Discussion.....	100
3.1.4.1 Applicability of pore model predictions on freeze-cast alumina ceramics.....	100
3.1.5 Conclusions.....	109
<b>4. Abstraction and 1st CAD approach.....</b>	<b>112</b>
4.1 Structural abstraction.....	112
4.2 1st CAD approach of the spine microstructure.....	115

5. Outlook.....	117
5.1 Transfer into a concrete-based column.....	117
5.2 Three-dimensional printing technique for porous ceramics.....	118
5.2.1 Bioinspired ceramic component.....	118
5.2.2 Systematical investigation of the pore model by Pabst and Gregorová (2014).....	119
6. Literature.....	120
Appendix .....	128
Danksagung.....	131

# List of abbreviations

## Technical abbreviations

BSE	Backscatter electron modus
CAD	Computer-aided design
DIW	Direct ink writing
SEM	Scanning electron microscopy
$\mu$ CT	Micro computed tomography

## Biological abbreviations

al	Aristotle's lantern
as	Aboral spine
C	Cortex
c	Cross strut
eb	Epibiont
M	Medulla
RL	Radiating layer
sl	Sheet of stereom layer
os	Oral spine
ps	Primary spine
t	Test

## Formula abbreviations

A	Area
a	Radius
$a_1$	Largest axis length
$a_2$	Smallest axis length
$c_1$	Largest axis length of the cross strut
$c_2$	Smallest axis length of the cross strut
$C_1$	Empirical constant describing the cell geometry
$C_4$	Empirical geometric constant
$C_6$	Empirical geometric constant
$C_6''$	Empirical geometric constant
D	Cross-sectional diameter of the sample under unloaded conditions
$\Delta D$	Change of the cross-sectional diameter of the sample under loaded conditions

$d$	Diameter of the sample
$\varepsilon$	Strain
$\xi_{lb}$	Cross-sectional ovalization
$[E]$	Eshelby-Wu exponent
$E$	Young's modulus
$E_S$	Young's modulus of the corresponding solid cell wall material
$E_{wall}$	Young's modulus of the corresponding solid wall
$E^*$	Young's modulus of the porous sample
$h$	Length of the sample
$K_{IC}$	Fracture toughness
$\eta$	Energy efficiency
$n$	Number of measurements
$m$	Mass
$M$	Factor
$\rho_S$	Density of the whole foam
$\rho_0$	Initial gas pressure
$\rho^*$	Density of the cell wall
$\sigma$	Stress
$\sigma_c$	Maximum compressive strength
$\sigma_{max}$	Peak value of the stress
$\sigma_p$	Modulus of rupture of the solid cell wall material
$t$	Cortex thickness
$\nu$	Poisson ratio
$V$	Volume of the specimen
$U_v$	Specific energy absorption per volume unit
$W$	Energy absorption
$X_0$	Young's modulus/ Strength in tension or compression of the solid material
$X_{Sample}$	Young's modulus/ Strength in tension or compression of the (porous) sample
$\phi$	Porosity
$\phi_{edge}$	Fraction of the solid in cell edges of the sample

# 1. Introduction

## 1.1 Natural materials and biomimetics

Many biological tissues and devices comprise remarkable engineering properties. The toughness of the coconut endocarp, the strength and lightweight of bamboo or the adhesion abilities of the gecko's feet are a few of the many examples of high-performance natural materials. Biological materials are a constant source of inspiration for solving a variety of technical challenges in architecture (Klang et al. 2016, Kovaleva et al. 2018, Grun et al. 2018), mechanical engineering (Born et al. 2017) and material sciences (Jeronimidis and Atkins, 1995). In recent years, more and more of these natural materials have been systematically studied with the objective of solving technical problems through the abstraction, transfer and application of knowledge gained from biological models. This sort of 'technology transfer' from nature to engineering is most often called biomimetics (ISO 18458/ 18459: 2015, en). It has to be mentioned that 'biomimetics' and 'bionics' are not used synonymously. According to the ISO, 2015 'Bionics' is described as a '*...technical discipline that seeks to replicate, increase, or replace biological functions by their electronic and/or mechanical equivalents.*' Therefore, 'bionics' and 'biomimetics' are not identical. One of the earliest and famous examples for biomimetics is the idea of Leonardo da Vinci to transfer the flight of birds into flying devices for human beings. Another classical example from the present day is the development of dirt- and water-repellent coating from the observation that practically nothing sticks to the surface of the lotus flower, known as 'lotus effect' (Barthlott 1990, Barthlott and Schimmel, 2010).

As researchers strive to develop better and better materials and devices as well, there is a lot to learn from nature. In many cases, the types of design requirements for materials (stiffness, strength, lightweight design, energy dissipation capacity) are similar in the engineering realm and in nature. However, it appears that natural and man-made materials often use different routes to solve similar engineering problems (Vincent et al. 2006). For instance, while researchers use a wide variety of chemicals and materials to achieve various properties, natural materials of living beings consist of relatively few constituent elements, which are used to synthesize a variety of polymers and minerals with incredible functional properties. The key is often a complex, hierarchical structuring of the natural materials (Jeronimidis and Atkins 1995, Currey 2005), which results from the fact that natural materials grow according to a recipe stored in the genes, rather than being fabricated according to an exact design. Living beings are capable to react and adapt constantly to environmental changes in an efficient and highly dynamic manner with their encoded range of possible reactions expressed as mutation, recombination and selection. In the evolutionary process, the efficient usage of natural resources is a significant evolutionary advantage and therefore a guiding evolutionary principle.

## 1.2 Motivation

Many plants, animals or specific organs of these organism have evolved strategies to cope with sudden mechanical loads and impacts caused by falling, rock falls, attack of feeding animals and various other environmental loads as wind gusts or wave movements. A typical mechanism of some biological structures is to avoid overcritical loads by dissipating energy by allowing failure of certain substructures, which are not significant for the survival of the whole organism. Some biological structures of animals combine this type of advantageous energy dissipative mechanism with a lightweight construction. The transfer of such desirable properties like strength, high energy dissipation capacity and lightweight into construction-specific materials and structures is of particular interest for buildings in regions with high seismic activity or exposed to dynamic loads. In view of the increasing scarcity of natural resources in contrast to a steadily growing population a resource-conserving building construction is of paramount importance at the present time as well. The development of a building material and/or structure combining lightweight design and a high energy dissipative property based on biological concepts found in nature is a subproject of the Collaborative Research Centre (CRC)-Transregio 141 'Biological Design and Integrative Structure – Analysis, Simulation and Implementation in Architecture'. Another subproject of the CRC-Transregio 141 is to produce a porous ceramic with a limited number of principles abstracted from the biological concept generator. Porous ceramics have many industrial applications, in which porosity can be positively taken into account, due to a wide range of application such as refractories, filtrations, biomaterials, catalyst supports, thermal insulators and lightweight structural components. The sea urchin spine of *Phyllacanthus imperialis* was chosen as biological concept generator, because it represents a lightweight construction undergoing energy dissipation by quasi-plastic deformation based on multiple fracturing, even though the constituting material is basically brittle magnesium calcite ( $\text{Ca}_x\text{Mg}_{1-x}\text{CO}_3$ ) with a very low content of organic matter and yet is organized in a hierarchical construction.

## 1.3 Sea urchin spine of *Phyllacanthus imperialis*

Sea urchins are members of an ancient group from the class Echinoidea in the Phylum Echinodermata that is hundreds of million years old and represent one of the taxonomically most diverse groups of marine invertebrates in the oceans of the world today (Pawson 2007). They are prevalent all over the marine world and live in both high-energy tidal environments and low energy abyssal depths. The sea urchins are divided into two dichotomously groups determined by their morphology and ecological niche: Regularia and Irregularia. The latter are characterized by a secondary bilateral symmetry containing rather thin fur-like spines and live endobenthic, meaning that they bury themselves in the sediment. Regularia show, in contrast, a pentamerous symmetry with comparable up to finger-thick spines and live epibenthic on the solid substrate.

The spine of the investigated species, *Phyllacanthus imperialis* (lance sea urchin), belong to the regular sea urchins, specifically to the order Cidaroida, which is a sister clade to all other echinoids. The animal

itself prevails widely in the backreef area in the littoral zone (depths up to 70 m) and wedges itself between the reefs during the daytime (Nebelsick 1992a; b, Nebelsick 1996). This species is not directly exposed to the highest energy environment and inhabits more protective areas with coral cover (Nebelsick 1992a; b). The primary spines of this species vary in size from the oral side, where they are comparatively small, to the aboral side (Fig. 1.1 (A), (B)). The large and robust aboral spines can protect the echinoid from predators such as fish, sea stars and several bird species (Kurz 1995, Kowalewski and Nebelsick 2003) and serve as locomotion as well as mechanical fixation structure between the reefs. In contrast to other echinoids, the mature primary spines are devoid of epidermis. In this manner, the skeleton is in direct contact with sea water. As a consequence, it is colonized by numerous epibionts (Fig. 1.1 (A), (B)) including perforating taxa (David et al. 2009). Besides the large primary spines, the test is also covered by blunt secondary spines, which are only a few millimeters in length (Fig. 1.1 (A): red square).

As with all microstructures of echinoderm skeletons, the primary spines consist of a porous three-dimensional meshwork of high-magnesium calcite ( $\text{Ca}_x\text{Mg}_{1-x}\text{CO}_3$ ) known as stereom (Smith 1980, Smith 1990). Magdans and Gies (2004) have shown that the  $\text{MgCO}_3$ -content varies between 2 to 12 mole percent in the spine structure. The trabeculae meshwork consists of highly ordered polycrystalline mesocrystals (Cölfen and Antonietti 2008). These mesocrystals comprise of highly ordered nanoparticle-sized domains, oriented parallel to the c-axis. Small quantities of organic material (Märkel et al. 1971) and amorphous calcium carbonate (ACC) are between and within the magnesium calcite domains (Seto et al. 2004). The type of stereom, which can be found in the skeleton, depends on the specific architecture of the skeleton and varies not only between the species, but also within one single element of the skeleton. The pores of the stereom are filled with stroma, consisting of fluids and several organic compounds like extracellular fibrils and connective tissue cells (Märkel et al. 1971). The stereom differentiation in echinoids was extensively studied by Smith (1980), who differentiated the stereom of plates into varying classes. According to Smith (1980), ten different types of stereom can be observed in echinoderms: labyrinthic, laminar, galleried, microperforate, rectilinear, fascicular, retiform, imperforate, simple and irregular perforate. The terminology by Smith (1980) is used here to describe the stereom network structure in the spine of *Phyllacanthus imperialis*.

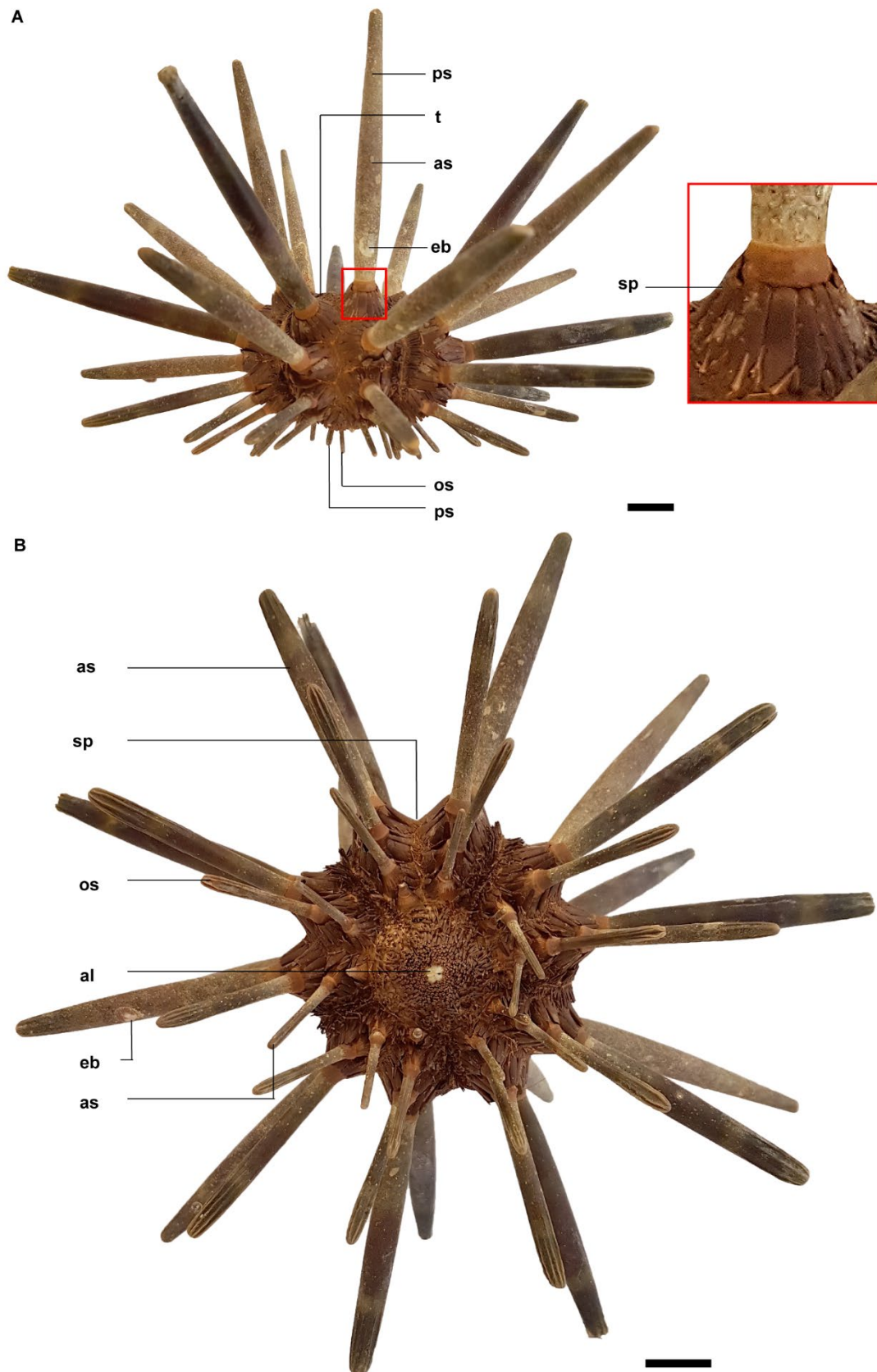


**Fig. 1.1:** Sea urchin *Phyllacanthus imperialis*. The lateral and the aboral side of the whole sea urchin *Phyllacanthus imperialis* is shown in (A) and (B), respectively. Main elements of the sea urchin: ps = primary spine, os = oral spine, al = Aristotle's lantern, sp = secondary spine, as = aboral spine, t = test, eb = epibiont. Scale bars: (A) = 1 cm, (B) = 1 cm.

In this context, the significant stereom definitions used for the internal spine structure of *Phyllacanthus imperialis* are presented in the following, which are the labyrinthic (Fig. 1.2 (A)), laminar (Fig. 1.2 (B)) and galleried stereom type (Fig. 1.2 (C)). The definition of the labyrinthic stereom is simple compared to the laminar and galleried stereom type and consists of an unorganized mesh of interconnecting struts (Smith 1980). The definition of the galleried and laminar stereom types is much more complex. Since these definitions are relevant in this thesis for the characterization of the internal spine structure of *Phyllacanthus imperialis*, the detailed description of the galleried and laminar stereom type stated by Smith (1980) is given in the following. Smith (1980) defines the galleried stereom as ‘... stereom [that] possesses long parallel galleries in one direction only and shows no pore alignment perpendicular to this direction. It is composed of parallel trabecular rods which are interconnected by struts in such a way as to produce cylindrical passages paralleling the rods [Fig. 1.2 (C)]. Viewed parallel to the galleries the pores are seen to be in an irregular polygonal arrangement with rods at the intersections of trabeculae [Fig. 1.3 (A), (B)]. Internal pore alignment is moderately well-developed so that each gallery penetrates deep into the test. [...] When viewed perpendicular to the galleries the long straight rods and passageways can be seen [Fig. 1.3 (C), (D)]. There is no alignment of lateral pores and these are usually smaller in diameter than the galleried pores (p. 10).’

In contrast, the laminar stereom type comprises ‘a multilamellar construction built up of thin sheets of stereom separated by trabecular struts. [...] The separation distance between the sheets is much greater than the thickness of individual sheets. Trabecular struts are usually thin and are orientated more or less perpendicular to the lamellae. [...] When viewed perpendicular to the lamination this stereom has a planar surface perforated by numerous closely spaced pores of large diameter’ (Smith 1980, p. 10).

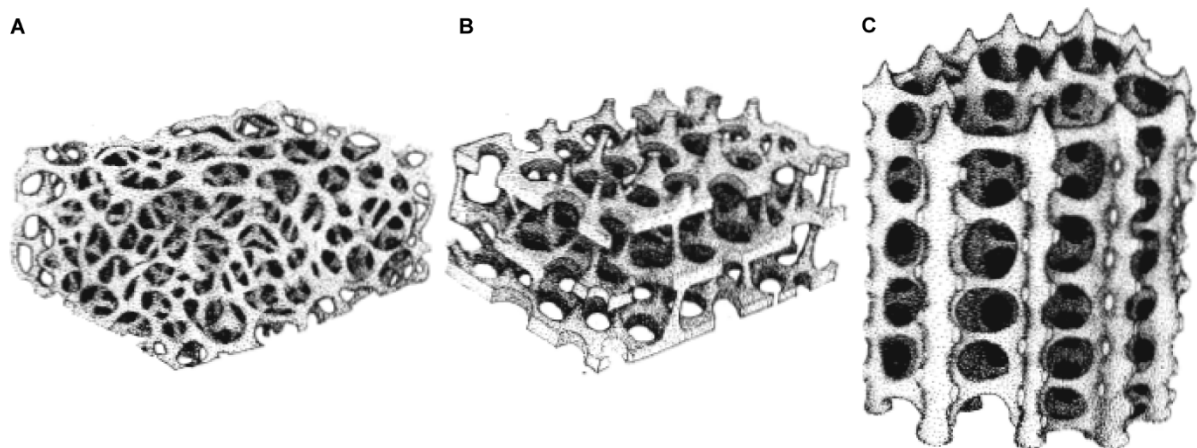


**Fig. 1.2:** Stereom types according to the nomenclature of Smith (1980). Following stereom fabrics are illustrated in (A), (B) and (C): labyrinthic, laminar and galleried stereom type, respectively. Modified after Smith (1980).

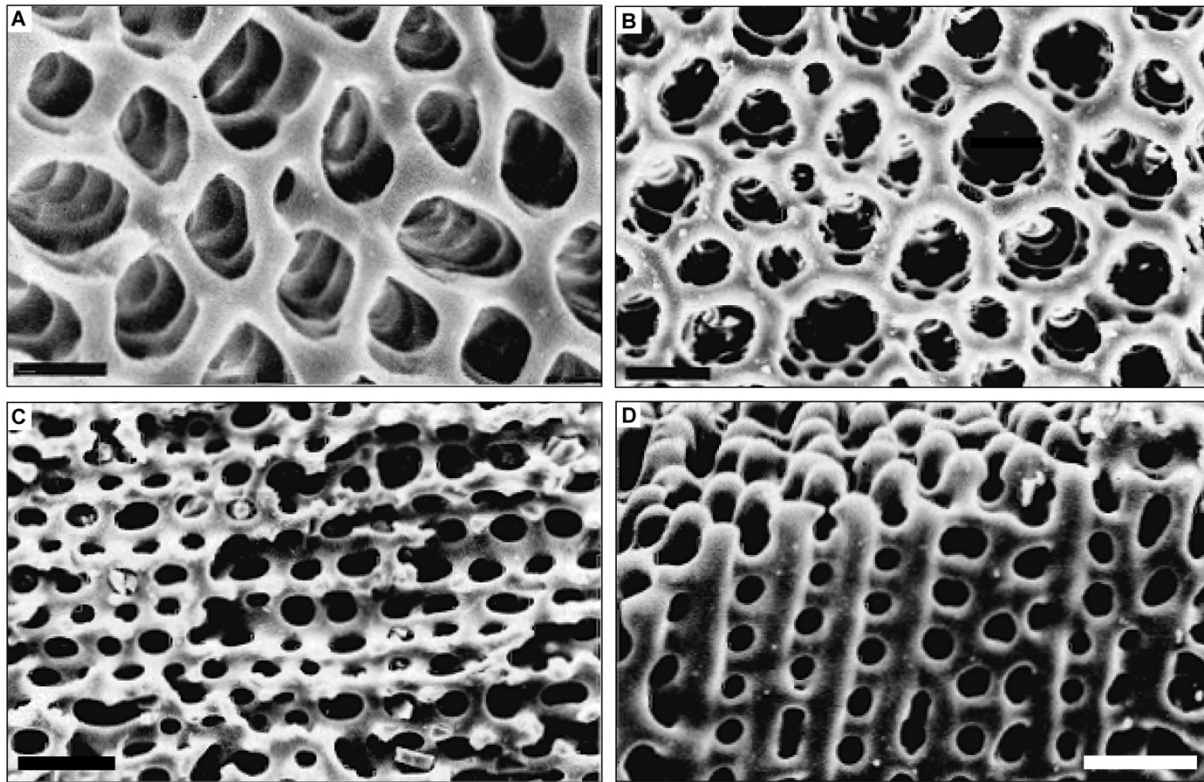


**Fig. 1.3:** SEM images of the galleried stereom, which occur in the interambulacral tubercle (A, B) and plates (C, D) of sea urchins. The images in (A) and (B) demonstrate the stereom network perpendicular, whereas the images in (C) and (D) display the stereom parallel to the crystallographic *c*-axis. Scale bars: (A) = 20  $\mu\text{m}$ , (B) = 20  $\mu\text{m}$ , (C) = 40  $\mu\text{m}$ , (D) = 40  $\mu\text{m}$ . Modified after Smith (1980).

In general, the primary spines of echinoids can be subdivided into the base and shaft including also the tip (Fig. 1.4 (A)). The base is restricted to the area below the milled ring (Fig. 1.4 (A)). The collar comprising Prouho's membrane is located directly above the milled ring (Fig. 1.4 (A)) and is defined as shaft. If the spine breaks off, the regeneration of the spine occurs at the site of Prouho's membrane (Burkhardt et al. 1983). The primary spine of *Phyllacanthus imperialis* contains three main structural areas from the outer to inner structure (Fig. 1.4 (B)): cortex, radiating layer and medulla. On the macroscopic level this classification can also be recognized by the different colors of the spine interior (Fig. 1.4 (A)). Grossmann and Nebelsick (2013) have described the stereom network in the medulla as laminar stereom type, whereas the stereom structure in the radiating layer were characterized as galleried stereom type using the nomenclature by Smith (1980). Presser et al. (2009a) characterized the radiating layer of the spine of *Phyllacanthus imperialis* as galleried stereom structure as well.

It was demonstrated that the spines of *Phyllacanthus imperialis* possess a high initial crushing strength,  $\sigma_c$ , of  $61 \pm 14$  MPa (Presser et al. 2009a). Weber et al. (1969) determined an  $\sigma_c$  of 72 MPa for the spines of *Stylocidaris affinis* belonging to the same family as *Phyllacanthus imperialis* (Cidarinae). Their mechanical behavior under uniaxial compression involves a high energy dissipation by graceful failure both in slow compression (Presser et al. 2009a) and in an impact type of loading (Presser et al. 2011). Presser et al. (2009a; b) has found that the enhanced energy dissipation, through which the material re-

gains high compression resistance well after the compression has started, is caused by the hierarchic structure of the spine from the microscale down to the nanoscale.

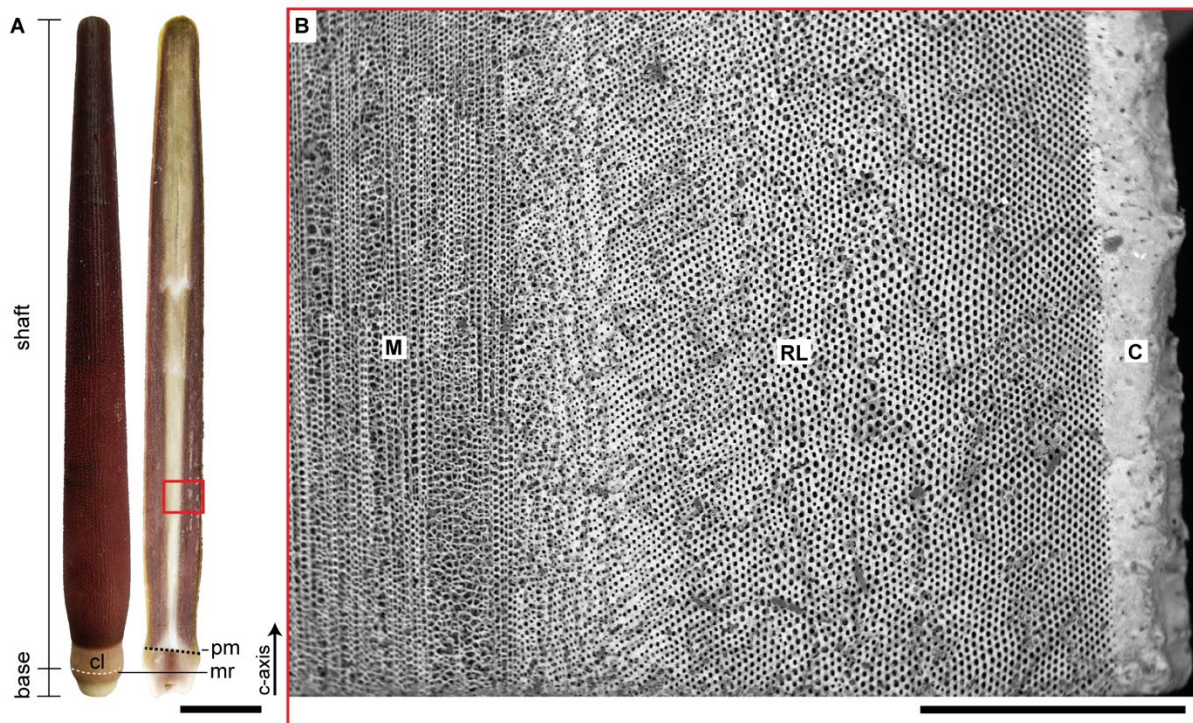


**Fig. 1.4:** Aboral spine of *Phyllacanthus imperialis* in the longitudinal view (parallel to the c-axis). The spine is separated into the base and shaft. The base is limited to the milled ring (mr). The shaft of the spine includes the collar (cl) and Prouho's membrane (pm). A back-scatter electron (BSE) image of the spine structure (red box) illustrates the three main structural units of the spine, which are as follows: the medulla (M), radiating layer (RL) and the cortex (C). Scale bars: (A) = 1 cm and (B) = 1 mm.

The mesocrystalline structure at the nanoscale prevents the typical cleavage of pure calcite along the cleavage plane. Instead, it provides crack branching where the crack stops at the grain boundaries as well. Therefore, the spine shows instead a conchoidal fracture behavior and thus an increased fracture toughness. The struts of the porous stereom network act furthermore as predetermined breaking points on the microscale (Presser et al. 2009b). The energy consuming breaking of these structures follows a layer-by-layer crushing mode, which keeps the material below intact (Presser et al. 2009a; b).

## 1.4 Freeze-casting

It has been shown in Presser et al. (2009b) that the manufacturing of a biomimetic porous ceramic containing cap-shaped layers of alternating porosities is basically feasible utilizing starch-blended slip casting. This modified slip casting method has its limitations. Ceramics manufactured with this method lack the homogenous and ordered pore geometry. Other techniques like the layer-by-layer deposition (Podsiadlo et al. 2007, Tang et al. 2003), filtration (Cheng et al. 2013, Yao et al. 2010), hydrogel casting (Zhang et al. 2015) and electrophoretic deposition (Chavez-Valdez et al. 2013) are time-consuming and

size limiting processes, which enable to fabricate ceramic layers with a thickness of approximately 200  $\mu\text{m}$  only. Freeze-casting produce, in contrast to the techniques mentioned above, porous ceramics with complex, three-dimensional pore structures that can also contain at least two different levels of open porosity and an ordered pore alignment. Mimicking those features is required in order to manufacture the abstracted concepts of the spine of *Phyllacanthus imperialis* into a porous bioinspired ceramic. In general, the freeze-casting technique has clearly become a focus of attention in the last decade concerning the manufacturing of complex pore geometries and open interconnected pore systems due its simple operation, cost efficiency and environmental friendliness.

The manufacturing process uses a ceramic suspension, which is directional frozen and then sublimated before sintering (Fig. 1.5). This process provides materials with a unique porous architecture, where the porosity is almost a direct replica of the frozen ice crystals. The pore morphology, orientation and average pore size can be tailored by altering process parameters such as slurry concentrations (Fukusawa et al. 2001, Deville 2008, Deville 2010), freezing temperatures (Peppin et al. 2006, Peppin et al. 2007, Peppin et al. 2008, Deville 2008), cooling rates (Hunger et al. 2013, Lichtner et al. 2015, Liu et al. 2018, Deville 2008) and use of additives (Munch et al. 2009, Deville 2008, Deville 2010).

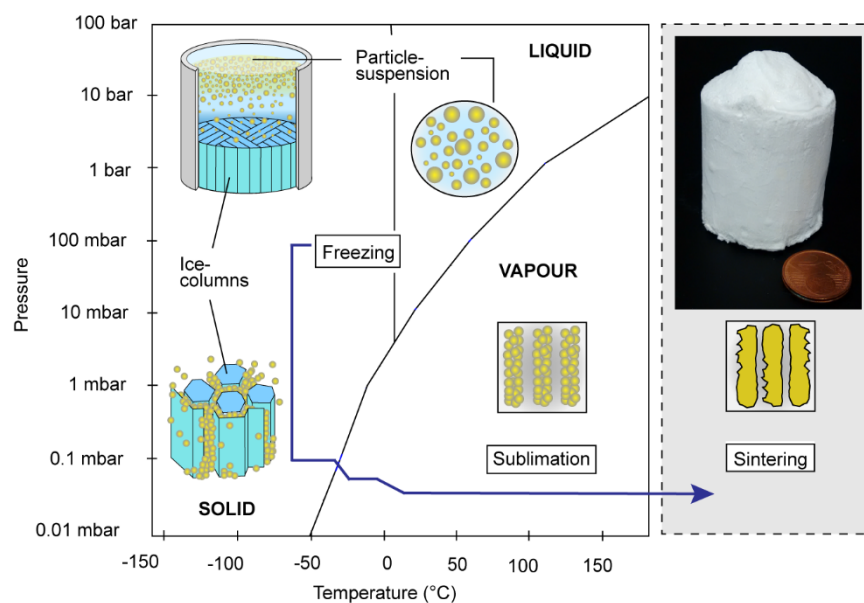


**Fig. 1.5:** Schematic overview of the freeze-casting process. Four main processing steps are part of the manufacturing process: preparation of the suspension, solidification via freezing of the suspension, sublimation and sintering.

However, this freedom adds significant difficulties when trying to understand the underlying principles that govern the relations between obtained microstructure and processing. A metastudy by Scotti and Dunand (2018), extending the initial data repository of Deville et al. (2016), has been published to summarize the understanding of the key processing-structure-property relationships in the recent freeze-casting literature and includes now additional parameter, which influence the microstructure: coursing

(Pawelec et al. 2015), gravity (Scotti et al. 2017), mold design (Husmann et al. 2015), surface wetting of the freezing substrate (Yang et al. 2015) and filler material (Zhang et al. 2017).

The pore structure of freeze-cast ceramics is largely determined by the morphology of the solidified fluid (Naviroj et al. 2017, Deville et al. 2011). Water is the most common fluid for the freeze-casting process, because of its environmental friendliness, low cost and easy handling and best application chances. Furthermore, when a unidirectional freeze-casting technique is employed, lamellar pore structures (Han et al. 2009), which exhibit a high mean aspect ratio can be fabricated. High aspect ratios are advantageous in applications such as batteries, heat and acoustic insulators, because open aligned channels promote fluid flow (Perry and Kandlikar 2006, Hasan et al. 2009).

However, for load-bearing applications, an increased interconnectivity between the cell walls is beneficial, because it improves the behavior of the material under compression (Munch et al. 2009, Porter et al. 2014, Zhang et al. 2010) and resembles the stereom architecture of the spine of *Phyllacanthus imperialis*, which is required for the manufacturing of a bioinspired ceramic. Generation of wall interconnectivity during the solidification can be attained by modifying the character of the suspension. This can be achieved in a water-based suspension by increasing the particle volume fraction (Tang et al. 2005) and/or the solidification velocity (Hunger et al. 2013, Wegst et al. 2010, Da Silva et al. 2015), through the use of additives as binders (Zhang et al. 2010) or cryoprotectants (Sofie and Dogan, 2001). Glycerol as additive and known as cryoprotectant in a water-based ceramic slurry is able to increase the interconnectedness between the lamellar cell walls by ceramic bridges (Fig. 1.6 (D)). It has been demonstrated that the quantity of ceramic bridges increases as the glycerol concentration increases (Zhang et al. 2010, Sofie and Dogan 2001). To suppress the preferential lamellar growth of ice crystals more intensively (Fig. 1.6 (C)) it is known from previous studies that the addition of gelatin in the conventional freeze-casting procedure induces rather a cellular morphology (Fig. 1.6 (B)) with a high degree of interconnectivity of the cell walls (Arabi and Zamanian 2013, Fukushima et al. 2014, Wu et al. 2010). This sort of pore morphology is caused by the increased viscosity of the suspension utilizing gelatin as additive. Dowell et al. (1962) has recognized that the formation of ice crystals in gelatin gels enhances the migration resistance of water during freezing. The water molecules, which surround the gelatin, form a discontinuous network and prevent the concurrent preferential growth of ice crystals. Instead, ice nuclei are formed spatially separated in the gelatin network. Thus, the ice crystals are reduced in size and show a circular morphology (Fukushima et al. 2014). A highly concentrated slurry further promotes the formation of microstructural bridges between the cell walls due to the fact that more particles might be entrapped by ice crystals.

A cellular pore morphology can also be fabricated through the combination of 5 and 10 wt.% of sucrose (with respect to dry powder mass) at a pH = 2.5 (by adding citric acid) in an alumina-water based suspension (Munch et al. 2009; Fig. 1.6 (A)). Using 4 wt.% sucrose in a water-based suspension creates, however, lamellar structures with a significant amount of bridges (Munch et al. 2009; Fig. 1.6 (E)).

Munch et al. (2009) have concluded that sucrose causes an interfacial instability at the solidification front facilitating the growth of bridges from the lamellar walls during directional solidification.

The combination of an increased microstructural wall interconnectivity to improve the mechanical properties and the circular open channels to facilitate the fluid flow in the ceramic is desired in many technical applications.

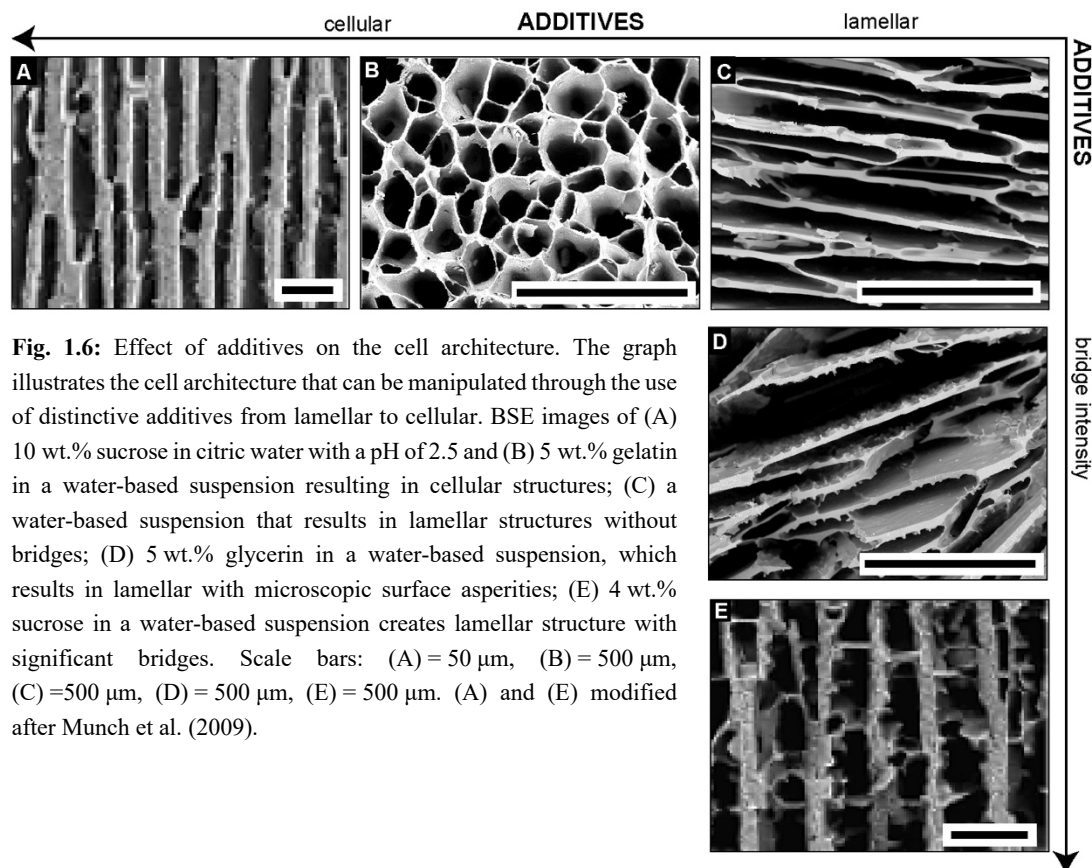


**Fig. 1.6:** Effect of additives on the cell architecture. The graph illustrates the cell architecture that can be manipulated through the use of distinctive additives from lamellar to cellular. BSE images of (A) 10 wt.% sucrose in citric water with a pH of 2.5 and (B) 5 wt.% gelatin in a water-based suspension resulting in cellular structures; (C) a water-based suspension that results in lamellar structures without bridges; (D) 5 wt.% glycerin in a water-based suspension, which results in lamellar with microscopic surface asperities; (E) 4 wt.% sucrose in a water-based suspension creates lamellar structure with significant bridges. Scale bars: (A) = 50  $\mu\text{m}$ , (B) = 500  $\mu\text{m}$ , (C) = 500  $\mu\text{m}$ , (D) = 500  $\mu\text{m}$ , (E) = 500  $\mu\text{m}$ . (A) and (E) modified after Munch et al. (2009).

## 1.5 Objectives

Two principal approaches can be distinguished in biomimetics referred to as bottom-up process of biomimetics (biology-push) and top-down process of bionics (technology pull) (Speck et al. 2017). This thesis is based on the bottom-up process (Fig. 1.7). In the bottom-up process, the discoveries and basic research of the biological role model are at the beginning of the biomimetic project. Consequently, the biological role model is investigated quantitatively in terms of its form-structure-function relationship and their mechanical, physical and chemical properties to obtain an understanding about the operating principles of the relevant structures, which might be interesting for technical implementation. The technical implementation in real demonstrators requires an abstracted model that summarizes the operating principles of the biological role model. In contrast to the bottom-up process, the top-down process focuses on a particular question in the light of a certain application, which is described in detail in Speck et al. (2017).

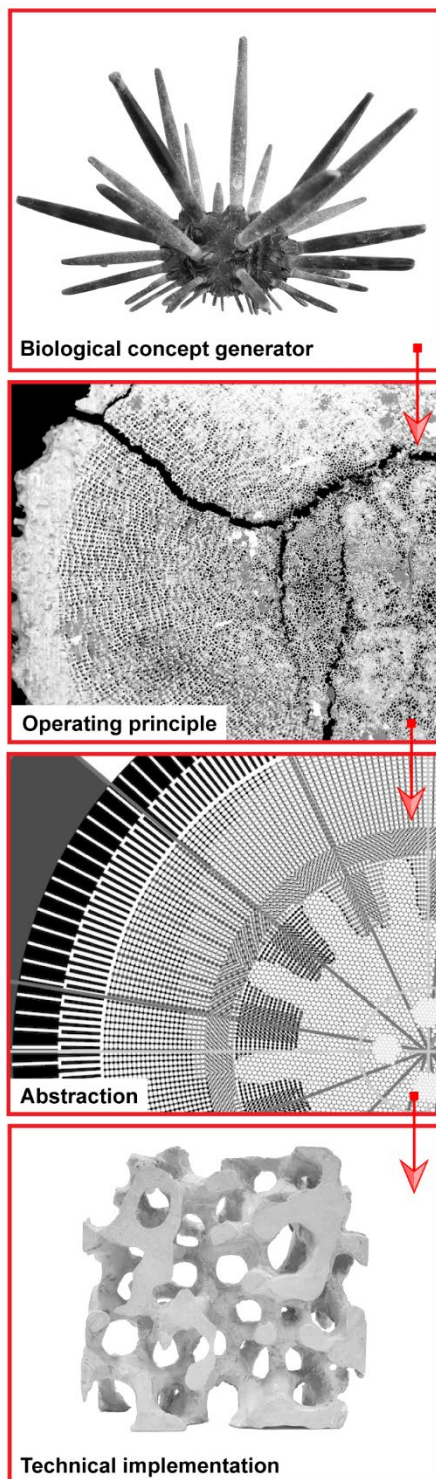


**Fig. 1.7:** Schematic overview illustrates the biomimetic bottom-up process (biology-push). The quantitative analyses are based on the adult, aboral spine of *Phyllacanthus imperialis*. Its operating principles are summarized in an abstracted model, which is relevant for the technical implementation into a ceramic- and concrete-based material.

On the bases of the bottom-up approach of biomimetics, the thesis aims for

a) a comprehensive understanding about the inner microstructure of the aboral adult spine of the sea urchin *Phyllacanthus imperialis*. It includes a characterization of the strut arrangement, their connectivity to each other and of the transformation zones between the different stereom architectures. Parameters like the strut thickness, pore size and the porosity of the varying structural areas within the spine structure have to be quantitatively obtained. Based on the microstructural results, it is attempted to define the border between the medulla and radiating layer. Such formulation of a strict border hence requires a definition of the medulla and radiating layer as well.

b) the development of a hypothesis concerning the growth mechanisms of the spine. A comparative observation of the microstructure between an aboral adult and aboral adolescence spine is therefore needed.

c) the relation of the material properties, fracture behavior and the energy absorption capabilities with its microstructural characteristics. On the basis of the results on the relationship between the mechanical and microstructural features, the function of the structural elements and its specific configuration within the spine has to be discussed in the light of the mechanical environment of the sea urchin.

d) cellular, highly porous bioinspired ceramics comprising the abstracted concepts of the spine of *Phyllacanthus imperialis*. Therefore, the bioinspired ceramic should contain comparable porosities like the sea urchin spine and an open-cell network with channel-like porosities, which is hence highly anisotropic in terms its pore shape. Gelatin and agar are exploited as additives in a water-based alumina suspension in

the freeze-casting route in order to create cellular pore morphologies.

e) discussion about the applicability of the mechanical predictions of the Gibson and Ashby (1997) and Pabst and Gregorová (2014) models for porous sea urchin spines and freeze-casted alumina ceramics. The honeycomb model provided by Zhang and Ashby (1992) is also included in the discussion of the pore models related to the freeze-casted ceramics.

f) a first step to introduce a computer-aided design (CAD) model, which comprises the basic abstracted structural configuration of the spine microstructure. The CAD approach represents a first and important step for the transfer of the abstracted principles into a concrete-based building material.

## 2. Spines of *Phyllacanthus imperialis*

### 2.1 Microstructure and morphology

#### 2.1.1 Introductory remarks

A structural and morphological investigation of the spines of *Phyllacanthus imperialis* has been conducted by Grossmann and Nebelsick (2013), who gave an overview about the strut thicknesses, pore sizes and structure of the stereom of an aboral and oral spine of *Phyllacanthus imperialis*. Besides the inner microstructure of the aboral spines, Grossmann and Nebelsick (2013) provide insights into the shape and surface sculpturing of the cortex as well. Grossmann and Nebelsick (2013) have utilized backscatter electron (BSE) images and  $\mu$ CT scans of aboral and oral spines of *Phyllacanthus imperialis*. BSE images displaying clearly the microstructure of an oral spine are, however, lacking in their analyses. Their  $\mu$ CT reconstructions are not related to one specific section recorded with high magnifications, but are rather related to the entire spine structure. In this way, it was recognizable that the spine consists of three areas of varying densities: from the outer almost dense shell, the density decreases from the outside to the spine interior. The center of the spine is called medulla, the outer shell is the cortex and in between of them is the radiating layer with its intermediate density (see section 1.3). The struts or any other microstructural details, however, are not recognizable in their  $\mu$ CT reconstructions of the spines. A detailed view of the strut configuration, their connectivity and transformation from one to the next stereom architecture is required to understand the microstructural reasons for the high strength under compression, on the one hand and the beneficial non-catastrophic fracture behavior of the aboral spine, on the other. To examine the latter aspects in detail, the microstructural results demonstrated here base on high-resolved  $\mu$ CT scans of a small section of the aboral spine, which is complemented by observations via BSE images.

The main focus of this chapter is the microstructure and morphology of an aboral adult spine of *Phyllacanthus imperialis*. The microstructure of an oral and aboral adolescence spine is described in this chapter as well. A detailed numerical analysis of the microstructure was not performed for the oral and aboral adolescence spine. The microstructure of an adolescence aboral spine and its comparison with an adult aboral spine is important for the interpretation of the effective growth mechanisms acting within the spine ontogenesis. The microstructural configuration of the oral and adult aboral spine indicates the adaptations to their specific mechanical environment and are discussed at the end of this chapter.

## 2.1.2 Material and methods

### 2.1.2.1 Material

The sea urchins were not killed for this thesis. The investigated primary spine material belongs to the tropical cidaroid *Phyllacanthus imperialis* (Lamarck 1816). The spine material was purchased from a material supplier (Mineralien- und Fossilienhandlung Peter Gensel, Weimar, Germany).

### 2.1.2.2 Scanning electron microscopy (SEM)

Spine segments (cut parallel and perpendicular to the c-axis) were investigated with a scanning electron microscope (Tabletop Microscope TM3030plus, Hitachi Ltd., Tokyo, Japan) at the Institute of Geosciences of the University of Tübingen. The backscatter electron mode (BSE) has been applied for the microscopic analysis at an acceleration voltage of 15 kV and at a working distance of 6500  $\mu\text{m}$ .

### 2.1.2.3 Micro computed tomography ( $\mu\text{CT}$ ) and data processing

The upper part of a spine (Fig. 2.1, red box) was scanned in a nano CT scanner (phoenix nanotom m, Fa. GE Sensing & Inspection Technologies GmbH, Germany) at the ITV Denkendorf. The samples were scanned at 800 kV/180  $\mu\text{A}$  with an exposure time of 800 ms to a resolution of 1.27  $\mu\text{m}$  per voxel. The acquired two-dimensional X-ray images were reconstructed with a Filtered Back Projection reconstruction algorithm. The  $\mu\text{CT}$  data are analyzed and reconstructed into three-dimensional objects using the Fiji 2.0.0 (ImageJ) software package. In order to determine the porosity xy-images were binarized using the iterative 'default' threshold based on Ridler and Calvard (1978). Based on this binarization process, the software calculates the amount of black and white in the image. The algorithm of the plugin BoneJ (Doube et al. 2010) has been used to determine the thickness of the struts. For this purpose, binarized images have been utilized for the evaluation of the thickness as well. The pore axis lengths were determined from the reconstructed three-dimensional objects applying the mode 'fit ellipse'.

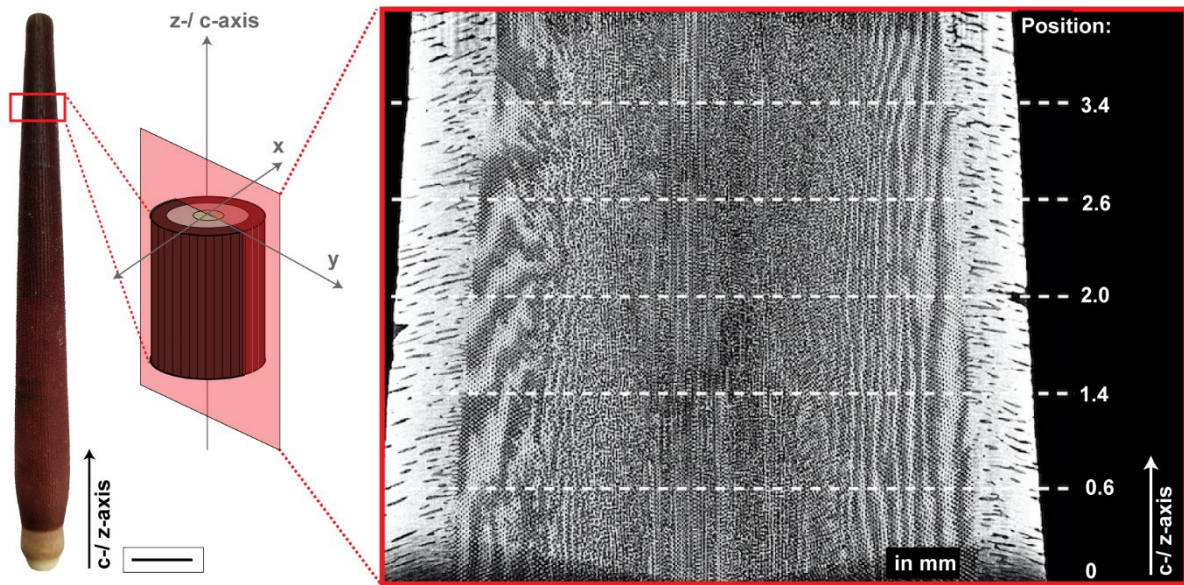


**Fig. 2.1:** Spine of the sea urchin *Phyllacanthus imperialis*. Red box illustrates the scanned area via  $\mu$ CT. A complete reconstruction of the scanned spine area as  $zx$ -plane can be seen on the right-hand side. Scale bar = 10 mm.

### 2.1.3 Nomenclature

Spines of sea urchins and also the skeletal plates forming the test of echinoids are composed from high-magnesium calcite (see section 1.3) and are mesodermal in origin (Weber 1969). The plates and the spines consist of a three-dimensional mesh of trabeculae. The trabeculae are sometimes called struts (Smith 1980). In this thesis, the terms trabecular rod and cross struts have their own definitions for the spine microstructure and are not utilized synonymously. A differentiation between both is based on their orientation to the  $c$ -axis of the spine: the trabecular rod is oriented parallel, whereas the cross strut is oriented perpendicular to the  $c$ -axis (Fig. 2.2 (A), (B)). The term ‘struts’ is used here as a collective term comprising trabecular rods as well as cross struts. Such differentiation of the structural elements constituting the stereom mesh is not made in the current literature. Smith (1980), however, has classified the arrangement of the stereom in different stereom types (section 1.3). Its nomenclature of the stereom is based on the microstructure of the coronal plates from echinoids. Grossmann and Nebelsick (2013) utilized the nomenclature of Smith to characterize the stereom mesh of the spine of *Phyllacanthus imperialis*. According to their structural analyses of the spine they have defined the medulla as laminar and the intermediate radiating layer as galleried. New findings of microstructure and the configurational shape display, however, that the characterization of Grossman and Nebelsick (2013) for the microstructure based on the nomenclature of Smith (1980) is not accurate for the spine of *Phyllacanthus imperialis*. The reason is that none of the defined stereom classes by Smith (1980) does cover the stereom meshes of the medulla and the radiating layer correctly.

Based on the new understanding about the microstructure of the spine of *Phyllacanthus imperialis*, the nomenclature of Smith (1980) is extended by two new stereom classes in this section, which are here the ‘layered’ and ‘columnar’ stereom, respectively (Fig. 2.2 (C), (D)). In order to avoid confusion due

to certain structural similarities the definition of the ‘layered’ and ‘columnar’ stereom type is provided below. The definitions also include a comparison with the galleried and laminar stereom type by Smith (1980). The ‘layered’ and ‘columnar’ stereom type are established as independent definitions in this way and are not synonyms for the galleried and laminar stereom type. The comparison and therefore the definitions are given in a descriptive way further below. The definitions of the ‘layered’ and ‘columnar’ stereom type are based on the numeric results from the trabecular thickness and pore axis length (cf. 2.1.4.3.1).

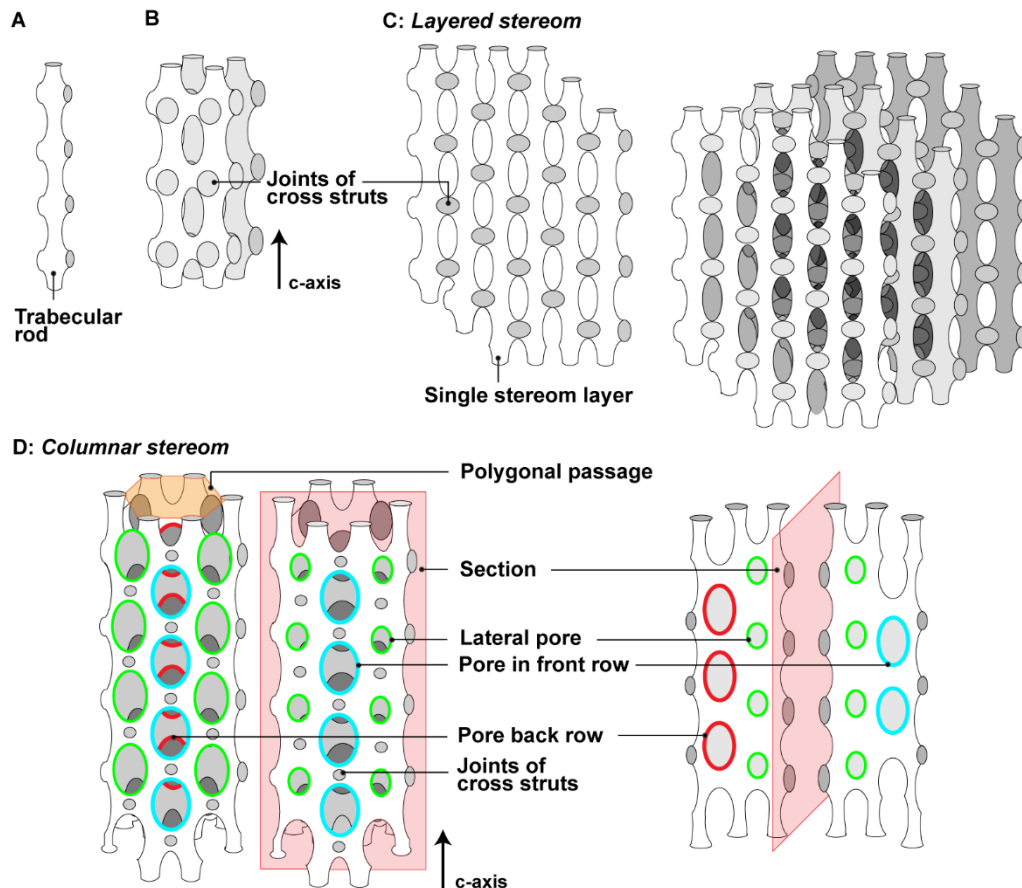


**Fig. 2.2:** Stereom types and their nomenclature. Trabecular rods and cross struts are the basic elements of the stereom fabrics displayed in (A) and (B). (C): One individual stereom layer consists of several trabecular rods, whereas a number of stereom layers form the so-called layered stereom type. The columnar stereom type is displayed in (D) where the trabecular rods are arranged in a circular array forming polygonal passages (orange). The pores in the front row (blue circles) show no straight congruency with the pores belonging to the back row (red circles). The lateral pores of the columnar stereom type are equal or smaller in size (green circles) compared to the adjacent pores (blue circles).

### *Layered stereom.*

The layered stereom is characterized by a lamellar construction, which is composed of thin sheets of stereom layers (Fig. 2.2 (C); Fig. 2.3 (A)). The stereom layers are separated from each other by cross struts. The separation distance between the sheets is regular and approximately equal to the thickness of the individual sheets (Fig. 2.3 (A)). This last-mentioned point is not given in the definition of the laminar stereom type in which the thickness of the sheets is smaller than the space between the individual sheets.

Each individual sheet is permeated by circular or elongated pores (Fig. 2.3 (B), (C)). The pore sizes on one individual sheet appears to be (very) even. Each sheet comprises a strict arrangement of pore rows parallel to the z/c-axis (Fig. 2.3 (B), (C)). The rows of pores are, however, arranged with a misalignment along the z/c-axis, which means that every second pore row is congruent (Fig. 2.3 (C): red arrow). The distance from one pore to the next is almost identical with the pore size. Such strict arrangement of pores and pore shape is not part of Smith's laminar stereom type. The definition by Smith (1980) stated, however, that the 'surface [is] perforated by numerous closely spaced pores of large diameters (p. 40)'. Therefore, it does not mention the kind of pore shape and arrangement, typical for an individual stereom layer. The accompanied SEM images by Smith (1980) give more references about the pore shape, size and arrangement on the stereom sheet. A surface with randomly arranged pores and varying sizes with a circular character can be observed and therefore do not agree with our observation for the layered stereom type.

The cross struts connecting each individual stereom layer are orientated perpendicular to the stereom sheets and are arranged in a periodic way, which means that every second row of cross struts is congruent analogously to the arrangement of pores (Fig. 2.3 (B): red arrow). The perpendicular orientation of the cross struts to the c-axis is to some extent similar to the laminar stereom type. Another similarity is the multilamellar construction of stereom sheets. Further similarities are not present between both stereom types.

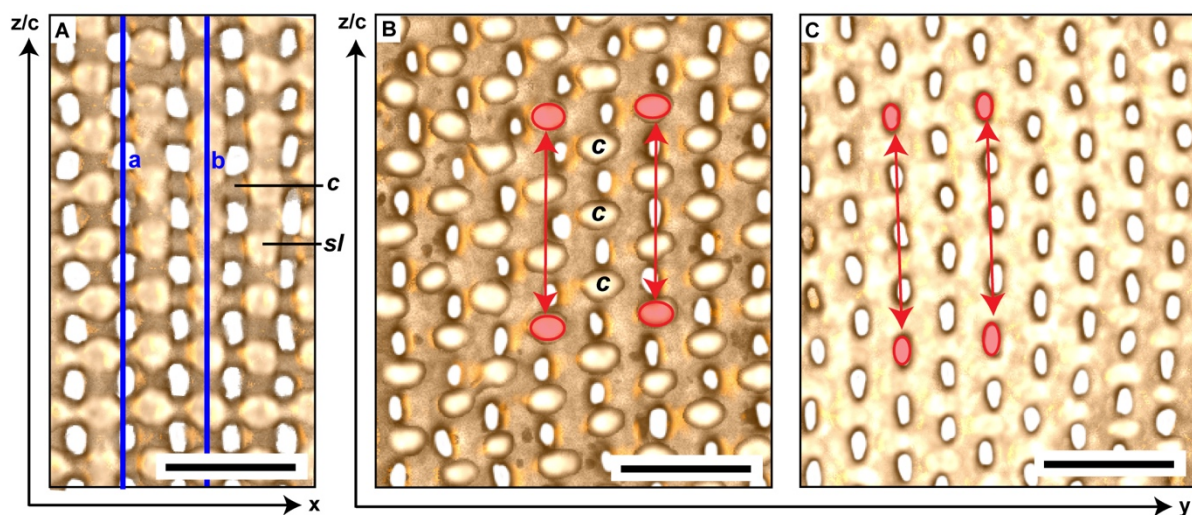


**Fig. 2.3:** Three-dimensional reconstruction of the layered stereom type based on  $\mu$ CT data. Sheets of stereom layers (sl) separated by cross struts (c) characterize the layered stereom type. The blue vertical lines (a) and (b) display the position of the cross sections, which are given in (B) and (C), respectively. The cross section in (B) shows a single stereom layer with cross struts, whereas the cross section in (C) reveals only the circular pores on the stereom sheet. The red arrow indicates the congruence of pores and cross struts in every second row. The scale bars: (A), (B) and (C) = 100  $\mu$ m.

*Columnar stereom.*

This stereom type consists of several long trabecular rods, which are linked by cross struts in such way to produce irregular polygonal passages parallel to the c-axis (Fig. 2.2 (D); Fig. 2.4 (A)). The number of trabecular rods forming one individual columnar stereom varies from 4 to 8 (Fig. 2.4 (A)). If one looks at the columnar stereom type perpendicular to the c-axis, it can be seen that the front and back front pore rows are not congruent (Fig. 2.4 (B), (C): blue and red arrows). In the galleried stereom type by Smith (1980) continuous passageways are present facing at the pores perpendicular to the c-axis, a clear differentiation to the columnar stereom type.

The columnar stereom type is characterized by circular pores (Fig. 2.4 (C)). The lateral pores appear to be smaller or equal in terms of their size compared to the adjacent pores (Fig. 2.4 (C)). The galleried stereom type, however, characterizes the pore size of the lateral pores as smaller than of the adjacent pores. Therefore, the galleried stereom type excludes neighboring equal sized pores in the structure.

Additionally, the lateral pores of the columnar stereom type are arranged in an offset manner to the adjacent pores (Fig. 2.4 (C): green and blue arrows). This misalignment of lateral pores to the adjacent pores is also formed in the galleried stereom type of Smith (1980).

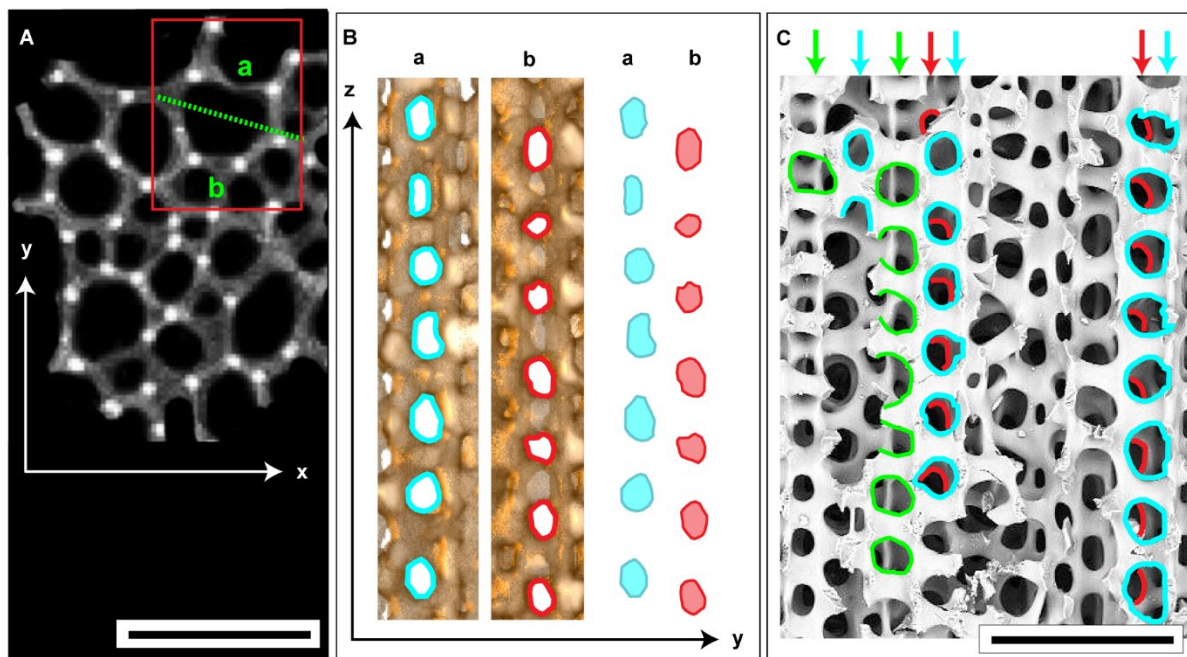


**Fig. 2.4:** Three-dimensional reconstruction and pore arrangement of the columnar stereom. Trabecular rods are displayed in (A) as white dots forming polygonal passages. (B): A cross section parallel to the z-axis of the reconstructed stereom column based on  $\mu$ CT data reveals that the pores on the side (a) and (b) (red and blue pores) show no congruency. A BSE image in (C) demonstrates the non-congruency of the pores from the back (red arrow) and front row (blue arrow) of the columnar stereom. Adjacent/lateral pores from the front pore rows are marked as a green arrow. The scale bars: (A) and (C) = 100  $\mu$ m.

## 2.1.4 Results

### 2.1.4.1 Differentiation between the ‘medulla’ and ‘radiating layer’

The adult spine of *Phyllacanthus imperialis* can be divided into three main areas: cortex, radiating layer and medulla (section 1.3). On the macroscopic level this classification can be recognized by the different colors of the spine interior (section 1.3). A precise definition of the border between the so-called ‘radiating layer’ and ‘medulla’ based on microscopic investigations of the stereom mesh was not yet introduced in the spine structure descriptors of *Phyllacanthus imperialis*. The determination of the ‘medulla-radiating layer-border’ necessitates a definition of the ‘medulla’ and ‘radiating layer’. The formulation of the definition is based on a detailed description of the occurring stereom types and their strut thicknesses from the inner to the outer spine structure. For the characterization of the appearing stereom types the terms ‘medulla’ and ‘radiating layer’ have been explicitly avoided in this section due to absence of a clear definition in the current literature and to avoid misunderstandings. This section displays the varying stereom types and arrangements that can occur directly at the spine tip, near the spine tip ( $\mu$ CT scanned section) and at the middle region of the spine shaft. The positions of the demonstrated regions are summarized in Fig. 2.5. The following characterization is based on images that display the area parallel to the c-axis of the spine.

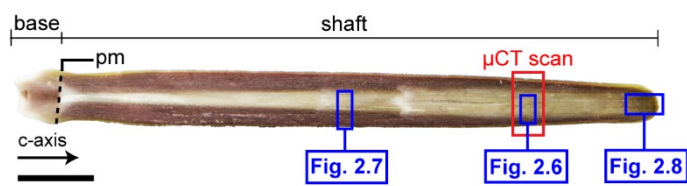


**Fig. 2.5:** Cross section of the spine *Phyllacanthus imperialis* parallel to the c-axis. Red box illustrates the  $\mu$ CT scanned area of the spine. The blue boxes indicate the position of the figures. pm = Prouho's membrane. Scale bar = 1 cm.

#### 2.1.4.1.1 Stereom types and strut arrangement

In the display of varying stereom types and its characterization considering the strut arrangement, the  $\mu$ CT scanned section representing the area near the spine tip is introduced firstly (Fig. 2.6), because of the clearer visibility of the microstructures compared to BSE images. The xy-plane of the spine is shown in Fig. 2.6 (A). The innermost area of the spine is characterized by large, polygonal passages. These polygonal passages are distributed also further out from the inner spine area in form of extended side branches. Starting from the extended side branches lateral strut routes run outwards directly into the cortex. Each lateral strut route is connected in a regular manner with the cortex. The red dashed line in Fig. 2.6 (A) indicates the position of the zx-plane, which is displayed in Fig. 2.6 (B). The center of the spine consists of areas displaying trabecular rods, which are arranged to columns (Fig. 2.6 (B, a<sub>1</sub>, a<sub>2</sub>)), on the one hand, and disorderly arranged struts (Fig. 2.6 (B, b<sub>1</sub>, b<sub>2</sub>)), on the other hand. Particularly towards to the center of the spine, it seems that the quantity of disorderly arranged struts increases compared to regular arranged strut pillars (Fig. 2.6 (B, a<sub>1</sub>, a<sub>2</sub>)). The disorderly strut configuration sequences form a very open structure and the pores are difficult to define as the stereom forms no planar

surface (related to the zy-section). The regular arrangement of the strut pillars belongs to the columnar stereom type, which is prevalent at the area outside the center of the spine (= extended side branches from the spine center). Further towards to the cortex, the regular and strict columnar stereom arrangement changes and forms an unorganized mesh of struts (Fig. 2.6 (B, c)). Compared to the disorderly strut configuration in the spine center, the thickness of the struts seems to be larger here. The three-dimensional tangle of interconnecting struts is limited to a very small space and changes to a blurred assembly of stereom layers towards to the spine exterior (Fig. 2.6 (B, d)). Further outward the blurred stereom layers become more and more apparent so that clear stereom layers are visible, having a regular arrangement and a slight curvature (Fig. 2.6 (B, e)). These stereom layers are part of the lateral strut routes (Fig. 2.6 (A)) and are classified as layered stereom.

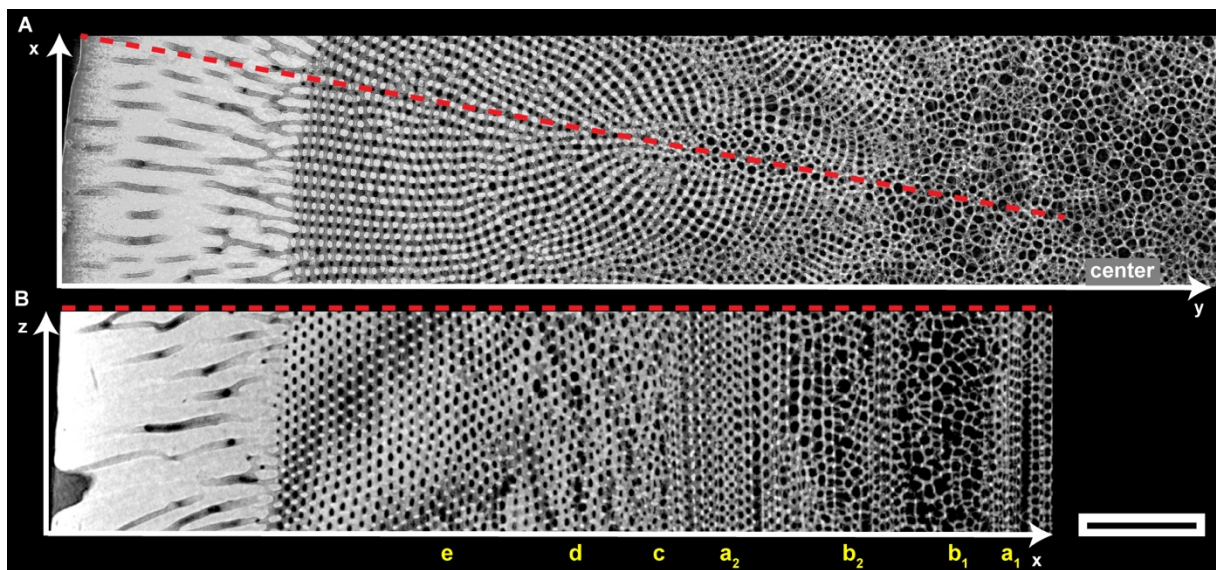


**Fig. 2.6:** Reconstruction of stacked images of the *Phyllacanthus imperialis* spine structure based on  $\mu$ CT images. The xy-plane is given in (A). The red dashed line in (A) displays the position of the vertical cross section, which is illustrated in (B) as zx-plane. Scale bar = 250  $\mu$ m.

The middle region of the spine shaft is displayed in Fig. 2.7. It is quite apparent that the columnar stereom type is substantially more present in the spine center compared to the region near the spine tip. Unorganized stereom meshes are negligible or simply non-existent in the spine center. The basically columnar stereom from the inner center is followed by a kind of transition zone consisting of a disorderly strut configuration and a blurred assembly of stereom layers (the same as described above). The blurred assembly of stereom layers becomes clearer and forms stereom sheets near the cortex.

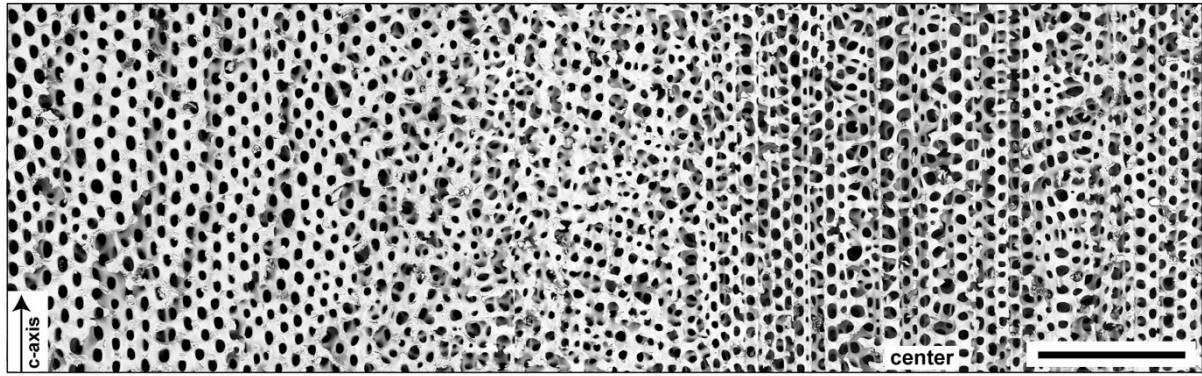


**Fig. 2.7:** BSE image of the spine microstructure of *Phyllacanthus imperialis*. The BSE image displays the cross-sectional plane parallel to the c-axis. The position of the BSE image is illustrated in Fig. 2.5. Scale bar = 250  $\mu\text{m}$ .

The microstructure of the spine tip is displayed in Fig. 2.8 (A), which shows essentially the inner center of the spine. An intensive stereom mélange comprising the columnar stereom type as well as sequences of unorganized stereom meshes can be observed at the lower half of the spine center (Fig. 2.8 (B)). The stereom mélange transforms into a fan-like structure (Fig. 2.8 (C)) resembling those found in the spine tip of *Heterocentrotus mammilatus* (Grossmann and Nebelsick 2013). Comparing both regions of the spine center, it can be recognized that the trabecular rods of the fan-like structure are thicker than those of the stereom mélange (Fig. 2.8 (B), (C)). The trabecular rods of the fan-like structure are arranged in a straight to slightly curved manner (Fig. 2.8 (C)). In this way, a regular arrangement of the pore rows has been formed towards to the spine tip, forming a layer-like stereom structure.

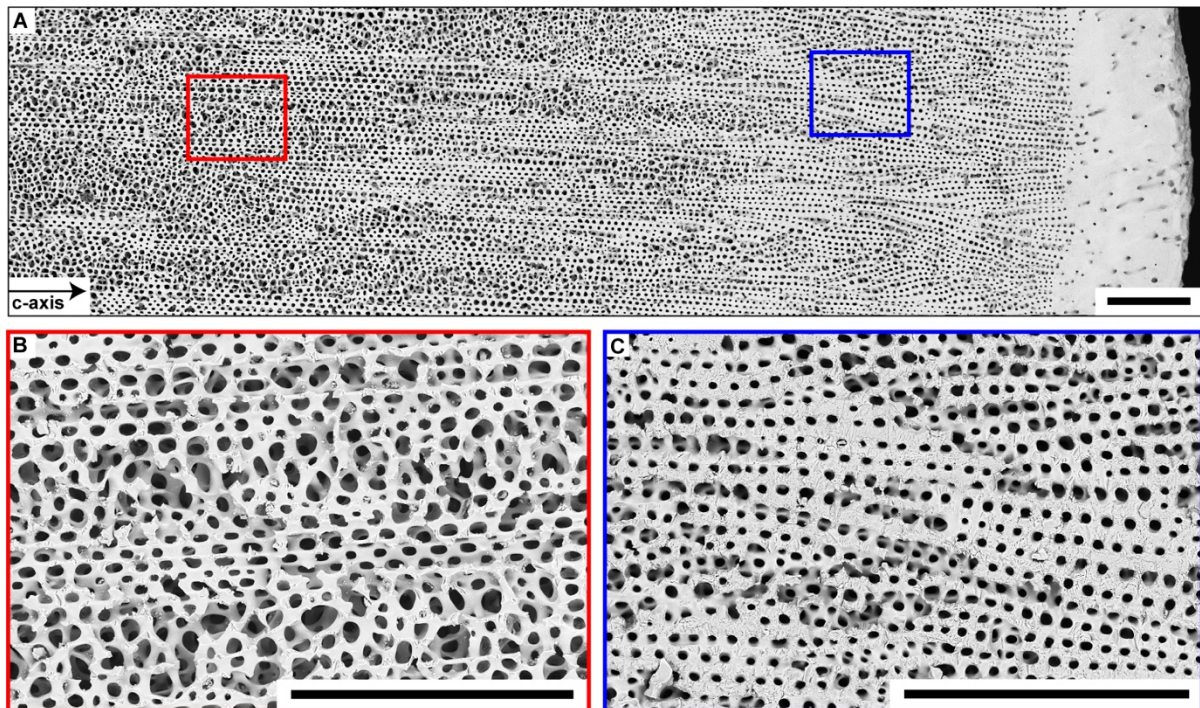


**Fig. 2.8:** BSE images display the spine microstructure of *Phyllacanthus imperialis* (parallel to the c-axis). The exact position of the images is seen in Fig. 2.5 and as red box in (A). The BSE image in (A) shows an overview of the spine tip, whereas a detailed view of certain areas is given in (B) and (C). Scale bars: (A), (B) and (C) = 300  $\mu\text{m}$ .

A closer look into the microstructure reveals that the transition from one to the next stereom type is not separated sharply in terms of the strut configuration. Unorganized stereom meshes and blurred assembling of stereom layers are present in the transition zones. This structural arrangement of the stereom is present both in the middle of the spine shaft and near of the spine tip. In contrast, the configuration of the spine center is dependent on the position of the c-axis: the middle region of the spine shaft is characterized by the columnar and minor parts of disorderly arranged struts, whereas the section near the spine tip is rather marked by an alternation of the columnar stereom type and irregular arranged struts. Since the microstructure of the spine is characterized by transition zones and heterogenous distribution of stereom types in the spine center, a categorization of the microstructure into the 'medulla' and 'radiating layer' cannot be performed only based on the stereom arrangement. Therefore, the trabecular thickness has been considered in determining the border between the 'medulla' and 'radiating layer' clearly. Therefore, the definitions of the medulla and radiating layer also consider the trabecular thickness as parameter.

#### 2.1.4.1.2 Calculated strut thickness

The distribution of the strut thickness from the  $\mu$ CT reconstruction (Fig. 2.6) is displayed in Fig. 2.9. The xy-plane of the spine shows that the struts of the polygonal passages located in the spine center and the lateral strut routes have varying thicknesses (Fig. 2.9 (A)). There is no transition zone regarding the struts thickness between both structural types. There is a clear border between the polygonal passages and the lateral strut routes in terms of the strut thickness: the polygonal passages have a strut thickness of  $< 10 \mu\text{m}$ , whereas the lateral strut routes are  $> 10 \mu\text{m}$ . The green dashed line in Fig. 2.9 (A) indicates the position of the zx-plane, which is displayed in Fig. 2.9 (B).

The distribution of the strut thickness makes obvious that the layered stereom type on the outer spine side and the transition zone, which consists of blurred assembly of stereom layers and unorganized mesh of struts are characterized by the same range of strut thickness of  $> 10 \mu\text{m}$  (corresponding to the lateral strut routes illustrated in Fig. 2.9 (A)). It can clearly be seen that there is a sharp border between the irregular mesh of struts and the adjacent columnar stereom type in the light of the thickness distribution. The columnar stereom type alternating with disorderly arranged struts in the spine center is related to the polygonal passages (Fig. 2.9 (A)) and therefore refers to the same strut thickness range of  $< 10 \mu\text{m}$ .

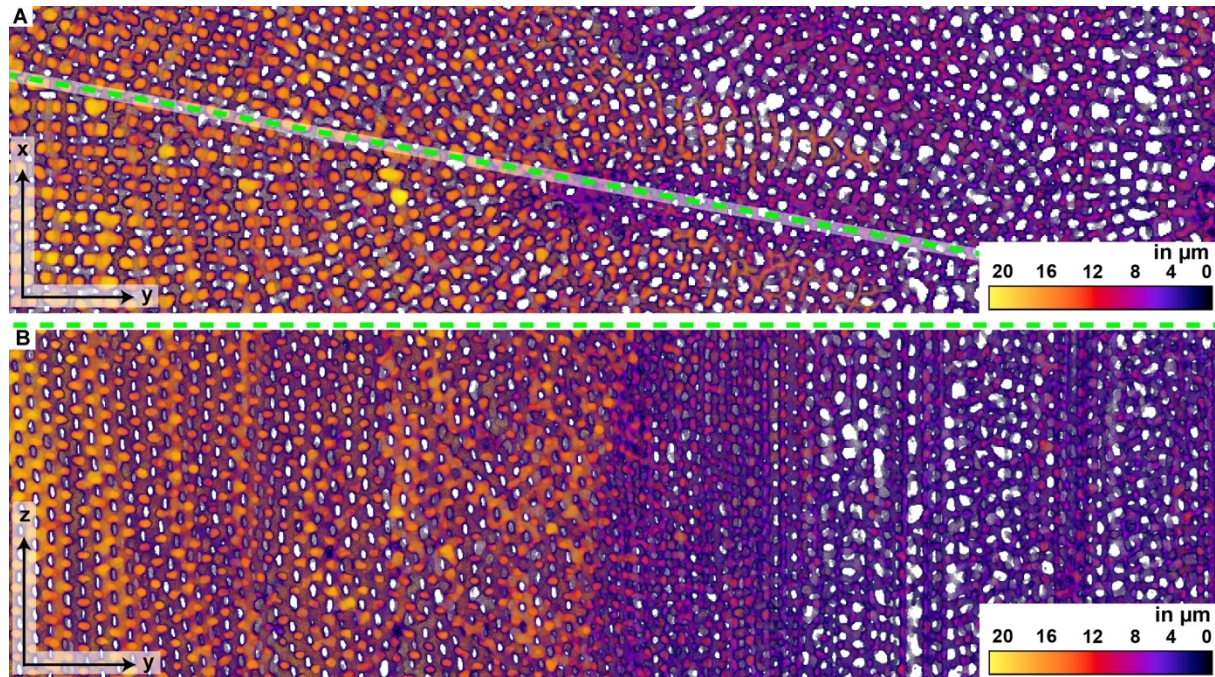


**Fig. 2.9:** Calculated strut thickness distribution in the microstructure of the spine of *Phyllacanthus imperialis* based on  $\mu$ CT data. The cross section in (A) demonstrates the zy-plane. The green dashed line represents the position of the cross section illustrated in (B), which is the zy-plane.

#### 2.1.4.1.3 Definition of the ‘medulla and ‘radiating layer’

The addition of the visual evaluation of the strut thickness distribution displays clearly that the categorization of the microstructure into the ‘radiating layer’ and ‘medulla’ is not strictly dependent on the configuration of the stereom itself, but is rather correlated with the strut thickness.

Only the use of the configurational shape of the strut meshes (expressed as stereom type) is rather misleading for the differentiation between the ‘medulla’ and ‘radiating layer’, since one structural form can occur multiply in the microstructure (i.e. the unorganized strut meshes). The definition of the ‘radiating layer’ and ‘medulla’ can be set for the microstructure of the spine of *Phyllacanthus imperialis* in consideration of the stereom mesh configuration and strut thickness as follows:

##### *Medulla.*

Microstructure is mainly marked by polygonal passages (perpendicular to the c-axis), which expand partially as radial side branches towards to the cortex. The polygonal passages belong typically to the columnar stereom type and often with a strut thickness of  $< 10 \mu\text{m}$ . The side branches of the medulla’s cross section form a circular base.

##### *Radiating layer.*

The microstructure is marked by the layered stereom type. The stereom sheets are arranged in form of layers in the spine structure, which appear curved or almost straight routes perpendicular to the c-axis.

Each layer/route is connected with the cortex and runs almost straight or slightly curved to the nearest radial side branches (perpendicular to the c-axis) of the medulla. The thickness of the struts is  $> 10 \mu\text{m}$ .

### 2.1.4.2 Numerical determination of the strut thickness and porosity

#### 2.1.4.2.1 Step-wise analysis of the strut thickness

The strut thickness of the radiating layer and medulla has been determined numerically by the analysis of stacked cubes from the  $\mu\text{CT}$  data. Each stacked  $\mu\text{CT}$  cube had a y-, x-, and z- edge length of  $140 \mu\text{m}$ ,  $160 \mu\text{m}$  and  $882 \mu\text{m}$ , respectively. Examples of the stacked  $\mu\text{CT}$  cube from the radiating layer and the medulla are illustrated in Fig. 2.10 (A). The results of the average strut thicknesses of each stacked  $\mu\text{CT}$  cube and their positions within the microstructure of the spine are displayed in Fig. 2.10 (B). Apparently, the radiating layer has a strut thickness gradient. The strut thickness decreases from the outside to the inside: it decreases from the average strut thickness of  $15.7 \mu\text{m}$  (= position 1) to a value of  $11.6 \mu\text{m}$  (= position 4; Fig. 2.10 (B)). Significantly smaller average values for the strut thickness have been determined for the medulla (Fig. 2.10 (B)) ranging between  $7.0$  and  $9.6 \mu\text{m}$  (Fig. 2.10 (B)). On basis of the data, the average strut thickness for the stereom structures in the medulla and radiating layer has been determined to be  $8 \pm 1.6 \mu\text{m}$  and  $13.7 \pm 2.0 \mu\text{m}$ , respectively (Fig 2.10 (C)).

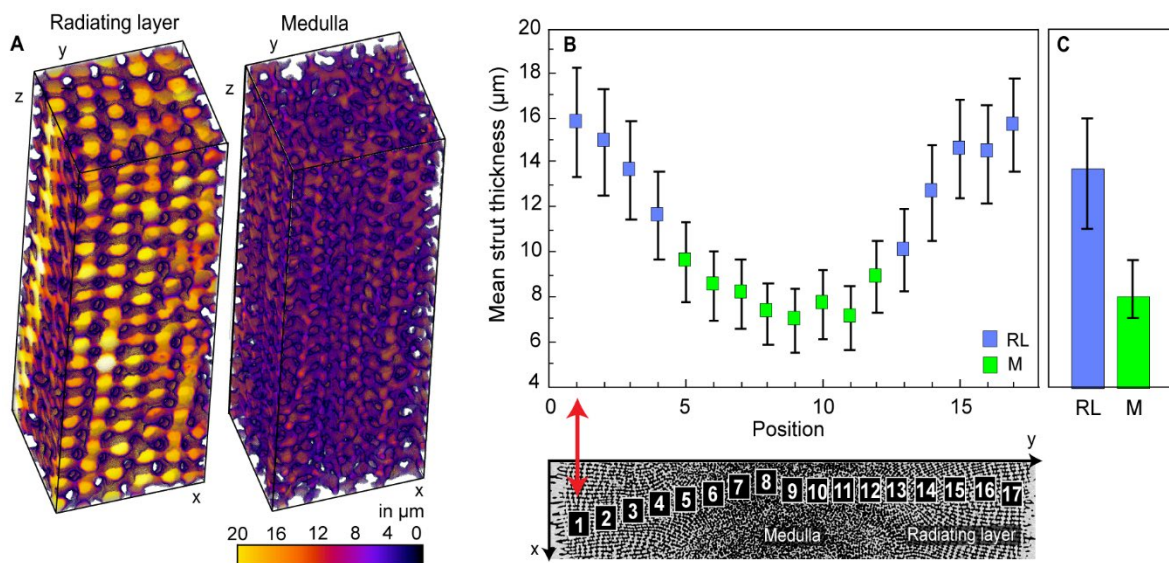


**Fig. 2.10:** Strut thicknesses of the radiating layer (RL) and medulla (M) based on  $\mu\text{CT}$  data of the spine *Phyllacanthus imperialis*. The determination of the strut thickness is based on a step-wise analyses of stacked  $\mu\text{CT}$  cubes. An example of the stacked  $\mu\text{CT}$  cube of the radiating layer and medulla is illustrated in (A). The average strut thicknesses and their positions in the microstructure is given in (B). The plot in (C) represents the average strut thickness for the radiating layer and medulla.

#### 2.1.4.2.2 Porosity of the radiating layer and medulla

The porosity of the radiating layer and medulla has been determined utilizing binarized xy-images of the  $\mu\text{CT}$  data. In this purpose, several binarized images have been chosen from a specific spine position

and have been quantified (section 2.1.2.3). The specific position of the xy-images is related to the cross section parallel to the c-axis of the  $\mu$ CT scanned spine segment (Fig. 2.1). Fig. 2.11 gives the results of the porosity of the radiating layer and medulla depending on the position within the spine microstructure (parallel to the c-axis). The porosity of the medulla varies between 82 and 88 %, whereas the radiating layer ranges between 74 and 79 %. The medulla can therefore be characterized by an average porosity of  $85.7 \pm 2.8$  % and the radiating layer of  $76.6 \pm 3.0$  % (Fig. 2.11 (C)).

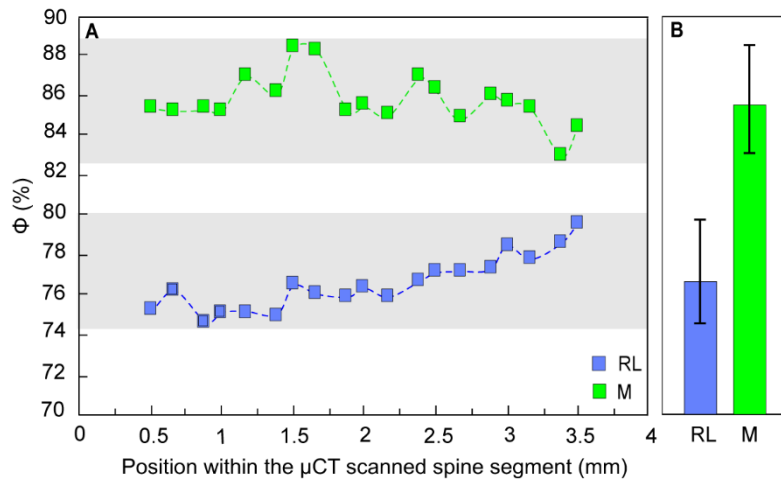


**Fig. 2.11:** Porosity,  $\phi$ , of the radiating layer (RL) and medulla (M) based on the  $\mu$ CT scan data of the spine *Phyllacanthus imperialis*. The position is related to the cross section parallel to the c-axis of the  $\mu$ CT-scanned spine segment (cf. Fig. 2.1). The porosity of the radiating layer and medulla as a function of the position within the spine microstructure is displayed in (A). The average porosity of the radiating layer and medulla is presented in (B).

### 2.1.4.3 The ‘layered’ and ‘columnar’ stereom type

#### 2.1.4.3.1 Numerical characterization of the ‘layered’ and ‘columnar’ stereom type

The numerical characterization of the layered and columnar stereom type is related mainly to the pore size expressed as  $a_2$  and  $a_1$  axis representing the smallest and the largest axis of the pore, respectively. In this context, the zx- and zy-planes were used to determine the pore axis lengths. Characterizing the layered stereom type includes also the size of the joints of the cross struts (expressed as axis length  $c_2$  and  $c_1$ ) and the distances of the pores on an individual stereom layer.

A stacked  $\mu$ CT section displaying parts of the layered and columnar stereom of the *Phyllacanthus imperialis* spine is illustrated in Fig. 2.12. Parts of the layered stereom is highlighted in the turquoise and green boxes, whereas the columnar stereom with its cross-sectional planes is displayed in the yellow boxes. The measurement of the respective axis is also shown in red. Tab. 2.1 summarizes the results of the pore distances on the stereom layer, pore axis lengths and axis lengths of the cross-strut joints. It displays the average values of the analysis. The statistical distributions of all parameters mentioned above (Fig. A.1, Fig. A.2) and examples of some analyzed  $\mu$ CT sections of the radiating layer are included in the appendix (Fig. A.3, Fig. A.4).

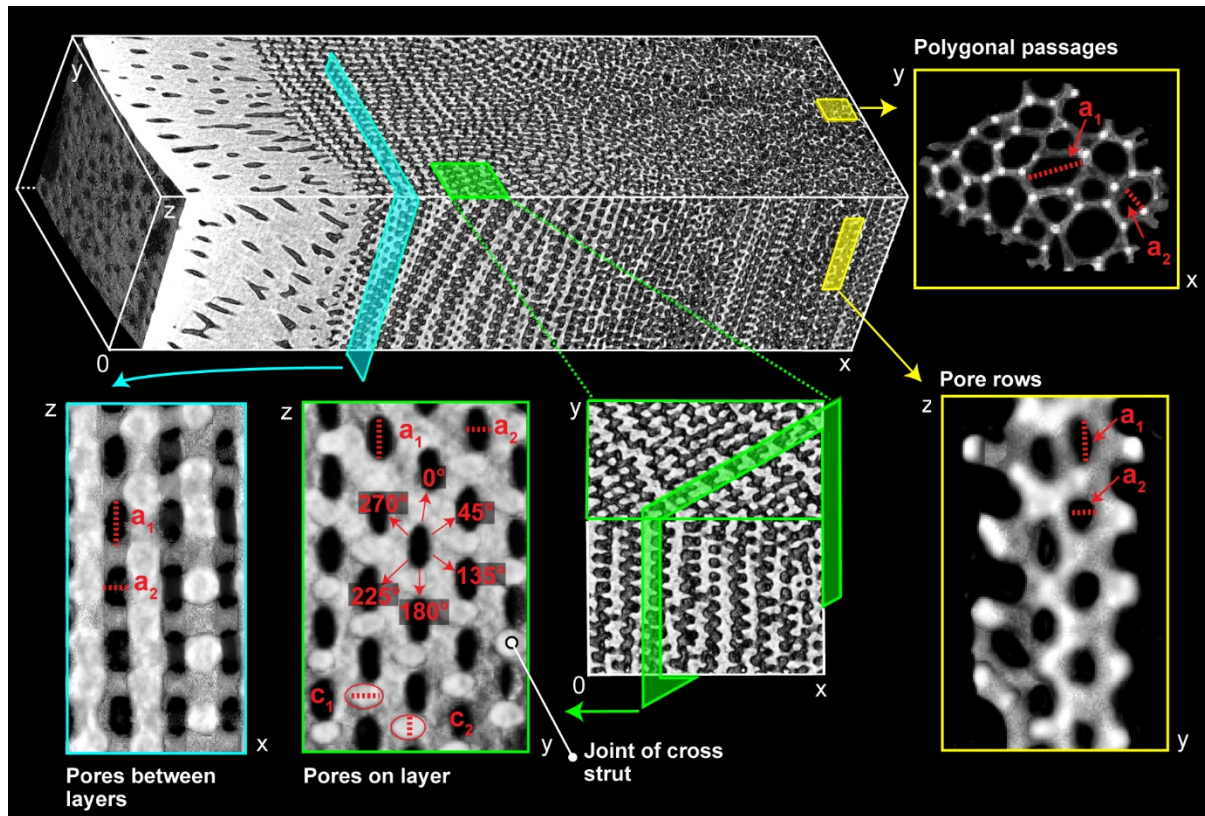


**Fig. 2.12:** A stacked  $\mu$ CT section displaying parts of the layered and columnar stereom of the spine of *Phyllacanthus imperialis*. The different cross-sectional planes of the layered stereom type are displayed in the turquoise and green boxes. Parts of the columnar stereom type are presented in the yellow boxes. The measurement of the axis is displayed in red and comprises the parameters as follows: pore sizes, pore distances and sizes of the cross struts. The smallest and largest axis is given as  $a_2$  and  $c_2$  as well as  $a_1$  and  $c_1$ , respectively.

**Tab. 2.1:** Stereom types in the spine of *Phyllacanthus imperialis* with their axis lengths of the pores, cross struts and pore distances. The values of  $a_1$  and  $c_1$  as well as  $a_2$  and  $c_2$  represent the longest and smallest axis, respectively. The respective pore distances on the stereom sheet from the layered stereom are displayed with their specific orientations. The average measured axis lengths are illustrated in Fig. 2.12.

Layered stereom type				Columnar stereom type	
ZY-plane (stereom sheet)				ZY-plane	
Joints of cross struts		Pore distance		Pore rows	
$c_1$ ( $\mu\text{m}$ )	$c_2$ ( $\mu\text{m}$ )	Orientation ( $^\circ$ )	Distance ( $\mu\text{m}$ )	$a_1$ ( $\mu\text{m}$ )	$a_2$ ( $\mu\text{m}$ )
16.8	9.5	0	14.1	19.6	17.4
Pores on layer		45	15.7		
$a_1$ ( $\mu\text{m}$ )	$a_2$ ( $\mu\text{m}$ )				
19.9	12.8	135	15.2		
ZX-plane		180	15.0		
Pores between layers		225	14.8	Polygonal passages	
$a_1$ ( $\mu\text{m}$ )	$a_2$ ( $\mu\text{m}$ )			$a_1$ ( $\mu\text{m}$ )	$a_2$ ( $\mu\text{m}$ )
17.7	10.1	270	14.0	22.0	17.4

The results of the layered stereom type indicate that the pores on the zy- and zx-plane reach similar average values in terms of their axis lengths (zx-plane:  $a_1 = 17.7 \mu\text{m}$ ,  $a_2 = 10.1 \mu\text{m}$ ; zy-plane:  $a_1 = 16.8 \mu\text{m}$ ,  $a_2 = 9.5 \mu\text{m}$ ). The statistical distribution of the pore axis lengths of the layered stereom type is displayed in Fig. A.1, Fig. A.2 and Fig. A.3 (Appendix). The different size of the average pores axis lengths of both sectional planes is an indicator for oval-shaped channels. The joints of the cross struts are characterized by an average  $c_1$  and  $c_2$  value of 16.8 and 9.5  $\mu\text{m}$ , respectively. Therefore, the average axis lengths of the cross struts reach a similar size as the pores on the stereom layers and the channels between the stereom layers (Tab. 2.1). The average pore distances on an individual stereom layer are in the range of 14.0 and 15.7  $\mu\text{m}$ . The numerical results indicate a high regularity and symmetry in which the pores and the cross struts are arranged with a strict order in the layered stereom type.

The statistical distribution of the pore axis lengths of the columnar stereom type is shown in Fig. A.4 (Appendix). The columnar stereom type is also characterized by a regular arrangement of pores (Fig. 2.12; zy-plane in yellow). The average pore axis lengths of the polygonal passages ( $a_1 = 22.0 \mu\text{m}$ ,  $a_2 = 17.4 \mu\text{m}$ ) and of the pore rows of the columnar stereom ( $a_1 = 19.6 \mu\text{m}$ ,  $a_2 = 14.7 \mu\text{m}$ ) are larger compared to the pores of the layered stereom type. The smaller difference between the average pore axis lengths of the columnar rows indicates that the pores have a rather circular than an oval character (Tab. 2.1).

#### 2.1.4.3.2 Numerical comparison with the galleried and laminar stereom type

Grossmann and Nebelsick (2013) analyzed the spine structure of *Phyllacanthus imperialis*. They characterized the medulla and the radiating layer consisting of the galleried and the laminar stereom, respectively. Besides their structural stereom classification of the medulla and radiating layer according to Smith (1980), they have determined the pore sizes and strut thicknesses of the respective stereom types as well. Smith (1980) has also characterized the galleried stereom type in regard to its pore size and strut thickness. But his results are related to the general galleried stereom architecture of external plate surfaces from echinoids and are thus not directly related to the microstructure of the spine of *Phyllacanthus imperialis*. Therefore, the data of the galleried stereom architecture of Smith (1980) might be considered as addition. This section focuses therefore on the comparison between average pore diameter and strut thickness emerging from this work (section 2.1.4.2.1 and 2.1.4.3.1) and from Grossmann and Nebelsick (2013).

Fig. 2.13 summarizes the relationship of the average pore sizes and strut thicknesses of the stereom structure prevailing in radiating layer and medulla. Grossmann and Nebelsick (2013) reported for the stereom structures in the radiating layer an average pore diameter of 20.2  $\mu\text{m}$  and average strut thickness of 17.8  $\mu\text{m}$  (Fig. 2.13). This is in agreement with the data obtained from this work for the stereom structures of the radiating layer (average pore diameter = 16.3  $\mu\text{m}$ , average strut thickness = 13.7  $\mu\text{m}$ ). Significant differences display, however, the average pore diameters and strut thicknesses of the stereom

structures occurring in the medulla (Fig. 2.13). Grossmann and Nebelsick (2013) have determined an average pore diameter and strut thicknesses of 18.6  $\mu\text{m}$  and 18.6  $\mu\text{m}$ , respectively. This study has determined an average pore diameter of 17.3  $\mu\text{m}$ , but the average strut thickness is 8.0  $\mu\text{m}$ , which is significantly smaller than the average strut thickness determined by Grossmann and Nebelsick (2013). This average strut thickness and pore diameter of the medulla are located in the field, which is characteristic for the galleried stereom type determined by Smith (1980) occurring in the external plate surfaces of echinoids (Fig. 2.13).

The difference in strut thickness between Grossmann and Nebelsick (2013) and our study is possibly due to natural variations. Slightly modified environmental changes for a short time may influence the calcification and resorption process in the skeleton of the sea urchin. Pore sizes and strut thicknesses of the spine microstructure may slightly vary within the same species in this way.

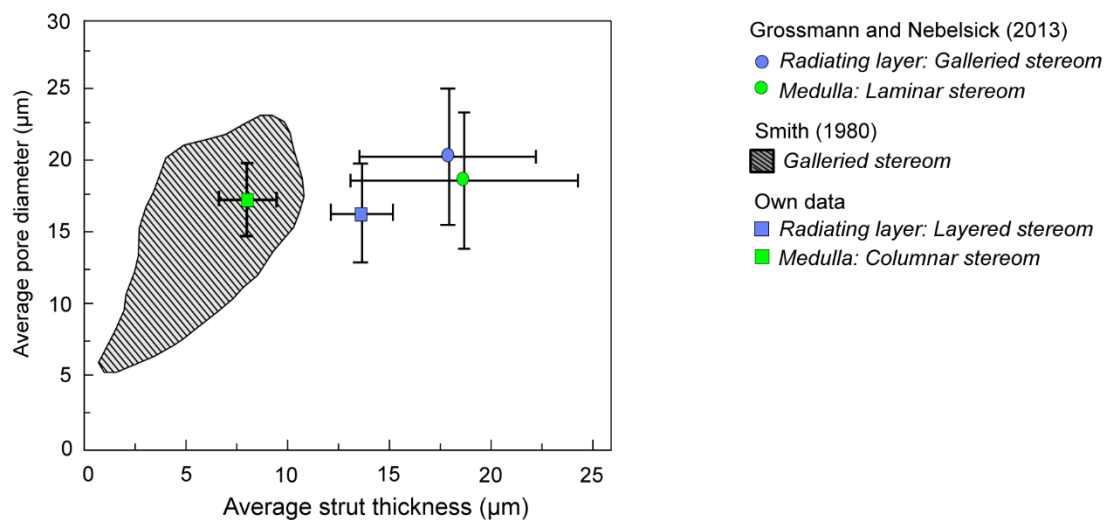


**Fig. 2.13:** Average pore diameters and strut thicknesses of certain stereom types. The displayed data of Grossman and Nebelsick (2013) and this study represent the results of the spine microstructure of *Phyllacanthus imperialis*. The data of Smith (1980) come from the general galleried stereom architecture occurring in external plate surfaces of echinoids.

#### 2.1.4.4 Superstructures

The microstructure of the spine of *Phyllacanthus imperialis* is also characterized by superstructures. Two types of superstructures can be distinguished in the spine microstructure. A superstructure comprises two stereom types, as their mutual distribution forms a superordinate structure. In another case, a superstructure can also appear in a single stereom type. In this case, the strut configuration is slightly modified resulting in a subordinate structure, which is not obviously visible on every cross-sectional level. This kind of superstructure can be limited to cross-sectional level and is therefore visible only on this level. The identified superstructures of the spine of *Phyllacanthus imperialis* are presented in the following.

Fig. 2.14 displays the superstructures of the medulla of the spine of *Phyllacanthus imperialis*. A reconstructed z-projection of the spine microstructure focusing mainly on the medulla is presented in

Fig. 2.14 (A). The area of the medulla is framed with a yellow line and forms radial side branches. In the center of the medulla is a dense and radial arrangement of cross struts forms a kind of ‘bulge’ (Fig. 2.14 (A), (B)). Since this bulge-like structure is visible on the xy-plane only, the bulge-like structure is here referred to as two-dimensional bulge and is a superstructure of the medulla. The two-dimensional bulge consists of radially arranged cross struts, which are oriented to the center of the bulge (Fig. 2.14 (B)). The center of the two-dimensional bulge comprises, however, rather a disordered arrangement of cross struts (Fig. 2.14 (B)). On the macroscopic scale, these bulges appear as bright, circular and dense structures, which are surrounded by areas of higher porosity (Fig. 2.14 (C)).

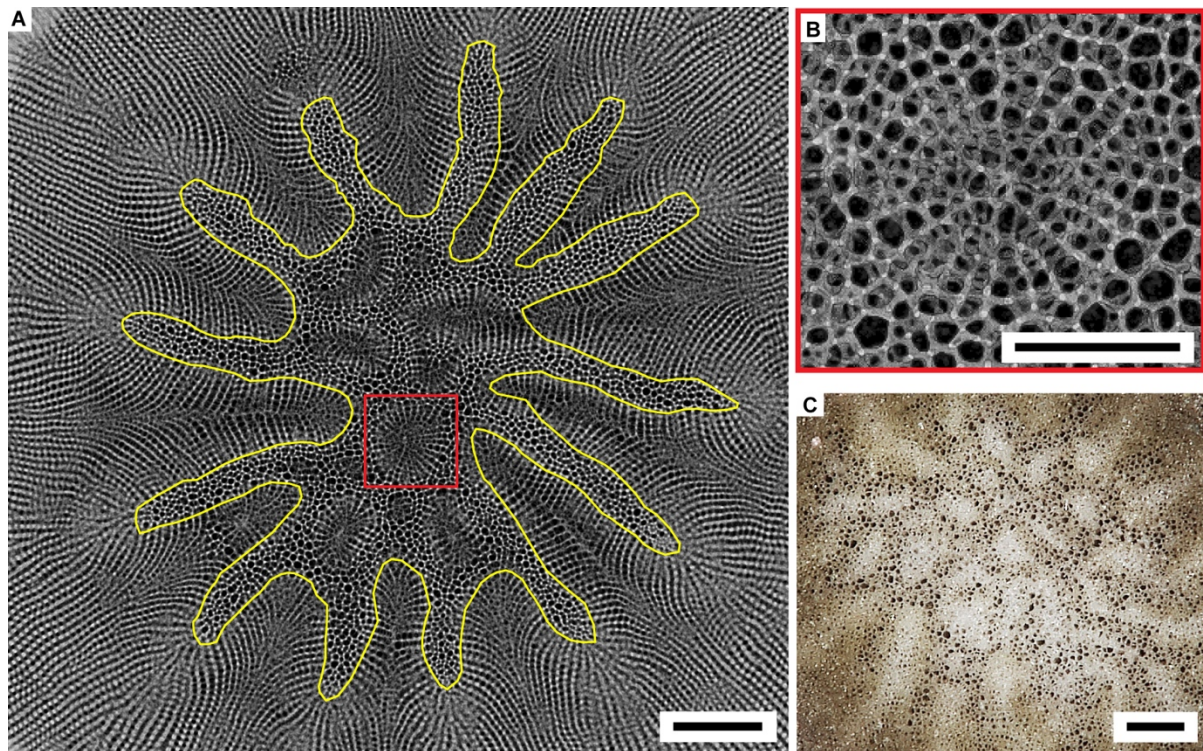


**Fig. 2.14:** Superstructures within the medulla of the spine of *Phyllacanthus imperialis*. The reconstructed z-projection of the spine based on  $\mu$ CT data is given in (A). The area marked with yellow lines is the medulla comprising the columnar stereom type and structural two-dimensional bulges. The structural shape of a single two-dimensional bulge is displayed in a greater resolution in (B; red box). An optical image of the medulla is given in (C). Scale bars: (A), (B) and (C) = 250  $\mu$ m.

The BSE images in Fig. 2.15 illustrate the medulla of the spine of *Phyllacanthus imperialis* with its two-dimensional bulges. Compared to the z-projection of the  $\mu$ CT data, the BSE mode does not reveal the radial character of the cross struts of the two-dimensional bulges (Fig. 2.15 (A)). The BSE images, however, illustrate that the cross struts of the two-dimensional bulges are larger compared to the adjacent cross struts (Fig. 2.15 (A), (B)). An image analysis of the strut thickness of the two-dimensional bulge confirms this statement (Fig. 2.15 (C)): the color of the cross struts appears to be brighter than of the adjacent cross struts, which is an indication for a larger strut thickness. A precise numerical quantification of the strut thickness of the two-dimensional bulge is rather inappropriate, since the color differences of the adjacent cross struts and of the bulge is very small.

The two-dimensional bulges are permanently present in the medulla of the spine shaft of *Phyllacanthus imperialis*, but are not found in the spine base, which is the area beneath Prouho's membrane (Fig. 2.15 (D)). The size, expansion and strut thickness of the polygonal passages in the medulla at the spine base appear to be much more regular than to those which are located in the spine shaft (Fig. 2.15 (D)).

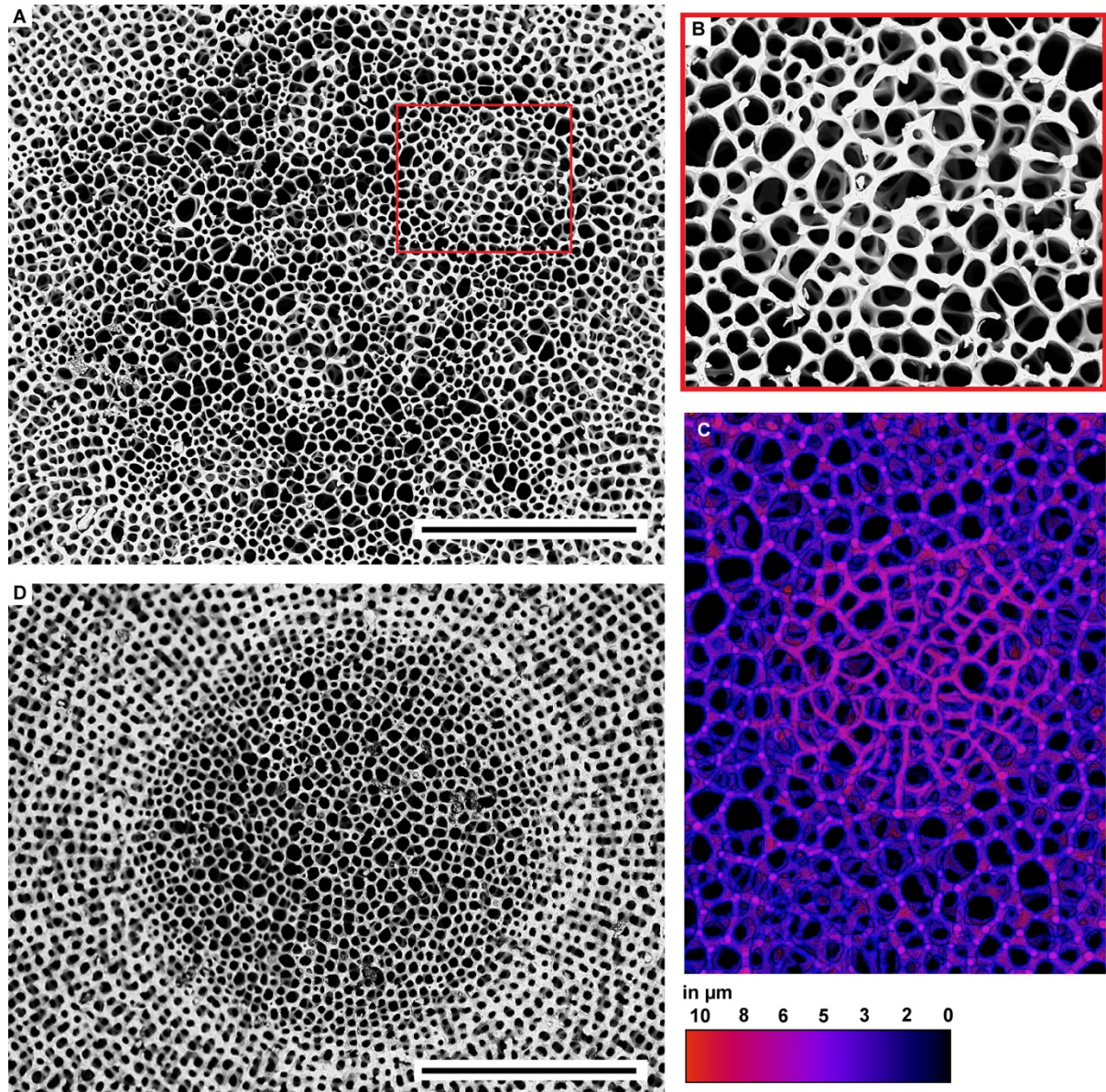


**Fig. 2.15:** Presence and absence of structural two-dimensional bulges within the medulla of the spine of *Phyllacanthus imperialis*. BSE image (A) displays the medulla, which consists of superstructures in the form of two-dimensional bulges. The BSE image (B) gives a greater resolution of a single two-dimensional bulge. The strut thickness of two-dimensional bulge and adjacent cross struts is visualized in (C). The morphology of the medulla beneath Prouho's membrane (cf. Fig. 2.5) is given in (D). The scale bars: (A) = 500 μm, (B) = 500 μm, (C) = 500 μm and (D) = 500 μm.

Taking the stereom structures of the radiating layer and medulla together, another superstructure becomes visible in the spine microstructure of *Phyllacanthus imperialis*. This kind of superstructure is described in more detail below. A reconstructed z-projection of the μCT scanned spine structure is

displayed in Fig. 2.16 (A). The radiating layer consists of several individual stereom layers (Fig. 2.16 (A): yellow solid lines). Each single stereom layer is connected with the cortex. Starting from the cortex, each single stereom layer runs directly to the nearest side branch of the medulla in a straight to slightly curved manner. In this way, a group of several stereom layers forms a ‘wedge-like’ structure that encloses a side branch of the medulla. This sort of superstructure, where a group of stereom layers enclose a side branch of the medulla, is here called ‘wedge’ (Fig. 2.16 (A): yellow dashed lines). In total, 13 wedges have been determined in the adult, aboral spine of *Phyllacanthus imperialis* (Fig. 2.16 (B)).

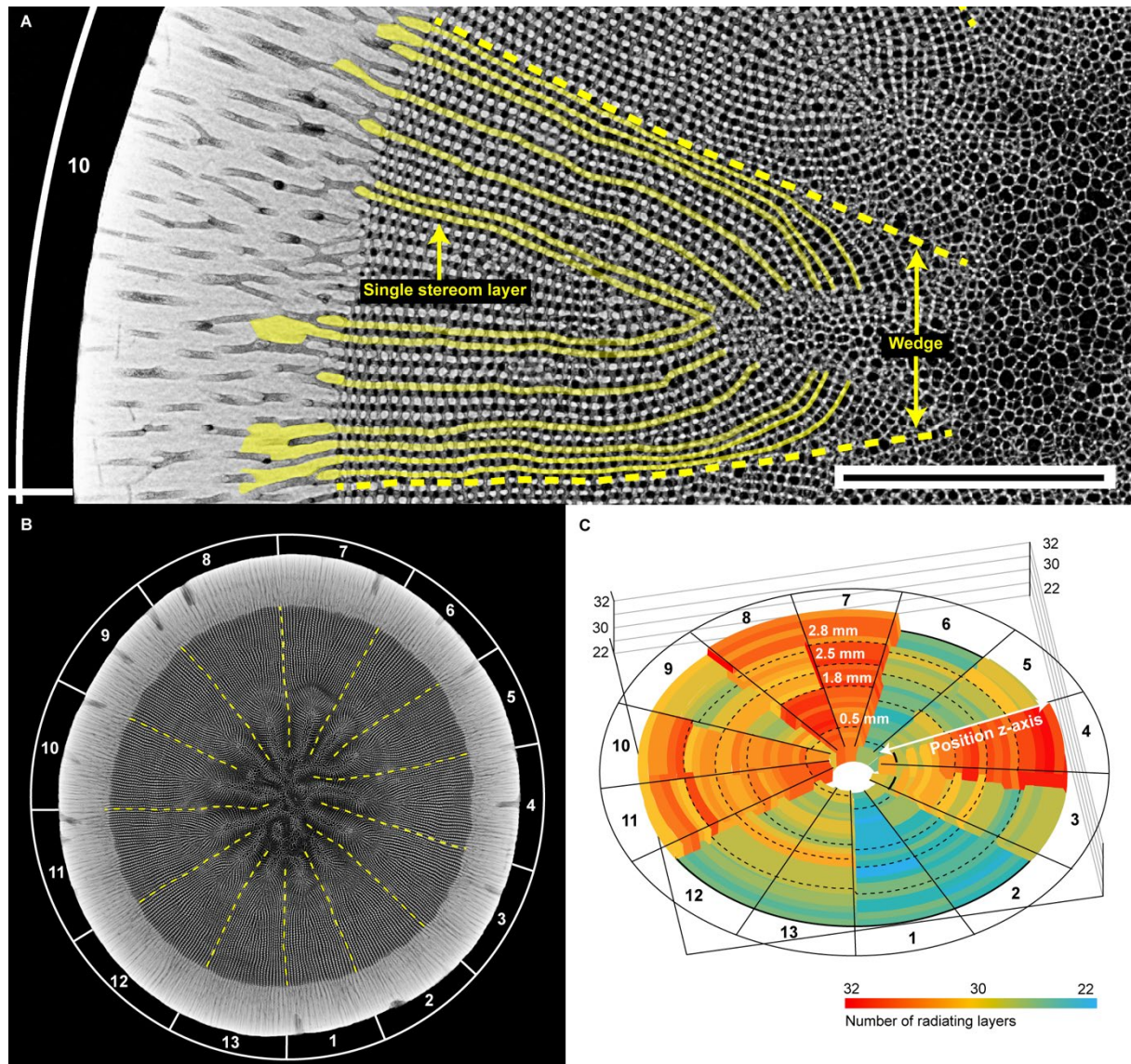


**Fig. 2.16:** Superstructure of the spine of *Phyllacanthus imperialis*. The reconstructed z-projection image ( $\mu$ CT) in (A) shows that several single stereom layers (yellow solid lines) form a wedge (dashed yellow line). The spine consists of 13 wedges, which is illustrated in (B). Results of the counting of the single stereom layers in each wedge are presented in (C). Scale bar: (A) = 500  $\mu$ m.

In order to establish whether the number of stereom layers is homogeneously distributed in the wedges, the stereom layers of each wedge have been determined as well. Several images displaying the z-projection of the  $\mu$ CT scanned spine structure have been considered for the counting of the stereom layers. The analyzed z-projection images can be assigned to a certain z-position (= c-axis) in the  $\mu$ CT scanned range of the spine segment (Fig. 2.1). The results of the counting of the single stereom layers, which are related to wedge system, are displayed in Fig. 2.16 (C). The position of each wedge is given here as number. The color bar shows the number of the stereom layers. The position of the images in  $\mu$ CT scanned range of the spine is given in form of mm-levels (Fig. 2.1). In this case, the outer region of the diagram represents the results that are based on z-projection images, which were taken from the top of the  $\mu$ CT scanned spine segment (z-position = 2.8 mm). Results of the z-projection images belonging to the lower area of the  $\mu$ CT scanned range are located inside of the plot (z-position = 0.5 mm).

The results display that 5 wedges consist of more than 28 single stereom layers (Fig. 2.16 (C)), which are wedge 4, 7, 8, 10 and 11. This number have been also determined in several z-projection images, when comparing the outer and inner area of the plot (Fig. 2.16 (C)). The wedges containing more than 28 single stereom layers are here classified as ‘dominant wedges’. Except of wedge 4, the dominant wedges are arranged in pairs. Overall, the dominant wedges are arranged in a roughly trigonal manner in the spine structure.

### 2.1.4.5 Cortex

#### 2.1.4.5.1 Inner structure

The inner microstructure of the cortex with its pore size, porosity and quantity of pores is displayed in this section. A stacked  $\mu$ CT section of the cortex is illustrated in Fig. 2.17 (A). The cortex is pervaded with pore channels oriented almost perpendicular to the z-axis.

The interior microstructure of the cortex can be visualized utilizing several sections (Fig. 2.17 (B)-(F)). Besides the small pores, the external morphology of the cortex contains also comparably large pores appearing very irregularly in their shape (Fig. 2.17 (B)). Their pore channels, however, cannot be pursued deeply into the internal microstructure of the cortex and are not present in the outer half of the cortex (Fig. 2.17 (B)-(D)). The quantity of pores increases visually from the outside to the inside (Fig. 2.17 (C)-(F)).

On the basis of the  $\mu$ CT sections, the pore size, porosity and the quantity of pores of each section has been determined in this way. The pore size distribution expressed as pore axis lengths ( $a_1$  = smallest axis and  $a_2$  = largest axis of the pore) of each section is displayed in Fig. A.5 (Appendix). An  $\mu$ CT section of the cortex is displayed in Fig. A.6 (Appendix). The results of the average pore diameters (see also Fig. A.5, Appendix) and the quantity of pores for each section are presented in Fig. 2.18. The largest average pore diameter of 28  $\mu$ m is found on the external surface of the cortex. The average pore diameter, however, remains almost constant from the outside to the inside (Fig. 2.18) and varies between

15  $\mu\text{m}$  (Interior (a)) and 17  $\mu\text{m}$  (Interior (c)). In contrast, a gradual increase of the quantity of pores is clearly visible from the inside to the outside of the cortex (Fig. 2.18): from the 950 pores (Exterior) the quantity of pores increases to about 2500 pores (Interior (c)).

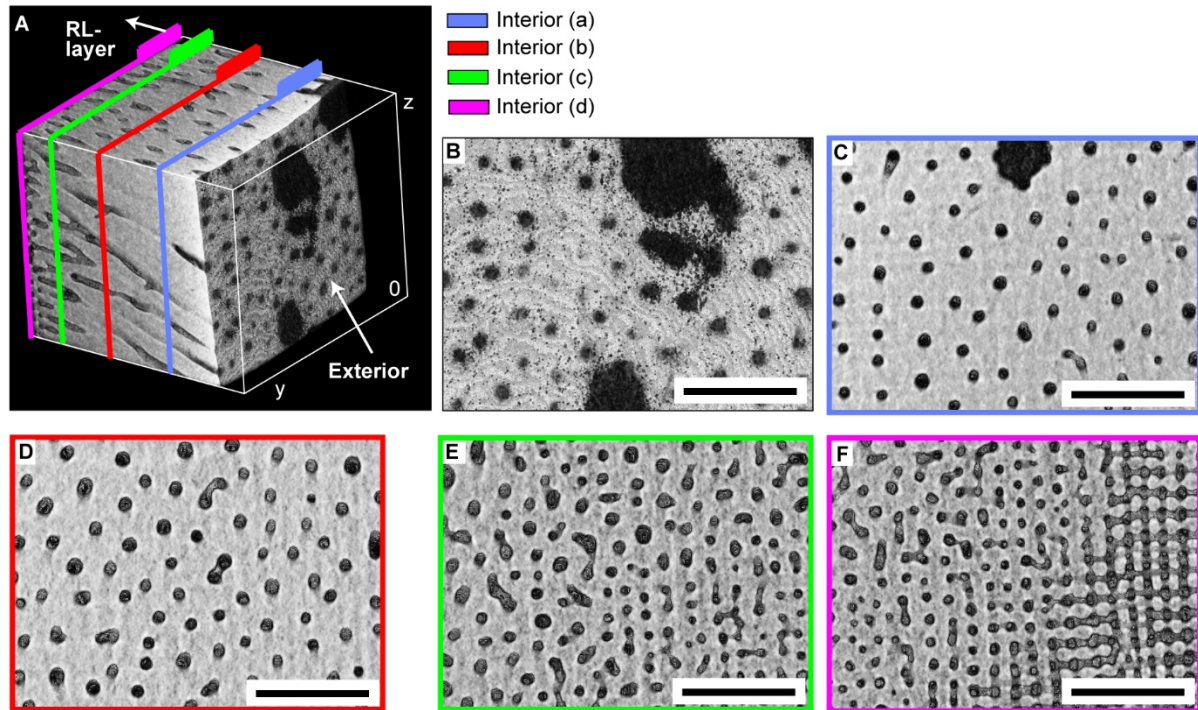


**Fig. 2.17:** Stacked  $\mu\text{CT}$  section of the cortex of the spine of *Phyllacanthus imperialis*. An overview of the cortex with the according section is given in (A). The BSE images (C-E) from the sections are colored in (A). The BSE in (B) displays the external surface of the cortex. Scale bars: (B), (C), (D), (E) and (F) = 150  $\mu\text{m}$ .

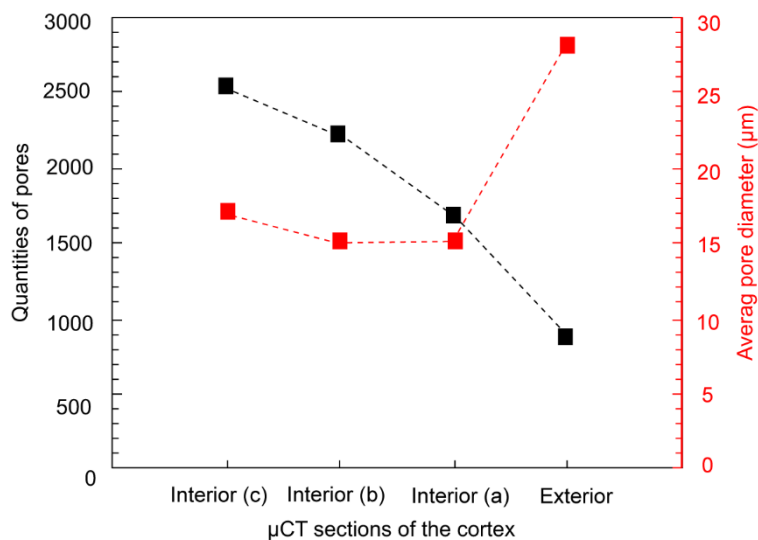


**Fig. 2.18:** Average pore sizes and quantities of pores utilizing  $\mu\text{CT}$  sections of the cortex belonging to the spine of *Phyllacanthus imperialis*.

The porosity of the microstructure of the cortex is illustrated in Fig. 2.19, in which the innermost  $\mu\text{CT}$  sections have been utilized to determine the porosity. Several binarized images of the same section have been utilized for the evaluation of the porosity. The position of the binarized images in  $\mu\text{CT}$  scanned range of the spine is given in form of mm-levels (Fig. 2.1) and is plotted against the porosity

(Fig. 2.19 (A)). The average values of the porosity of each  $\mu$ CT section is shown in Fig. 2.19 (B) and summarizes the results of the porosity of several images along the z-axis (Fig. 2.19 (A)). The average porosity increases from the outside to the innermost cortex structure: from an average of  $11 \pm 0.9$  %, the porosity increases up to an average of  $18 \pm 1.0$  %. The grey column in Fig. 2.19 (B) represents the average porosity of the whole cortex calculated from the average porosity of all  $\mu$ CT sections, which is  $15.2 \pm 3.2$  %.

The relative constant pore size with an increasing number of pores and hence expanding porosity from the outside to the inside indicates that the pore channels branch out increasingly towards to the spine interior.

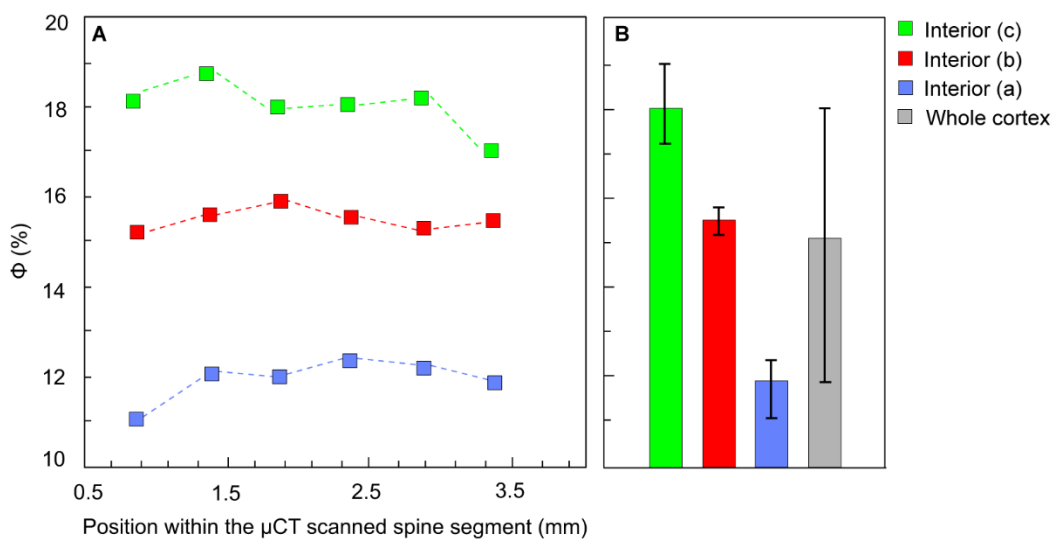


**Fig. 2.19:** Porosity,  $\phi$ , of the cortex of the spine of *Phyllacanthus imperialis*. The porosity of certain  $\mu$ CT sections of the cortex is displayed in (A). The porosity has been determined using binarized images of the  $\mu$ CT scanned range. Each porosity value is therefore related to a specific position in the  $\mu$ CT scanned range. The average porosity of each  $\mu$ CT section and of the whole cortex is displayed in (B).

#### 2.1.4.5.2 Outer structure

The external morphology of the cortex of the spine of *Phyllacanthus imperialis* is displayed below and based on BSE images (Fig. 2.20). The whole external spine structure has been considered in the morphological investigations in this context (Fig. 2.20 (A)). The spine tip is characterized by smooth line-type ridges oriented parallel to the c-axis (Fig. 2.20 (B), (C)) and is also permeated by few pores, which mainly occur in the areas between the ridges (Fig. 2.20 (B), (C)). In total, 13 ridges have been determined at the spine tip, which most likely correlate with the internal wedge system of the spine microstructure (cf. section 2.1.4.4). Further down along the c-axis of the spine, the ridges on the surface become increasingly flatter and are separated by pore rows. Few pores disrupt (perpendicular to the c-axis) the flattened ridges and create rather circular spots (Fig. 2.20 (D): red arrow). The lower part of the external surface of the spine still contains line-type arrangement of the ridges, but they are not present

anymore as smooth straight lines such as at the spine tip. A single line-type ridge comprises several swollen polygonal spots, which appear irregular in their size and shape (Fig. 2.20 (E)). On this scale, there are also no large pores visible between the area of the ridges (Fig. 2.20 (E)). The swollen polygonal spots appear to be more regular in size and shape further down along the c-axis of the spine (Fig. 2.20 (F)), but are still arranged in a line-type manner. No noticeable larger pores are apparent in this section as well (Fig. 2.20 (F)). Near to the spine base, the line-type arrangement of the swollen polygonal spots is not present anymore. The swollen polygonal spots are rather randomly arranged at the spine surface (Fig. 2.20 (G)).

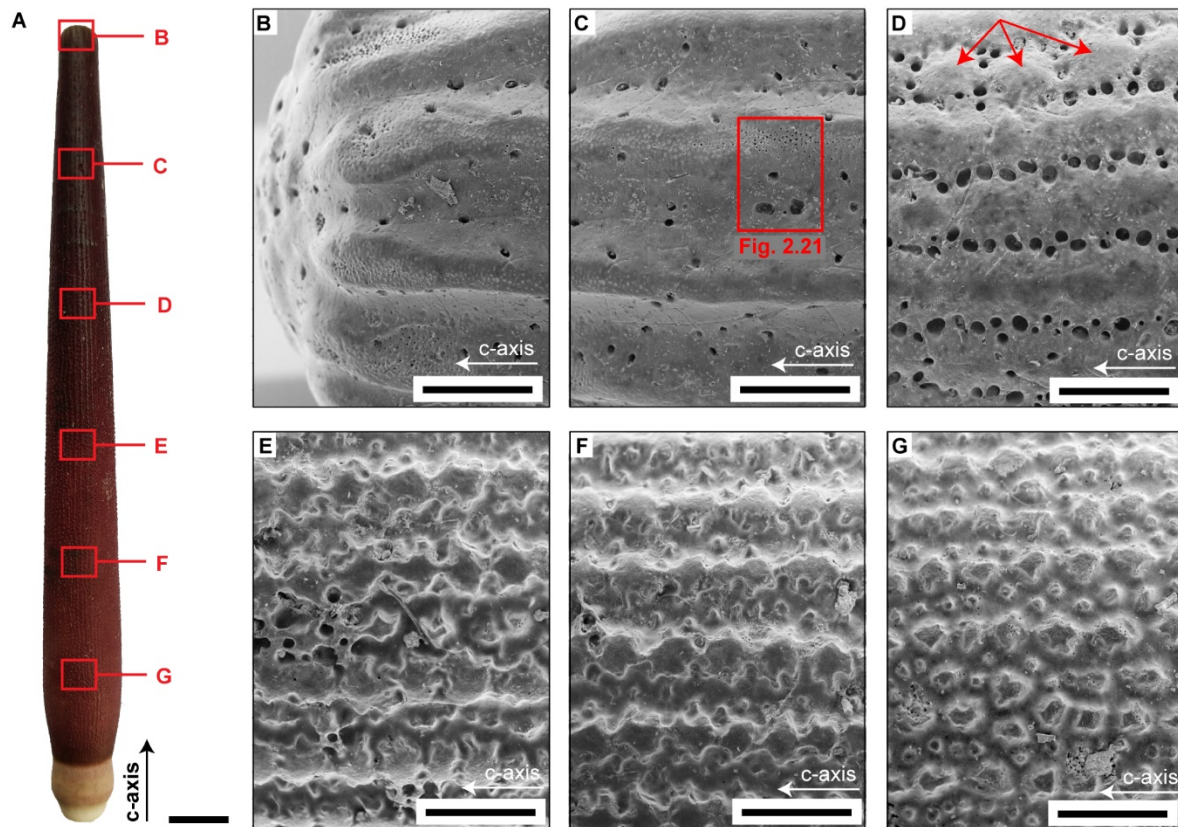


**Fig. 2.20:** Morphology of the external surface of the cortex of the spine of *Phyllacanthus imperialis*. Each position of the BSE images is illustrated in (A). The morphology of the cortex surface is displayed in (B), (C), (D), (E), (F) and (G). Scale bars: (A) = 1 cm, (B) = 1 mm, (C) = 1 mm, (D) = 1 mm, (E) = 1 mm, (F) = 1 mm and (G) = 1 mm.

A higher magnification of the Fig. 2.20 (C) is shown in Fig. 2.21. Besides the clustering of smaller pores on the surface of the spine tip (Fig. 2.21 (A)), a higher magnification reveals basically the polycrystalline character of the external surface of the cortex due to the individual irregular crystallites oriented in all directions (Fig. 2.21 (B), (C)).

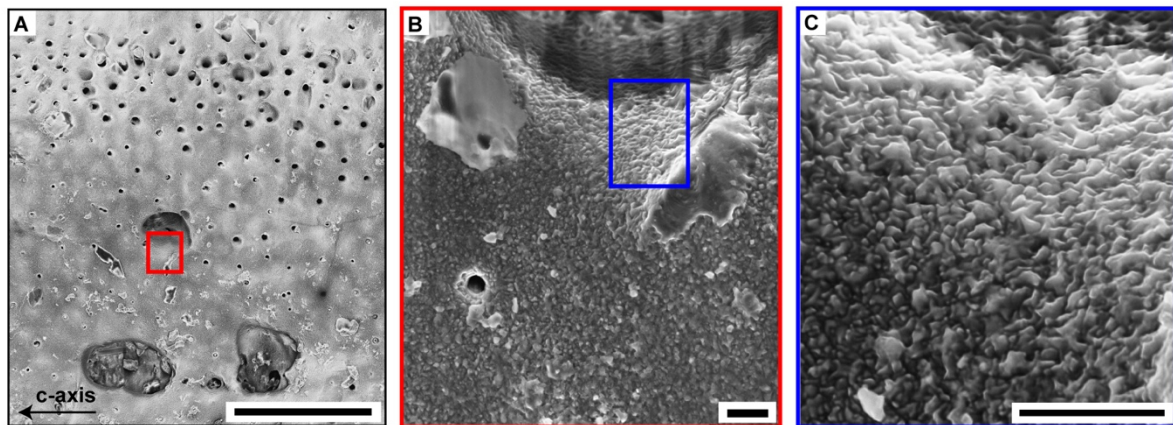


**Fig. 2.21:** A detailed view of the morphology of the external cortex surface of the spine of *Phyllacanthus imperialis*. The BSE image in (A) displays a small section illustrated in Fig. 2.21 (C) in a higher magnification. The BSE images in (B) and (C) show the cortex surface in a very high magnification. It consists of individual irregular crystallites. Scale bars: (A) = 250  $\mu\text{m}$ , (B) = 10  $\mu\text{m}$  and (C) = 10  $\mu\text{m}$ .

#### 2.1.4.6 Proportion of the radiating layer, medulla and cortex

The quantity of the medulla, radiating layer and cortex have been determined utilizing BSE images (perpendicular to the c-axis) of the spine of *Phyllacanthus imperialis*. The medulla, radiating layer and cortex are here referred to as ‘structural elements’ of the spine. Several BSE images have been quantified in terms of their structural elements and have been chosen from a specific position along the c-axis of the spine shaft (Fig. 2.22: blue lines). In order to understand, however, the changes and influences between the structural elements, several z-projection images from the  $\mu\text{CT}$  scanned range (Fig. 2.22: red box) of the spine segment have been analyzed.

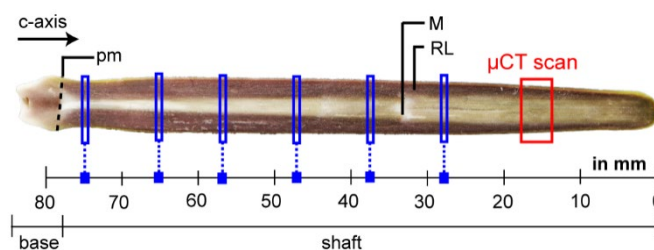
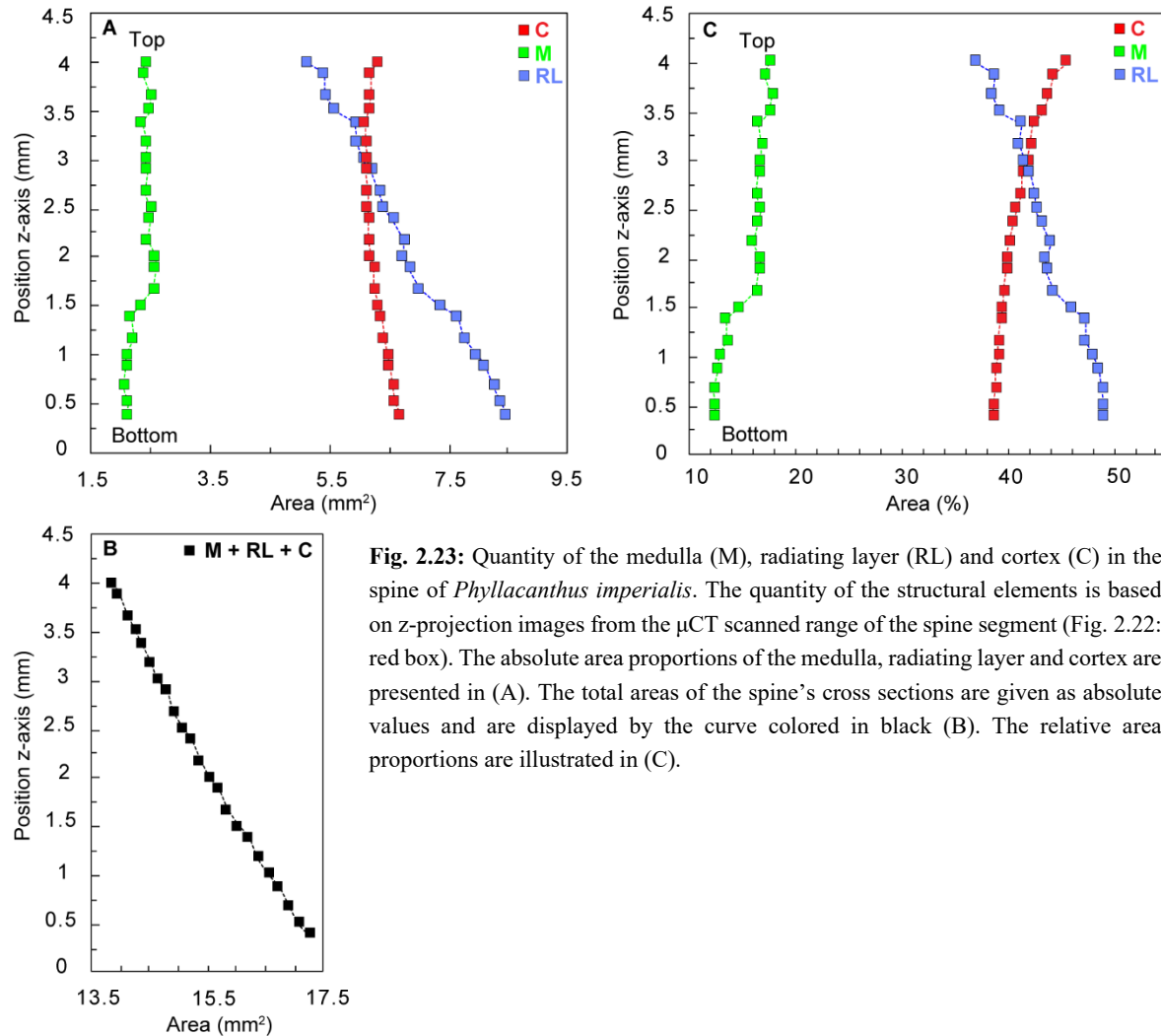


**Fig. 2.22:** Cross section of the spine *Phyllacanthus imperialis* (parallel to the c-axis). Red box displays the  $\mu\text{CT}$  scanned area of the spine. Blue lines indicate the position of the BSE images, which have been utilized for determining the area proportion of the radiating layer (RL), medulla (M) and cortex. pm = Prouho's membrane.

Results of the absolute area proportions of the structural elements and their total amounts in the z-projection images (from the  $\mu\text{CT}$  scanned range) are displayed in Fig. 2.23 (A) and (B). From these, the relative values have been determined to evaluate the correlations and influences between the structural elements (Fig. 2.23 (C)).

The relative area proportion of medulla and radiating layer are inversely correlated, but the slope of the curve progressions is different of both along the z-axis: the fluctuation of the relative area proportion of the medulla is larger than of the radiating layer. The cortex, in contrast, displays no fluctuations along the z-axis in terms of its relative area proportions. It rather shows an almost linear increase to the spine

tip and therefore appears to be independent from the fluctuations of the medulla and radiating layer. The inverse correlation of the medulla and radiating layer on the small spatial range indicates a dynamic interaction that is unaffected by the cortex.



Several BSE images, which were selected at particular positions along the c-axis were also quantified in terms of the quantity of the structural elements. The absolute values of the area occupied by the individual structural elements and their total amounts in the particular spine's cross section are displayed in Fig. 2.24. The relative values determined from the BSE images and  $\mu$ CT scans are summarized in Fig. 2.25. It presents an overview of the area proportion of the structural elements and shows their relationship to one another over the entire c-axis of the spine. The cortex and medulla are both inversely correlated with the relative area proportion of the radiating layer (Fig. 2.25 (A), (B)). There is also a positive correlation between the medulla and cortex when moving towards to the spine tip (Fig. 2.25 (C)). As the graphs show, in addition to the correlation of the structural elements to one another that the radiating layer covers the largest proportion in the spine. Its proportion increases from the spine tip to the spine basis (Fig. 2.25 (A), (B)): from 38 %, the relative area proportion in the spine

increases up to 87 %. Significantly smaller relative area proportions display the medulla and cortex (Fig. 2.25 (C)). Both remain below an area proportion of less than 20 % in total. In contrast to the area proportion of the radiating layer, the proportion of medulla and cortex increase towards to the spine tip. The cortex has the largest amount of both at the tip (45 %), whereas the medulla reaches only a relative value of 18 %. Extremely small area proportions of medulla and cortex were determined near the spine basis. Both of them have an area proportion of less than 10 %, whereas the radiating layer reaches a relative area proportion of 87 % at this point.

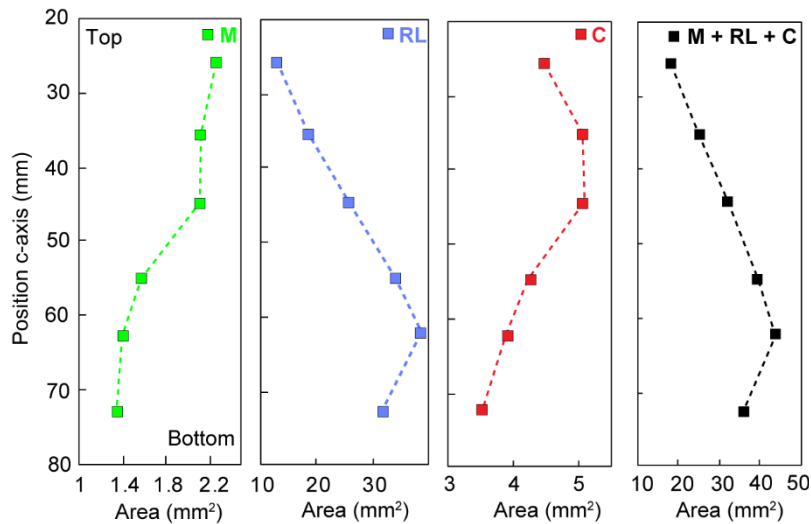


**Fig. 2.24:** Quantity of the medulla (M), radiating layer (RL) and cortex (C) in the spine of *Phyllacanthus imperialis*. The quantities of the structural elements are based on BSE images. The BSE images were chosen from specific positions along the c-axis of the spine shaft (Fig. 2.22). The absolute area proportions of the medulla, radiating layer and cortex are given as red, green and blue curve, respectively. The total areas of the spine's cross sections are displayed as absolute values and are displayed by the curve colored in black.

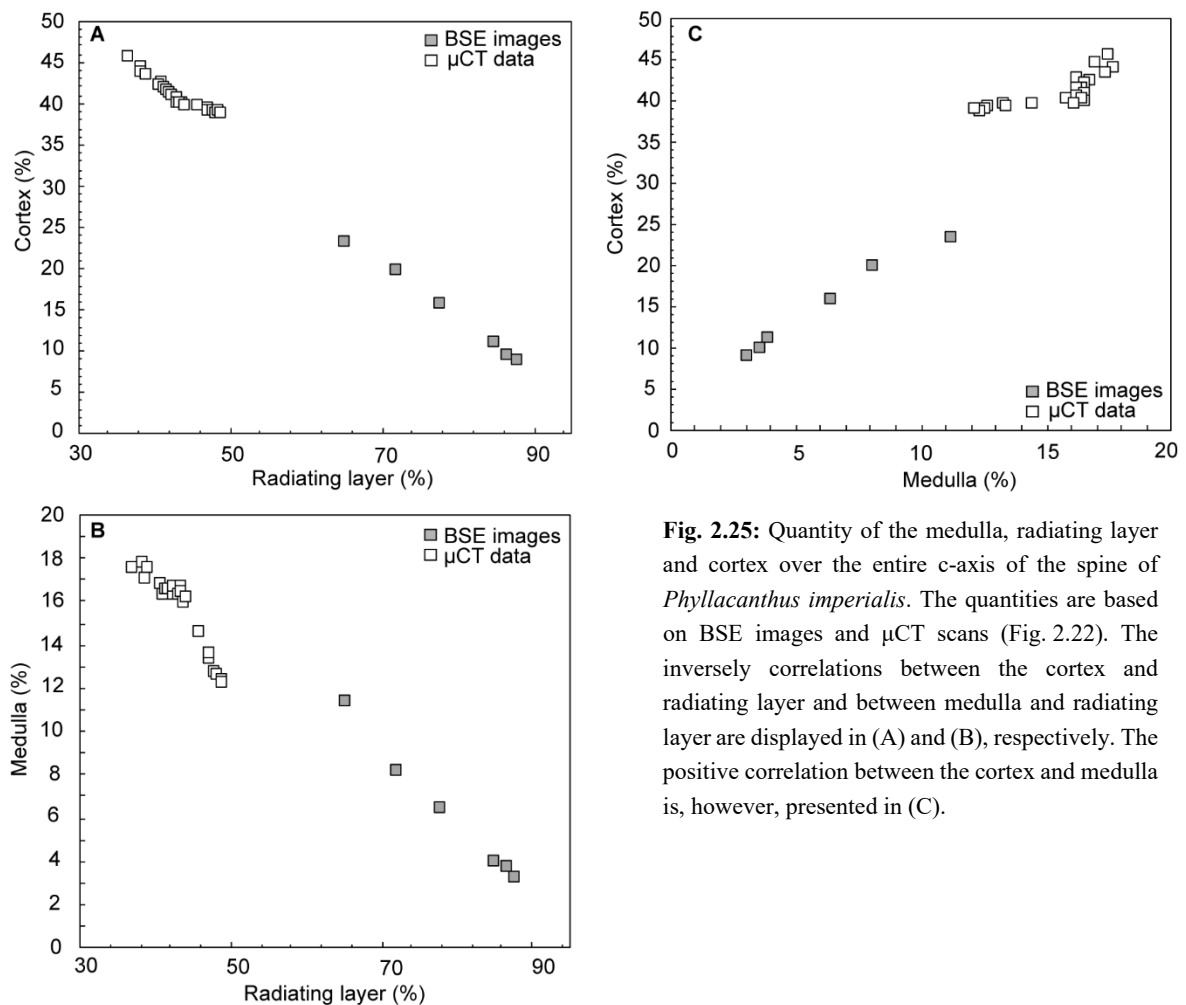


**Fig. 2.25:** Quantity of the medulla, radiating layer and cortex over the entire c-axis of the spine of *Phyllacanthus imperialis*. The quantities are based on BSE images and  $\mu$ CT scans (Fig. 2.22). The inversely correlations between the cortex and radiating layer and between medulla and radiating layer are displayed in (A) and (B), respectively. The positive correlation between the cortex and medulla is, however, presented in (C).

### 2.1.4.7 Microstructure of an oral spine and adolescent aboral spine

This section deals with the microstructure of the internal stereom meshwork of adolescent aboral and oral spines. The investigations are based on BSE images (Fig. 2.27). The size of the oral spine is smaller by a factor of 10 compared to the aboral spine. The internal microstructure of the oral tip and near the spine base has been investigated (Fig. 2.26: red lines) and is presented in section 2.1.4.7.1. Only one position of an adolescent aboral spine is presented in section 2.1.4.7.2, because the internal stereom meshwork shows no significant changes along the c-axis. The exact position of the internal microstructural investigations of an adolescent aboral spine is seen in Fig. 2.26 (red line).



**Fig. 2.26:** Spines of *Phyllacanthus imperialis*. An example of an aboral adult, aboral adolescent and oral spine is illustrated in this image. Scale bar = 1 cm.

### 2.1.4.7.1 Oral spine

The internal microstructure of the oral spine representing the area near to the spine tip is displayed in Fig. 2.27. The shape of the spine is characterized by 6 lateral side branches consisting mainly of cortex parts (Fig. 2.27 (A)). It appears that the lateral side branches are only present on one side of the spine (Fig. 2.27 (A)). The inner center of the spine microstructure is highly porous (Fig. 2.27 (A)) and is surrounded by a dense intermediate structure. It appears in such way, as if the struts of the intermediate structure have been ‘amalgamated’ with a material (Fig. 2.27 (B)). In this way, the struts and pores are only vaguely defined and therefore hardly recognizable at a few positions (Fig. 2.27 (B)). Some open pores disrupt the dense structures of the intermediate structure of the spine (Fig. 2.27 (B)).

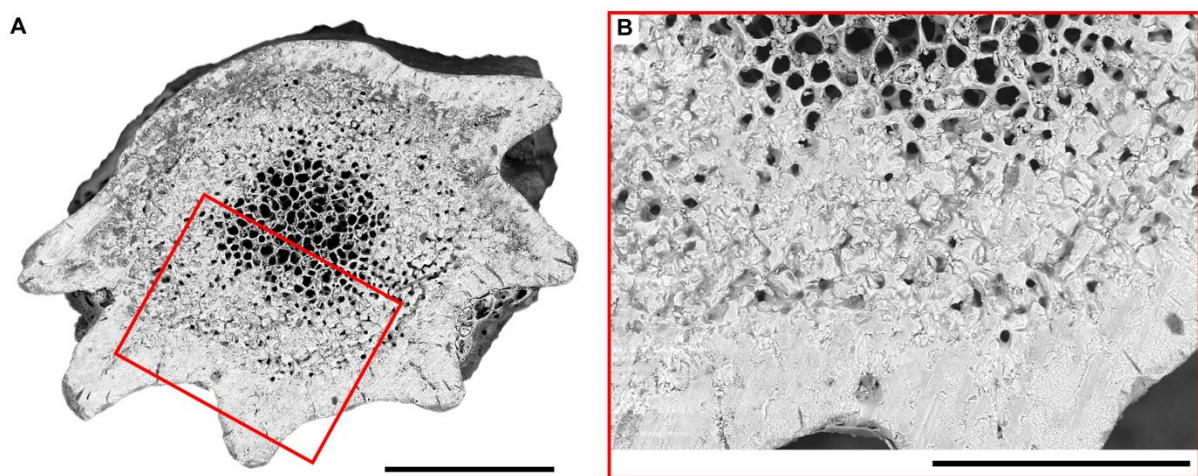


**Fig. 2.27:** Microstructure of the oral spine of *Phyllacanthus imperialis*. The BSE image (A) shows the cross section near to the spine tip. A higher magnification of the intermediate structure between the highly porous inner area and cortex is displayed in (B). Scale bars: (A) = 500  $\mu\text{m}$  and (B) = 300  $\mu\text{m}$ .

Fig. 2.28 displays the internal microstructure of the spine center, the intermediate structure of the spine and the cortex parallel to the c-axis near the spine tip. The inner center of the spine consists mainly of trabecular rods, which create straight pore rows by their slightly displaced arrangement and their cross struts. The shape and size of the pores appear to be more regular near to the subsequent intermediate structure than those in the center of the spine. The center of the spine is characterized by ordered pore rows as well as by large, irregular spaces between the trabecular rods. The intermediate structure of the spine is also mainly characterized by an almost dense structure as mentioned above. Some places reveal, however, vague struts. Significantly more struts can be seen very close to the cortex. The trabecular rods display rather a wavy-like shape at these positions. Like in the aboral spine, the cortex is pervaded by pore channels as well.

Despite the amalgamated material, the trabecular rods and the cross struts are still visible on the cross-sectional and -longitudinal section. This is an indication for a secondary transformation of the intermediate structure, where the pores of the primary stereom mesh were filled with additional material.

The secondary transformation of the intermediate structure might be accompanied with a decomposition of the primary meshes.

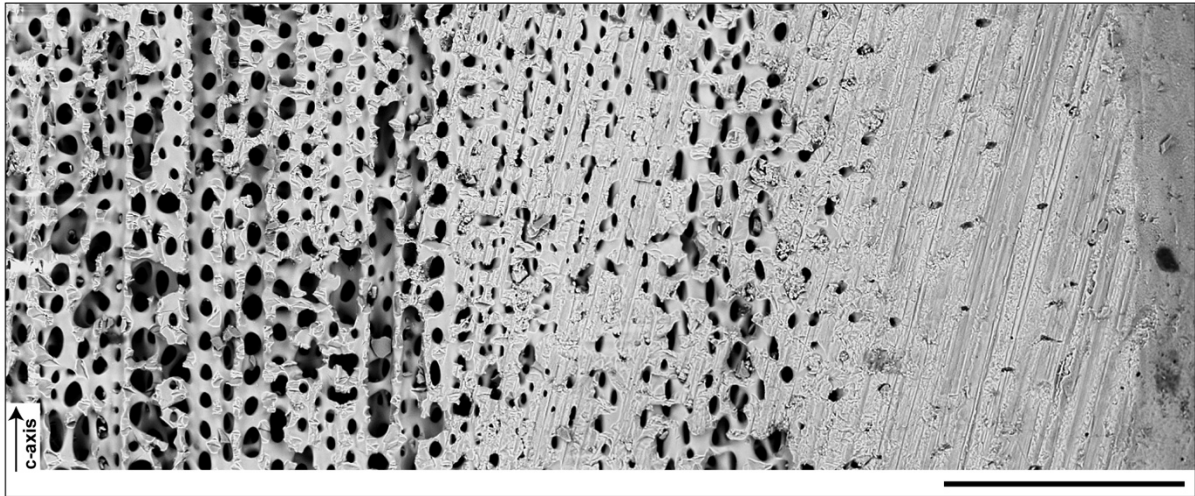


**Fig. 2.28:** Microstructure of the oral spine of *Phyllacanthus imperialis*. The BSE displays the area parallel to the c-axis and represents the area near to the spine tip. Scale bar = 300  $\mu\text{m}$ .

The internal microstructure near the spine base is displayed in Fig. 2.29. Two lateral side branches remain on the spine facing each other along the larger axis of the spine cross section (Fig. 2.29 (A)). The intermediate structure between the cortex and highly porous center consists of a mixture of amalgamated materials and struts (near the spine center (Fig. 2.29 (B))). Adjacent to the cortex, the intermediate structure displays clear struts running almost straight to the cortex (Fig. 2.29 (B)). The denser part of the intermediate structure shows also vaguely the contours of some struts (Fig. 2.29 (B)). The center of the spine structure is characterized by numerous minute polyhedral pieces on the struts, which appear to be isolated and in clusters (Fig. 2.29 (C)). Some pores of the inner spine center are filled with these polyhedral-shaped pieces (Fig. 2.29 (D)). The polyhedral shape of the pieces is clearly visible in a higher magnification of the filled pores (Fig. 2.29 (E)). A lot of these minute polygons cover the struts of the inner spine center (Fig. 2.29 (C), (E)).

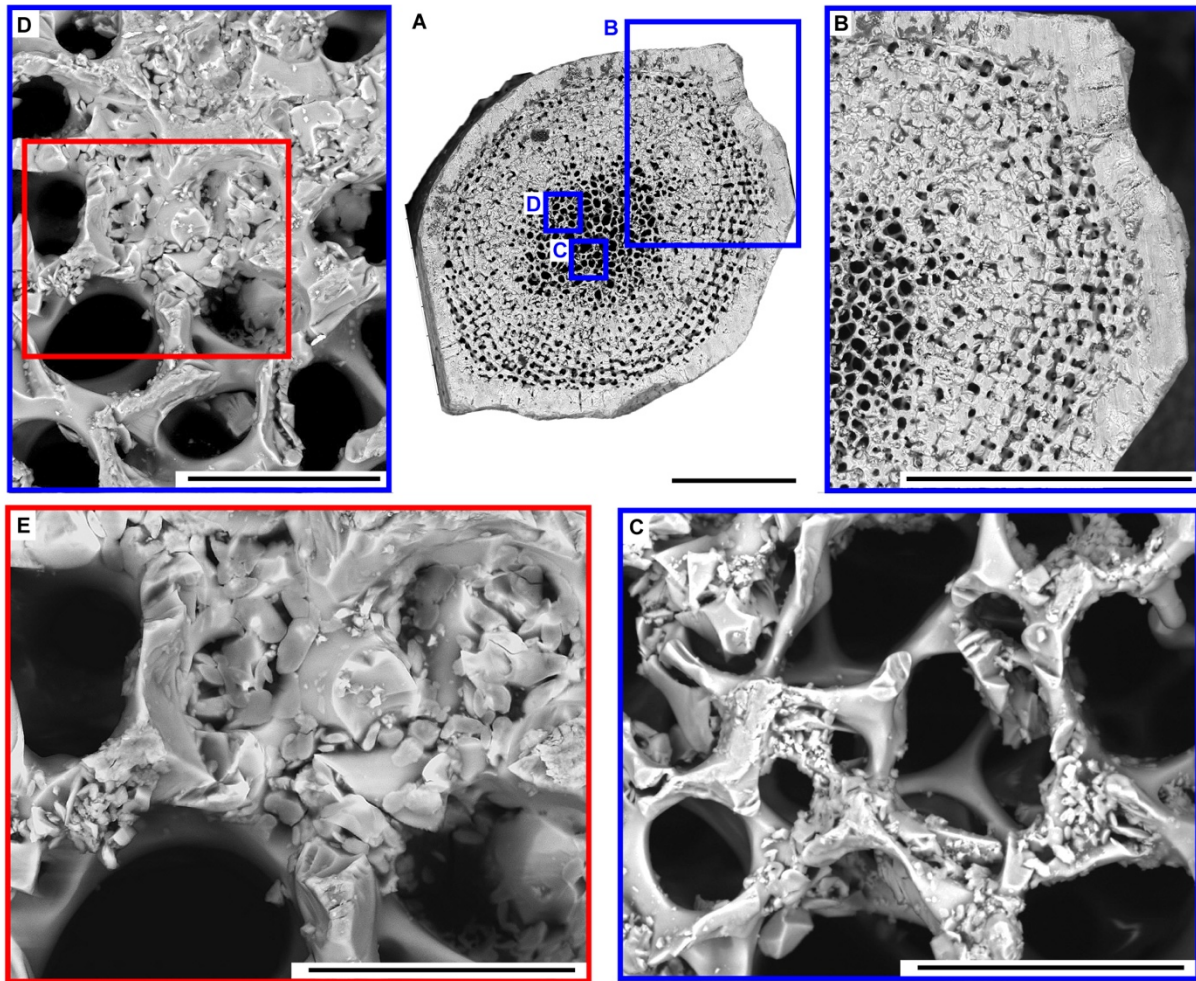


**Fig. 2.29:** Microstructure of the oral spine of *Phyllacanthus imperialis*. The BSE images display the cross sections (perpendicular to the c-axis) near to the spine base. An overview of the oral spine is seen in (A) including the areas, which are shown in a high magnification (= blue squares). The intermediate spine structure is presented in (B). The inner spine center and its strut structure is displayed in (C), (D) and (E). Scale bars: (A) = 500  $\mu\text{m}$ , (B) = 500  $\mu\text{m}$ , (C) = 30  $\mu\text{m}$ , (D) = 50  $\mu\text{m}$  and (E) = 30  $\mu\text{m}$ .

#### 2.1.4.7.2 Adolescent aboral spine

The internal microstructure of an adolescent aboral spine is displayed in Fig. 2.30. Unlike in the oral spine, the intermediate structure here contains no amalgamated phases and is rather characterized by struts running almost straight to the cortex (Fig. 2.30 (A)). The almost straight strut routes form stereom layers, which are arranged in wedge-like structures similar to those in the adult aboral spine (Fig. 2.30 (A)). The intensity of the interlocking of the wedges with the inner structure is less intensive, because the lateral side branches are poorly developed. In this way, the wedges appear to be rather isolated from the inner spine microstructure (Fig. 2.30 (A)). The inner microstructure is characterized by a circular base in cross section (Fig. 2.30 (A)).

The pores of the inner spine structure are also filled with groups of polygonal-shaped pieces similar to those of the oral spine structure (Fig. 2.30 (B)). Numerous minute mineral polygons cover the struts of

the inner spine structure as well (Fig. 2.30 (C)). A cluster of minute polygons, however, can be seen on fractured struts (Fig. 2.30 (C)).

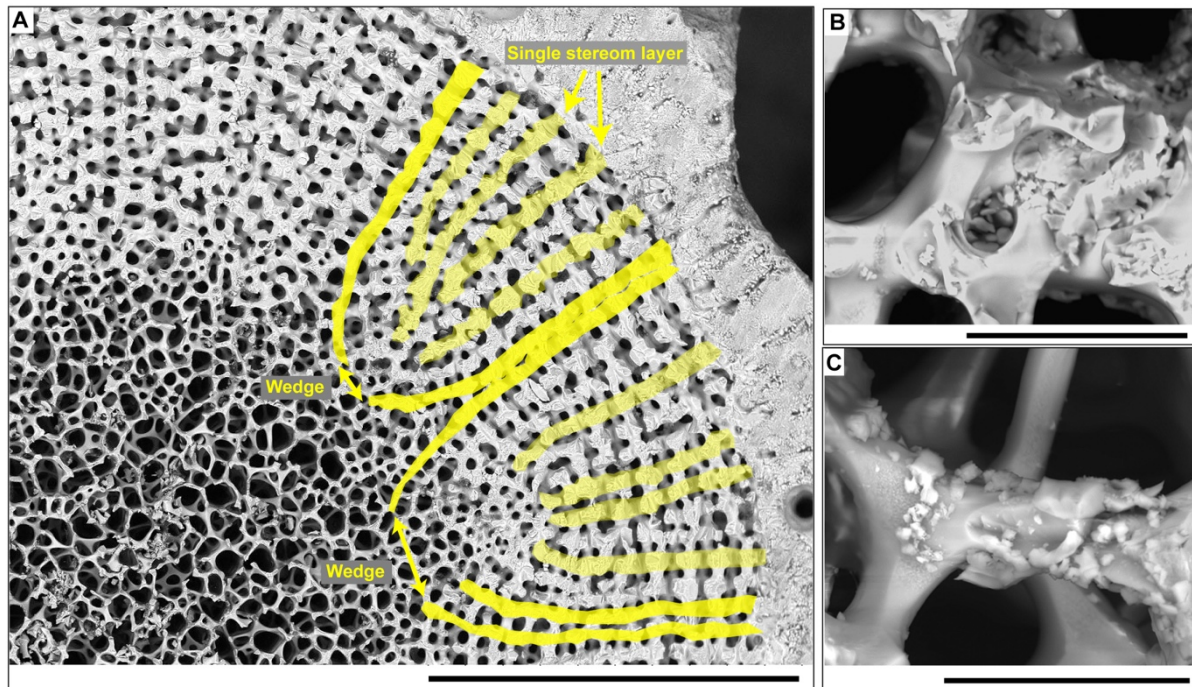


**Fig. 2.30:** Microstructure of an adolescent aboral spine of *Phyllacanthus imperialis*. The BSE images display the microstructure near to the spine base. A cross section of the spine (perpendicular to the c-axis) is shown in (A). Highlighted in yellow are the single stereom layers forming wedge-like structures in the spine interior. The struts of the inner spine center, which are partly covered and filled with minute polygons are displayed in (B) and (C). Scale bars: (A) = 500  $\mu\text{m}$ , (B) = 30  $\mu\text{m}$  and (C) = 20  $\mu\text{m}$ .

## 2.1.5 Discussion

### 2.1.5.1 Growth mechanism

Smith (1990) concluded from high resolution TEM studies of other authors (see Smith 1990, Tab.1) that the main actors of the biomineralization in all five echinoderm classes are the sclerocyte and phagocyte cells. The two cell types have been suggested to be migratory coelomocytes or to share a common ancestor with these. The calcification process in echinoderms is strictly intracellular and based on syncytial sclerocytes, which already coat available calcite surfaces on which growth is to take place or may be formed independent of pre-existing stereom. Märkel and Röser (1983) observed that the sclerocytes are anchored to the stereom trabeculae by means of cytoplasmic processes, which ramify into filiform and convolute distal processes closely pressed on the trabecula of the stereom. A detailed description of the calcification process based on syncytial sclerocytes and its cell arrangement is given by Smith (1990) and Märkel and Röser (1983). The calcoclast function, however, that means the calcite resorption is controlled by phagocytic cells. This cell type occurs individually throughout the stroma and shows long, straight pseudopodia that extend through the pore space. The syncytial phagocytic cells

can be formed above the milled ring of the spine shell and are able to autotomize (= spontaneous casting of body parts, especially when the organism is injured or under attack) the shaft. It has been found that individual phagocytic cells occur in a high density at areas where skeletal damage has happened (Heatfield 1971, Shimizu and Yamada 1976, Dubois 1989).

A comparison of the internal microstructure between the adolescence aboral and adult aboral spine indicates that calcite resorption is an essential feature during the growth of the spines, which influences the shaping of the inner stereom elements. The adult aboral spine is characterized by a wedge-like arrangement of the stereom layers (section 2.1.4.4) where the tip of each wedge is disrupted by the lateral side branches of the inner spine center (Fig. 2.31 (C)). In contrast, an adolescent aboral spine is characterized by a wedge-like interlocking with the inner spine structure as well, but the intensity of the interlocking is weakly defined, because the lateral side branches are poorly developed in this growth stage (Fig. 2.31 (B)). These observations indicate that medulla, radiating layer and cortex do not grow separately from one another and in a chronological order starting from the center to the outside and instead that all three structural areas grow simultaneously. Structural modifications like the extension of the lateral side branches from the center, which are accompanied with a reconstruction of the wedges during the growth, can only be justified if strut material is resorbed and precipitated again at another strut position. If only a chronological and separate growth of each structural area would be present without resorption and calcification, the almost circular arrangement and the poorly developed lateral side branches of the spine center would be still visible in the adult aboral spine. Furthermore, an expansion of the inner spine structure in form of lateral side branches to the outside would probably have not occurred during the growth of the aboral spine. The restructuring of the wedge system during growth is an indication for a dynamic interaction between resorption and calcification of strut material in the inner aboral spine of *Phyllacanthus imperialis*.

The calcite etching phagocytes of echinoderms may be compared with the vertebrate osteoclasts and the calcite building sclerocytes with the osteoblasts. This dynamic accumulation, degradation and remodeling process is required in order to repair microcracks and to remodel to current functional demands of the mechanical loading. The latter one is characteristic of Wolff's law, which states that bone in vertebrates will adapt to loads under which it is placed (Wolff 1986). If loading on a particular bone rises, the bone will remodel itself over time to become stronger to resist the current loading conditions. A structural investigation of femoral heads has experimentally proven this kind of correlation of bone architecture remodeling and mechanical loading: the bone trabecular orientation aligned with principal stresses (Wolff 1986, Boylell and Kim 2011). An adaption to the changes of the mechanical environment results in an optimal bone configuration, which is associated with an increased mechanical efficiency. The ability to adapt to the mechanical environment resulting in an optimal configuration of the trabecular architecture and the dynamic remodeling processes associated with an accumulation and degradation of skeletal material can be analogously transferred to the spines of

*Phyllacanthus imperialis*. Varying internal microstructures in the oral and aboral spine allow interpretation in terms of their specific functions.

Section 2.1.4.7.1 demonstrated that dense material phases are present in a larger extent near to the tip of the oral spine than near to the spine base (Fig. 2.31 (A)). The larger extent of material phases is required in the spine tip, since the highest punctual load concentrates at the spine tip due to the locomotion of the sea urchin. The punctual load acting on the oral spines is significantly smaller in terms of the intensity and duration compared to the aboral spines. The sea urchins mainly utilize the aboral spines to wedge themselves into the reef cavities during day time. A high mechanical loading occurring over several hours implies that the aboral spine architecture has to adapt to such loading conditions. Consequently, the microstructure differentiates between the oral and aboral spine, because of the varying mechanical environments. Since the oral spine are at least 10 times smaller in size compared to the aboral spines, the weight of dense material phases in the intermediate structures is negligible for the oral spines. A dense material phase in the aboral spine would increase significantly the weight of the spine. Therefore, the sea urchin requires a high expenditure of energy to move the aboral spine. A light-weight architecture would thus no longer be guaranteed in the aboral spines. Another disadvantage of the dense material phases is that it contains no crack deflection and blunting mechanisms such as the stereom network. Cracks can rather evolve unhindered through the material phases. As a result, larger segments can be removed from the structure and the spine breaks in all likelihood in a catastrophic manner. The aboral spine is characterized by a highly differentiated strut network (section 2.1.4.4), which ensures a light-weight architecture and can withstand high mechanical loadings. To what extent the superstructures, the varying quantities of the cortex, radiating layer and medulla as structural elements contribute to the load capacity and to the beneficial fracture behavior in the aboral spines of *Phyllacanthus imperialis* will be presented in depth in chapter 2.2.

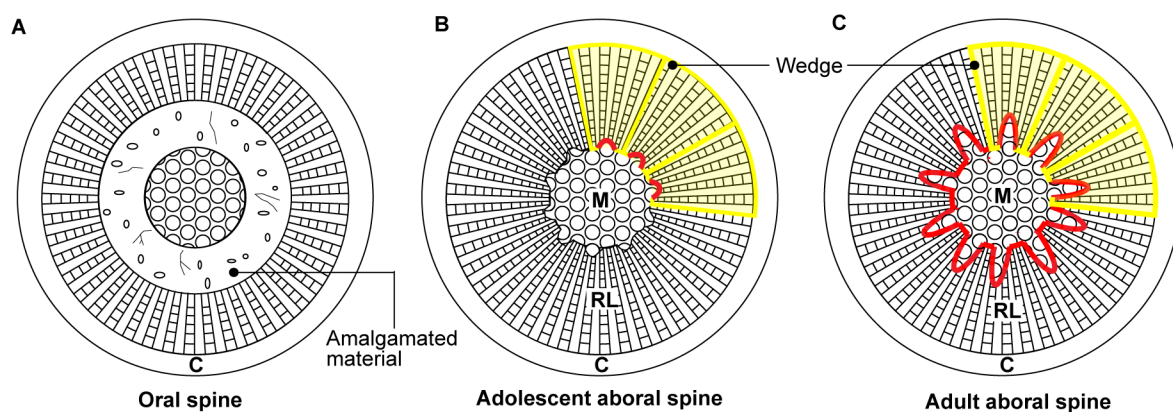


**Fig. 2.31:** Schematic overview of the microstructures of an oral, adolescent and adult aboral spine of *Phyllacanthus imperialis*. The oral spine with its dense intermediate structure is displayed in (A). The schematic microstructure of an adolescent aboral spine is seen in (B). (C) illustrates the microstructure of an adult aboral spine. C = Cortex, RL = Radiating layer, M = Medulla.

### 2.1.6 Conclusions

- (1) For an accurate description of the stereom structures in the adult aboral spine of *Phyllacanthus imperialis*, a nomenclature of the stereom network was introduced, which differentiates, inter alia, between the terms ‘cross struts’, ‘trabecular rods’ and ‘struts’. The term ‘struts’ is here a general term of the stereom mesh including both ‘cross struts’ and ‘trabecular rods’. The latter two terms can be differentiated according to their orientation to the crystallographic c-axis of the spine. This nomenclature can also be transferred into other cellular-like materials in nature for instance bones, sponges and corals.
- (2) New structural units were introduced based on the microstructural investigations of the adult aboral spine of *Phyllacanthus imperialis*, since the structural units by Smith (1980) do not describe the stereom structure of the spine completely. The new defined structural units are the so-called ‘layered’ and ‘columnar’ stereom type and represent a useful addition to the current categorization by Smith (1980).
- (3) The medulla and the radiating layer were defined according to the configuration of the struts and distribution of the strut thickness for the adult aboral spine of *Phyllacanthus imperialis*.
- (4) A step-wise analysis of the strut thickness of the spine microstructure has revealed that the thickness of the struts in the radiating layer decreases gradually towards to the medulla: it decreases from the average strut thickness of 15.7  $\mu\text{m}$  to a value of 11.6  $\mu\text{m}$ . Significantly smaller average values of the strut thickness were determined for the medulla ranging between 7.0 and 9.6  $\mu\text{m}$ . The average porosity of the radiating layer, medulla and cortex is  $76.6 \pm 3.0 \%$ ,  $85.7 \pm 2.8 \%$  and  $15.2 \pm 3.2 \%$ , respectively.
- (5) It was discovered that the aboral spine of *Phyllacanthus imperialis* is characterized by superstructures. The radiating layer comprises several individual stereom layers, which form wedge-like structures. Each wedge of the radiating layer encloses a single lateral side branch of the medulla. In total, 13 wedges are present in the spine. Dominant wedges, which contain more than 28 stereom layers, are arranged in a roughly trigonal manner in the spine structure. The medulla, however, is characterized by small bulges, which consist of dense radial arrangements of struts. It was demonstrated that the strut thickness of the bulges is slightly larger compared to the adjacent strut material of the medulla.
- (6) A highly branched system of pore channels with constant pore sizes throughout the inner structure characterizes the cortex of the spine of *Phyllacanthus imperialis*. The degree of branching of the pore channels increases from the outside to the inner cortex. It was shown that the surface morphology of the cortex varies along the z-/c- axis of the spine.
- (7) A comparison of the microstructure between an adolescent aboral spine and an adult aboral spine of *Phyllacanthus imperialis* has demonstrated that calcite resorption is an essential feature during the

growth of the spines and shaping of the inner stereom elements. The growth process of the spines, which is accompanied with a reconstruction of the inner stereom structure is characterized by a dynamic interplay of calcite resorption and precipitation.

(8) The different microstructures of the aboral and oral spines of *Phyllacanthus imperialis* are an indication for specific adaptations to the particular mechanical environment. It was demonstrated that the oral spine contains additional amalgamated material in the intermediate structures of the spine. Viewed at a higher magnification, some pores are filled with polygon-shaped pieces. Minute polygon-shaped pieces are distributed on the struts as well. The oral spines of *Phyllacanthus imperialis* are mainly used for locomotion. Therefore, the punctual load acting on the oral spine takes place in a short time interval in contrast to the aboral spine. Their spine architecture is adapted to punctual loadings acting for several hours due to the wedging into the reef cavities during day-time.

## 2.2 Mechanical characteristics

### 2.2.1 Introductory remarks

This chapter relates material properties, fracture behavior as well as the energy absorption capability of the spine segments from the aboral spine of *Phyllacanthus imperialis* to its microstructural characteristics. The material properties expressed as maximum compressive strength ( $\sigma_c$ ) and the Young's modulus ( $E$ ) were determined via uniaxial compression of spine segments. To characterize each spine segment in terms of its microstructure, a 'structural factor' is introduced to cover numerically the microstructural set up, in addition to the porosity of the spine segments. Besides the spine segments, certain areas of the spine segments were isolated and prepared in form of small cylinders and uniaxially compressed to understand their mechanical effectiveness. Cylinders were prepared, which either contain exclusively the radiating layer or medulla or combinations of radiating layer and medulla to compare the material properties, failure behavior and energy absorption capacity. One example of a radiating layer-cylinder is displayed in Fig. A.7 (see Appendix). At the end of the chapter, specific mechanical pore models are applied on the material properties of the spine segments including the (special) spine cylinders. The chapter comprises also a discussion of the potential mechanical functions of the microstructural setup of the aboral spine.

### 2.2.2 Sample characterization and methods

#### 2.2.2.1 Sample preparation

Adult aboral spines of *Phyllacanthus imperialis* were utilized as samples (dried samples without any further treatment from the Philippines) for the mechanical characterization. Several aboral spines were sectioned perpendicular to the c-axis with a diamond saw (Buehler med 1000, ITW Test and Measurement GmbH, Esslingen, Germany) using a blade thickness of 500  $\mu\text{m}$ . In this way, spine segments were fabricated with coplanar ends for the uniaxial compression tests. The coplanar ends are required to achieve uniform loading during the uniaxial compression experiments. To avoid bending and buckling during the uniaxial compression, each spine was cut into segments with a 2:1 length/diameter ratio (Bargel and Schulze 2008, Weber 1969).

Certain structural elements of the spine segments have been separated from each other by utilizing a drill bench with hollow drills as attachments. Single cylinders were prepared from the spine segments, which were cut previously into spine segments with a 2:1 length/diameter ratio as well. In this way, cylinders were fabricated containing only the core elements of the spine segments. The core includes here both the medulla and radiating layer, but no cortex. The inner diameter of the hollow drill was 6 mm for the fabrication of cylinders consisting only of the core element of the spine segment.

Cylinders from spine segments were also prepared to obtain exclusively parts of the medulla and radiating layer. The inner diameter of the hollow drill was 5 mm to get cylinders comprising the radiating layer only. A significantly smaller diameter of the hollow drill is required to prepare cylinders consisting only of medulla. A hollow drill with an inner diameter of 3 mm was used in this case. All spine segments as well as the spine cylinders were cleaned in an ultrasonic bath as last step of preparation.

### 2.2.2.2 Sample characterization

The spine microstructure was characterized using optical light microscopy and SEM. For determining the quantity of the medulla, radiating layer and cortex in the spine segments, only the digital light microscope (Hirox RH-2000, Hirox Europe Ltd., Limonest, France) was used. The length of the spine segments and of the spine cylinders as well as the diameters of the spine cylinders were determined with a digital caliper. The microstructure of uniaxial loaded core cylinders of the spine, however, was investigated utilizing the SEM. After a first significant acoustic signal in the initial stage of loading, the uniaxial compression was stopped to examine the cracks on the core cylinder. The operation conditions of the SEM are described in section 2.1.2.2. The porosity of the spine segments and spine cylinders was determined gravimetrically by assuming a density of 2.711 g/cm<sup>3</sup> for calcite (DeFoe and Compton 1925). Therefore, the volume of the spine segments and cylinders was calculated by measuring the area of the cross section, A, on the microscopic images and multiplying it with the mean height, h. Together with the mass, m, the porosity was estimated from the following equation:

$$\phi [\%] = \left( 1 - \left( \frac{m [\text{g}]}{A [\text{cm}^2] \times h [\text{cm}] \times 2.711 [\text{g} \times \text{cm}^{-3}]} \right) \right) \times 100 \quad (1)$$

### 2.2.2.3 Mechanical testing

Uniaxial compression tests were conducted in a universal testing machine (Instron 3180, Instron Deutschland GmbH, Pfungstadt, Germany). The spine segments and spine cylinders were placed on a Si<sub>3</sub>N<sub>4</sub> plate on the crosshead and pressed against a tungsten carbide compression die. The force was measured simultaneously by a force transducer. A photograph and schematic view of the measuring principles of the universal testing machine is illustrated in Klang et al. (2016). All experiments were performed with a crosshead movement speed of 0.5 mm/min. During the uniaxial compression tests of the specimen, the fracture behavior and the displacement was monitored by a video extensometer (LIMESS RTSS-C02, LIMESS Meßtechnik GmbH, Krefeld, Germany).

From the geometry of the spine specimens, the critical strength,  $\sigma_c$ , has been calculated from the load at the first crack formation. The displacement recorded from the video extensometer was used for calculating the Young's modulus, E, from the slope of the linear elastic increase in the stress ( $\sigma$ )–strain ( $\epsilon$ ) plots.

## 2.2.3 Results

### 2.2.3.1 Uniaxial compression of spine segments

#### 2.2.3.1.1 Correlation of the microstructure with material properties

To quantify the structural relationship of the spine segments with the mechanical behavior in uniaxial compression, the spines were divided into the cortex (= shell) and the compliant core. The core itself is composed of medulla and radiating layer (Fig. 2.32). A simplified division of the spine segment into a core-shell structure helps to model the influence and behavior of the cortex in the spine segment during uniaxial compression. As can be seen in section 2.1.4.6, the quantity of the cortex and core varies along the c-axis of the spine (Fig. 2.32). Therefore, a ‘structural factor’ was created to summarize the quantity of cortex and core in each spine segment. The structural factor is composed of the radius of the spine segment,  $a$ , which was normalized by the cortex thickness,  $t$  (Fig. 2.32: marked in red). Such a structural parameter, expressed as radius to thickness ratio  $a/t$ , was first established and utilized by Dawson and Gibson (2007), Karam and Gibson (1995a) and Karam and Gibson (1995b), who used the  $a/t$  ratio to characterize and model the shell-core system of plant stems, animal quills and bird feather rachis in terms of their mechanical efficiency.

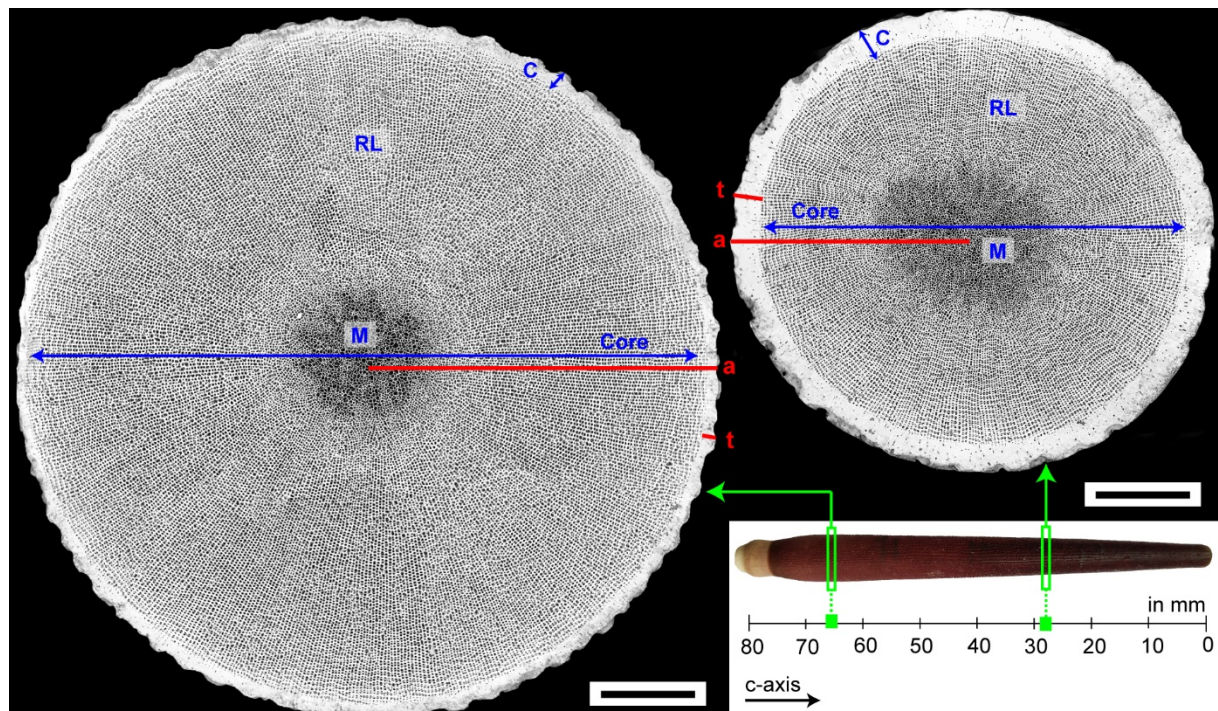


**Fig. 2.32:** BSE images and photograph of an aboral adult spine from *Phyllacanthus imperialis*. The BSE images display the cross section perpendicular to the c-axis and represent the area near to spine tip (right-hand side) and base (left-hand side). The spine can be divided into the medulla (M), radiating layer (RL) and cortex (C). The medulla and radiating layer form together the core of the spine segment. The thickness of the cortex and the radius of the spine segment is marked as  $t$  and  $a$ , respectively. Scale bar = 1 mm.

Their model analyzes the resistance of several natural dense cylindrical shells supported by an elastic honeycomb- or foam-like cellular core to local buckling with that of an equivalent hollow shell without a compliant core. Thin-walled cylindrical shells are common in engineering for instance civil engineering structures, offshore oil platforms or aircraft fuselages. Typical shell radius to thickness ratios for a variety of cylindrical engineering structures can be seen in Fig. 2.33.

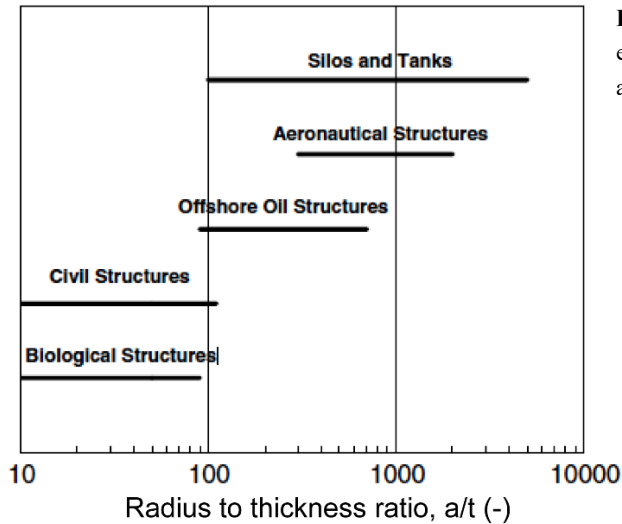


**Fig. 2.33:** Radius to thickness ratio  $a/t$  for several engineering cylindrical structures. Modified after Dawson and Gibson (2007).

Fig. 2.34 summarizes the  $a/t$  ratio dependency as a function of  $t$ , the porosity,  $\phi$ , and of the area percentage of the medulla and cortex over the entire spine lengths, which includes the  $\mu$ CT data (Fig. 2.34: green squares) and evaluated BSE images (Fig. 2.34: red squares) from the section 2.1.4.6. The dimensions and relative values of the area occupied by the structural elements in cross section were also considered from the coplanar spine segments, which were used for the uniaxial compression (UC) tests (Fig. 2.34: black squares). The cortex thickness is inversely correlated with the  $a/t$  ratio in relation to the entire spine lengths and is larger by a factor of 2.5 at the spine tip compared to the spine base (Fig. 2.34 (A)). Low  $a/t$  ratios are, in principle, an indication for a large value of the cortex thickness. It emerged from the evaluation of the porosities of the structural areas that the cortex has the lowest porosity ( $15.2 \pm 3.2\%$  (cf. section 2.1.4.2.2)) compared to the radiating layer and medulla with  $76.6 \pm 3.0\%$  and  $85.7 \pm 2.8\%$ , respectively. A large proportion of the cortex is therefore associated with low values of porosity of the spine segment (Fig. 2.34 (B)). With an decrease of the thickness of the cortex, the porosity increases constantly up to a value of 67%. The porosity of the spine segments does not increase significantly any further, even though the  $a/t$  ratios rises: from an  $a/t$  ratio of 9.4, the  $a/t$  ratio increases up to a value of 15.3 (Fig. 2.34 (B)). This range of  $a/t$  ratio is still characterized by an area percentage of the cortex between 20 to 35% in the spine segments (Fig. 2.34 (C)). The medulla has, however, an area proportion of merley between 5 to 15% (Fig. 2.34 (D)).

It seems that the low percentage of the medulla is not able to significantly influence the porosity of the spine segments. Despite the fact that the segments belonging to the lower half of the spine are

characterized by small values of the area percentage of the cortex, the highly dense structure of the cortex (with a porosity of  $15.2 \pm 3.2$  %) is influencing the porosity of the spine segments more than the structures constituting the medulla.

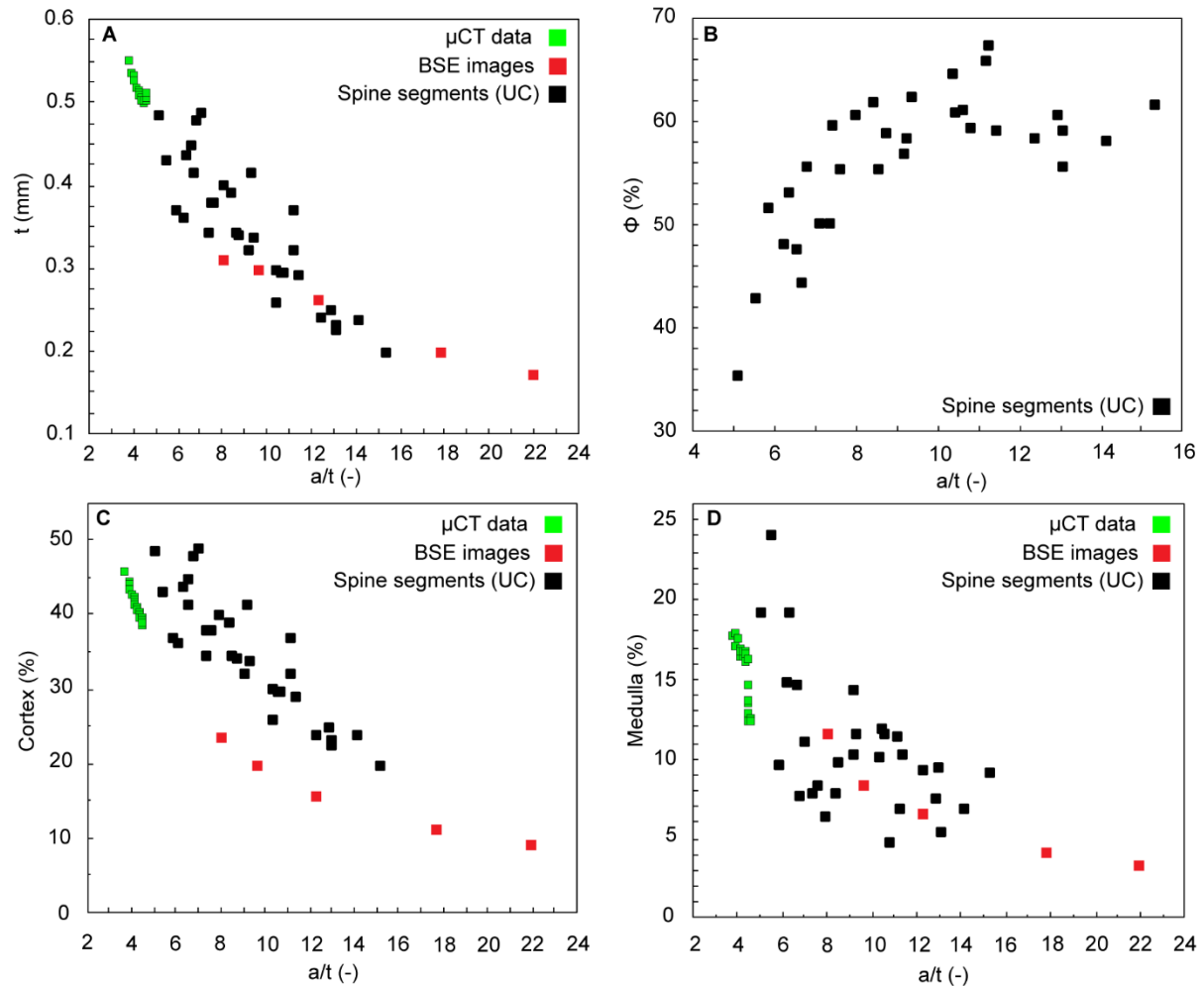


**Fig. 2.34:** Overview of the  $a/t$  ratio dependency as a function of the cortex thickness,  $t$ , the porosity,  $\phi$ , and of the area percentage of the medulla and cortex over the entire spine lengths of *Phyllacanthus imperialis*. The correlations include the  $\mu$ CT data and evaluated BSE images from section 2.1.4.6. The dimensions and relative values of the area occupied by the structural elements in cross section were also considered from the coplanar spine segments, which were used for the uniaxial compression (UC) tests. The cortex thickness, the area percentage of the cortex and medulla are inversely correlated with the  $a/t$  ratios of the spine segments, which are displayed in (A), (C) and (D), respectively. The correlation of the  $a/t$  ratio with the porosity is shown in (B).

The Young's modulus and the  $\sigma_c$  as a function of the  $a/t$  ratio of the spine segments are displayed in Fig. 2.35. The color bar indicates the volume fraction of the cortex in percent. The Young's modulus and the  $\sigma_c$  increases when the  $a/t$  ratio becomes smaller (Fig. 2.35 (A), (B)), which is associated with a rise of the volume fraction of the cortex. The stiffness and strength of the spine segments is therefore accompanied with the thickness of the cortex. The volume fraction of the cortex influences also the fracture behavior of the spine segments. A differentiation is made between two failure modes, named failure mode I and II (Fig. 2.35 (A), (B)). The details of each failure mode are presented in section 2.2.3.1.2.

The uniaxial compression experiments of the spine segments reveal that the failure mode changes between an  $a/t$  ratio of 8 and 9.2 (Fig. 2.35 (A), (B): red arrows), which is in the porosity range between 55 and 60 %. This range marks the turning point in the plot where the porosity and the  $a/t$  ratio are correlated with one another (Fig. 2.34 (B)). Spine segments from the lower half of the spine have larger  $a/t$  ratios of more than 9.2. These spine segments, characterized by  $a/t$  values of larger than 9.2, belong to failure mode I. Their values for the Young's modulus and of the  $\sigma_c$  vary between 4.6 and 10.8 GPa and 45.8 and 73.8 MPa, respectively (Fig. 2.35 (A), (B)). Spine segments, however, which are characterized by smaller  $a/t$  ratios of 8 can be assigned to the upper half of the spine including the spine tip. Their values for the Young's modulus and of the  $\sigma_c$  range between 6 and 16.4 GPa and 43 and 113 MPa, respectively (Fig. 2.35 (A), (B)). These spine segments undergo failure mode II and are characterized by an enhanced stiffness and strength compared to the spine segments, which are associated with the lower half of the spine.

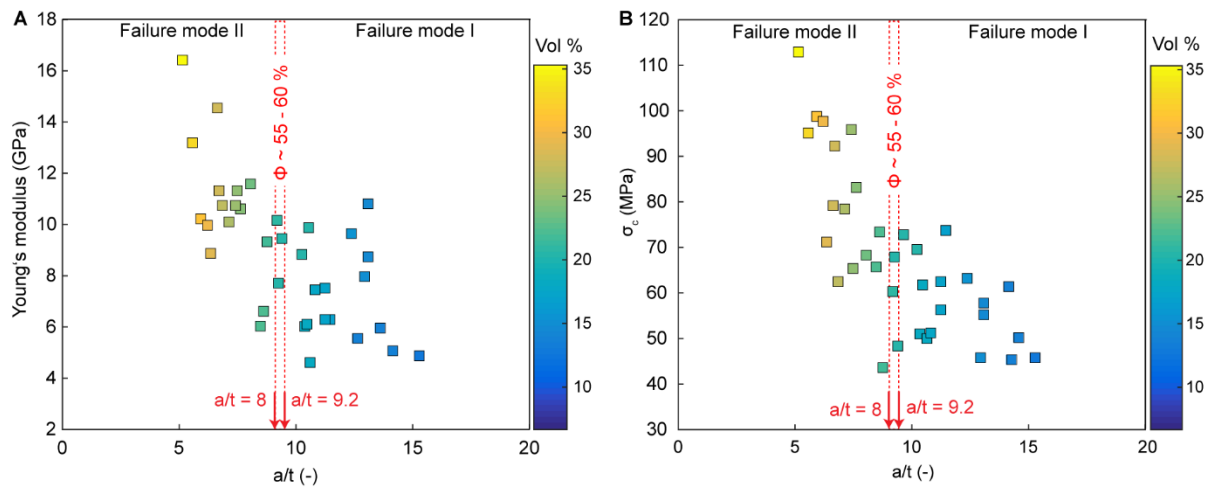


**Fig. 2.35:** Relationship of the material properties with the  $a/t$  ratio of the spine segments of *Phyllacanthus imperialis*. The Young's modulus and the maximum compressive strength,  $\sigma_c$ , as a function of the  $a/t$  ratio is displayed in (A) and (B), respectively. The color bar indicates the volume fraction of the cortex of the spine segment. The red arrows show the transition from failure mode I to II of the spine segments.

### 2.2.3.1.2 Failure mode I and II of the spine segments

Typical stress-strain curves and corresponding microphotographs of the failure mode I and II of the spine segments are illustrated in Fig. 2.36 and Fig. 2.37, respectively. Failure mode I shows a high plateau strength after the  $\sigma_c$ , which is similar to cellular materials (Ashby and Medalist 1983, Brezny and Green 1990). In contrast, failure mode II is characterized by a sharp decrease of the strength after the  $\sigma_c$  and followed by a constant low level of strength, which is approximately comparable to the brittle failure behavior in terms of the progression in the stress-strain curve. The fracture behavior of failure mode I and II can be described briefly as follows: failure mode I is characterized by a rigid connection of the cortex-core systems, because the cortex remains attached to the core during the entire compressive loading. Failure mode II is rather characterized by breaking up the core-shell system, since the cortex

flakes off the spine structure after reaching the load-limit of the spine segment (Fig. 2.37). The classification for cellular solids in compression by Gibson (2005) can be transferred to both failure modes (Fig. 2.36 (A), Fig. 2.37 (A)): a linear elastic regime, the ‘quasi-ductile’ regime (post collapse) and densification.

After a brief alignment period and the subsequent linear elastic increase, the first drop in stress of the failure mode I is characterized by the generation of individual horizontal cracks, which occur mainly in the upper region of the spine segment (Fig. 2.36 (B), b). Those horizontal cracks continue to propagate around the whole spine segment (Fig. 2.36 (B), c). Originating from the horizontal ring crack, vertical cracks initiate to propagate through the spine segment (Fig. 2.36 (B), d: red dashed line). Simultaneously, the lower part of the spine segment is affected by crushing (Fig. 2.36 (B), d-e). After complete crushing of the upper section between the bottom and the ring crack by continued spallation, the stress oscillates on a kind of plateau region (Fig. 2.36 (A)). At the same time, a lath-like segment splits off from the spine structure (Fig. 2.36 (B), f). The size of the lath-like segment is small compared to the remaining spine segment. The stress oscillates further on a kind of plateau level irrespective of the material loss, which indicates the relative structural integrity of the remaining spine segment. Another lath-like segment flakes off from the spine structure, which is, in turn, associated with a significant drop in stress (Fig. 2.36 (B), g: red arrow). After more than 50 % crushing of the remaining spine segment, a significant increase in the stress is observed and marks the last stage of the failure mode I (Fig. 2.36 (A), (B), h).

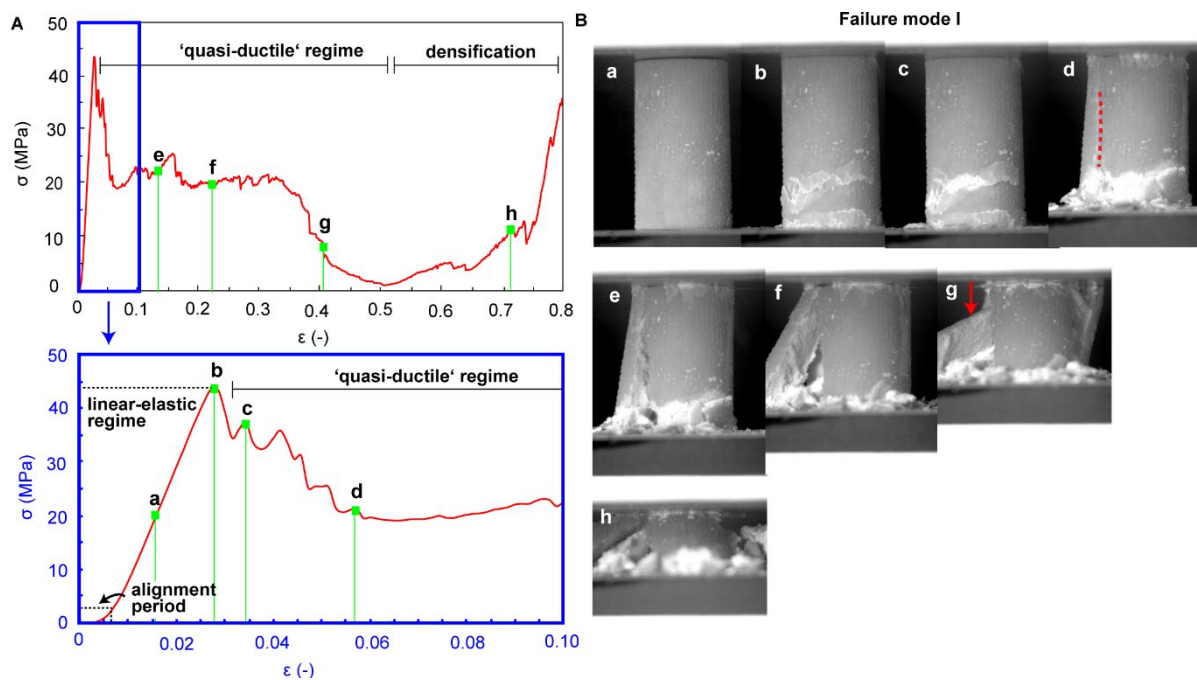


**Fig. 2.36:** Spine segment of *Phyllacanthus imperialis* under uniaxial compression. A representative stress ( $\sigma$ )-strain ( $\epsilon$ ) curve (A) is displayed of failure mode I. The microphotographs (B) showing the characteristic stages of the failure behavior of failure mode I.

In contrast to failure mode I, the failure mode II is characterized by a brief stress-strain period, in which the cortex displays a kind of mechanical reaction before reaching the  $\sigma_c$  of the spine segment (Fig. 2.37 A). After the linear-elastic increase, the cortex starts to dismantle slowly from the spine structure (Fig. 2.37 (D), b), which can be suggestively seen, since the color of the cortex appears to be lighter compared to the undamaged cortex (Fig. 2.37 (B), a). The dismantling of the cortex occurs at 65 MPa (Fig. 2.37 (A)). It is marked by an inflexion point, after which the gradient of the stress curve is lower than 65 MPa. The dismantling of the cortex occurs, when the  $\sigma_c$  acting on the cortex equals the stress, which is accompanied with the dismantling of the cortex. The dismantling balanced the maximized stress acting on the core-cortex interface. The longitudinal spallation of the cortex in larger quantities (Fig. 2.37 (A), (B), c) occurs after reaching the  $\sigma_c$  of the spine segment. Thus, the core becomes exposed (Fig. 2.37 (B), c and d). In few milliseconds, horizontal and vertical cracks propagate simultaneously through the core (Fig. 2.37 (B), e-f). The length and thickness of the vertical cracks becomes larger with continuous compression. After complete crushing of the upper section of the core (Fig. 2.37 (B), g and h), which is associated with a significant decrease in the stress, several lath-like segments separate thereafter from the remaining core. These lath-like segments tilt increasingly to the side with further compression (Fig. 2.37 (B), i). Due to the tilting of the segments, the stress drops again (Fig. 2.37 (A)). The last stage of failure mode II is also characterized by a densification of the remaining segments (Fig. 2.37 (A), (B), j-k)).

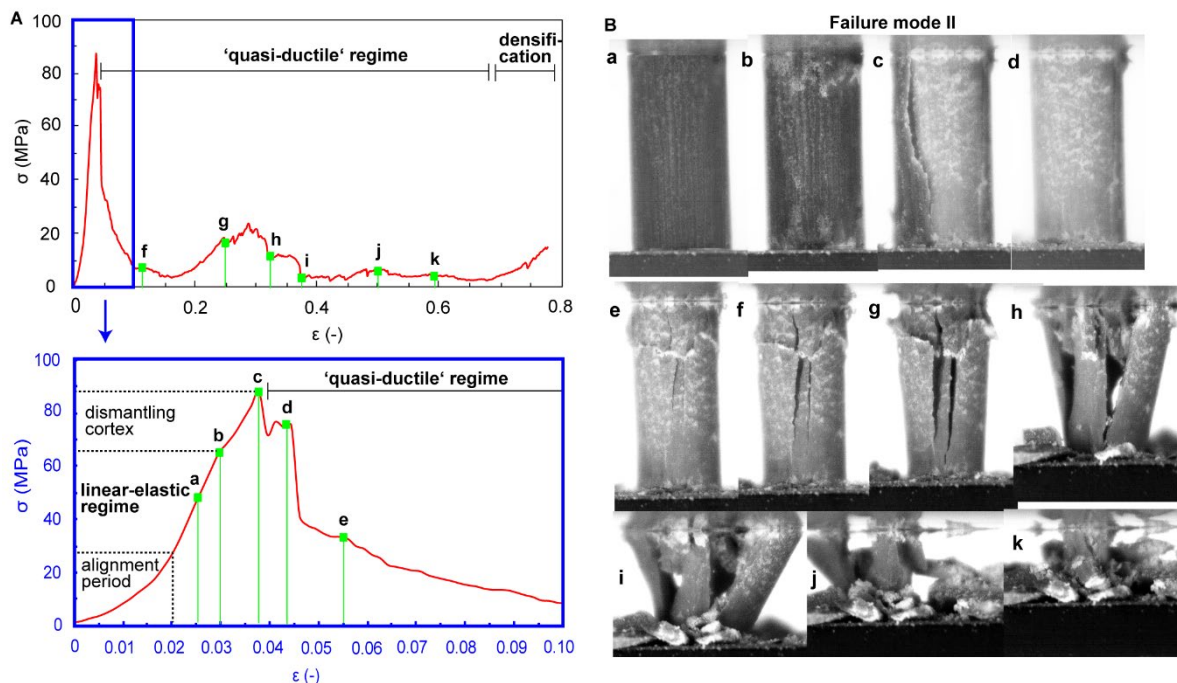


**Fig. 2.37:** Spine segments of *Phyllacanthus imperialis* under uniaxial compression. A typical stress ( $\sigma$ )-strain ( $\epsilon$ ) curve of failure mode II is presented in (A). The corresponding relevant microphotographs of the fracture behavior are listed in (B).

### 2.2.3.1.3 Failure mode II: case ‘quasi bulging’ of the cortex

Despite the dismantling, the cortex is able to ovalize minimally in order to balance the stress acting on the core-shell interface (Fig. 2.38 (A), a, b). This kind of minimal bulging happens between 60 and 70 MPa (Fig. 2.38 (C)). The stress of the initial dismantling of the cortex ( $\sigma = 65$  MPa), which were previously described, is in the same pressure range. The cross-sectional ovalization can be expressed through the following dimensionless parameter (Pan and Hsu 1999, Kyriakides and Shaw 1982):

$$\xi_{lb} = \frac{\Delta D}{D_0} \quad (2)$$

The diameter  $D_0$  defines here the unloaded condition of the spine and  $\Delta D$  is the change of the diameter with increasing loading (Fig. 2.38 (B)), which is here 7.8 mm and 0.7 mm, respectively. Therefore, the cross-sectional ovalization ( $\xi_{lb}$ ) is 0.089. In order to avoid misunderstandings and to differentiate between the observed bulging of the cortex and the elastic buckling observed in natural materials (Dawson and Gibson 2007, Karam and Gibson 1995a, Karam and Gibson 1995b), the ovalization of the cortex is here referred to as ‘quasi bulging’. This ‘quasi bulging’ creates circumferential stress in the cortex (Gibson et al. 2010). When the circumferential stress exceeds the circumferential strength, it causes longitudinal chipping of the cortex (Fig. 2.38 (A) c, d: red arrows). Nevertheless, the cortex is capable to ovalize again (Fig. 2.38 (A), d), which is accompanied by an increase in stress until reaching the  $\sigma_c$  of the spine segment. Afterwards, the cortex is strongly fractured (Fig. 2.38 (A), e) and spalls off in large quantities or completely from the spine structure, which is associated with a large drop in stress (Fig. 2.38 (A), f).

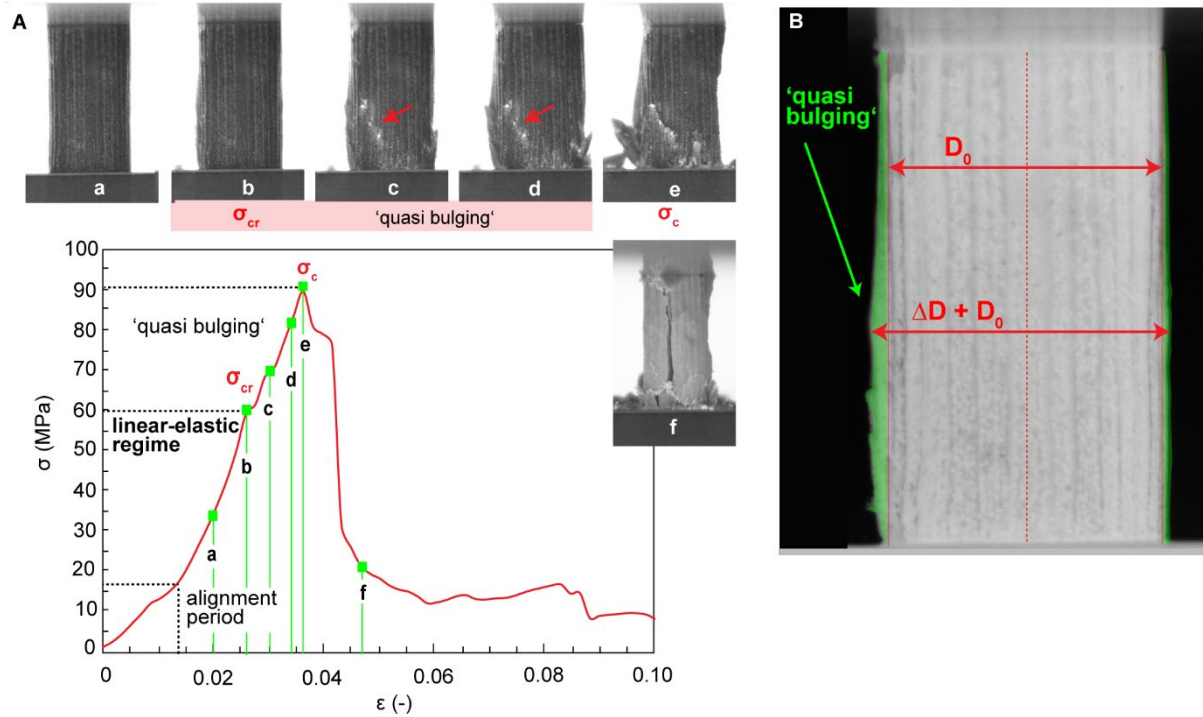


**Fig. 2.38:** Spine segment of *Phyllacanthus imperialis* under uniaxial compression. (A): The stress ( $\sigma$ )-strain ( $\epsilon$ ) curve and corresponding microphotographs displaying the fracture behavior of the spine segment. It demonstrates the minimal bulging of the cortex, which is here referred to as 'quasi-bulging'. A higher magnification of the 'quasi bulging' (in green) is displayed in (B). The ovalization is defined as  $D/D_0$ . The parameter  $D_0$  marks the diameter at unloaded condition of the spine segment, whereas the change of the diameter of the spine segment at increased loading is expressed as  $\Delta D$ .

#### 2.2.3.1.4 Energy capacity of failure mode I and II

The specific energy absorption per volume unit,  $U_v(\epsilon)$ , of the spine segments, which undergo failure mode I and II, has to be determined to quantify their mechanical effectiveness. The parameter  $U_v(\epsilon)$  is composed of the ratio of the energy absorption,  $W(\epsilon)$ , and volume of the spine segment destroyed during compression,  $V(\epsilon)$ :

$$U_v(\epsilon) = \frac{W(\epsilon)}{V(\epsilon)} \quad (3)$$

The energy absorption,  $W(\epsilon)$ , is a measure of the total amount of energy that was dissipated during straining and calculated by integrating the area under the stress-strain curve, which is given as:

$$W(\epsilon) = \int_0^\epsilon \sigma(\epsilon) d\epsilon \quad (4)$$

Another parameter to characterize the energy absorption capacity of materials is the energy absorption efficiency. This parameter quantifies the failure behavior of the spine segments and was taken from metal foams literature. The energy absorption efficiency,  $\eta(\epsilon)$ , characterizes a material's ability to absorb

stress as it compresses by normalizing the energy absorbed by the maximum stress observed (Yu et al. 2009):

$$\eta(\varepsilon) = \frac{1}{\sigma_{\max}\varepsilon} \int_0^{\varepsilon} \sigma d\varepsilon \quad (5)$$

where  $\sigma_{\max}$  is the peak value of stress during the uniaxial compression. In this case, the value of the  $\sigma_{\max}$  equals  $\sigma_c$ .

The curves of the  $U_v(\varepsilon)$  of the spine segments, which fracture by failure mode I and II, are displayed in Fig. 2.39 (A). Failure mode I remains on a relatively constant level of  $U_v(\varepsilon)$  at high strain rates, which is effective in dissipating energy. Failure mode II is rather characterized by a peak value of the  $U_v(\varepsilon)$  that decreases sharply and remains then on a constant low level of the  $U_v(\varepsilon)$ . A boxplot summarizes the average values of the  $U_v(\varepsilon)$  and its distribution at the strain of 0.3, 0.5 and 0.7 (Fig. 2.39 (B)). The converted values of the  $U_v(\varepsilon)$  into the  $\eta(\varepsilon)$ , which are related to the specific strain are presented in Fig. 2.39 (C). For spine segments, which undergo failure mode I, the average  $\eta(\varepsilon)$  drops to a value of 65 % at a strain of 0.7. In contrast to the spine segments, which undergo failure mode I, the failure mode II is characterized by a huge drop in terms of the  $\eta(\varepsilon)$ : the average values decrease down to 30 % at a strain of 0.7. The comparable large average  $\eta(\varepsilon)$  values of the spine segments, which are subjected to failure mode I, are an indication for an improved mechanical efficiency after reaching the  $\sigma_c$  of the spine segments. Both failure modes are characterized by quasi-ductility based on multiple fracturing, which means that the spine segments are able to dissipate energy through the generation of a horizontal and vertical crack system and segmentation.

The difference between failure mode I and II is the intensity of the structural segmentation of the spine segments. During compressive loading, the exposed core of the spine segments undergoing failure mode II, is divided structurally into several lath-like segments, which tilt increasingly to the side with continuous loading. Therefore, the structural integrity is no longer ensured and the capability to absorb energy is thus reduced greatly. The rigid connection of the cortex–core system (a characteristic for spine segments undergoing failure mode I) is able to reduce the intensity of the structural segmentation. A complete separation of the spine segment in several small lath-like segments does not occur in this case. The major proportion of the spine segment remains the same, even though small lath-like segments flake off laterally. Since the quantity of the remaining material is larger compared to the spine segments characterized by failure mode II, the spine segments are therefore still able to dissipate energy even at high strain levels. This, in turn, results in comparable large average values of the  $U_v(\varepsilon)$  and  $\eta(\varepsilon)$  for spine segments undergoing failure mode I, which is due to the basically kept structural integrity of the spine segments even at high strain levels.

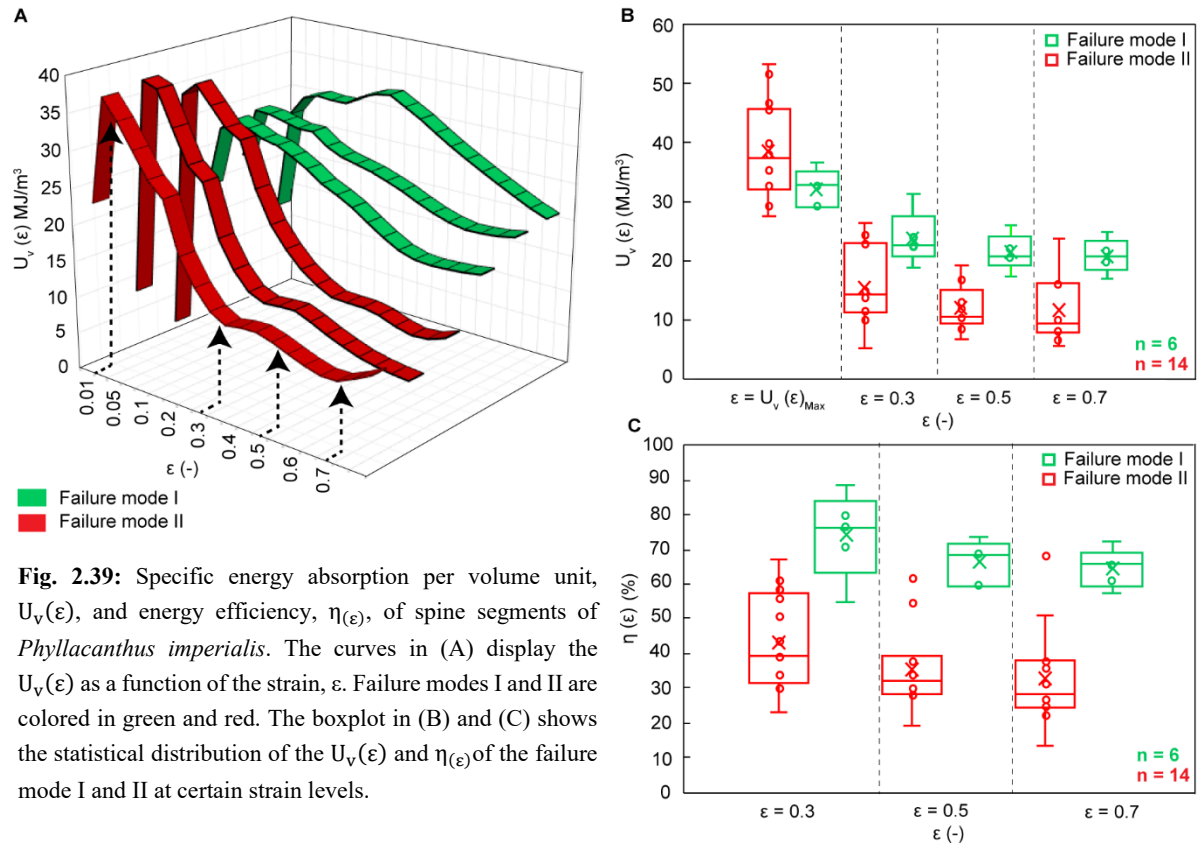


**Fig. 2.39:** Specific energy absorption per volume unit,  $U_v(\epsilon)$ , and energy efficiency,  $\eta(\epsilon)$ , of spine segments of *Phyllacanthus imperialis*. The curves in (A) display the  $U_v(\epsilon)$  as a function of the strain,  $\epsilon$ . Failure modes I and II are colored in green and red. The boxplot in (B) and (C) shows the statistical distribution of the  $U_v(\epsilon)$  and  $\eta(\epsilon)$  of the failure mode I and II at certain strain levels.

### 2.2.3.2 Uniaxial compression of the structural elements of the spine

This section deals with the behavior of prepared cylinders under uniaxial compression, which contain certain isolated structural elements of the spine (cf. section 2.1.4.6: ‘structural elements’). Cylinders were tested in uniaxial compression, which contain either the medulla only or the radiating layer. The cores of the spine segments, which consist of the medulla and radiating layer as structural units (without the cortex), were uniaxial loaded in order to quantify in detail the mechanical effectiveness in comparison to the medulla- and radiating layer-cylinders. For this purpose, the material properties, failure modes and their energy capacities are demonstrated for all tested spine cylinders in a comparative way. This section ends with the display of the crack propagation (perpendicular to the c-axis) of a loaded core cylinder in order to combine the current knowledge of the failure behavior with the inner microstructure of a spine.

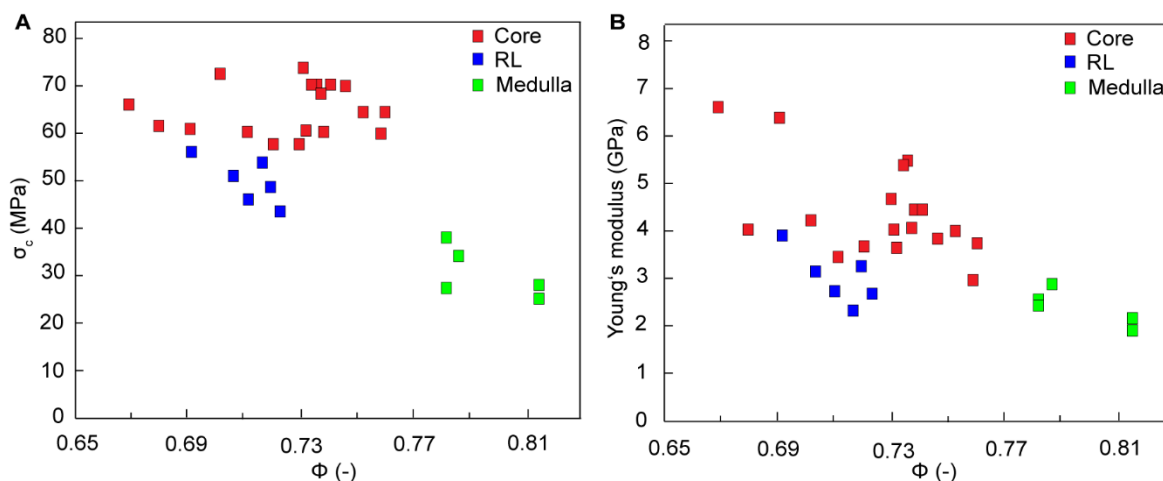
#### 2.2.3.2.1 Correlation of the structural elements of the spine with the material properties

Fig. 2.40 displays the material properties, expressed as  $\sigma_c$  and Young’s modulus, as a function of the porosity of the uniaxial loaded cylinders, which contain isolated structural elements of the spine (see above). The porosity of the cores varies between 66 and 76 % (Fig. 2.40 (A), (B)). Their variation in the porosity values is caused by the volume fraction of the radiating layer and medulla. Both are

characterized by different porosity values (cf. section 2.1.4.2.2). In addition, the natural variation of the porosity of both in the medulla and radiating layer has to be considered in this context as well. A larger volume fraction of the stereom structures, which constitute the medulla, increases the porosity of the cores. In turn, larger volume fractions of the stereom structures, which create the radiating layer, decrease the porosity of the cores. The porosities of the radiating layer-cylinders vary in a comparable smaller range of 69 and 72 % and are in good agreement with the porosity range (Fig. 2.40 (A), (B)), which was determined by the image analysis of the  $\mu$ CT data (cf. section 2.1.4.2.2; porosity ranges between 74 and 79 % of the radiating layer).

Despite of the almost same porosity ranges, the values of the  $\sigma_c$  and for the Young's modulus vary between core and radiating layer-cylinders (Fig. 2.40 (A), (B)). The values of the  $\sigma_c$  and for the Young's modulus of the latter is in the range of 56 and 43 MPa and between 2.3 and 3.9 GPa, respectively (Fig. 2.40 (A), (B)). Comparatively larger values of the material properties have, however, the cores. The values of the  $\sigma_c$  varies between 53 and 74 MPa and the values for the Young's modulus is in the range between 3.0 and 6.7 GPa (Fig. 2.40 (A), (B)).

The medulla-cylinders have the smallest values of the  $\sigma_c$  and Young's modulus: the values of the  $\sigma_c$  and Young's modulus are less than 40 MPa and less than 3 GPa, respectively. Taking only the medulla-cylinders and radiating layer-cylinder into consideration, the varying values of the material properties are clearly a function of the porosity and are also strongly correlated with the strut thicknesses of the medulla and radiating layer. In comparison to the radiating layer, the medulla is characterized by significantly smaller strut thicknesses (cf. section 2.1.4.2.1). Section 2.1.4.2.1 has shown that the thickness of the struts of the stereom structures, which constituting the medulla are reduced by a factor  $> 2$  compared to the strut thickness of the radiating layer.



**Fig. 2.40:** A correlation of the maximum compressive strength,  $\sigma_c$ , and Young's modulus with the porosity,  $\phi$ , of the cores, radiating layer-cylinders (RL) and medulla-cylinders is given in (A) and (B), respectively.

### 2.2.3.2.2 Failure mode of ‘medulla-cylinders’ and ‘radiating layer cylinders’

The fracture behavior of the radiating layer-cylinders and the medulla-cylinders is displayed in Fig. 2.41. First the fracture behavior of the radiating layer-cylinders is described below. After the linear elastic increase, the radiating layer-cylinder balances the stress by crumbling (Fig. 2.41 (A), b: red arrow) and flaking of smaller parts from the upper section of the cylinder (Fig. 2.41 (A), c). After crumbling of the thinned upper section (Fig. 2.41 (A), d: red arrow), smaller parts flake off laterally from the upper section (Fig. 2.41 (A), e). The crumbling and flaking are associated with a gradual loss of the stress (Fig. 2.41 (A): green arrow 1)). The remaining lower section is mainly crushed at high strain levels, which is, in turn, accompanied with a gradual increase in the stress (Fig. 2.41 (A), f-g, blue arrow 2). The last stages of compression are marked by a stress-plateau, which decreases gradually through continuous crushing (Fig. 2.41 (A), h-j, blue arrow 3). The fracture behavior of medulla-cylinders is quantitatively similar (Fig. 2.41 (B)), but the stress here is significantly lower compared to the stress acting on the radiating layer-cylinders. The ‘quasi’ ductile regime of the medulla is characterized, on the one hand, by a gradual decrease of the stress (Fig. 2.41 (B, blue arrow 1)) and, on the other hand, by an gradual increase of the stress at high strain levels (Fig. 2.41 (B, blue arrow 2)). This, in turn, means that the same fracturing mechanisms that were characterized for the radiating layer-cylinders act also on the medulla-cylinders, which are as follows: crumbling, flaking and crushing.

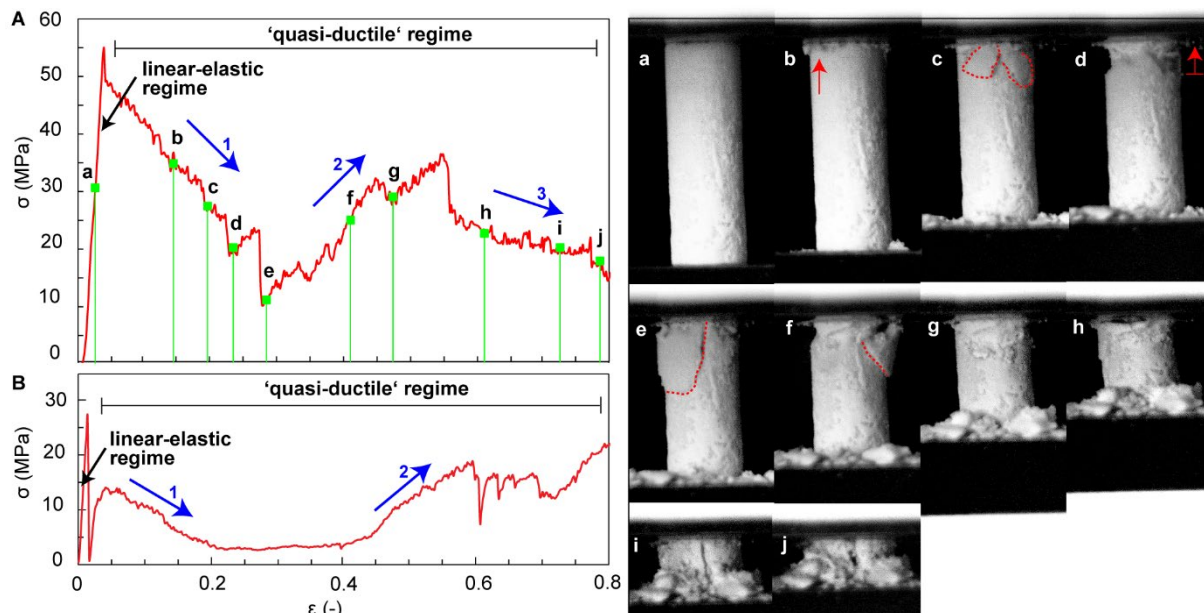


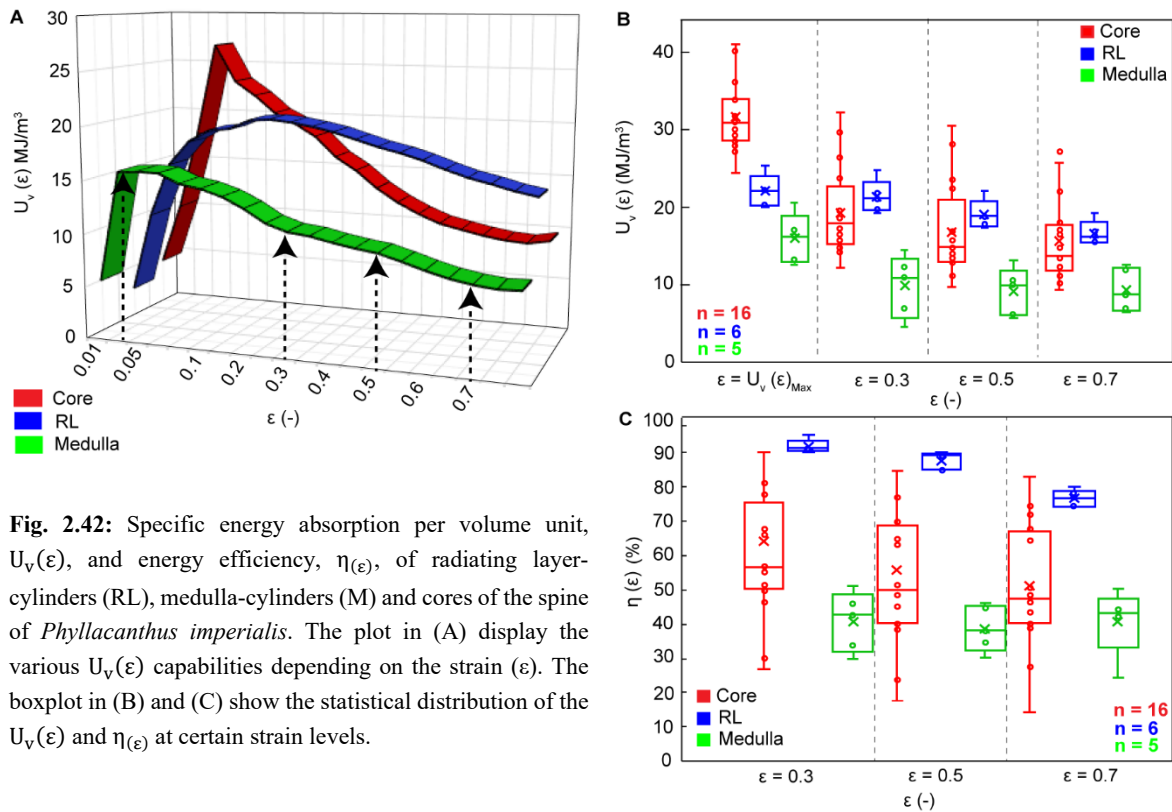
**Fig. 2.41:** The stress ( $\sigma$ )-strain ( $\epsilon$ ) curves of the radiating layer-cylinder (A) and medulla-cylinder (B). The cylinders were tested under uniaxial compression. The microphotographs on the right-hand side demonstrate the fracture behavior of the radiating layer-cylinder.

### 2.2.3.2.3 Energy capacity of the ‘medulla-cylinders’, ‘radiating layer cylinders’ and the core

The curves of the  $U_v(\epsilon)$  in dependence of the strain for the cores, radiating layer- and medulla-cylinders are displayed in Fig. 2.42. The curve of the  $U_v(\epsilon)$  of the core is characterized by a peak value, but decreases gradually with increasing strain (Fig. 2.42 (A)). The  $U_v(\epsilon)$ -strain curves of the compressed radiating layer- and medulla-cylinder, show, however, quantitatively a smoother decrease of the  $U_v(\epsilon)$  after achieving the maximum value of the  $U_v(\epsilon)$ . A boxplot (Fig. 2.42 (B)) summarizes the average values of the  $U_v(\epsilon)$  distribution of the cores, radiating layer- and medulla-cylinders as a function of the strain ( $\epsilon = 0.3, 0.5, 0.7$ ). The converted values of the  $U_v(\epsilon)$  into the  $\eta_{(\epsilon)}$  are displayed in Fig. 2.42 (C). The  $\eta_{(\epsilon)}$  values of the radiating layer-cylinders are large in comparison to the cores and medulla-cylinders even at high strain levels. They are characterized by an average  $\eta_{(\epsilon)}$  value of 76 % at a strain of 0.7, whereas the cores have an average value of 47 %. In contrast to the cores and radiating layer-cylinders, the lowest average values of the  $\eta_{(\epsilon)}$  are achieved by the medulla-cylinders over the entire strain in principle. At a strain of 0.7, the average value of the  $\eta_{(\epsilon)}$  drops to 43 %.

Varying  $\eta_{(\epsilon)}$  values are an indication for different effective fracture modes, which are, in turn, dependent on the structure and form of the specimen. Section 2.2.3.2.2 has demonstrated that radiating layer-cylinders mainly crumble under compression. Simultaneously, small parts of the radiating layer-cylinders flake off laterally. On the whole, their material losses are comparatively low. Therefore, the radiating layer-cylinders tend to remain their structural integrity compared to the cores, which are affected by structural segmentation into several lath-like parts. Consequently, the structural integrity of the cores is weakened. In this way, the cores are not able to absorb the high stress anymore compared to the radiating layer-cylinders at the same strain.

The fracture mode of crumbling, which occurs at radiating layer-cylinders, indicates that each pore row of the stereom network (perpendicular to the c-axis) is crushed in a step-wise manner. The cracks cannot distribute continuously in the strut structure, since the cracks, which propagate along the struts, are stopped by the pores. Consequently, the pores lead to crack blunting. The constant level of energy consumption of the radiating layer-cylinders, which are characterized by a comparatively low drop of the  $U_v(\epsilon)$  at high strain levels, indicates that continuously new energy has to be invested in order to induce new cracks into the undisturbed surface of further struts, since the pores act as crack arrestor. The medulla-cylinder and the radiating layer-cylinder are both subjected to similar failure modes (cf. section 2.2.3.2.2). Both are characterized by different porosities, which affect directly the quantity of  $\eta_{(\epsilon)}$ .



#### 2.2.3.2.4 Crack propagation in the core

The cores have a larger stiffness and strength compared to radiating layer-cylinders, although both share approximately similar porosities. Differences in the strength and stiffness are due to the internal configuration of the strut network. Fig. 2.43 displays the propagation of cracks in the core. The uniaxial loading of the core was stopped after the first acoustic signal occurred.

Two stages of cracks are visible in Fig. 2.43: the initial stage and an advanced stage of crack propagation. The initial stage is characterized by the fact that the crack starts to propagate directly along the border between the medulla and radiating layer (Fig. 2.43: red box). The crack propagation along the medulla-radiating layer-border indicates that the stress is mainly concentrated at the transformation zone. This transformation zone can be seen as interface between the radiating layer and medulla. Hence, the core comprising the radiating layer and medulla can be simplified as core-shell system. Several studies on natural core-shell systems under uniaxial compression (Karam and Gibson 1995a, Karam and Gibson 1995b) have shown that the stress in the core is maximized at the shell-core interface and decays radially inward. This analogy to the Karam and Gibson models (Karam and Gibson 1995a, Karam and Gibson 1995b) is limited to the stress distribution in the initial stages of uniaxial compression only. The reason for this limitation is that the porous core-shell systems by Karam and Gibson (1995a) are subjected to elastic asymmetrical buckling of the shells supported by elastic cores at high strain levels, whereas the simplified core-shell system (core = medulla, shell = radiating layer) of the spine is affected here by quasi-brittle fracturing as described further below.

With further compressive loading, the crack propagates outwards along the stereom layers of the radiating layer. A segment starts to separate from the core in this way (Fig. 2.43). From this it appears that the lath-like separation of the spine at high strain levels is structurally caused by the wedges of the spine interior. The wedges give the direction of the crack propagation and limit therefore the size of the separated segments due to the shaping of the wedge system. The wedge-like interlocking of the lateral side branches of the medulla with the stereom layers of the radiating layer, which creates by itself their own structural unit, ensures a large mechanical stability of the core.

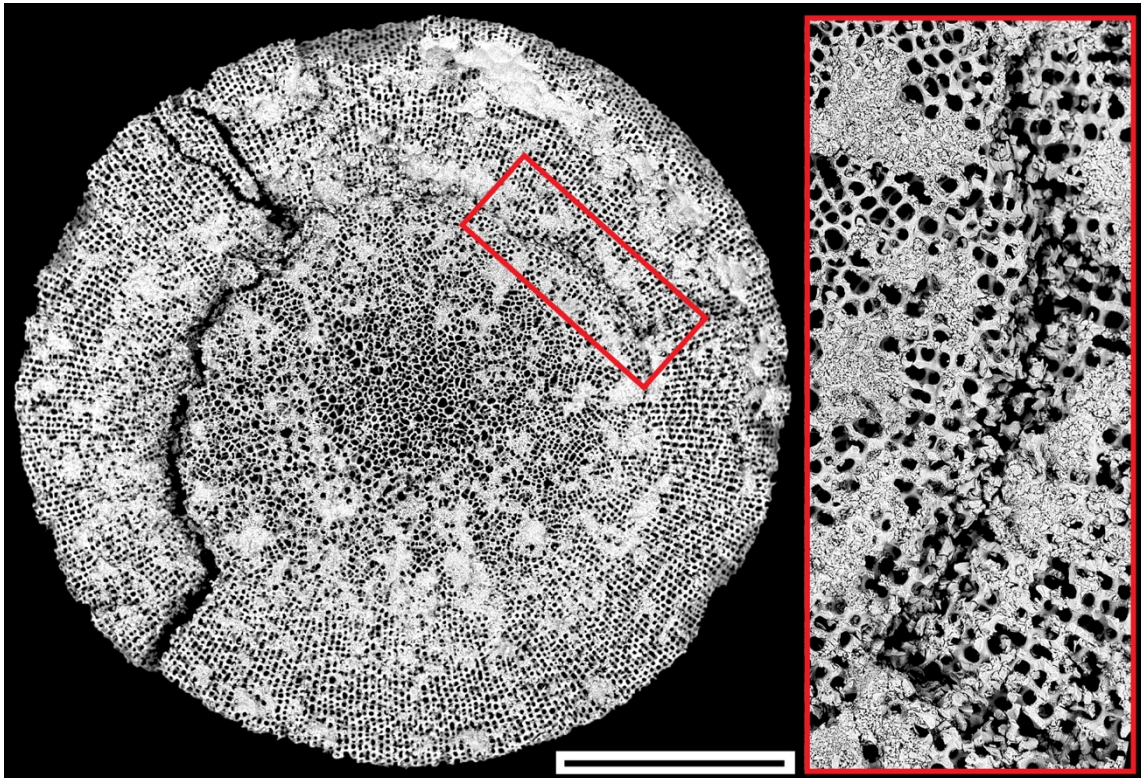


**Fig. 2.43:** BSE images of the core of the spine *Phyllacanthus imperialis*. The core was uniaxial loaded until the first acoustic signal occurred. The initial crack propagation near to the medulla is displayed in a high magnification in the red box. Advanced stage of the crack propagation is displayed on the left-hand side, where the crack is deflected along the stereom layer. Scale bar = 1 mm.

## 2.2.4. Discussion

### 2.2.4.1 Mechanical prediction by pore models

A comparison of the observed data with mechanical model predictions can provide insights into the compressive deformation behavior of the spine segments of *Phyllacanthus imperialis*. The semi-empirical analytical models of Gibson and Ashby (1997) relate to the deformation mechanisms of cell walls and edges. They differentiate between the open-cell and closed-cell pore morphology. These models have been applied to different mechanical properties such as fracture toughness, creep or Young's modulus.

The Young's modulus of brittle cellular solids is related to a measure of relative porosity  $\left(\frac{\rho^*}{\rho_S}\right)$  for the closed-cell and open-cell foam respectively as

$$\text{Closed-cell foam:} \quad E^* = E_S \left[ \phi_{\text{edge}}^2 \left(\frac{\rho^*}{\rho_S}\right)^2 + (1 - \phi_{\text{edge}}) \frac{\rho^*}{\rho_S} + \frac{\rho_0 (1 - 2\nu)}{E_S (1 - \rho^*/\rho_S)} \right] \quad (6)$$

$$\text{Open-cell foam:} \quad E^* = E_S C_1 \left(\frac{\rho^*}{\rho_S}\right)^2 \quad (7)$$

Eq. (6) and (7) describe the material failure for brittle foams and are related to the Young's modulus of the materials. The density of the cell wall and of the whole foams is  $\rho_S$  and  $\rho^*$ , respectively. The parameter  $E_S$  corresponds to the Young's modulus of the corresponding solid cell wall material. Gibson et al. (2010) use a Young's modulus for biogenic calcite of 77 – 79 GPa and Presser et al. (2009a) give a Young's modulus of  $76.6 \pm 1.9$  GPa. A value of 78 GPa has been adopted for  $E_S$ . The skeletal material of the spine is a natural composite material, due to the varied  $\text{MgCO}_3$  concentrations, minor quantities of organic matter and ACC in the  $\text{Ca}_x\text{Mg}_{1-x}\text{CO}_3$  structure of the spine. Therefore, the value of  $E_S$  can be considered here as an approximation to the skeletal composite material of the spine. The parameter  $\phi_{\text{edge}}$  is the solid fraction contained in the cell edges (the remaining fraction  $1 - \phi_{\text{edge}}$  is in the cell faces). The first term of Eq. (6) accounts for deformation in the cell edge, the second term gives the contribution of cell stretching and the third term is the contribution of the gas pressure (where the initial gas pressure in the cell and the Poisson's ratio of the foam is given as  $\rho_0$  and  $\nu$ , respectively). The parameter  $\phi_{\text{edge}}$  of 1 and the Poisson ratio of calcite of 0.322 (Ito et al. 2017) have been taken into account for Eq. (6). Gas trapped in cells can increase the stiffness, but this effect is negligible at a gas at atmospheric pressure of  $0.1 \text{ MN/m}^2$  to the modulus of the foam (Roberts and Garboczi 2001, Gibson et al. 2010). The atmospheric gas pressure has to be considered for elastomeric foams of low relative density less than 10 % (Gibson et al. 2010).  $C_1$  is an empirical geometric constant describing the cell geometry. Finite element analysis of random three-dimensional Voronoi foams with struts of circular cross section find that  $C_1 = 0.8$  (Vajjhala et al. 2000).

The equations, which relate to the Young's modulus of the materials, have been chosen, because the Young's modulus is a well-defined physical value, which can be read from text books, instead of the value for the modulus of rupture (MOR),  $\sigma_S$ , of the solid cell wall material.

Under compression, the cell walls of open foams bend at low  $\left(\frac{\rho^*}{\rho_S}\right)$  and with increasing  $\left(\frac{\rho^*}{\rho_S}\right)$  of larger than 0.1 in the elastic deformation regime. In this case, the contribution of the compression of cell walls becomes more significant. For closed-cell foams, the cell edges both bend and contract, while membranes that form cell faces stretch under compression.

Pabst and Gregorová (2014) present another pore model to cover the brittle fracture behavior. They expanded a spheroidal pore shape model of Kingery and Coble (1956) by introducing the Eshelby (1957)-Wu (1966) exponent, [E], to describe the Young's modulus-porosity relation by a power law equation as follows:

$$E^* = E_S (1 - \phi)^{[E]} \quad (8)$$

The Eshelby (1957)-Wu (1966) exponent is directly related to a geometrical shape factor of the pore expressed as aspect ratio that covers anisometric and isometric pore shapes with 3-fold rotation symmetry. Under consideration of the Poisson's ratio for calcite ( $\nu = 0.322$ , Ito et al. 2017), the Eshelby (1957)-Wu (1966) exponent ranges from 2 -  $\infty$  for oblate pores and 2 - 2.3 for prolate pores in loading direction. Fig. 2.43 displays the Young's modulus as a function of porosity,  $\phi$ , of the spine segments, cores, radiating layer- and medulla-cylinders.

Fitting Eq. (8) to the plotted data, the relationship between the Young's modulus and porosity of the plotted data covers an Eshelby (1957)-Wu (1966) exponent between 3.0 and 2.0 (Fig. 2.44), which reflects well the dominant pore shapes from spherical to columnar. The prediction by the open-cell model, which has a similar, but not identical curve progression as the curve given by an Eshelby (1957)-Wu (1966) exponent of 2.3, can be approximated by the obtained data as well. The closed-cell model shows no agreement with the obtained data at all. The smallest deviation from the curves defining the prediction of the open-cell model and covering an Eshelby (1957)-Wu (1966) exponent of 2.3 display the cores, radiating layer- and medulla-cylinders. Spine segments with an a/t ratio of larger than 11 display a comparable large deviation. Their values vary between an Eshelby (1957)-Wu (1966) exponent of 2 and 3. Spine segments, however, with an a/t ratio of lower and/ or equal to 8 accumulate in a larger number at the curve belonging to an Eshelby (1957)-Wu (1966) exponent of 3. The deviation of the latter data from the pore model prediction for prolate pores describing an Eshelby (1957)-Wu (1966) exponent of 2.0 - 2.3 is probably caused by the large volume fraction of the cortex in the spine segments.

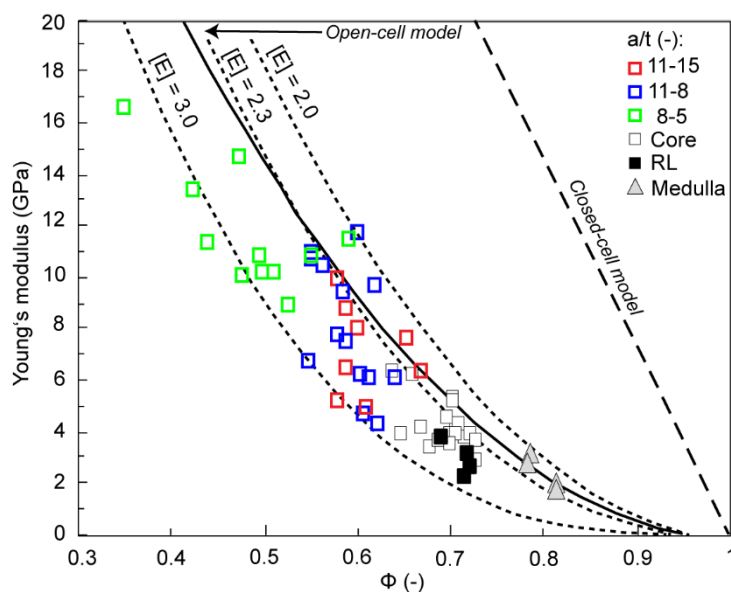


**Fig. 2.44:** Plot of the Young's modulus as a function of the porosity,  $\phi$ , of the spine segments of *Phyllacanthus imperialis*. The data of the spine segments are plotted as open squares, which are defined by their a/t ratio (colored squares). The results of the radiating layer-cylinders (RL), medulla-cylinders (M) and the cores are displayed as white and black square and grey triangle, respectively. The open-cell and closed-cell model by Gibson and Ashby (1997) is displayed as solid black line and dashed black line. The Pabst and Gregorová (2014) prediction for different Eshelby-Wu exponents, [E], is given as dotted lines.

### 2.2.4.2 The strength – modulus chart

Fig. 2.45 summarizes the relationship of strength and stiffness of all uniaxial tested spine materials (medulla-, radiating layer-cylinders, cores and spine segments with cortex). In principle, materials, which are characterized by a particularly high resilience (viz. the ability to bend without breaking according to Gibson et al. (2010)), are located rather on the right-hand side (see Fig. 2.45). The medulla- and radiating layer-cylinders are located on the left-hand side in Fig. 2.45 indicating a reduced resilience compared to the cores and spine segments. As described in section 2.2.3.2, varying values of the strength and stiffness of the medulla- and radiating layer-cylinders are a function of the porosity (see Fig. 2.40). The cores display a larger strength and stiffness compared to the medulla- and radiating layer-cylinders. As stated in section 2.2.3.2.1 and section 2.2.3.2.4 before, the cores require less material than the radiating layer-cylinders. Therefore, the core is more efficient in terms of the ability to provide stiffness and strength with the minimal use of material. The cores, radiating layer- and medulla-cylinders can be approximated by a linear relationship between the  $\sigma_c$  and Young's modulus, which is defined as follow:

$$\frac{\sigma_c}{E} = 0.016 \quad (9)$$

The medulla-cylinders differ slightly from the function in Eq. (9), whereas the radiating layer-cylinders and cores cover well the linear relationship. The values of  $\sigma_c$  and for the Young's modulus of the spine segments cannot be approximated with the function in Eq. (9), the data distribute randomly on the right-hand side of the plot. The stiffness of the spine segment is increased by addition of an almost dense shell like the cortex on the cores. In contrast, the strength of the segments is not further increased significantly through the addition of the cortex on the cores. The mechanical performance seems to be relatively equal of spine segments consisting of an  $a/t$  ratio of 11 - 8 and 11 - 15, because the data sets of both scattering in the same plateau-like numerical range. Both latter spine segments are characterized by failure mode I (cf. section 2.2.3.1.1). Spine segments, however, which have an  $a/t$  ratio of lower than 8, are characterized by larger values of the strength and stiffness and fracture by failure mode II (cf. section 2.2.3.1.1). They distribute in a rather linear way in Fig. 2.45 and can be approximated by the function of the  $\sigma_c$  and Young's modulus as follows:

$$\frac{\sigma_c}{E} = 0.0069 \quad (10)$$

In principle, the larger values of the strength and stiffness are an indication for a larger resilience compared to spine segments, which are characterized by an  $a/t$  ratio of larger than 8. As mentioned in section 2.2.3.1.1, the  $a/t$  ratio of the spine segments correlates with the position in the spine (along the  $c$ -axis): Spine segments with an  $a/t$  ratio of larger than 8 belong to the lower half, whereas segments,

which are characterized by an  $a/t$  ratio of lower than 8, can be assigned to the upper half of the spine of *Phyllacanthus imperialis*.

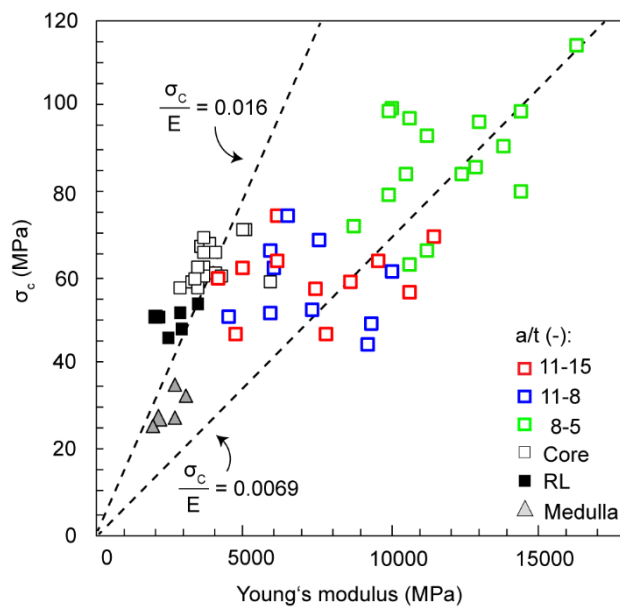


**Fig. 2.45:** Relationship of the maximum compressive strength,  $\sigma_c$ , to the Young's modulus for spine segments of *Phyllacanthus imperialis*. The plot summarizes the strength and stiffness of the spine segments in dependency of their  $a/t$  ratio, of radiating layer-cylinders (RL) and medulla-cylinders (M).

### 2.2.4.3 Implications of the function of the structural elements of the aboral spine

The level of compressive loading condition acting on the sea urchin spine segment in the experimental setting ( $> 500$  N) is significantly higher than the mechanical loading conditions, which prevail in the natural habitat of the sea urchins. Such compressive loading conditions in the experimental setting would probably press the spine into the test and therefore fracture the test of the sea urchin, before the spine would fracture or dissipate energy. Thus, the ability to dissipate energy advantageously is not necessarily an adaptation to its mechanical environment, but rather a positive by-product of the porous, hierarchically organized material by itself. Nevertheless, the results of the mechanical testing of the spine segments offer room for interpretation for potential implications of the function of the structural elements of the aboral spine of *Phyllacanthus imperialis*. As stated in section 2.1.5, the sea urchins wedge themselves during the day time inside the reef cavities in order to protect themselves against the high hydrodynamic environment and predators. The spine tip is directly in contact with the hard substrate due to the wedging. A high resilience at the spine tip is therefore required, since a high punctual load, which lasts for hours, act on the tip of the spine. The high-volume fraction of the cortex at the spine tip is thus useful to enhance the resilience in principle. The lateral protrusions of the cortex (cf. section 2.1.4.5.2) at the spine tip contribute not just as additional thickening, but may also dissipate the principal stress advantageously.

The ‘quasi bulging’ of the cortex (failure mode II) occurring in spine segments from the upper half of the spine (Fig. 2.45) might be an indication for a reduced rigidity, which, in turn, emerged due to evolutionary adaption of the sea urchin to its ecological niche. In principle, a solid solution hardening of the material is achieved by the Mg incorporation in the crystal structure (Magdans and Gies 2004). Dery et al. (2014) have shown that the average Mg concentration in the cortex is 5.1 mole percent  $\text{MgCO}_3$ . This is significantly lower than the concentrations observed in the medulla (5.9 mole percent  $\text{MgCO}_3$ ) and the radiating layer (8.1-0.5 mole percent  $\text{MgCO}_3$ ). A decrease of the Mg in the cortex reduce also the degree of brittleness, which allows therefore minimal elastic reactions. These minimal elastic reactions are expressed in pure compressive loading of the spine segments as ‘quasi bulging’. The ‘quasi bulging’ prevents a catastrophic brittle failure of the cortex, when the  $\sigma_c$  is reached on the cortex. From a purely material-specific perspective, the stress is balanced by the modulus of ‘quasi bulging’ leading to an increase of the  $\sigma_c$  of the spine segment (section 2.2.3.1.3), which is also a positive feature of the spine material per se. *Phyllacanthus imperialis* does not exploit this characteristic in its ecological niche. A minimal degree of elasticity of the cortex at the spine tip is nevertheless required, since the sea urchin has to modify the pressure for the wedging according to the prevailing hydrodynamic conditions. Changing flow velocities and the occurrence of predators imply a highly dynamic environment for the sea urchin. It further means that the spine is subjected to constant dynamical changes of the mechanical environment during the wedging between the reef cavities. The pressure acting on the spine is constantly readjusted to the changes of the environment. Therefore, the punctual load at the spine tip fluctuates during the wedging. The cortex at the spine tip has to react also dynamically in form of a minimal degree of elasticity. A cortex, which is too rigid would directly lead to the actual material fracture of the upper spine segment. This interpretation of the results extends the rather chemical function of the cortex given by Dery et al. (2014). They have argued that the low Mg concentration in the cortex compared to the inner core and the increased density of the cortex is responsible for the large acidification resistance. Probably the large acidification resistance enabled them to survive the Permian-Triassic crisis, which was associated with severe acidification events of the ocean.

### 2.2.5. Conclusions

The spine of *Phyllacanthus imperialis* performs several functions from the mechanical point of view. The respective mechanical function is dependent on the proportion of the cortex and core, which is, in turn, related to the position in the spine (along the c-axis). Varying proportions of the cortex and core influence the resilience and the intensity of the energy dissipation, which are here concluded as 1) and 2):

1) An a/t ratio of smaller than 8 is a characteristic for segments from the upper half of the spine. The upper half of the spine is characterized for its high resilience to mechanical stress. Just before reaching

the  $\sigma_c$ , the segments from the upper half of the spine display a kind of ‘quasi bulging’ of the cortex, which is probably an indication for a reduced degree of brittleness/ rigidity. This is related to lower Mg concentration in the cortex compared to the inner core. A decrease of the Mg reduces also the degree of brittleness or rigidity in the cortex, which allows thus a minimal elastic reaction expressed as ‘quasi bulging’ of the spine segment under compressive loading. The ‘quasi bulging’ mode of the spine segment balances the stress leading to an increase of the  $\sigma_c$  of the spine segment.

2) Segments from the lower half of the spine display an  $a/t$  ratio of larger than 8 and are characterized by a rigid cortex-core connection. They display comparatively large values of the effective energy absorption at advanced stages of compression, which is a similar behavior to cellular materials under uniaxial compression. The reason for this is that the cortex keeps widely the structural integrity of the segments and provides thus that the degree of segmentation is kept as low as possible. Conversely, segments from the upper half are strongly subjected to structural segmentation, since the cortex was spalled off right after reaching the load-limit. Therefore, the core is not stabilized anymore by the cortex. The lower half of the spine has been optimized towards keeping further material losses as low as possible, when the upper half of the spine does not exist anymore.

The varying mechanical efficiencies of the cortex can be assigned and limited to specific areas in the stress-strain diagram: the cortex, which is present in the upper half of the spine, is highly effective at the beginning of the compression. The cortex in the lower half of the spine is, however, significantly effective after the first material failure happens, which means at high strain levels. Overall, the cortex performs several functions on the mechanical point of view.

A comparison of the material properties of the radiating layer and core representing varying strut configurations, but similar densities have shown that the core is characterized by larger strength and stiffness at high strain levels. The reason for the differences in the material properties of both is the varying designs of the strut network’s internal configuration. The relation of the mechanical characteristics with the microstructure of the core is listed below as item 3):

3) The inner structure of the spine, the core, is optimized in terms of the ability to provide stiffness and strength with a minimal use of material. The wedge-like interlocking of the lateral side branches of the medulla with the stereom layers of the radiating layer, which creates by itself their own structural unit, ensures a high mechanical stability of the core. The lath-like separation of the spine at high strain levels is structurally caused by the wedges of the spine interior. The wedges give the direction for the crack propagation and limit therefore the size of the separated segments due to the shaping of the wedge system.

Since the sea urchins wedge themselves between the reef cavities, a high resilience at the spine tip is therefore required to withstand the high punctual loading, which can last for hours. The high-volume fraction of the cortex at the spine tip thus enhances the resilience in principle. The lateral protrusions of the cortex at the tip of the spine contribute not just as additional thickening, but also might dissipate the principal stress advantageously. The cortex is characterized by lower Mg concentrations compared to the inner structural elements of the spine. Low Mg concentrations reduce the rigidity of the cortex and allow minimal elastic reaction that was experimentally visible under extreme loading conditions of the spine segment ('quasi bulging'). A minimal degree of elasticity of the cortex at the spine tip is reasonable, since the sea urchin have to modify the pressure for the wedging according to the prevailing hydrodynamic conditions. The pressure acting on the spine is constantly readjusted to the changes of the flow velocities and the occurrence of predators.

## 3. Technical transfer into ceramics

### 3.1 Freeze-casting

#### 3.1.1 Introductory remarks

In order to transfer the spine microstructure of *Phyllacanthus imperialis*, freeze-casting as manufacturing method was utilized to fabricate ceramic lab-scale samples. Cellular unidirectional cell geometries and cell structures with varying cell sizes can be manufactured using the freeze-casting technique. More details about freeze-casting as manufacturing technique are presented in section 1.4. Gelatin and agar as additives in an alumina-water suspension have been used to fabricate ceramics with a high interconnectivity between the cell walls. Ceramics containing different cellular structures and their mechanical characteristics and evaluation in terms of the degree of interconnectivity of the cell walls are presented in this section. The applicability of the prediction of mechanical properties of the Gibson and Ashby models and of the honeycomb model provided by Zhang and Ashby in a broader view for freeze-cast alumina ceramics are discussed in this chapter. Furthermore, a proposed proportionality of strength and stiffness was established and implemented into the spheroidal pore model by Pabst and Gregorová (2014). To what extent the stiffness and strength relationship is applicable into the Pabst and Gregorová (2014) formalism is also discussed at the end of this chapter.

#### 3.1.2 Material and methods

Unidirectional alumina scaffolds were manufactured via the freeze-casting route from a water-based alumina suspension. As additives gelatin was used on one hand and agar on the other. In the following the preparation of the alumina-gelatin-water and alumina-agar-water suspension is described. The design of the molds for the alumina slurry, the condition of the sublimation and sintering are presented afterwards.

##### 3.1.2.1 Gelatin as additive

**Tab. 3.1:** Concentration of the solid loading of Al<sub>2</sub>O<sub>3</sub> and gelatin of the water-based alumina suspension.

Name	$\phi$ sintered foam	Total concentration of Al <sub>2</sub> O <sub>3</sub>		Total concentration of gelatin with regard to water		Dolapix CE 64 (cm <sup>3</sup> )
	(vol.%)	(wt.%)	(vol.%)	(wt.%)	(vol.%)	
G_6.8_16.5	77 - 79	44.0	16.5	5	6.8	0.47
G_3.5_16.5	77 - 79	44.0	16.5	2.5	3.5	0.47
G_1.8_16.5	77 - 79	44.0	16.5	1.25	1.8	0.47
G_9.9_14.4	-	40.0	14.4	7.5	9.9	0.20
G_6.8_14.4	86 - 87	40.0	14.4	5	6.8	0.20
G_3.5_14.4	82 - 84	40.0	14.4	2.5	3.5	0.20

Water suspensions of gelatin powder (Ewald-Gelatine GmbH, Bad Sobernheim, Germany) were prepared with a solid loading of 9.9, 6.8, 3.5 and 1.8 vol.% (Tab. 3.1). Homogenization of the gelatin suspension was carried out at 60 – 70 °C by stirring for 1 h. Under continuous stirring of the gelatin suspension, the 99.99 %  $\alpha$ -alumina powder (TM-DAR Taimicron of Taimei Chemicals Co,  $d_{50} = 1.2 \mu\text{m}$ ,  $\rho = 3.98 \text{ g/cm}^3$ ) was added slowly in small measures to obtain a solid load of 16.5 and 14.4 vol.% by dispersing them with 0.47 and 0.20  $\text{cm}^3$  of Dolapix CE 64 (Zschimmer & Schwarz GmbH & Co KG Chemische Fabriken, Lahnstein, Germany), respectively (Tab. 3.1). The volume of Dolapix was fixed at 0.5 % of the solid content (recommendation of the manufacturer). The dispersion was carried out with an ultrasonic processor UP400S (Hielscher Ultrasonics GmbH, Teltow), equipped with 20-mm titanium sonotrode (Amplitude 50 %, cycle 0.5 s), for every alumina-gelatin suspension for 5 minutes. A constant rotation of the beaker at the titanium sonotrode ensured a homogeneous distribution of the alumina particles and temperature. The temperature of the alumina-gelatin suspension was monitored and kept below 80 °C to avoid hydrolysis of the gelatin.

### 3.1.2.2 Agar as additive

**Tab. 3.2:** Concentration of the solid loading of  $\text{Al}_2\text{O}_3$  and agar of the water-based alumina suspension. \*pH value = 4.0 with citric acid.

Name	$\phi$ sintered foam (vol.%)	Total concentration of $\text{Al}_2\text{O}_3$		Total concentration of agar with regard to water		Total concentration of sucrose with regard to water		Dolapix CE 64 ( $\text{cm}^3$ )
		(wt.%)	(vol.%)	(wt.%)	(vol.%)	(wt.%)	(vol.%)	
A_4.3_8.6	86	30	8.6	2.5	4.3	5	3	0.13
AC_4.3_8.6	84	30	8.6	2.5	4.3	5*	3*	0.13
A_4.3_5.9	90	20	5.9	2.5	4.3	-	-	0.1

The manufacturing of the foams based on three different water suspensions of 100 % pure agar powder E406 (Special ingredients Ltd., United Kingdom) with a solid loading of 4.3 vol.%. A homogenized suspension was achieved at a temperature of 60 – 90 °C under continuous stirring for 2 h. One ceramic was prepared with a water-agar suspension only (Tab. 3.2: A\_4.3\_8.6). The addition of 99.5 % sucrose (Sigma, St. Lois, MO) and a solid loading of 3 vol.% in the water-agar suspension formed the basis for two additional ceramics, whereby one water-agar-sucrose suspension was further manipulated by a reduction of the pH (pH = 4.0 of the slurry) using citric acid (Tab. 3.2: AC\_4.3\_8.6). A homogenized water-agar-sucrose suspension was achieved at a temperature in the range of 60 – 90 °C after 2 h of stirring. Under continuous stirring of all three suspensions and retaining the temperature between 60 – 90 °C, the alumina powder was added slowly in small measures. A solid loading of 5.9 vol.% alumina powder was achieved in the water-agar suspension. The water-agar-sucrose suspensions, however, comprise a solid loading of 8.6 vol.% alumina powder. The appropriate volume of

Dolapix CE 64 of each slurry was adjusted according to the solid loading (Tab. 3.2). By using the procedure stated in section 3.1.2.1 the alumina particles were kept in suspension.

### 3.1.2.3 Mold designs, sublimation and sintering conditions

**Tab. 3.3:** Temperature, pressure and duration of the sublimation phase.

Temperature (°C)	Pressure (mbar)	Duration (h)
-60	0.1	22
-30	0.1	22
-20	0.05	22
0	0.05	16
+20	0.03	12
+50	0.03	18
+50	1013	16

Polytetrafluorethylene (PTFE) tubes (with an inner diameter of 25 mm and a height of 35 mm) were used as molds that were placed on a copper plate with a thickness of 3 mm. Before filling the alumina slurry into the PTFE tubes, the copper plate was cooled at a temperature of -60 °C. After 4 h of directional freezing, the frozen specimen was carefully removed from the PTFE tubes by slightly heating the PTFE tubes. The temperature, pressure and duration of the sublimation of the ice crystals under vacuum are listed in Tab. 3.3. The obtained green bodies were sintered in a conventional furnace. Each intermediate temperature was achieved with a constant ramp speed of 1 °C/min. In the first stage the temperature was increased to 550 °C and dwelled for 2 h; subsequently the specimens were heated to 900 °C and dwelled for 2 h. Finally, the target sintering temperature of 1350 °C was reached and held for 4 h.

The basic mold design was also manipulated through the addition of silicon and copper plates (Fig. 3.1). Two mold designs were tested with a selected slurry composition, which corresponds to the ceramic G\_6.8\_16.5 (Tab. 3.1). Mold design I consists of triangle-shaped silicon slices, which are arranged in a circular array and which alternate with the copper plate at the bottom of the mold (Fig. 3.1). The side walls are lined with copper stripes (thickness = 500 µm), which alternate with areas consisting of Teflon. The side walls of the mold design II are only lined with a thin copper film (thickness = 500 µm; Fig. 3.1). In addition, a silicon ring (width = 4 mm) was placed at the bottom of the mold (Fig. 3.1). It covers the outermost area of the copper plate only. The bottom of the inner circle was left empty.

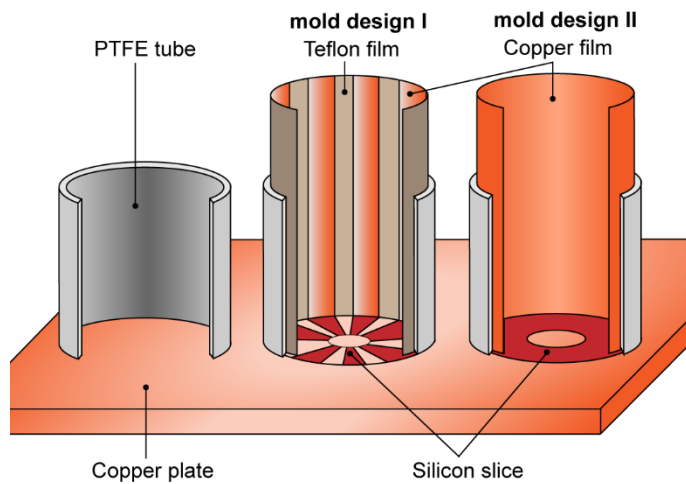


**Fig.3.1:** Mold designs, which were utilized for the manufacturing of ceramics containing a directional pore system. Basic setup consists of a simple Polytetrafluorethylene (PTFE) tube that is mounted on the copper plate. Changes of the pore channel orientation and gradation have been attempted with mold designs I and II.

### 3.1.2.4 Microstructural characterization

The microstructure of the ceramics was investigated with a scanning electron microscope (Tabletop Microscope TM3030 plus, Hitachi Ltd., Tokyo, Japan) in the backscatter electron modus (BSE) at an acceleration voltage of 15 kV and at a working distance of 6800  $\mu\text{m}$ . Pore sizes (pore axis length and pore diameter) were determined utilizing the software Fiji 2.0.0 (ImageJ). In total, 100 pores were considered for each ceramic species.

From the ceramic A\_4.3\_5.9, the thickness and pore axis length were determined via  $\mu\text{CT}$  scans by using Fiji 2.0.0. The  $\mu\text{CT}$  scans were performed at the University of Freiburg (Plant Biomechanics Group). A Skyscan 1174 (Bruker), which operates at 35 kV and 5 W was used for the scan of the ceramic specimen. The reconstructions of the  $\mu\text{CT}$  data were performed utilizing the Skyscan software. The pixel size in the  $\mu\text{CT}$  image is 3.5  $\mu\text{m}$ . Three-dimensional views of the 2\*2\*2 mm section were created in Fiji 2.0.0.

The porosity of the ceramics was determined using Eq. (1). Instead of the density of calcite, a theoretical density of  $\alpha\text{-Al}_2\text{O}_3$  of 3.97  $\text{g}/\text{cm}^3$  (Sun et al. 2016, Hautcoeur et al. 2018) was implemented in Eq. (1).

### 3.1.2.5 Strut network

By using the plugin ‘Angiogenesis Analyzer’ for Fiji 2.0.0, the cellular strut network was evaluated based on cross sections perpendicular to the freezing direction of infiltrated ceramic specimens. The strut network of the ceramics, which were manufactured by utilizing a water-gelatin suspension with a solid loading of 16.5 vol.% alumina (Tab. 3.1: G\_6.8\_16.5, G\_3.5\_16.5, G\_1.8\_16.5) were considered in this analysis, since they represent the three main types of branching, which can occur among the gelatin-alumina series. The analysis of the strut network of each ceramic type comprises four images in total.

In the following, the detected constituting elements of the network and their definitions according to Carpentier (2012) are described below.

Nodes are pixels that have at least three neighbors, which correspond to bifurcation (Fig. 3.2 (A): yellow). A segment is limited by two junctions, whereby a junction is composed of several nodes and branches (Fig. 3.2 (A)). Isolated elements are displayed as dark blue lines (Fig. 3.2 (A)). A master segment consists of three segments that are limited by two junctions (Fig. 3.2 (B)). Junctions, however, which link at least three master segments are called master junction (Fig. 3.2 (C)). Meshes display closed areas composed of segments or master segments (Fig. 3.2 (C)).

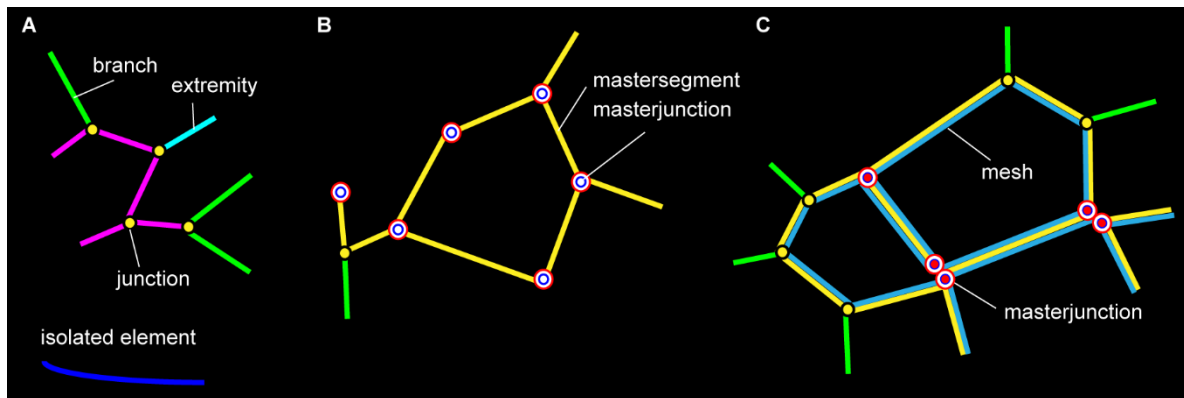


Fig. 3.2: Detection of constitutive elements of the cellular network by using Angiogenesis Analyzer (Fiji 2.0.0).

### 3.1.2.6 Mechanical characterization

Uniaxial compression tests were carried out using a universal testing machine (Instron 4502, Instron Deutschland GmbH, Pfungstadt, Germany) with a constant crosshead movement speed of 0.5 mm/min. The ceramic cylinders were placed on a Si<sub>3</sub>N<sub>4</sub> plate on the crosshead and pressed against a tungsten carbide compression die. The force was measured simultaneously by a force transducer. During the tests, the fracture behavior was monitored with a video extensometer (LIMESS Meßtechnik GmbH, Type RTSS\_HS) capturing one side of the tested specimen.

## 3.1.3 Results

### 3.1.3.1 Microstructure of the gelatin series

Different pore morphologies can be achieved utilizing varying gelatin concentrations in the water-based alumina suspension. A circular shape of the cells displays the ceramics, which were manufactured with a gelatin concentration of 9.9 and 6.8 vol.% (Fig. 3.3). The ceramic types G\_6.8\_14.4 and G\_9.9\_14.4 have a concentration of solid loading of 14.4 vol.% in common and differentiate in terms of their gelatin concentrations. Smaller pore sizes are present in the ceramic manufactured with the higher gelatin concentration of 9.9 vol.% (Fig. 3.3 (A), (B)). The latter has an average pore diameter of 50 µm (Fig. 3.5 (A)), whereas a larger average pore diameter of 90 µm has been characterized for the ceramic type G\_6.8\_14.4 (Fig. 3.5 (A)). The reduced pore sizes are caused by the continuous gelatin network, which enhances the permeability of water and prevent thus the concurrent preferential growth of ice crystals (Arabi and Zamanian 2013, Fukushima et al. 2014). It appears that the directionality of the cell

channels becomes vaguer and obtains more a foam-like character for the ceramic manufactured with a larger gelatin concentration (Fig. 3.3 (A.2), (B.2)). A larger solid loading does not change tremendously the pore size and morphology of the ceramic, which is the case for the ceramic type G\_6.8\_16.5 in comparison with the ceramic type G\_6.8\_14.4. The latter is characterized by an average pore diameter of 90  $\mu\text{m}$  (Fig. 3.5 (A)). Due to the larger concentration of the solid loading, the cell walls appear to be thicker compared to the ceramic type G\_6.8\_14.4. The struts of the ceramic types G\_9.9\_14.4, G\_6.8\_14.4 and G\_6.8\_16.5 are not fully solidified and are characterized by an internal porosity (Fig. 3.3 (A.3), (B.3), (C.3)).

Utilizing the lower concentration of gelatin of 3.5 vol.% leads rather to cellular oblate pore structures (Fig. 3.4). A solid loading of 14.4 and 16.5 vol.% was utilized at this gelatin concentration and the ceramic types are called here G\_3.5\_14.4 and G\_3.5\_16.5, respectively. The oblate cells of both are largely aligned in one direction (Fig. 3.4 (A), (B)). The variability of cell sizes is optically reduced at larger solid loadings (Fig. 3.4 (B)). In contrast, the ceramic type G\_3.5\_14.4 is also characterized by oblate cells, which are aligned in one specific direction, but the cells are additionally separated by comparably smaller cells (Fig. 3.4 (A)). Due to the irregular cell shape of both, only one cell axis was determined in this case. The distance,  $d_1$ , is the shortest cell axis of the oblate cells. The average  $d_1$  value of the ceramic types G\_3.5\_14.4 and G\_3.5\_16.5 is 64 and 60  $\mu\text{m}$ , respectively (Fig. 3.5 (B)). Therefore, the main oblate cells appear to be similar for both, even with varying solid loadings. A reduction of the solid loading leads to numerous smaller cells appearing in the ceramic (Fig. 3.4 (A)), which separate the comparably larger oblate cells from each other. It appears that the larger oblate cell rows alternate with rows containing the smaller cells, but under maintenance of the equal cell orientation in principle. At higher magnification the cell walls are visibly not completely solidified (Fig. 3.4 (A.1), (B.1)) and characterized by an internal porosity as well. This is not surprising, because all ceramics presented here were subjected to the same sintering conditions (cf. section 3.1.2.3). In contrast to the ceramics manufactured with a gelatin concentration of 9.9 and 6.8 vol.%, the ceramic types G\_3.5\_14.4 and G\_3.5\_16.5 are characterized by surface asperities on the cell walls (Fig. 3.4 (A.2), (B.2)), which appear as vein-like system (Fig. 3.4 (A): red box, (B): red box). Fig. 3.4 (A.3) demonstrates the alternation between large, straight cell channels and closely positioned walls (parallel to the freezing direction), which comprise in itself prolate pores.

The cellular oblate cell network is not present at a gelatin concentration of 1.8 vol.% and at a solid loading of 16.5 vol.% (Fig. 3.4 (C)). This ceramic type, G\_1.8\_16.5, is rather characterized by disjointed cell walls, which are arranged without any specific alignment perpendicular to the freezing direction (Fig. 3.4 (C)). Just like the both ceramics described before, the cells walls are also characterized by surface asperities that occur mainly on one side of the cell wall (Fig. 3.4 (C): red box). The cell walls are aligned straightly and parallel to the freezing direction (Fig. 3.4 (C.2)) and have an average distance of 77  $\mu\text{m}$  one to another (Fig. 3.5 (B)). The internal strut porosity is displayed in Fig. 3.4 (C.1).

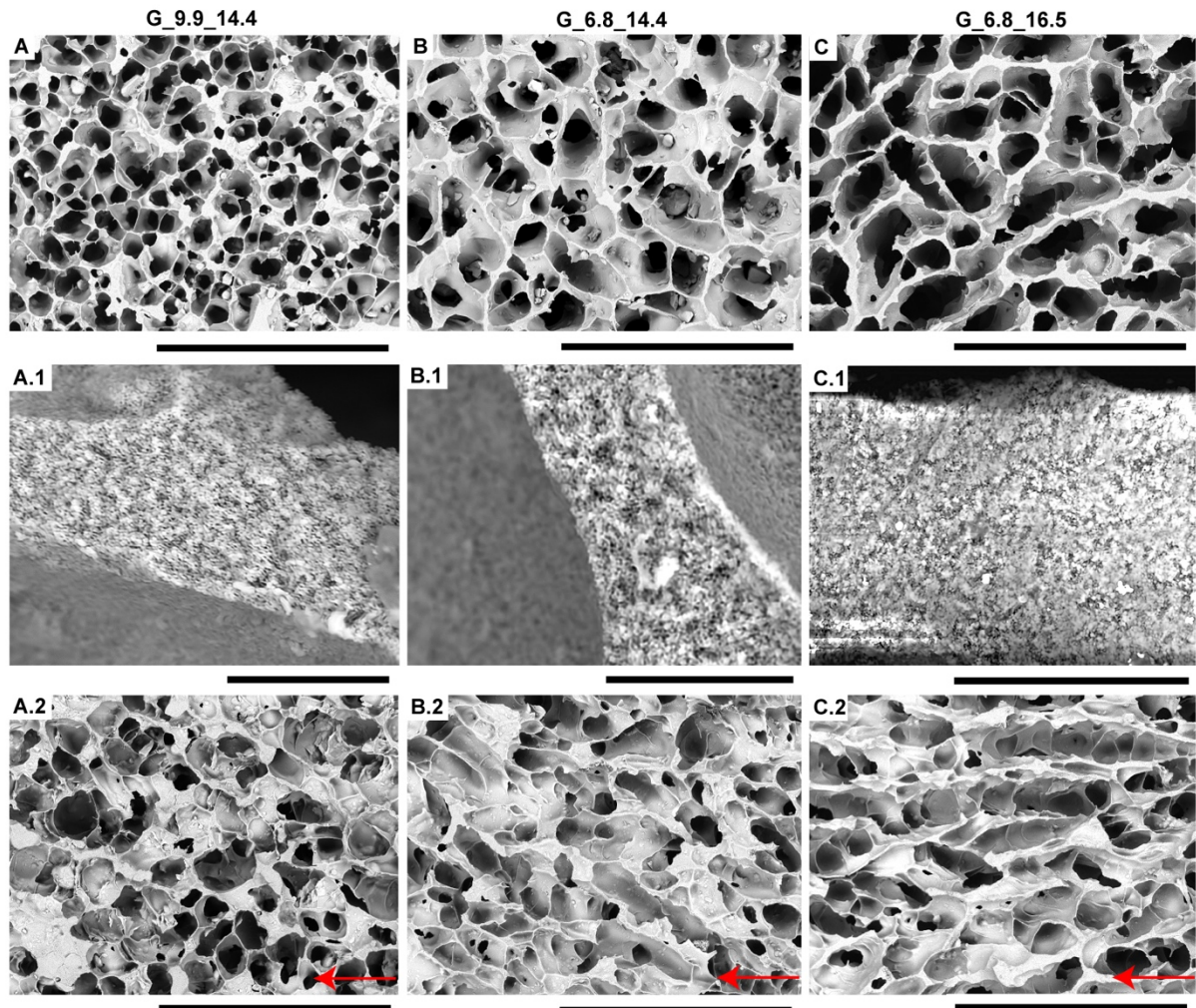


**Fig. 3.3:** BSE images of the microstructure of the alumina ceramics from the gelatin series. The columns (A), (B) and (C) belong to the ceramic type G\_9.9\_14.4, G\_6.8\_14.4 and G\_6.8\_16.5, respectively. The cross section (perpendicular to the freezing direction) of the ceramics is displayed in (A), (B) and (C). The images in (A.1), (B.1) and (C.1) show unconsolidated cell walls of the ceramics. The images in (A.2), (B.2) and (C.2) show the cross section of the ceramics parallel to the freezing direction. The red arrow demonstrates the freezing direction. Scale bars: (A), (B) and (C) = 500  $\mu\text{m}$ ; (A.1), (B.1) and (C.1) = 10  $\mu\text{m}$ ; (A.2), (B.2) and (C.2) = 500  $\mu\text{m}$ .

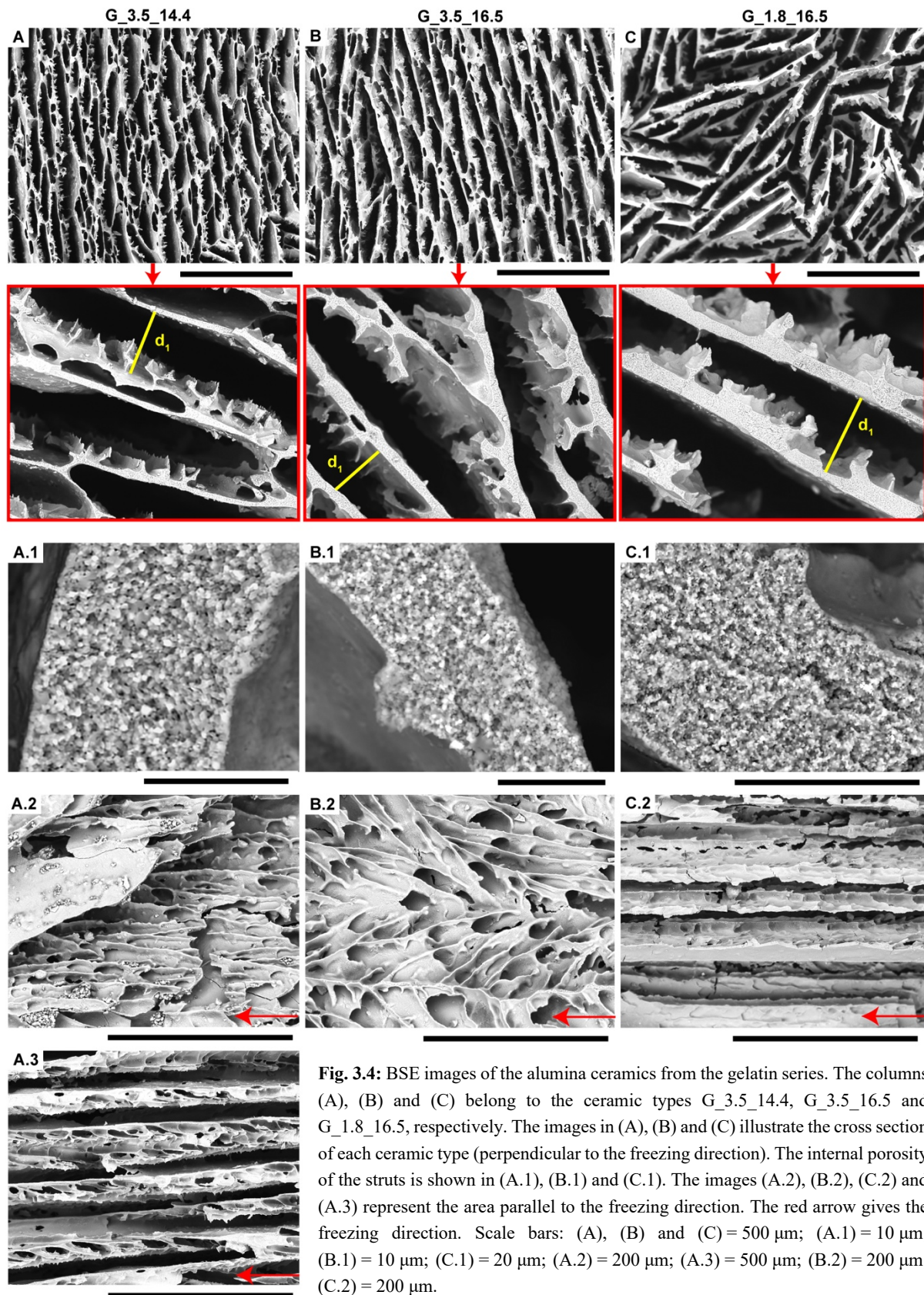


**Fig. 3.4:** BSE images of the alumina ceramics from the gelatin series. The columns (A), (B) and (C) belong to the ceramic types G\_3.5\_14.4, G\_3.5\_16.5 and G\_1.8\_16.5, respectively. The images in (A), (B) and (C) illustrate the cross section of each ceramic type (perpendicular to the freezing direction). The internal porosity of the struts is shown in (A.1), (B.1) and (C.1). The images (A.2), (B.2), (C.2) and (A.3) represent the area parallel to the freezing direction. The red arrow gives the freezing direction. Scale bars: (A), (B) and (C) = 500  $\mu\text{m}$ ; (A.1) = 10  $\mu\text{m}$ ; (B.1) = 10  $\mu\text{m}$ ; (C.1) = 20  $\mu\text{m}$ ; (A.2) = 200  $\mu\text{m}$ ; (A.3) = 500  $\mu\text{m}$ ; (B.2) = 200  $\mu\text{m}$ ; (C.2) = 200  $\mu\text{m}$ .

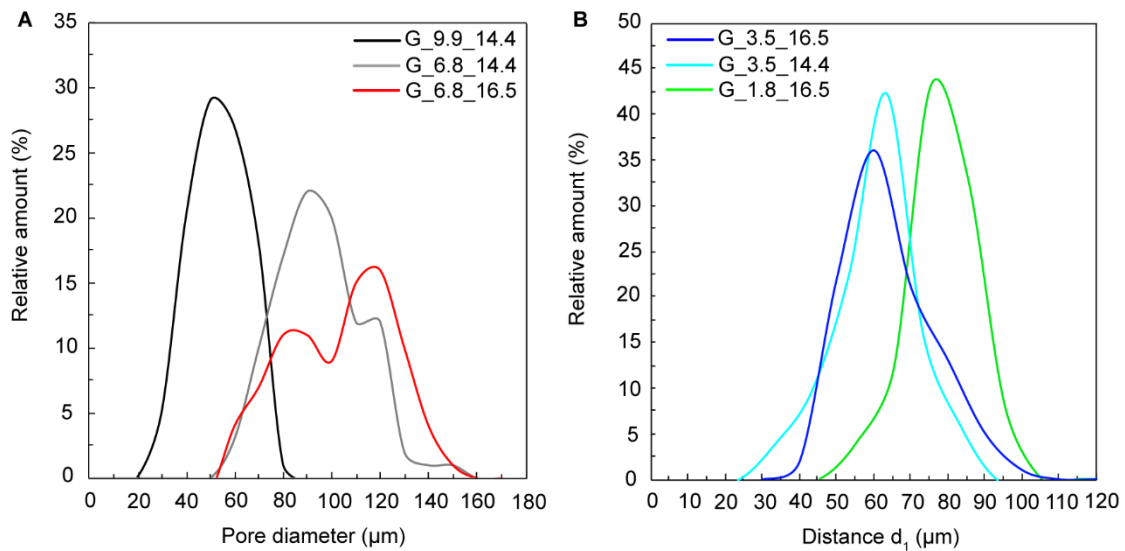


**Fig. 3.5:** Distribution ( $n = 100$ ) of the pore diameter and pore axis length of the alumina ceramics from the gelatin series. The pore diameter distribution of the ceramic types G\_9.9\_14.4, G\_6.8\_16.5 and G\_6.8\_14.4 is displayed in (A). The distribution of the pore axis length from the ceramic types G\_3.5\_16.5, G\_3.5\_14.4 and G\_1.8\_16.5 is shown in (B).

### 3.1.3.1.1 Analysis of the strut network

The quantification of the cellular network of the three main structural types, which appear in the gelatin series is illustrated in Fig. 3.6. In this case, ceramics with a solid loading of 16.5 vol.% were selected for the evaluation of the cellular network. They varied, however, in terms of their gelatin concentrations, which were applied for their manufacturing. The following gelatin concentrations comprise the selected ceramic specimens (G\_6.8\_16.5, G\_3.5\_16.5 and G\_1.8\_16.5): 6.8, 3.5 and 1.8 vol.% (Tab. 3.1). The designations of the detected elements are illustrated in Fig. 3.6. (D). A detailed description of the constituting elements was presented in section 3.1.2.5.

The degree of interconnectivity, which is expressed here as meshes, master segments, segments, junctions and nodes, reaches quantitatively the largest number in the ceramic type G\_6.8\_16.5 (Fig. 3.7: red columns; cf. Fig. 3.6 (A)). Such a quantitatively large number of the interconnectivity of the cell walls is not given for the ceramic types G\_3.5\_16.5 and G\_1.8\_16.5 (Fig. 3.7: blue and green columns). The quantity of meshes, master segments, segments, junctions and nodes are significantly decreased compared to the ceramic type G\_6.8\_16.5. On the other hand, the quantity of the detected elements such as extremities, isolated elements and branches is relatively large for both of the ceramic types G\_3.5\_16.5 and G\_1.8\_16.5 (Fig. 3.7: blue and green columns). The aforementioned elements like extremities, isolated elements and branches rather characterize the degree of non-connectedness of the cell walls. Therefore, these latter elements have been detected rarely in the ceramic type G\_6.8\_16.5, because the cell walls are strongly interconnected with each other.

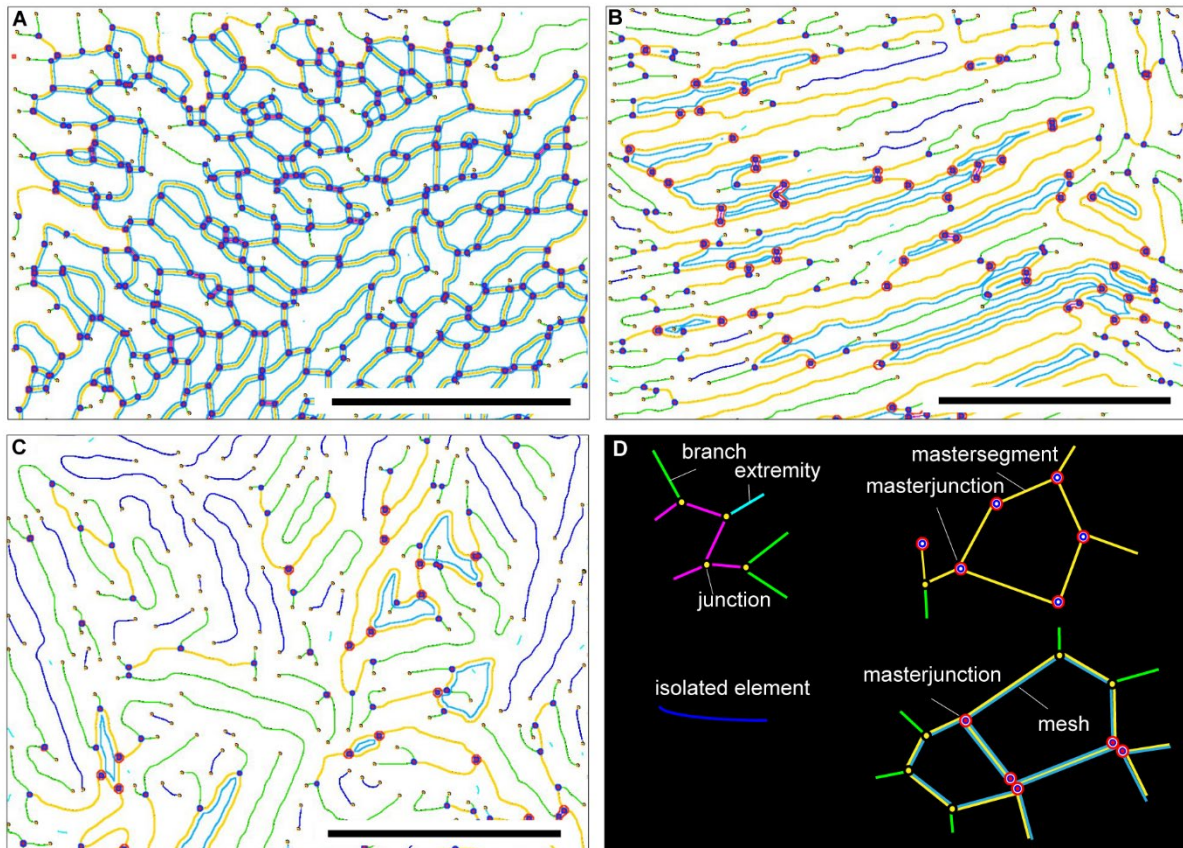


**Fig. 3.6:** Detected elements of the cellular network utilizing Angiogenesis Analyzer (Fiji 2.0.0). The quantification of the cellular network is based on BSE images of infiltrated ceramics and has considered the ceramics G\_6.8\_16.5 (A), G\_3.5\_16.5 (B) and G\_1.8\_16.5 (C). The designations of the detected elements are summarized in (D). Scale bar = 1 mm.

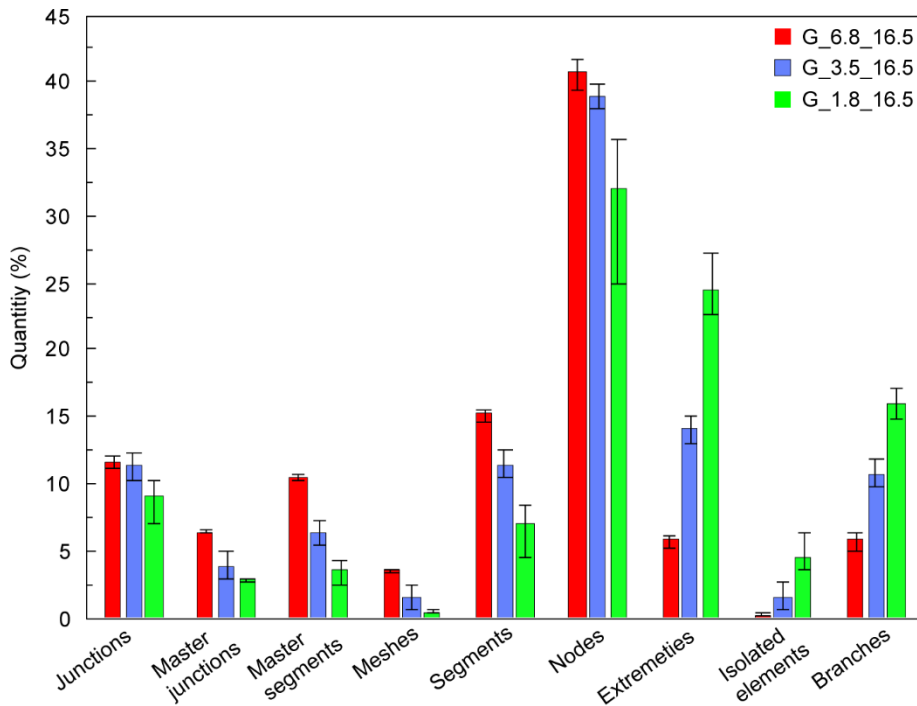


**Fig. 3.7:** Results of the cellular network using Angiogenesis Analyzer (Fiji 2.0.0).

### 3.1.3.2 Microstructure of the agar series

Utilizing agar as additive, ceramics can be manufactured with a solid loading of less than 9 vol.%. A solid loading of 8.6 vol.%, which was utilized for the ceramic types A\_4.3\_8.6 and AC\_4.3\_8.6, leads to porosities of 86 and 84 %, respectively (cf. Tab. 3.2). A larger porosity was achieved in the ceramic type A\_4.3\_5.9 that was manufactured with a solid loading of 5.9 vol.% (cf. Tab. 3.2). The different manufacturing methods of the ceramics from the agar series are explained in detail in section 3.1.2.2.

The ceramic type A\_4.3\_8.6 consists essentially of lamellar cell walls, which are arranged in one direction (Fig. 3.8 (A)) and have an average distance of 200  $\mu\text{m}$  to each other (Fig. 3.9). They appear in the cross-sectional view (perpendicular to the freezing direction) rather disconnected (Fig. 3.8 (A)) and contain no cross struts. Numerous cell walls display a wavy-like character (parallel to the freezing direction), so some of the cell walls meet and create a junction (Fig. 3.8 (A.2): yellow arrow). In general, the cell walls appear flaky with panels detaching on several places (Fig. 3.8 (A.2)). This, in turn, results in rather loose composed cell walls (Fig. 3.8 (A.2)). The ceramic type AC\_4.3\_8.6 was manufactured with the same concentration of agar, solid loading and sucrose such as in the ceramic type described before. Additionally, the pH of the ceramic suspension was adjusted with citric acid to a pH value of 4 during the manufacturing process. This leads to spherical cell shapes in the ceramic type AC\_4.3\_8.6 (Fig. 3.8 (B)). The average diameter of the pores is 210  $\mu\text{m}$  (Fig. 3.9). The cell walls are connected with adjacent cell walls by cross struts parallel to the freezing direction (Fig. 3.8 (B.2)). In this way, the spaces between the cell walls appear to have a prolate shape (Fig. 3.8 (B.2)). The cell walls are also characterized by flaky cohesion.

A solid loading of 5.9 vol.% and an agar concentration of 4.3 vol.% without the use of sucrose and reduction of the pH has created widely open cell channels, which form polygonal cells at several places in the ceramic type A\_4.3\_5.9 (Fig. 3.8 (C)). The cell edges display no signs of flocculation and thus show rather sharp cell edges and surfaces (Fig. 3.8 (C)). The cell walls by themselves, however, are strongly penetrated by cracks and appear to be strongly fragmented (Fig. 3.8 (C.2)). The internal porosity of the struts is displayed in Fig. 3.8 (C.1). The internal porosity of the struts is also present in the ceramic types A\_4.3\_8.6 and AC\_4.3\_8.6 from the agar series (cf. Fig. 3.8 (A.1), (B.1)).

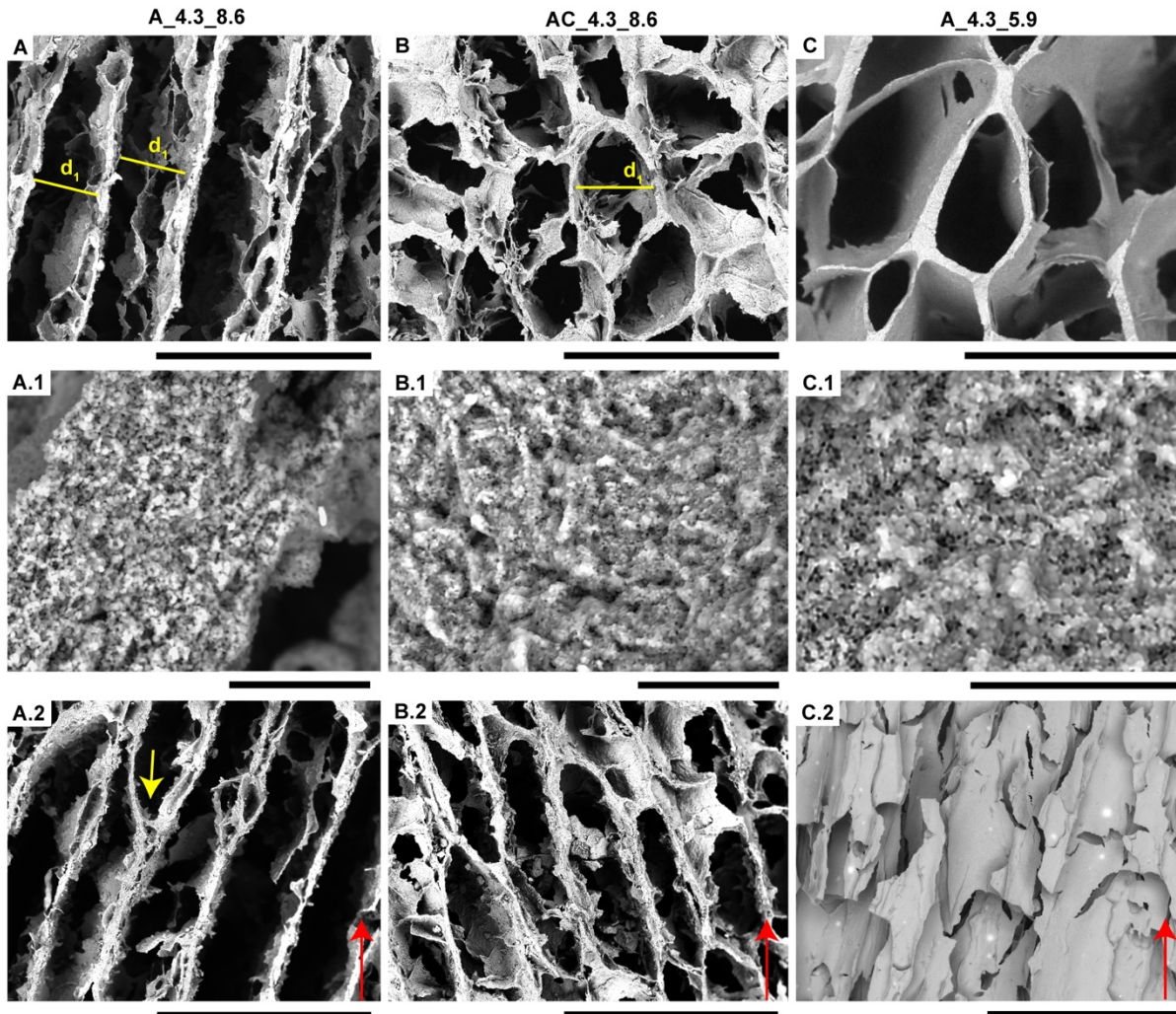


**Fig. 3.8:** BSE images of the microstructure of the alumina ceramics from the agar series. The (A) row displays the ceramic A\_4.3\_8.6. The ceramic AC\_4.3\_8.6 is shown in the (B) row, whereas the ceramic A\_4.3\_5.9 is displayed in row (C). The concentration of the solid loading, agar and sucrose concentration is given in Tab. 3.2. The cross section of the ceramics (perpendicular to the freezing direction) is displayed in (A), (B) and (C). The images in (A.1), (B.1) and (C.1) show the internal porosity of the struts. The images below ((A.1), (B.2) and (C.3)) display the area parallel to the freezing direction. The freezing direction is given as red arrow. Scale bars: (A) = 500  $\mu\text{m}$ , (B) = 500  $\mu\text{m}$ , (C) = 500  $\mu\text{m}$ ; A.1 = 10  $\mu\text{m}$ , B.1 = 10  $\mu\text{m}$ , C.1 = 10  $\mu\text{m}$ ; A.2 = 500  $\mu\text{m}$ , B.2 = 500  $\mu\text{m}$ , C.2 = 2 mm.

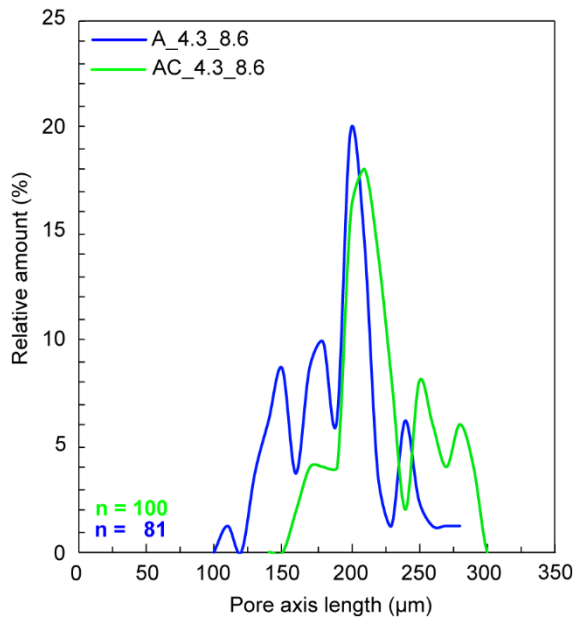


**Fig. 3.9:** Pore axis length of the ceramics from the agar series. The pore axis length gives the distance between the cell walls (cf. Fig. 3.8 (A), (B)) of the cross section (perpendicular to the freezing direction).

A  $\mu$ CT reconstruction of the ceramic type A\_4.3\_5.9 reveals the cellular arrangement of the cell walls. The cell walls by themselves appear to be rather loose without being connected together by other cell walls (Fig. 3.10). The cell walls display strong curvatures and are randomly oriented in the ceramic. Therefore, the distance from one cell wall to the adjacent was not determined due to the irregular arrangement of the cell walls and the curvatures. In contrast, the strut thickness was determined based on the  $\mu$ CT reconstruction. An average strut thickness of 27  $\mu$ m was determined (Fig. 3.11 (A)), whereby a lot of struts reach a thickness of less than 27  $\mu$ m (Fig. 3.11 (B)).

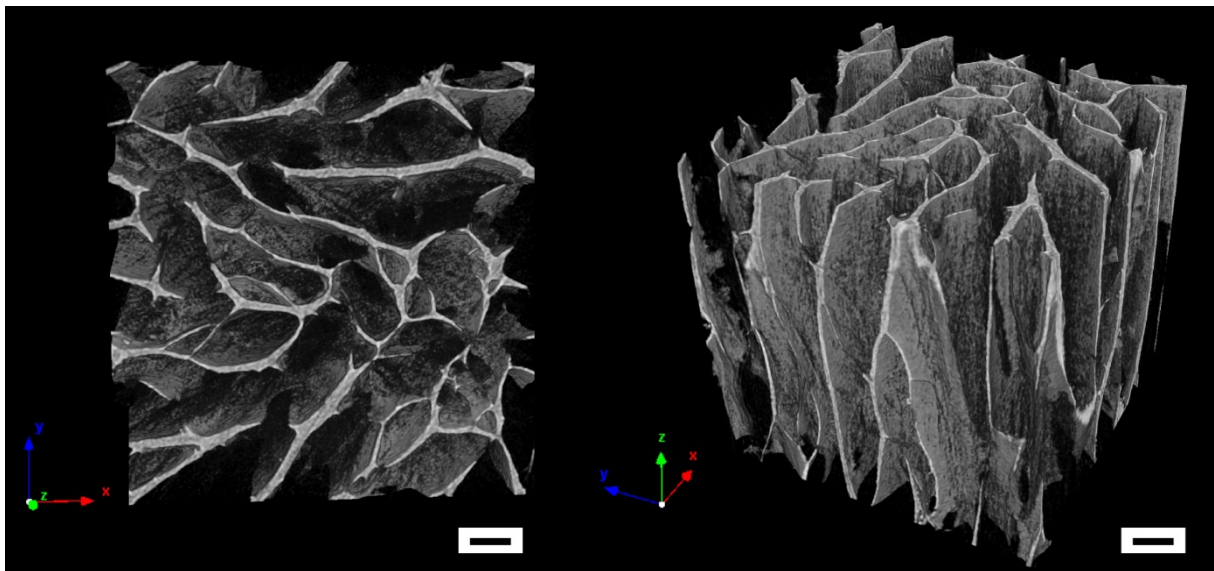


**Fig. 3.10:** Reconstruction of the  $\mu$ CT data of the ceramic type A\_4.3\_5.9. The cell walls are characterized by strong curvatures and display little preferred orientation. Distribution of the cell wall thickness are displayed in Fig. 3.11. Scale bar = 200  $\mu$ m.

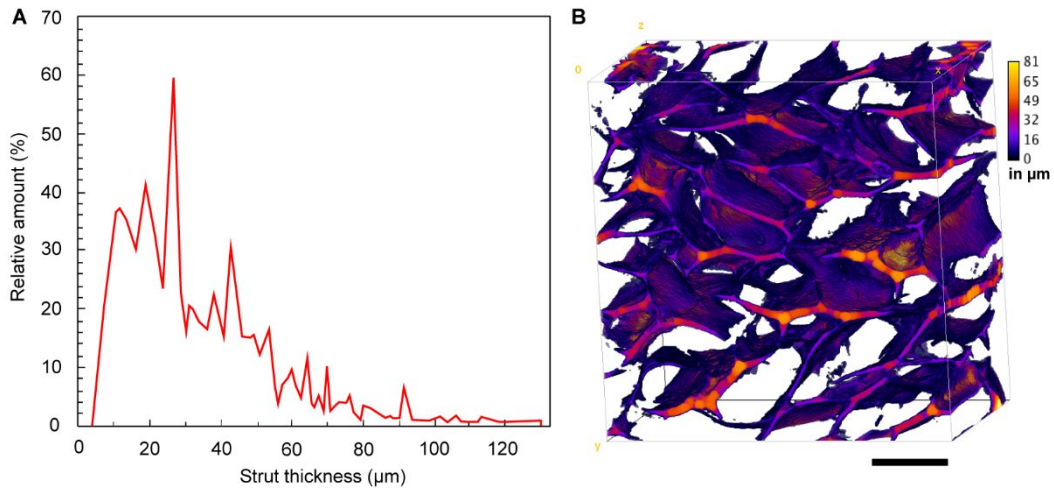


**Fig. 3.11:** Determination of the strut thickness of the ceramic type A\_4.3\_5.9 from the agar series. The strut thickness is based on  $\mu$ CT data. The distribution of the strut thickness is displayed in (A). Results of the visual strut distribution is shown in (B). Scale bar = 200  $\mu$ m

### 3.1.3.3 Uniaxial compression of the ceramics

The following ceramics from the gelatin series were tested mechanically: G\_6.8\_16.5, G\_3.5\_16.5, G\_1.8\_16.5, G\_6.8\_14.4 and G\_3.5\_14.4. From the agar series, only the ceramic type A\_4.3\_5.9 was tested under uniaxial compression. Fig. 3.12 displays the used symbols in diagrams of material properties, fracture behavior and the energy absorption capacity. Each figure deals with one specific strut arrangement caused by the use of varying gelatin concentrations in the manufacturing process. Details of the mechanical behavior of the ceramics, which are characterized by roundish cell channels with a high degree of connectedness of the cell walls as well as ceramics comprising cellular oblate cells are shown in section 3.1.3.3.2. It includes also the fracture behavior of ceramics, which are characterized by numerous isolated cells.

The classification for cellular solids in compression by Gibson (2005) can also be transferred to the failure modes of the ceramics: a linear elastic regime, the ‘quasi-ductile’ regime (post collapse) and densification. The stage of densification is not necessarily always involved at the end of uniaxial compression of the ceramic. A strong structural segmentation can lead to several segments, which could disaggregate simultaneously. Therefore, the uniaxial testing can be considered as terminated, since no segment is in contact with the compression die anymore.

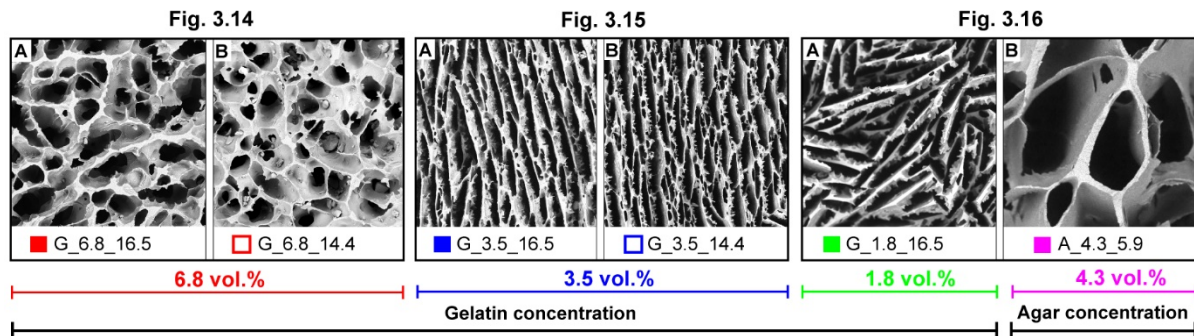


**Fig. 3.12:** Freeze-cast alumina ceramics, which were tested under uniaxial compression. The utilized symbols are displayed below.

### 3.1.3.3.1 Material properties

The results of the material properties, expressed as  $\sigma_c$  and the Young's modulus, of the freeze-casted alumina ceramics are displayed in Fig. 3.13. For the sake of clarity, the composition of the ceramics in terms of the solid loading and concentration of the additive are differentiated in Fig. 3.12 by using different colors and symbols. The ceramics, which were manufactured with a gelatin concentration of 6.8, 3.5 and 1.8 vol.%, are marked as red, blue and green squares, respectively. The open and filled squares give the concentration of the used solid loading: a solid loading of 16.5 and 14.4. vol.% can be assigned in each case to the filled and open squares.

Ceramics, which were manufactured with the same solid loading have approximately the same range of porosity, but differentiate in their values of the strength and stiffness. The values of the material properties indicate that the configuration and arrangement of the cell walls influence significantly the strength and stiffness of the ceramics. The previously presented values of the stiffness and strength of the three ceramic types were evaluated in terms of their strut network in section 3.1.3.1.1. By combining the material properties with the results of the strut network, it can be observed that the degree of interconnectivity of the cell walls correlates with the values of the stiffness and strength of the ceramics. The largest values of the stiffness and strength achieves the ceramic type G\_6.8\_16.5, which is characterized by the largest quantity of detected elements such as meshes, master segments, segments, junctions and nodes indicating, in turn, that the cell walls are strongly interconnected among each other. The ceramic type G\_1.8\_16.5 has the lowest stiffness and strength of the three ceramic types from the gelatin series. The largest quantity of isolated elements, branches and extremities was observed in this ceramic type. The isolated cell walls are incapable to withstand lateral motions by shear stress. A strong interconnectivity of the cell walls, on the other hand, ensures additional stiffening, which rises the mechanical stability of the ceramic. The same correlation is observed in the ceramics manufactured with a lower solid loading of 14.4 vol.% ((Fig. 3.12 (A), (B): open squares). It involves the ceramic types G\_6.8\_14.4 (red open squares) and G\_3.5\_14.4 (blue open squares). Their porosity ranges between 82 and 87 %. The values of the  $\sigma_c$  and for the Young's modulus of the ceramic type G\_6.8\_14.4 are between 16 and 20 MPa and between 677 and 1329 MPa, respectively. The ceramic type G\_3.5\_14.4 has lower values of the  $\sigma_c$  and for the Young's modulus: the values of the  $\sigma_c$  vary between 7 and 12 MPa,

whereas the values for the Young's modulus are between 108 and 400 MPa. Comparing Fig. 3.3 (C) and Fig. 3.4 (A), it can be seen that the quantity of the isolated cell walls is larger in the ceramic type G\_3.5\_14.4. It becomes clear that the mechanical stability is dependent on the strut arrangement. When the cell walls are strongly linked with each other, the mechanical stability is also increased in this context. The lowest strength and stiffness come from the ceramic type from the agar series. This ceramic type has a value of the  $\sigma_c$  of 0.7 MPa and a Young's modulus of just 23 MPa. The ceramic type is characterized by wide channels without any intermediate struts/ bridges. This results in long bearing distances. Thus, the cell walls are subject to high shear stresses and bending moments under uniaxial loading and are therefore not able to withstand high mechanical loadings.

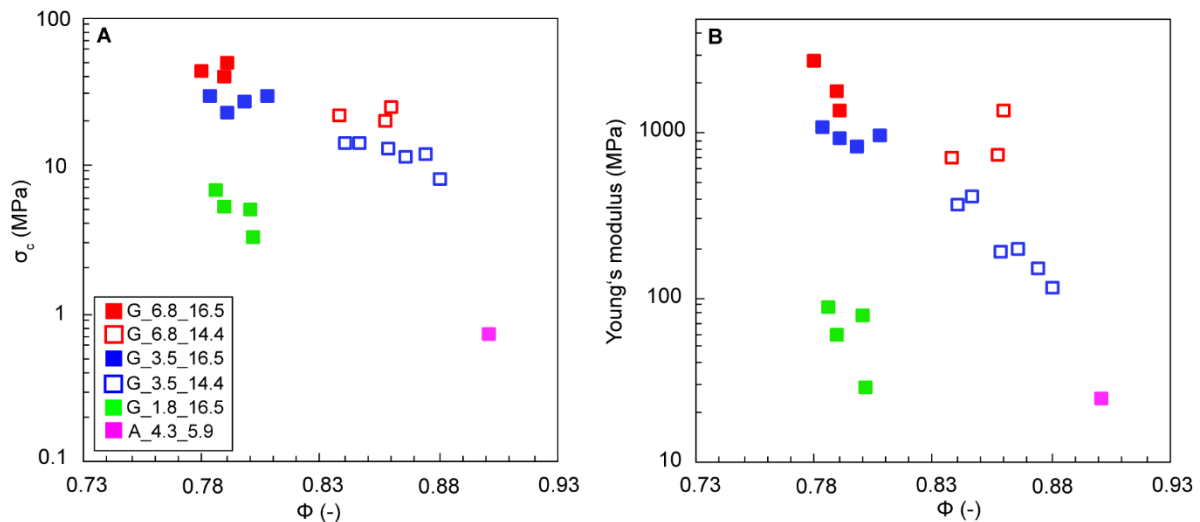


**Fig. 3.13:** The maximum compressive strength,  $\sigma_c$ , and Young's modulus values of the ceramics from the gelatin and agar series. The plot (A) displays the relationship of the  $\sigma_c$ , (B) the Young's modulus as a function of the porosity,  $\phi$ .

### 3.1.3.3.2 Ceramic type 'circular cell shape'

Fig. 3.14 displays the stress-strain curves and corresponding microphotographs of the fracture behavior of the ceramics, which are characterized by circular cell shapes and a high degree of interconnectedness of the struts.

After the linear elastic increase, the ceramic compensates the stress by crumbling (Fig. 3.14 (A): a, b and Fig. 3.14 (B): a, b) and subsequently flakes into smaller parts starting from the upper region of the ceramic (Fig. 3.14 (A): c, d, e, f and Fig. 3.14 (B): c, d, e). The two fracture mechanisms make it possible to avoid stress decreasing drastically in large scales in the 'quasi' ductile regime. By the mode of crumbling and flaking the ceramic is rather capable to keep the acting stress on a constant level (Fig. 3.14 (A), (B): starting from a strain of 0.2) before the densification starts (Fig. 3.14 (B): f).

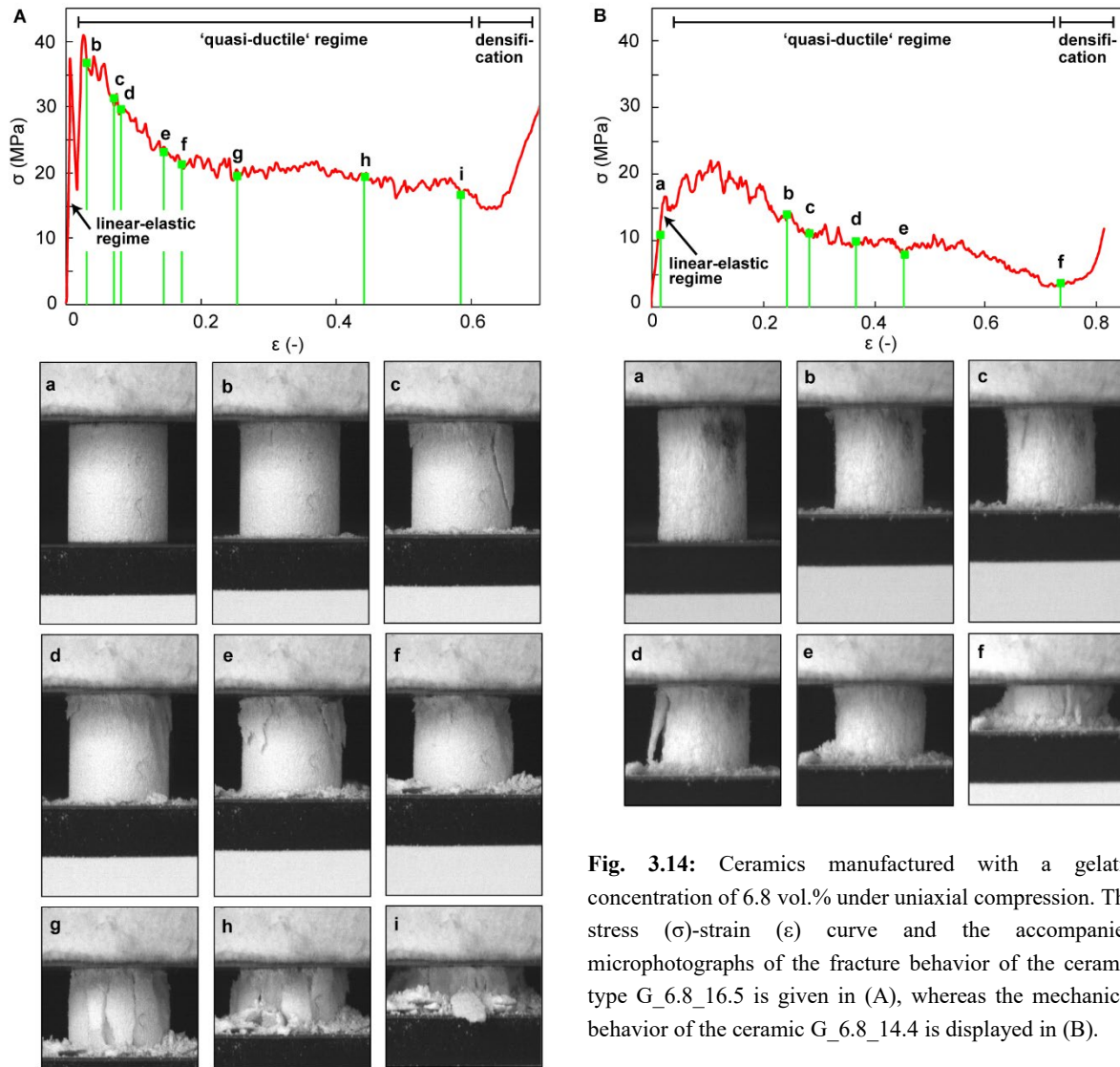


**Fig. 3.14:** Ceramics manufactured with a gelatin concentration of 6.8 vol.% under uniaxial compression. The stress ( $\sigma$ )-strain ( $\epsilon$ ) curve and the accompanied microphotographs of the fracture behavior of the ceramic type G\_6.8\_16.5 is given in (A), whereas the mechanical behavior of the ceramic G\_6.8\_14.4 is displayed in (B).

### 3.1.3.3.3 Ceramic type ‘cellular oblate cell shape’

The stress-strain curves and accompanied microphotographs of the fracture behavior of the ceramic types, which contain rather cellular oblate cell shapes and several disjointed cell walls integrated in the microstructure are presented in Fig. 3.15. Compared to the ceramic types ‘circular cell shape’, which were presented before, these ceramic types here are essentially characterized by a steeper gradual decrease of the compensating stress (Fig. 3.15 (A), (B)). After reaching the  $\sigma_c$ , both show clearly the formation of vertical cracks (Fig. 3.15 (A): b, c and Fig. 3.15 (B): b), which intensify with continuous loading (Fig. 3.15 (A): d, e and Fig. 3.15 (B): c, d).

This multiple propagation of vertical cracks in the ceramic results in a division into several lath-like segments, which tilt increasingly to the side with continuous loading (Fig. 3.15 (A): f, g, h, i and Fig. 3.15 (B): e, f, g).

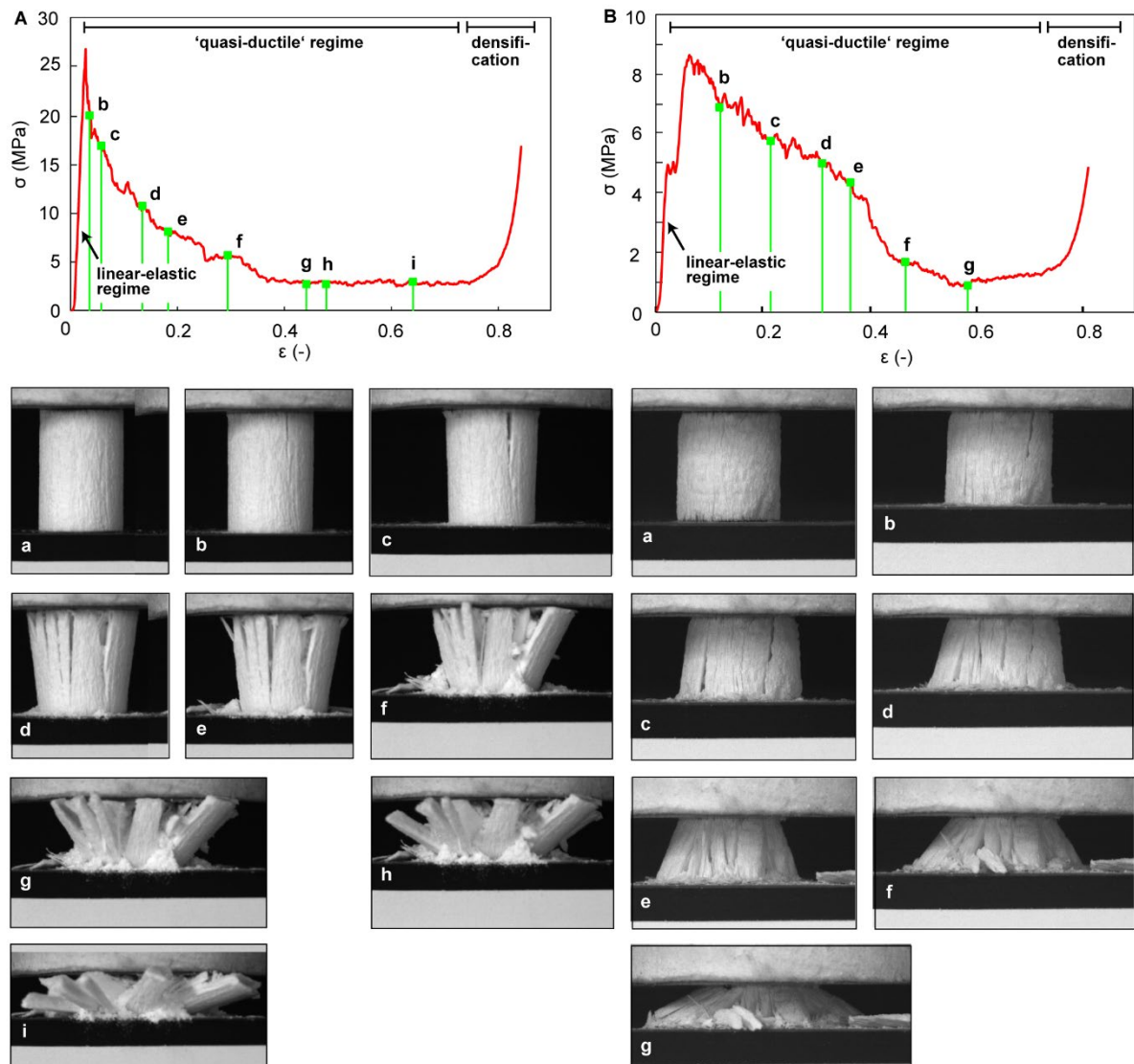


**Fig. 3.15:** Uniaxial compression tests of the ceramics manufactured with a gelatin concentration of 3.5 vol.%. The stress ( $\sigma$ )-strain ( $\epsilon$ ) curve and accompanied microphotographs of the fracture behavior of the ceramic type G\_3.5\_16.5 is shown in (A). The failure mode and related stress ( $\sigma$ ) – strain ( $\epsilon$ ) curve of the ceramic G\_3.5\_14.4 is given in (B).

#### 3.1.3.3.4 Ceramic type ‘disjointed cell walls’

The fracture behavior displayed as microphotographs and the stress-strain curves of the ceramic types, which contain in their majority disjointed cell walls in the microstructure, are presented in Fig. 3.16. The course of the stress-strain curve in Fig. 3.16 (A) resembles those exhibited by the ceramic type ‘cellular oblate cell shape’. The stress-strain curve is also characterized by a large drop in stress after achieving the  $\sigma_c$ , which is associated with the propagation of a vertical crack systems (Fig. 3.16 (A): b). An intensification of the vertical cracks, which is associated with a segmentation of the ceramic into several lath-like segments occurs as well with continuous loading (Fig. 3.16 (A): c, d). In contrast to the failure mode of the ceramic type ‘cellular oblate cell shape’, the ceramics here do not undergo a densification, since the lath-like segments were already tilted sideways (Fig. 3.16 (A): f).

This kind of fracture mechanism, which develops a vertical crack system leading subsequently to a structural segmentation, can also be observed in the ceramic from the agar series (Fig. 3.16 (B): a-g). Compared to the stress-strain curve of the ceramic presented in Fig. 3.16 (A), the stress-strain curve here is rather characterized by a gradual increase of stress after the load-limit was reached (Fig. 3.16 (B)). However, starting at a strain of 0.07, the stress fluctuates around an average plateau value until the first vertical cracks propagate through the structure (Fig. 3.16 (B): b). After the vertical crack formation, the stress decreases gradually with continuous loading, since the structural integrity of the ceramic progressively decreases, which is, in turn, accompanied with a structural segmentation of the ceramic (Fig. 3.16 (B): c, d, e, f). The remaining segments are densified in the last stage of compression (Fig. 3.16 (B): g).

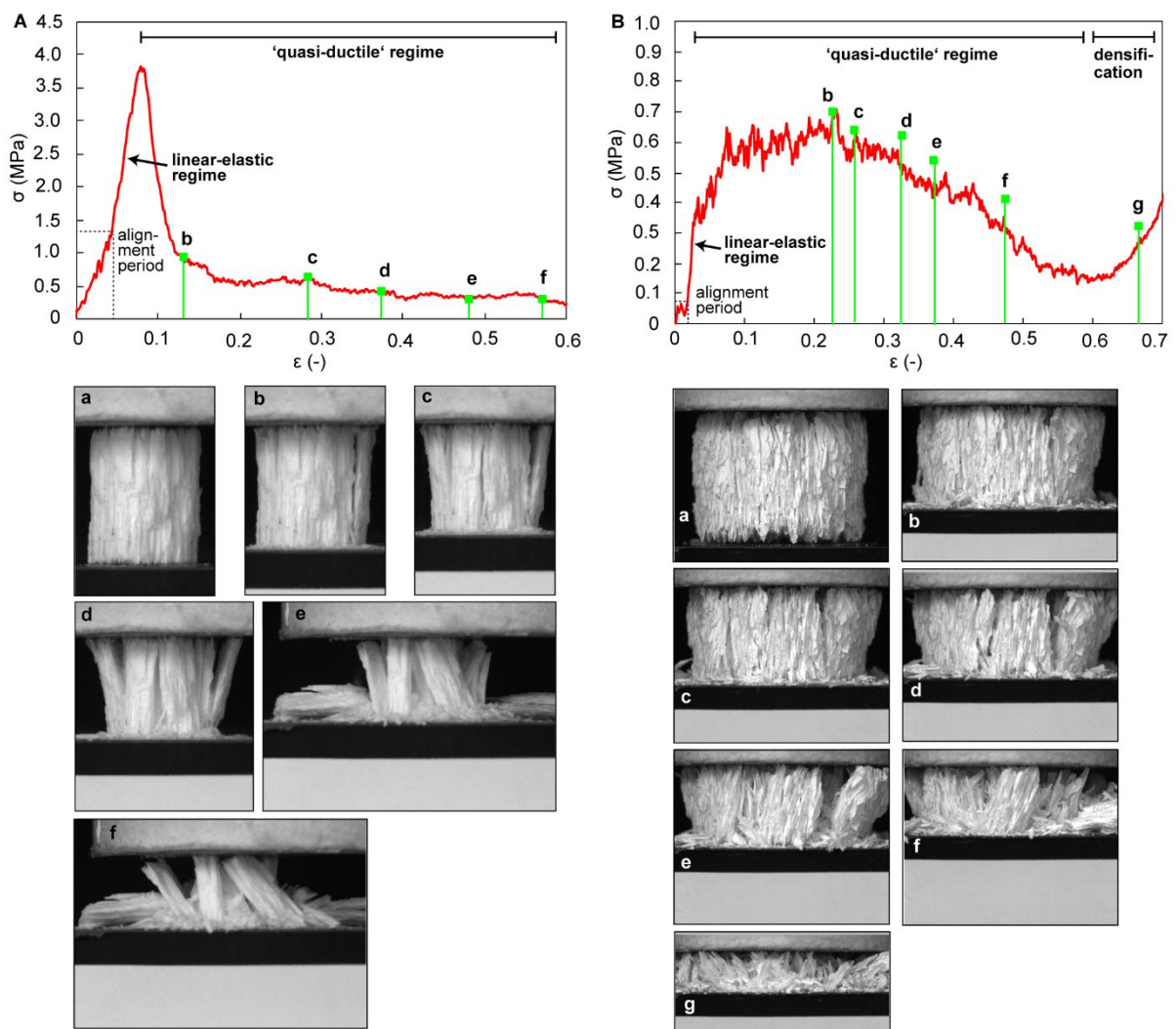


**Fig. 3.16:** Ceramics under uniaxial compression from the gelatin and agar series. The stress ( $\sigma$ )-strain ( $\epsilon$ ) curve and accompanied microphotographs of the fracture behavior of the ceramic G\_1.8\_16.5 are displayed in (A). The mechanical behavior of the ceramic A\_4.3\_5.9 from the agar series is given in (B).

### 3.1.3.3.5 Energy absorption capacity

The specific energy absorption per volume unit,  $U_v(\epsilon)$ , and the energy efficiency,  $\eta_{(\epsilon)}$ , was calculated from the stress-strain curves utilizing Eq. (3), (4) and (5). The curves of the  $U_v(\epsilon)$  of the ceramics manufactured from the gelatin series are displayed in Fig. 3.17 (A). The curve of the  $U_v(\epsilon)$  of the ceramic from the agar series is not shown, due to the comparable low capability of the  $U_v(\epsilon)$ . All ceramic types are characterized by a peak value of the  $U_v(\epsilon)$ , which decreases gradually with increasing strain. The average values of the  $U_v(\epsilon)$  and their distribution at a strain of 0.3 and 0.5 are summarized in Fig. 3.17 (B). The maximum values of the  $U_v(\epsilon)$  and their distribution are displayed in Fig. 3.17 (B) as well. The ceramic type ‘circular pore shape’ reaches the largest values of the  $U_v(\epsilon)$ . The ceramics comprising disjointed cell walls, are characterized by the lowest values of all manufactured ceramics. The ceramics with the cellular, oblate cell walls are in between of them.

The converted values of the  $U_v(\epsilon)$  into the  $\eta_{(\epsilon)}$  of the ceramics are summarized in Fig. 3.17 (C). It can be observed that the decrease of the  $\eta_{(\epsilon)}$  values from those ceramics, which belong to the ceramic type ‘circular pore shape’, is not as large as from ceramics, which are characterized by disjointed cell walls and a cellular oblate cell shape. At a strain of 0.5, the average values of the  $\eta_{(\epsilon)}$  remain above 80 % for both of them. A significantly larger decrease of the average values of the  $\eta_{(\epsilon)}$  display the ceramics of the ceramic type ‘disjointed cell walls’ and ‘cellular oblate cell shape’: at a strain of 0.5, the average values of the  $\eta_{(\epsilon)}$  of the ceramic G\_3.5\_16.5, G\_3.5\_14.4 and G\_1.8\_16.5 fall beneath 65 %.

Variations of the average values of the  $\eta_{(\epsilon)}$ , especially at the strain of 0.5, indicate that different fractures modes are effectively involved in the ceramics. The varying fracture modes are mainly determined by the internal configuration of the cell walls within the ceramic. Two main categories of fracturing were observed during the uniaxial compression of the ceramics:

- a) a simultaneous interplay of flaking and crumbling;
- b) an intensification of vertical cracks leading to a segmental division of the ceramic into several lath-like segments.

The fracture mode b) occurs at ceramics, which belong to the ceramic type ‘disjointed cell walls’ and ‘cellular oblate cell shape’. Both are characterized by numerous disjointed cell walls. As mentioned in section 3.1.3.3.1, the isolated and disjointed cell walls are subject to shear stress and therefore susceptible to high deflection during the uniaxial compression. Consequently, larger segments can spall off from the structure. In this way, the structural integrity is no longer ensured and the capability to absorb stress is thus reduced greatly.

In contrast, ceramics, which belong to the ceramic type ‘circular pore shape’, undergo progressive crumbling and flaking of small lateral pieces. The strong connectivity of the cell walls to each other prevents shearing and thus bending moments of the cell walls. Therefore, the stiffening increases the mechanical stability and keeps the material loss comparatively low. It implies that the major proportion of the ceramics tends to retain its structural integrity. Consequently, a high quantity of stress is therefore needed to break the strong cohesive structure.

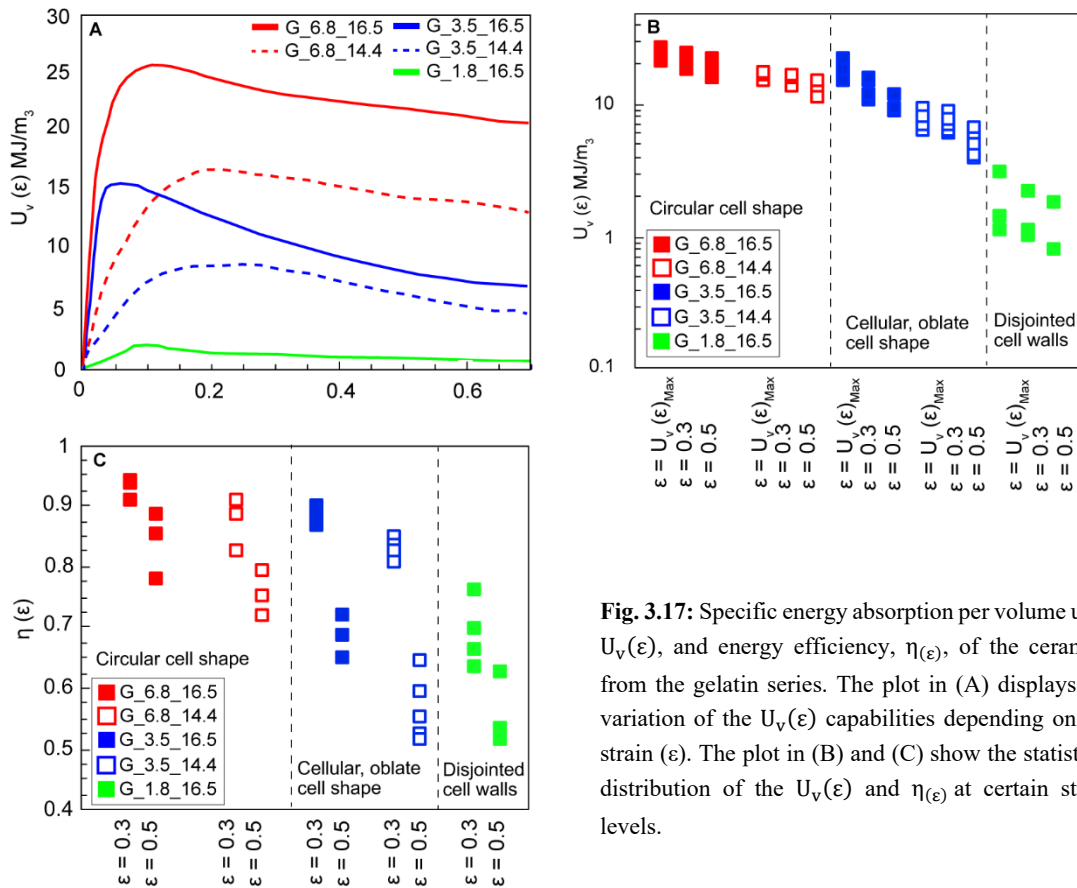


**Fig. 3.17:** Specific energy absorption per volume unit,  $U_v(\epsilon)$ , and energy efficiency,  $\eta(\epsilon)$ , of the ceramics from the gelatin series. The plot in (A) displays the variation of the  $U_v(\epsilon)$  capabilities depending on the strain ( $\epsilon$ ). The plot in (B) and (C) show the statistical distribution of the  $U_v(\epsilon)$  and  $\eta(\epsilon)$  at certain strain levels.

### 3.1.3.4 Gradation and separate structural areas in one ceramic

The manufacturing of a graded pore system is possible by using mold design I (Fig. 3.18 (A)). The gradation is limited to the lower region of the mold, which is directly adjacent to the bottom plate of the mold. The gradation is thus limited to the first 10 % of height from the ceramic.

The inner structure of the ceramic consists of polygonal pores with almost directional cell channels (parallel to the freezing direction) and is thus termed as ‘Zone C’ (Fig. 3.18 (B), (C)). The pore diameters are between 50 and 180  $\mu\text{m}$ . Further outwards the diameter of the polygonal pores becomes smaller (Fig. 3.18 (C)). They reach a pore diameter of approximately 30 to 50  $\mu\text{m}$ , whereby larger pores are visible at few specific points as well (Fig. 3.18 (C)). This area is stated as ‘Zone B’ (Fig. 3.18 (A)). The cell channels are oriented almost parallel to the freezing direction and tilt increasingly to the side towards the outside (Fig. 3.18 (B)). Very large channel sizes are present in the outermost area of the ceramic, namely in the ‘Zone A’ (Fig. 3.18 (B)). Due to the varying channel sizes in ‘Zone A’, it is not feasible to determine an approximate value of the cell size (Fig. 3.18 (A)).

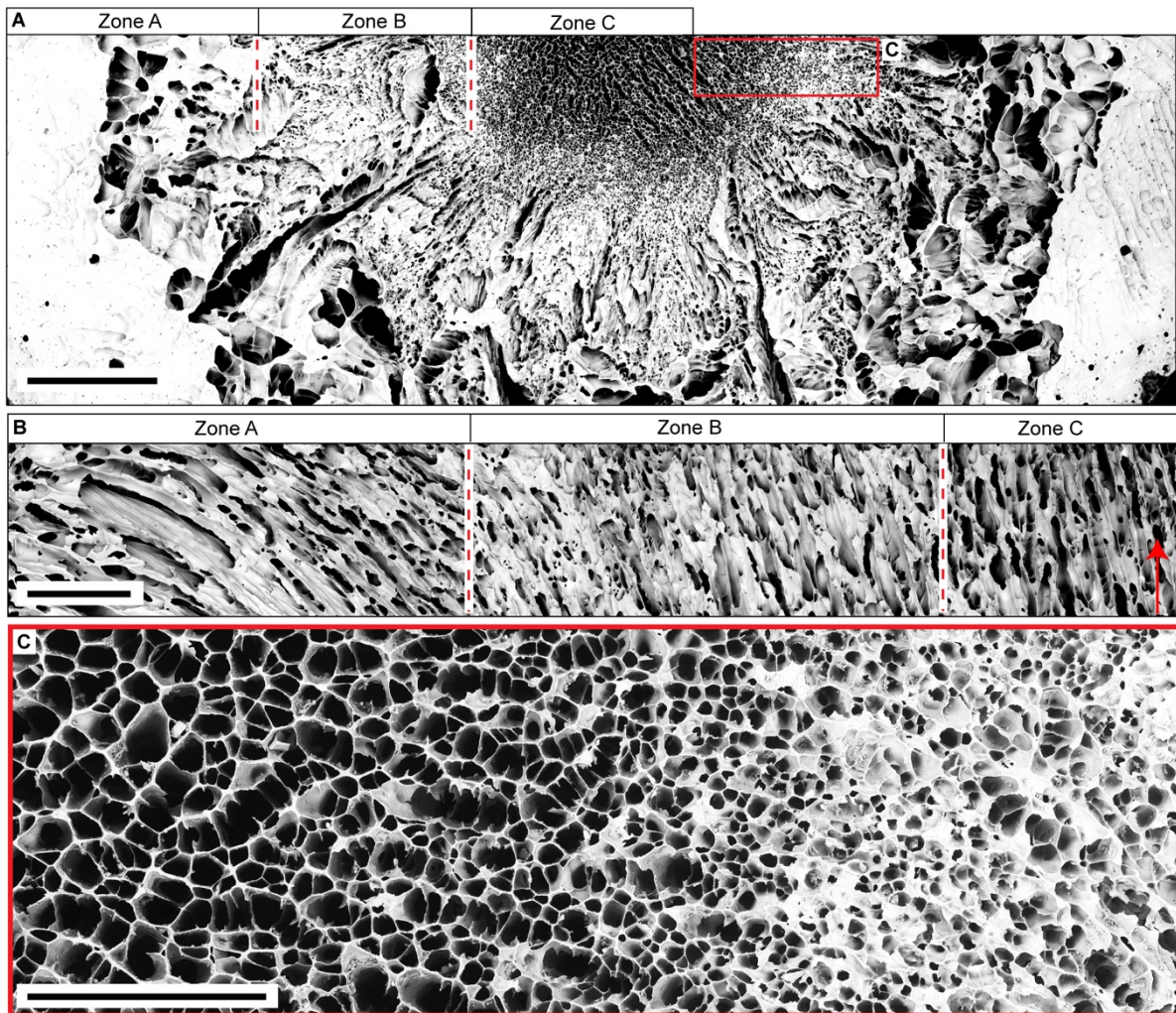


**Fig. 3.18:** Graded ceramic manufactured by utilizing mold design I. The microstructure of the ceramic and its division in different zones is displayed in (A) that illustrates the cross-sectional area perpendicular to the freezing direction. The orientation of the cell channels is given in (B). The red arrow demonstrates the freezing direction. A higher magnification of the graded structure is displayed in (C). The area is marked as red rectangle in (A). Scale bars: (A) = 2 mm, (B) = 500  $\mu\text{m}$ , (C) = 500  $\mu\text{m}$ .

Using mold design II creates two separated structural areas in the ceramic (Fig. 3.19). In contrast to the limited extension in height of the ceramic manufactured with mold design I, the two structural separated areas have no limitation in height. The outermost area of the ceramic appears to have a foam-like character (Fig. 3.19 (A), (B)), which transforms into tilted cell channels inside of the ceramic (Fig. 3.19 (C)). It should be noted that the shaping of several cell channels is rather blurred at some places. This outermost area is called ‘Zone A’ (Fig. 3.19 (A), (B), (D)). Clearly defined cell channels are visible in the inner zone of the ceramic, which is here called ‘Zone B’ (Fig. 3.19 (D)). The cell shape is polygonal as well and reaches a cell diameter between 60 and 160  $\mu\text{m}$  (Fig. 3.19 (C)). Cell channels of ‘Zone B’ are oriented almost parallel to the freezing direction (Fig. 3.19 (C)).

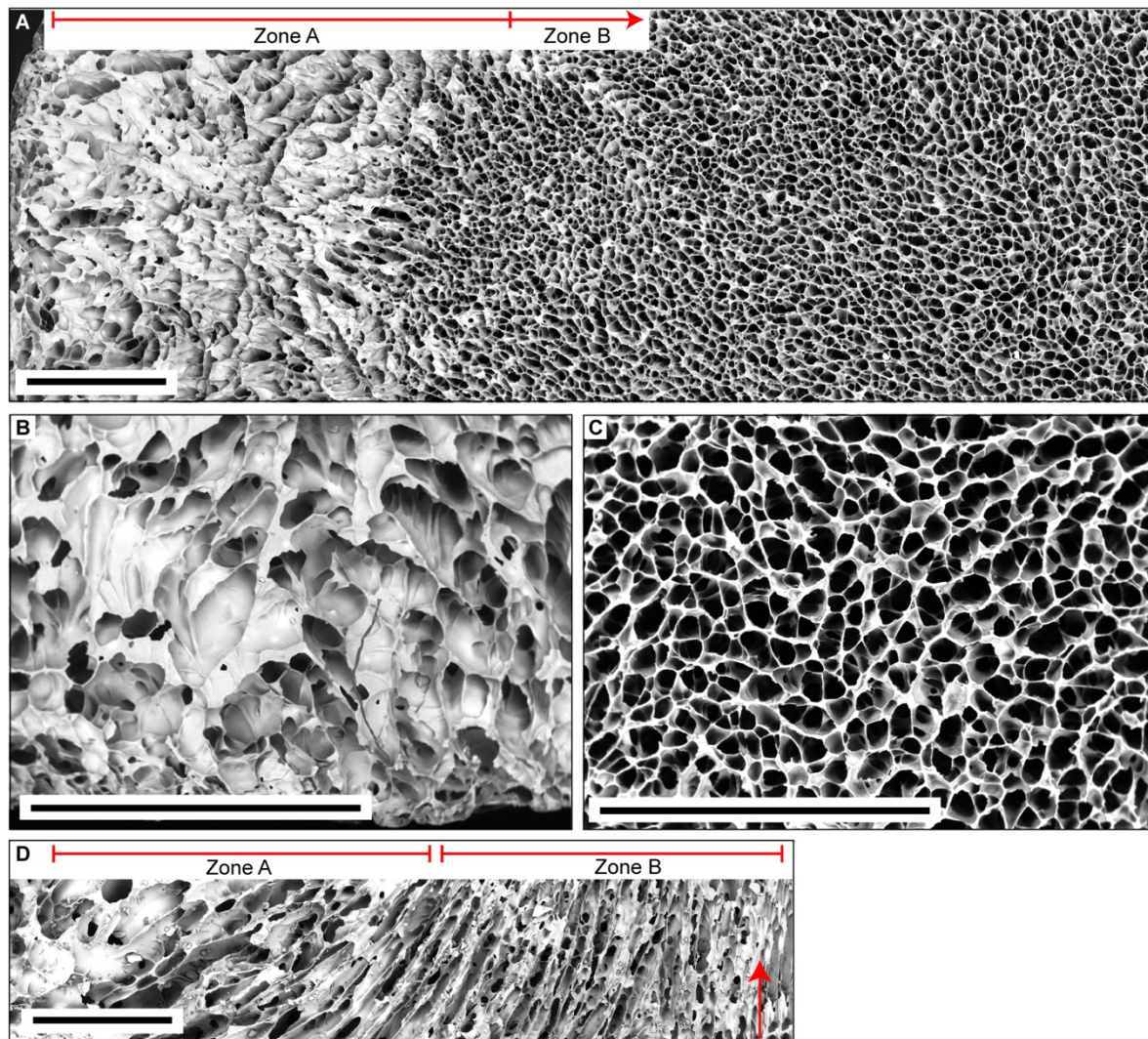


**Fig. 3.19:** Ceramic manufactured with mold design II. The cross-sectional area (perpendicular to the freezing direction) is illustrated in (A). The separate structural units are ‘Zone A’ and ‘Zone B’. A higher magnification of the ‘Zone A’ and ‘Zone B’ is demonstrated in (B) and (C), respectively. The orientation of the cell channels from both zones is displayed in (D). The red arrow indicates the freezing direction. Scale bars: (A) = 2 mm, (B) = 2 mm, (C) = 2 mm, (D) = 2 mm

The characterization of mechanical properties of the varying cell channel orientations and sizes are conducted via the ‘pin indentation method’. The experimental setup of the pin indentation tests is displayed in detail in Schmier et al. (2016). A tungsten-carbide pin (diameter = 1 mm) penetrated perpendicular to the freezing direction into both ceramics with a cross head movement of 0.5 mm/min. The results of the pin indentation tests are displayed in Fig. 3.20. A high stress distribution is obtained during the testing of the outer region of both ceramics (Fig. 3.20 (A), (B)), which represents ‘Zone A’ in both cases.

The stress distribution decreases from the outer region to the inner region of the ceramics, which is here displayed as ‘Zone B’ and ‘Zone C’ (Fig. 3.20 (A), (B)). Additionally, widths of the stress peaks decrease in these zones. Due to the orientation of the cell channels in the ‘Zone B’ and ‘Zone C’, which are oriented perpendicular to the applied stress, the heights and widths of the stress peaks are a function of the channel size and cell wall thickness. This is, in turn, recognizable in Fig. 3.20 (A) when comparing

the ‘Zone B’ and ‘Zone C’ with each other. ‘Zone B’ is characterized by high stress peaks and narrow widths of the stress peaks, which reflect significant smaller cell diameters and larger cell wall thicknesses (Fig. 3.20 (A), (B)). The widths of the stress peaks are larger in ‘Zone C’ due to the larger cell channels (Fig. 3.20 (A)). A decrease of the stress peaks is here associated with a reduction of the cell wall thicknesses.

Similar stress distributions can be observed in ‘Zone C’ and ‘Zone B’ of the ceramics, which were manufactured with mold design I and II, respectively (Fig. 3.20 (A), (B)) indicating similar channel orientations, cell sizes and cell wall thicknesses.

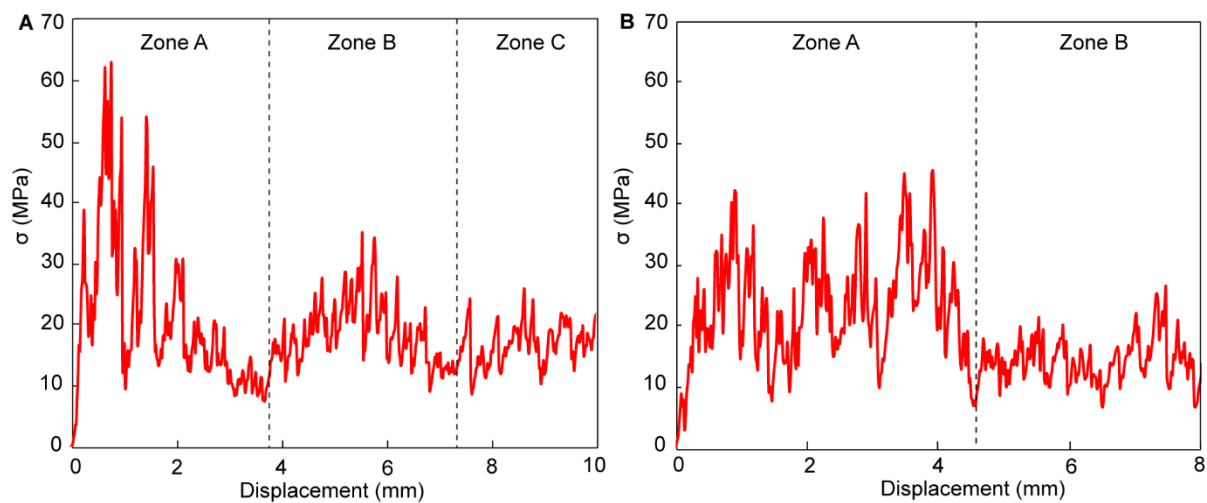


**Fig. 3.20:** Mechanical recording of the cell channels via pin indentation of the ceramics manufactured with mold design I and II. Both ceramics were locally loaded perpendicular to the freezing direction. The stress ( $\sigma$ )/displacement curve (A) and (B) belong to the ceramics, which were manufactured with mold design I and II, respectively.

### 3.1.4 Discussion

#### 3.1.4.1 Applicability of pore model predictions on freeze-cast alumina ceramics

A comparison of the experimentally measured data with mechanical model predictions can provide insights into the compressive deformation behavior of freeze-cast ceramics. The mechanical response of porous ceramics was modeled by representing the cellular structure in several ways. The semi-empirical Gibson and Ashby (1997) prediction uses a dimensional analysis to model the deformation and failure mechanism in cell walls and edges observed in cellular materials. Their approach does not define the exact cell geometry, but assumes that the cell geometry is generally similar in foams of different relative densities. They categorize the varying predictions according to their connectivity of the cell edges and faces to each other and differentiate between the pore morphologies (Gibson and Ashby 1997) open-cell, closed-cell and honeycomb. These models have been applied to different mechanical properties such as fracture toughness, creep or Young’s modulus (Ashby and Medalist

1983). For the compressive strength the formulas for the closed-cell, open-cell and honeycomb are, respectively:

*Closed-cell (brittle crushing):*

$$\sigma = \sigma_P \left( C_6 \left( \phi_{\text{edge}} \frac{\rho^*}{\rho_s} \right) + C_6'' (1 - \phi_{\text{edge}}) \frac{\rho^*}{\rho_s} \right) \quad (11)$$

*Open-cell model (brittle crushing):*

$$\sigma = \sigma_P C_4 \left( \frac{\rho^*}{\rho_s} \right)^{\frac{3}{2}} \quad (12)$$

*Honeycomb model (out-of-plane):*

$$\sigma = 6 E_{\text{wall}} \left( \frac{\rho^*}{\rho_s} \right)^3 \quad (13)$$

These three models are commonly used for freeze-cast materials to compare measured and predicted values of the compressive strength. The listed formulas for the closed- and open-cell model displayed above, describe the material failure for brittle foams.  $C_6$ ,  $C_6''$  and  $C_4$  are empirical geometric constants ( $C_6 = 0.65$ ,  $C_6'' = 1$  and  $C_4 = 0.2$ ). The parameter  $\phi_{\text{edge}}$  is the solid fraction contained in the cell edges (the remaining fraction  $1 - \phi_{\text{edge}}$  is in the cell faces). The parameter  $\phi_{\text{edge}}$  was defined as 1 for the freeze-casted alumina ceramics. The apparent density of the dense and cellular material is defined as  $\rho_s$  and  $\rho^*$ , respectively. The modulus of rupture (MOR) of the solid cell wall material is defined as  $\sigma_P$ . As with other brittle materials, this parameter depends strongly on the microstructure (i.e. the grain size, grain size distribution and porosity). High purity grades of the alumina and solidified cell walls with a general low internal wall porosity lead to high measured values of the  $\sigma_P$ . Therefore, the  $\sigma_P$  can be different depending on the sintering temperature. According to Brook (1991) the MOR for pure alumina (99.5 %) is  $> 400$  MPa. At a sintering temperature of  $1500$  °C, the  $\sigma_P$  of highly pure alumina was measured up to  $850$  MPa (Gao et al. 2000) utilizing the spark plasma (SPS) sintering technique. Lower sintering temperatures of  $1350$  °C, in contrast, have led to a  $\sigma_P$  of approximate  $450$  MPa (Gao et al. 2000). The freeze-cast alumina ceramics were also sintered up to the target temperature of  $1350$  °C (cf. section 3.1.2), so the value for the  $\sigma_P$  of  $450$  MPa was used for the open- and closed cell model. Many authors used values for the comparison of the out-of-plane honeycomb model of the strength by Zhang and Ashby (1992). This prediction includes as  $E_{\text{wall}}$ , which is the Young's modulus of the corresponding solid wall. The formula describes the mechanical response of an elastic honeycomb foam, which is uniaxial loaded along its  $x_3$  direction, where the cell walls undergo bulging and buckling in a periodic way. This plastic behavior was found in foams with a relative low density of  $< 0.12$  (Zhang and Ashby 1992)). With increasing densities, the material will fracture during collapse.

The open- and closed-cell models for brittle crushing by Gibson and Ashby (1997) were also considered for the freeze-casted alumina ceramics. There is some agreement only for cases with anisotropic dendritic branching of cell walls indicating open cell walls (Fig. 3.21: Vijayan et al. 2015). The freeze-cast alumina ceramics, which are characterized by directional cell channels, are neither well described by the closed- nor the open-cell model.

A fair agreement of the obtained strength of honeycomb structures consisting of aluminum alloy 5052 (Hou et al. 2012, Theobald et al. 2010) with the prediction by Eq. (13) was obtained (Fig. 3.21: red symbols, red dashed line). The elastomeric honeycomb structures from Hou et al. (2012) and Theobald et al. (2010) fail by buckling, since they are characterized by relative low density of  $< 0.12$ .

Furthermore, Eq. (13) predicts extremely high compressive strength values (Fig. 3.21: dashed line for  $E_{\text{wall}} = 380 \text{ GPa}$ ) for alumina ceramics. The experimental data of the literature are orders of magnitude below predictions using the value for  $E_{\text{wall}}$  of dense alumina (ca. 380 GPa). Fitting the honeycomb formula to the freeze-cast materials, an  $E_{\text{wall}}$  of 100 to 900 MPa can be obtained. The freeze-cast alumina ceramics from Ferraro et al. (2018) and Deville et al. (2016) are also located in the range of the obtained  $E_{\text{wall}}$  values. They have obtained an  $E_{\text{wall}}$  of 230 MPa. Arguments to explain the general low  $E_{\text{wall}}$  (Ferraro et al. 2018) of such approaches by an incomplete densification of the cell walls (Ferraro et al. 2018) are very unlikely, because the values would ask for a porosity of more than 90 % in the wall material, which is clearly not the case (cf. Fig. 3.3 and Fig. 3.4).

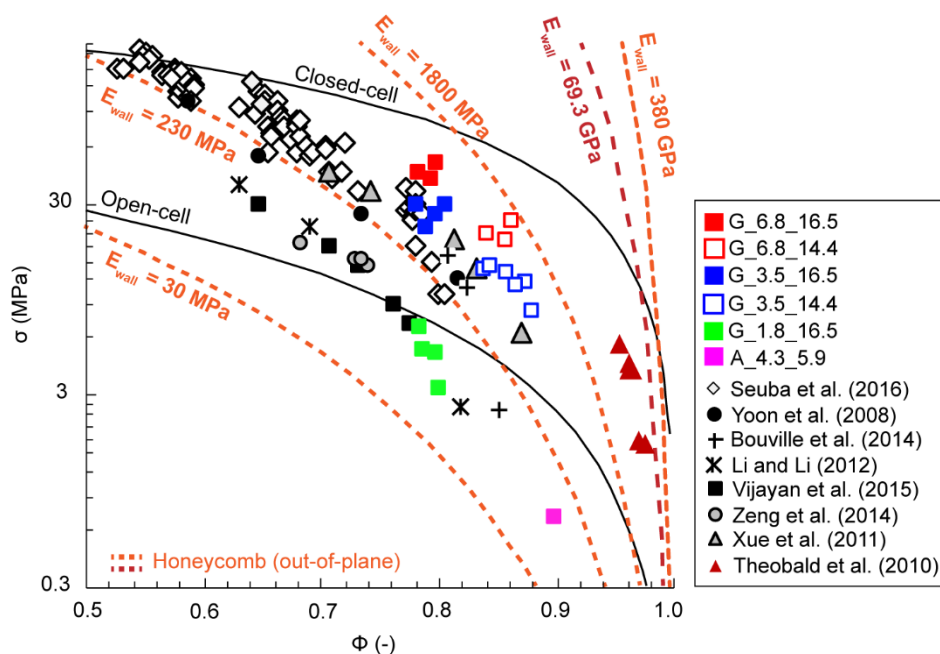


**Fig. 3.21:** Plot of the compressive strength of the freeze-cast alumina ceramics as a function of the porosity,  $\phi$ . The colored symbols represent the maximum compressive strength,  $\sigma_c$ , of the ceramics from the gelatin series. The maximum compressive strength of the ceramic type A\_4.3\_5.9 is also illustrated. Grey, black and white symbols are literature data. The dark red triangles represent honeycomb structures consisting of aluminum alloy 5052 (Hou et al. 2012; Theobald et al. 2010). The honeycomb predictions are displayed as orange and red lines. The open- and closed-model for alumina ceramics are displayed as solid line.

Under the assumption that an incomplete densification of the struts leads to low values of the Young's modulus, the experimental and obtained values of the Young's modulus from the honeycomb model should consequently be the same. In the current literature, Young's modulus values from ceramics manufactured via freeze-casting are rare. When the values of the experimental and obtained Young's modulus are the same, the values should lie on the dashed line in Fig. 3.22. The values for the Young's modulus from freeze-cast alumina ceramics of Vijayan et al. (2015) and from the gelatin series are not located on the dashed line. They lie above and below the dashed line instead. This means that the stated proportionality of the compressive strength to the Young's modulus with  $\sigma = 6 E$  from the honeycomb model is not suitable as prediction for the compressive strength for porous freeze-casted ceramics. Porous ceramics, which undergo brittle failure cannot meet the honeycomb prediction in principle, since the prediction covers rather elastomers (Zhang and Ashby 1992).

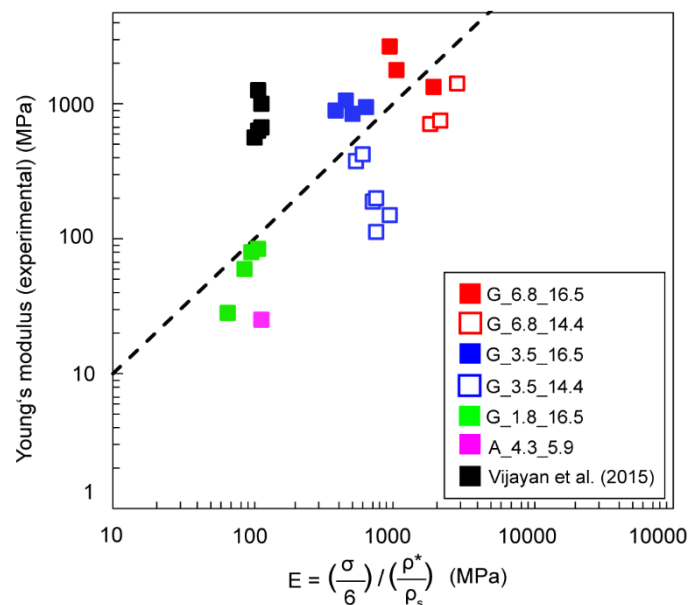


**Fig. 3.22:** Parity plot comparing experimental and theoretical Young's modulus values, which were predicted by Eq. (13). Besides the ceramics from the gelatin series and the ceramic type A\_4.3\_5.9, the Young's modulus values of Vijayan et al. (2015) were also integrated in this plot.

The prediction by Pabst and Gregorová (2014) was made for isotropic and anisotropic ceramics with pure brittle failure. As stated in section 2.2.4.1 before, a lot of pore morphologies such as spheroidal, columnar and disk-shaped pores as special or asymptotic limit cases can be covered with this relation, since the Eshelby-Wu exponent is directly related to the aspect ratio of the pores with 3-fold rotation symmetry. Therefore, the columnar prolate channels of the freeze-cast alumina ceramics can be treated with this relation, which is displayed in section 2.2.4.1 as Eq. (8). The parameter  $E^*$  is the Young's modulus of the corresponding cell wall material, which is given for alumina according to Hulbert (1993) with 400 GPa (purity > 99.7 wt.%). With  $\nu = 0.2$  for alumina, the Eshelby (1957)-Wu (1966) exponent ranges from 2 -  $\infty$  for oblate pores and from 2 - 2.3 for prolate pores in loading direction. Fitting Eq. (8) to the freeze-cast alumina ceramics, the relationship of the Young's modulus and porosity of the

ceramics covers an Eshelby (1957)-Wu (1966) exponent between 2.6 and 5.5 (Fig. 3.23). The Eshelby (1957)-Wu (1966) exponent of the ceramics, which were categorized as ‘circular cell shape’ ranges between 2.3 and 3.2. The ceramics characterized by the cellular, oblate cell shape can be approximated to an Eshelby (1957)-Wu (1966) exponent of 3.6 and the ceramics comprising disjointed cells walls to an Eshelby (1957)-Wu (1966) exponent of 5.5. In between are the ceramics of Vijayan et al. (2015) regarding their values of the Eshelby (1957)-Wu (1966) exponents. Despite of their columnar prolate character of the ceramics ‘circular cell shape’ and ‘cellular, oblate cell shape’, the Eshelby (1957)-Wu (1966) exponents deviate from the predicted range of 2.0 - 2.3 for columnar, prolate pores. The large Eshelby (1957)-Wu (1966) exponents reflect the dominant pore shape of oblate pores. Varying strut thicknesses, a broad pore distribution, slightly tilted and bent cell walls as well as unconsolidated struts may contribute as structural defects to the deviation from an Eshelby (1957)-Wu (1966) exponent of 2.3. The listed structural features contribute to a corresponding scattering in defect population size, since failure during compressive loading is attributed to growth and quantity of these defects.

The porosity-Young’s modulus relation in Fig. 3.23 demonstrates that brittle materials containing oblate pore forms result in lower values of the Young’s modulus.

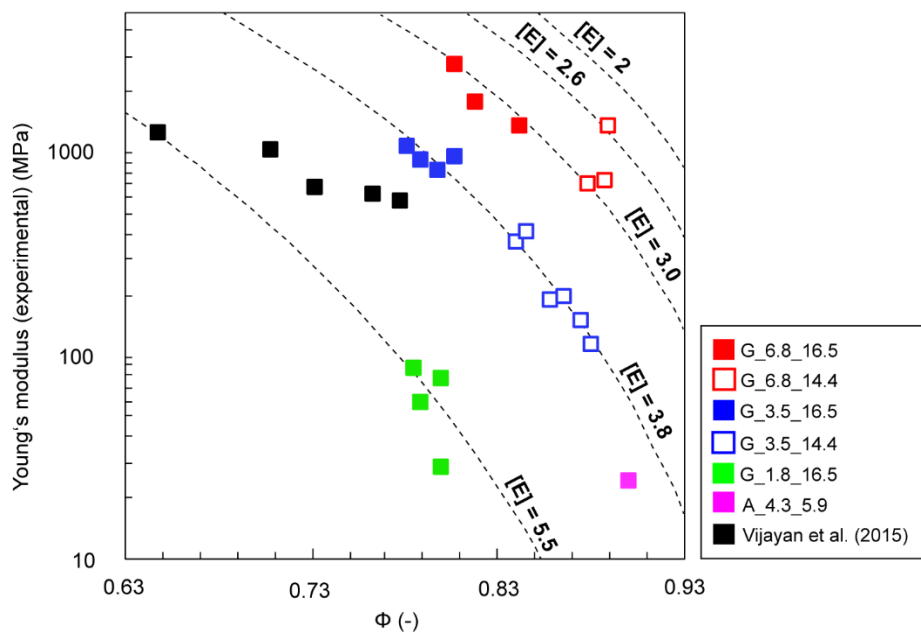


**Fig. 3.23:** Dependency of Young’s modulus and porosity,  $\phi$ , of the ceramics from the gelatin series including also the ceramic A\_4.3\_5.9 from the agar series and the ceramics from Vijayan et al. (2015). The dashed lines represent the Eshelby-Wu exponents ( $= [E]$ ) from Eq. (8).

The physical principles behind the Pabst and Gregorová relation were developed for the porosity-Young’s modulus relation. However, it was shown, that it can also be applied for other properties like thermal conductivity and other elastic moduli (Pabst and Gregorová 2014) like bulk and shear modulus. Fig. 3.24 displays the Eshelby (1957)-Wu (1966) exponent for the bulk, shear and Young’s modulus for a  $\nu = 0.2$  as a function of the aspect ratio. The Eshelby (1957)-Wu (1966) exponents of the three elastic

moduli are located very close for prolate pores (but not exact identical) tending asymptotically to infinity, whereas the values differ for oblate pores. In order to demonstrate in what extent this relation between the elastic-moduli and the pore shape is applicable to freeze-cast alumina ceramics, the relationship between the  $\sigma_c$  and Young's modulus needs to be investigated more closely.

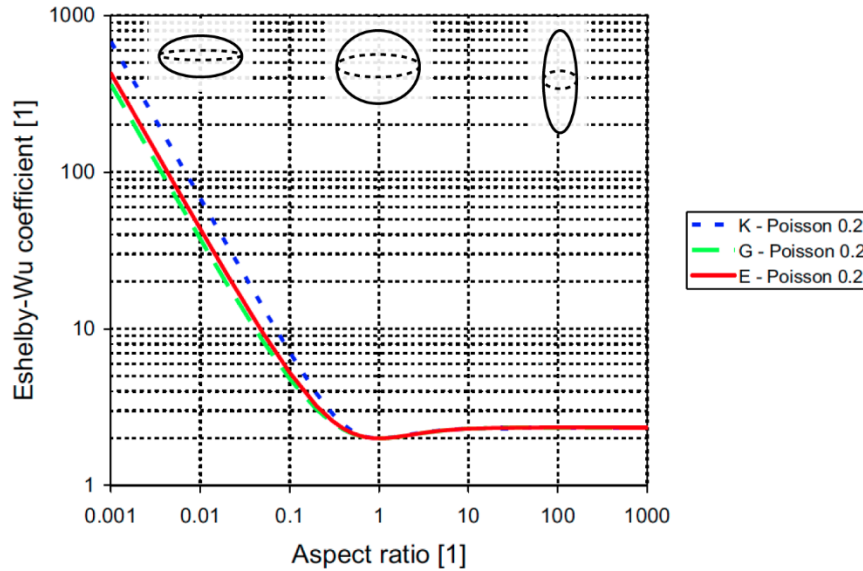


**Fig. 3.24:** Plot shows the aspect ratio dependence of the Eshelby (1957)-Wu (1966) exponent of the bulk (blue dashed line), shear (green dashed line) and Young's modulus (red solid line) for a Poisson ratio of 0.2. Modified according to Pabst and Gregorová (2014).

The  $\sigma_c$  and Young's modulus relationship of the freeze-cast ceramics is summarized in Fig. 3.25. The ceramics characterized by the circular cell channels exhibit a high resilience, since they are located on the right-hand side of the diagram. The ceramics comprising the isolated, disjointed cell walls demonstrate in contrast the lowest strength and stiffness of the presented ceramic morphologies. The freeze-cast ceramics cannot be approximated by a linear function between the  $\sigma_c$  and Young's modulus (Fig. 3.25 (A), grey dashed line). They can be rather approximated by a quadratic function (see Eq. (14)) of the  $\sigma_c$  and Young's modulus (Fig. 3.25 (A), (B): black dashed lines).

The significance and meaning of  $\sigma_c^2/E$  as well as the formula-specific physical background will be clarified in the following. The quadratic function of the  $\sigma_c$  and Young's modulus is used in material property charts as characteristic material-specific value in order to quantify the maximum elastic strain energy per unit volume of materials (Ashby 2006, Ashby et al. 2007), which is defined as

$$\frac{\sigma_c^2}{E} = M_7 \quad (14)$$

The freeze-casted ceramics cannot be covered with one individual quadratic function only. Therefore, two quadratic functions were fitted to cover the dataset completely, which are defined as

$$\frac{\sigma_c^2}{E} = 0.88 \quad (15)$$

and

$$\frac{\sigma_c^2}{E} = 0.64 \quad (16)$$

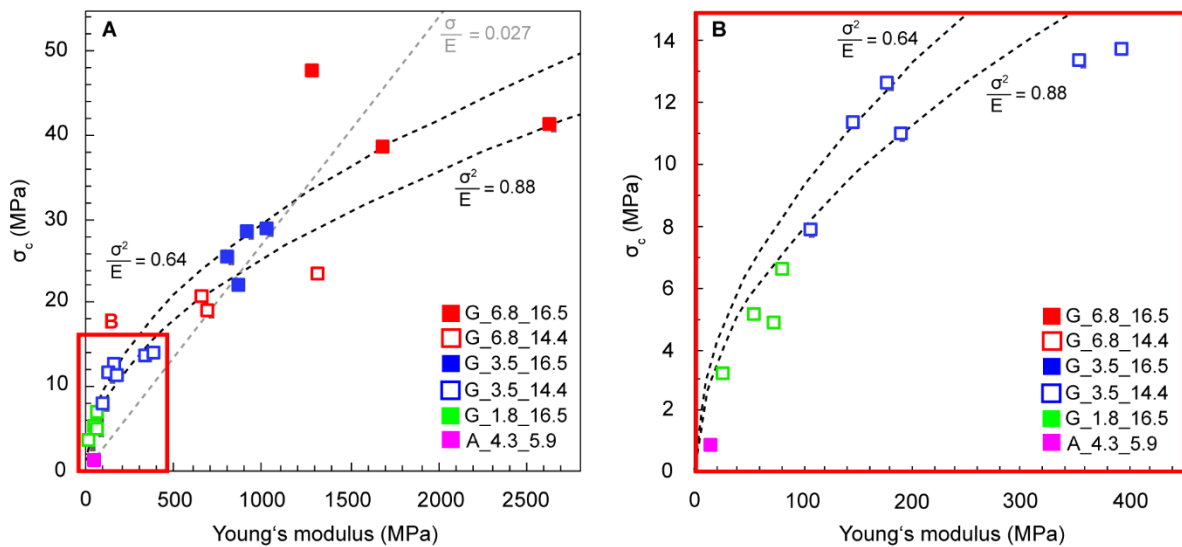


**Fig. 3.25:** (A): Relationship of the maximum compressive strength,  $\sigma_c$ , with the Young's modulus for freeze-cast alumina ceramics. It includes the ceramics from the gelatin series and the ceramic A\_4.3\_5.9 from the agar series. The two black dashed lines demonstrate an approximation of the data by the quadratic functions of the  $\sigma_c$  and Young's modulus. A linear approximation of the  $\sigma_c$  and Young's modulus is displayed as grey dashed line. (B): A higher magnification of a part of the diagram demonstrates the approximation and therefore the good agreement of the data by two quadratic functions in detail.

Fig. 3.26 summarizes the maximum elastic strain energy per unit volume for several natural cellular materials and engineering materials including the freeze-casted alumina ceramics as well. Materials that excel at storing elastic strain energy per unit volume are characterized by having high values of the material index,  $M_7$ , like steel, aluminum or carbon fiber reinforced polymer (CFRP) of more than  $4 \text{ MJ/m}^3$  (Fig. 3.26). Corals, trabecular bones, corks and parenchyma behave more rigidly. Therefore, the natural, cellular materials achieve small values of the maximum elastic strain energy per unit volume with less than  $0.2 \text{ MJ/m}^3$  (Fig. 3.26). The freeze-casted alumina ceramics were characterized by a maximum elastic strain energy between  $0.64$  and  $0.88 \text{ MJ/m}^3$ .

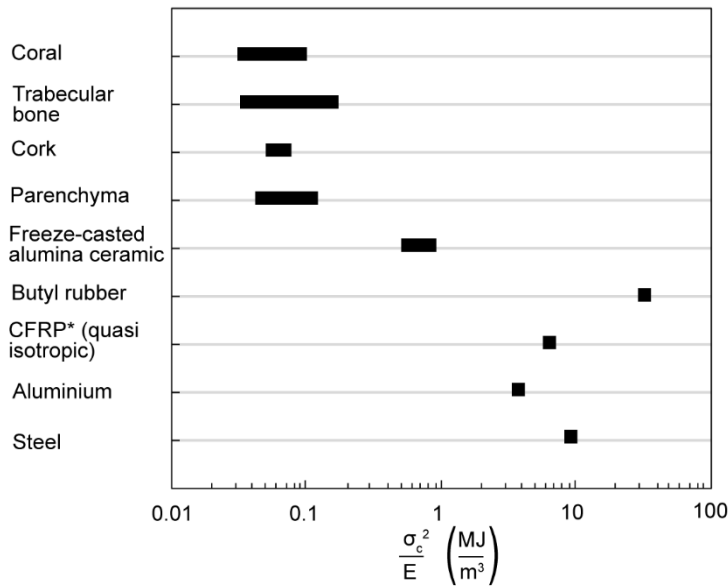


**Fig. 3.26:** The maximum elastic strain energy per unit volume,  $\sigma_c^2/E$ , of natural cellular materials, freeze-casted alumina ceramics and engineering materials. Data were obtained from Gibson et al. (2010).

\*CFRP: Carbon fiber reinforced polymer

The quadratic relation in Eq. (14) with its material index  $M_7$  is based on the formula for the theoretical strength of a material,  $\sigma_{th}$ . The theoretical strength of a material is subjected to brittle fracture, where the bonds are separated over the fracture surface (Gross and Seelig 2006). Therefore, surface energy is required in order to form two new surfaces. Thus, the theoretical strength is the maximum stress a material can withstand before it breaks and is proportional to the root of the Young's modulus,  $E$ , and its surface energy,  $\gamma$  (Kelley 1973, Gross and Seelig 2006):

$$\sigma_{th} = \sqrt{\frac{\gamma \cdot E}{a_0}} \quad (17)$$

The interatomic distance is given by  $a_0$ , which is a measure for the range of interatomic forces (Kelley 1973). The following relationship can be obtained by changing Eq. (17) according to the quadratic function of the theoretical strength and Young's modulus:

$$\frac{\sigma_{th}^2}{E} = \frac{\gamma}{a_0} \quad (18)$$

Since the surface energy of alumina is  $1.0 \text{ J/m}^2$  (Kelley 1973), the stress required to break a bond is

$$\frac{\sigma_{th}^2}{E} = \frac{1}{a_0} \quad (19)$$

The relation of  $\sigma_c^2/E$  and its implementation and applicability into the pore model by Pabst and Gregorová (2014) is presented in the following part. Therefore, both functions, Eq. (15) and Eq. (16),

were inserted into the Pabst and Gregorová relation (Eq. (8)) and converted according to the Eshelby (1957)-Wu (1966) exponent, which is given as

$$[E] = \frac{\left( \ln \left( \frac{\sigma_c^2}{E^*} \right) \right)}{\left( \ln (1 - \phi) \right)} \quad (20)$$

The factor M was taken from Eq. (15) and Eq. (16) as 0.64 and 0.88, respectively. The conversion according to the Eshelby (1957)-Wu (1966) exponent from Eq. (8) is, in turn, given as

$$[E] = \frac{\left( \ln \left( \frac{E_s}{E^*} \right) \right)}{\left( \ln (1 - \phi) \right)} \quad (21)$$

A parity plot (Fig. 3.27) displays the Eshelby (1957)-Wu (1966) exponents determined by Eq. (20) and Eq. (21). The dashed line in Fig. 3.27 illustrates a good agreement of the Eshelby (1957)-Wu (1966) exponents determined by Eq. (20) and Eq. (21). The ceramic types ‘circular cell shape’ and ‘cellular oblate cell shape’ meet the dashed line in principle, which indicates that the Eshelby (1957)-Wu (1966) exponents of the Young’s modulus and  $\sigma_c$  are approximately the same for prolate pores. In contrast, the values of the Eshelby (1957)-Wu (1966) exponent differentiate for oblate pores, since the data of the ceramics characterized by isolated cell walls do not meet the dashed line. It follows the stated relation from Pabst and Gregorová (cf. Fig. 3.24) where the aspect ratio is described as a function of the Eshelby (1957)-Wu (1966) exponent of the bulk, shear and Young’s modulus for a  $\nu = 0.2$ .

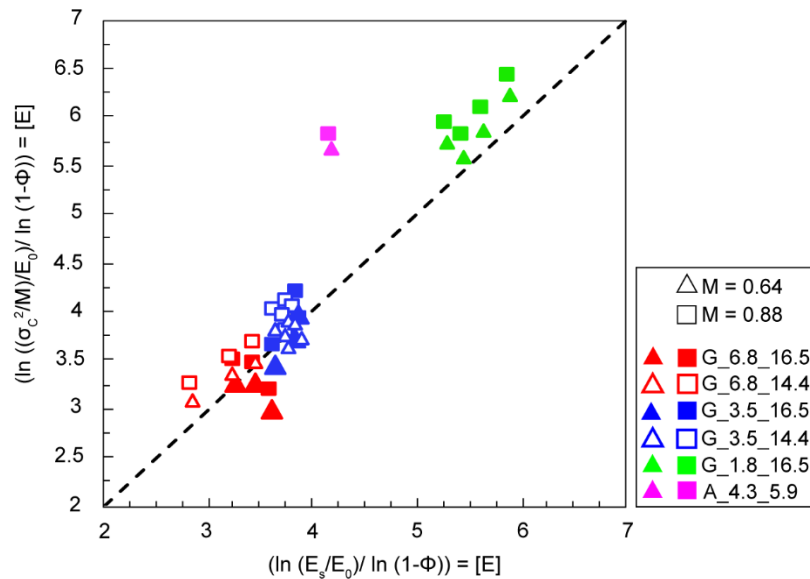


**Fig. 3.27:** Parity plot comparing the Eshelby (1957)-Wu (1966) exponents (= [E]) of Eq. (20) and Eq. (21). It includes the results of the Eshelby (1957)-Wu (1966) exponent of the ceramics from the gelatin series and the ceramic A\_4.3\_5.9 from the agar series.

### 3.1.5 Conclusions

1) Directional prolate cell channels were manufactured utilizing gelatin as additive in a water-based alumina slurry. The configuration of the pore system, i.e. the degree of the interconnectivity of the cell walls and the quantity of isolated cell walls, is dependent on the gelatin concentration. The quantity of solid loading has little influence on the shaping of the pores. Starting at a gelatin concentration of 6.8 vol.% with a gradual reduction of the gelatin concentration by 50 % has shown that polygonal, cellular oblate pore systems can be manufactured in this way as well as structures with several disjointed cell walls.

2) It was demonstrated that agar in a water-based alumina slurry can be used as additive to fabricate directional cell channels in ceramics. Continuous lamellar cell channels, which have a cellular character due to a wavy-like appearance of the cell walls, have been manufactured utilizing sucrose and agar. Through a combination of agar, sucrose and the adjustment of the pH of the slurry to a value of 4 (with citric acid), ceramics with rather spherical channels were manufactured, in which the degree of the interconnectivity of the cell walls is increased. Both ceramic types are characterized by cell walls with a flaky cohesion. Wide polygonal cell channels without any flocculation at the cell walls were manufactured by utilizing only agar as additive.

The following conclusions (3 - 6) are related to the ceramics from the gelatin series and to the ceramic type A\_4.3\_5.9 from the agar series:

3) The strength and stiffness of the ceramic strongly relate to the shaping of the pore system and the degree of interconnectivity of the cell walls. Large values of the stiffness and strength were obtained for ceramics with strongly interconnected cell walls. Ceramics with a high quantity of isolated cell walls were characterized with rather low values of strength and stiffness.

4) It was shown that the fracture behavior of the ceramics under uniaxial compression is likewise strongly related to the shaping of the cell channels and cell wall arrangement. Two main fracture modes of failure were identified for the freeze-cast alumina ceramics:

- a) a progressive interplay of flaking and crumbling;
- b) an intensification of vertical cracks leading to a segmental division of the ceramic into several lath-like segments.

Failure mode a) is related to ceramics, which contain directional pore systems with a high degree of interconnectivity of the cell walls. In contrast, ceramics with an increased quantity of isolated cell walls are rather characterized by failure mode b). Failure mode a) leads to a widely maintained structural integrity and very low loss of material of the ceramic even at advanced stages of uniaxial compression. A vertical crack propagation and its intensification at high strain levels leads to a segmental division of the ceramic, which is, in turn, associated with failure mode b).

5) A graded pore structure with varying orientations of the cell channels can be manufactured with mold design I (inner areas of the PTFE cylinder are characterized by an alternation of copper stripes and Teflon areas). The gradation is limited to the first 10 % of the ceramic in height and disappears at increasing height. Depending on the cell channel size and orientation, the graded ceramic may be divided into three distinct zones. The cell channel sizes decrease from the center towards to the exterior of the ceramic. The outer region of the ceramic is, however, characterized by cell channels that are more or less oriented perpendicular to the freezing direction. The highest variation of the cell channel size is concentrated at the outer region of the ceramic. Separate structural units (viz. a quasi 'core-shell' structure), which comprise different cell channel orientations, can be manufactured in one ceramic by utilizing mold design II (inner area of the PTFE cylinder is marked by a thin copper film). The different structural units are uniformly present in the entire ceramic in height. The cell channels in the center are oriented parallel to the freezing direction and are tilted increasingly towards to the outer region of the ceramic.

6) The physical constraints of the honeycomb model provided by Zhang and Ashby (1992) are not given for freeze-cast alumina ceramics with a directional pore system, because it models an elastic/ plastic honeycomb foam behavior. The spheroidal pore model by Pabst and Gregorová (2014) for pure brittle materials is a reasonable approach to cover the physical constraints for freeze-cast alumina ceramics. The 'circular cell shape' and 'cellular, oblate cell shape' ceramics exhibit a high resilience in the light

of strength and stiffness, which are associated with low Eshelby (1957)-Wu (1966) exponents reflecting the dominant prolate shape. The ceramics, which are characterized by isolated, disjointed cell walls have the lowest strength and stiffness. Their high values of the Eshelby (1957)-Wu (1966) exponents indicate an oblate pore shape. The relation of the elastic moduli and the pore shape by Pabst and Gregorová (2014) is applicable to freeze-cast alumina ceramics.

7) It has been demonstrated that the freeze-casted alumina ceramics can be defined by a quadratic function of the  $\sigma_c$  and Young's modulus including the material index  $M_7$ , which is defined as maximum elastic strain energy per volume unit. The quadratic relation of the  $\sigma_c$  and Young's modulus with the material index  $M_7$  has its formula-specific background on the formula for the theoretical strength of a material.

## 4. Abstraction and 1<sup>st</sup> CAD approach

This section presents one part of the abstracted structural model of the spine microstructure of *Phyllacanthus imperialis*, which summarizes the essential key elements of the spine microstructure. The different key elements are assigned to specific levels of abstraction. Section 4.2 presents a first approach of a computer-aided design (CAD) model of a part of the spine microstructure.

### 4.1 Structural abstraction

**Tab. 4.1:** Division of structural and material specific key elements of the spine of *Phyllacanthus imperialis* on the macroscopic and microstructural level.

1 <sup>st</sup> abstraction level (macrostructure)		
Shell	Porous core	
2 <sup>nd</sup> abstraction level (microstructure): Stereom types		
Perforate stereom: Branching of channels	Layered stereom: Wedges, cross struts	Columnar stereom: -
3 <sup>rd</sup> abstraction level ('meta-level'): Configuration, Shaping, Crystallinity		
Outer poly- and inner monocrystalline layer (Dery et al. 2014)	Trigonal arrangement of dominant wedges	Radiating nodes

The extensive structural investigation of the spine microstructure of *Phyllacanthus imperialis* utilizing light microscopy, SEM technique (BSE mode) and  $\mu$ CT reconstructions allow to create an abstracted map of the structural key elements (Fig. 4.1). These key elements can be distributed on certain levels of abstraction (Tab. 4.1).

Obviously the microscopic and macroscopic division into a 'core-shell' structure marks the first level of abstraction, whereby the core might be further divided according to its porosity into two cylinders: the radiating layer and medulla. The second level of abstraction comprises a detailed structural understanding of the stereom arrangement. Earlier investigations (Grossmann and Nebelsick 2013, Dery et al. 2014) of the structure leads to a division of the core into the galleried and laminar stereom type. This structural segmentation describes not accurately the spine microstructure of *Phyllacanthus imperialis*. Furthermore, it is incomplete in the consideration of the whole spine microstructure, because it focuses on singular structural components only. It does not consider the relative structure (shaping and configuration) of elements to each other, but excludes the relation of the shaping and transition from one structural element to the next one. Section 2.1.4 demonstrated that the formal division of the spine microstructure in certain stereom types can be further extended through new findings of the configuration of the stereom as well as clustering.

In Fig. 4.1 the configuration of the inner core elements and afterwards the core-shell connection is described schematically. The radiating layer comprises single stereom layers (Fig. 4.1: yellow area), which together form wedge-like structures. Each wedge is not completely closed, but rather encloses a side branch of the inner spine center. Both structural elements are interwoven with each other.

In total, 13 wedges are present in the spine structure (Fig. 4.1: blue dashed lines). The stereom layers are connected with ordered cross struts arranged in certain distances along the z-axis (Fig. 4.1: red lines). Six of the 13 wedges can be regarded as dominant wedges (Fig. 4.1: grey outer area), because they contain more than 28 stereom layers. These dominant wedges are grouped in two units and are arranged approximately in a trigonal way. In contrast to the microstructural stereom types, the specific trigonal arrangement of the dominant wedges is not obviously visible utilizing SEM and  $\mu$ CT reconstructions. A precise quantification of the stereom layers within the spine microstructure visualized the trigonal arrangement of the wedges for the first time (see section 2.1.4.4). The dominant wedges can therefore be categorized into their own level of abstraction referred to as 'meta level of abstraction'. The 'meta level of abstraction' includes also the bulges of the spine center (Fig. 4.1: marked as pink structures). The cortex appears to be isolated on the first level of abstraction. Therefore, the transition of the outermost stereom to the core seems to be abrupt. On the second level of abstraction, the strong connection between the perforate and laminar stereom becomes clear (Fig. 4.1). Each single stereom layer is connected with the cortex (Fig. 4.1). The spaces between the stereom layers and the cross struts are the channel openings (Fig. 4.1: green lines). The transition from the exterior of the cortex to the inner spine structure is a graded one: the channel sizes remain almost constant (aside from the extreme large ones at the exterior), but the number of channels increases more than twice from the outside to the inside.

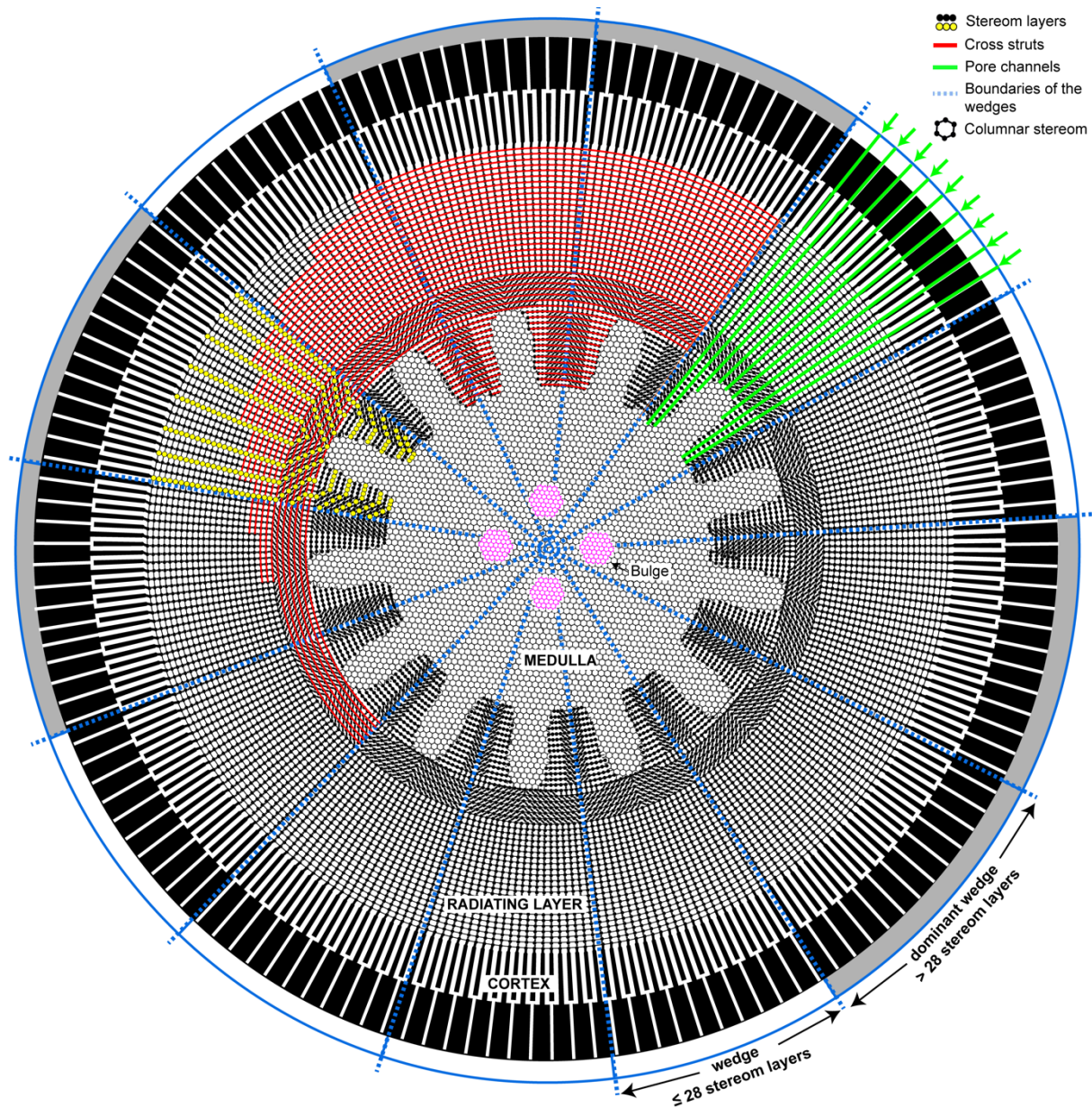


**Fig. 4.1:** Abstraction of the microstructure of the adult spine of *Phyllacanthus imperialis*. The division of the structural key elements into several abstraction levels is summarized in Tab. 4.1.

## 4.2 1st CAD approach of the spine microstructure

Based on the current understanding of the spine microstructure of *Phyllacanthus imperialis*, a first approach of a CAD model has been created utilizing the software SketchUp (Trimble Inc., California, USA). The first CAD approach displays one way to model the wedge-like structure of the radiating layer with its single stereom layers and the side branches of the medulla. The trabecular rods themselves consist of stacked columns (Fig. 4.2 (A), (B)). The trabecular rods were narrowed to create the columnar stereom structure of the medulla (Fig. 4.2 (B)).

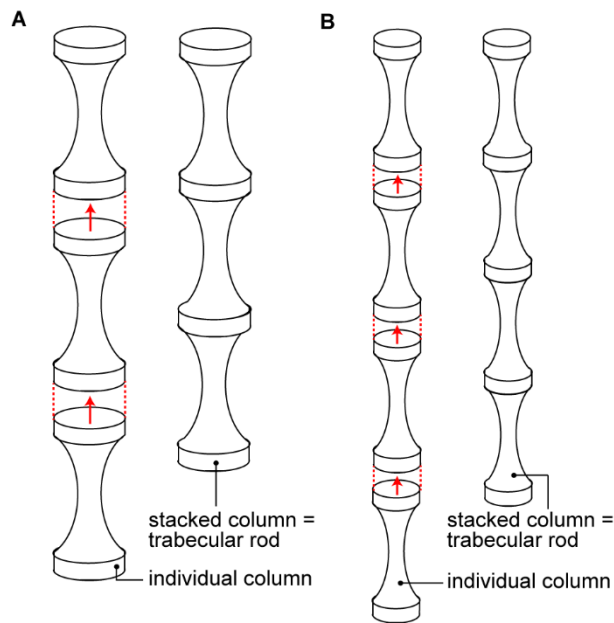


**Fig. 4.2:** Structural composition of the trabecular rods in the CAD model. Each individual trabecular rod consists of individual columns. The size of the used trabecular rods is different for the structures in the radiating layer (A) and medulla (B).

Each stereom layer consists of several rows of stacked columns (Fig. 4.3: black arrows). The upper and lower part of the columns are connected by cross struts, which were simplified as beams in the model (Fig. 4.3). This approach of the wedge-like microstructure in the CAD model can reflect to some extent the spine structure of *Phyllacanthus imperialis*. However, some further improvements are crucial. The offset of pores, which is a characteristic of the stereom layers, could not be transferred into the CAD model. It means, in turn, that the trabecular rod as basic element of the CAD model has to be refined in such way that an offset of pore rows can be created in the stereom layers. Furthermore, the trabecular rods and cross struts of the stereom layers are different in their size in the first CAD approach of the wedge. The next CAD model should contain equal sized struts.

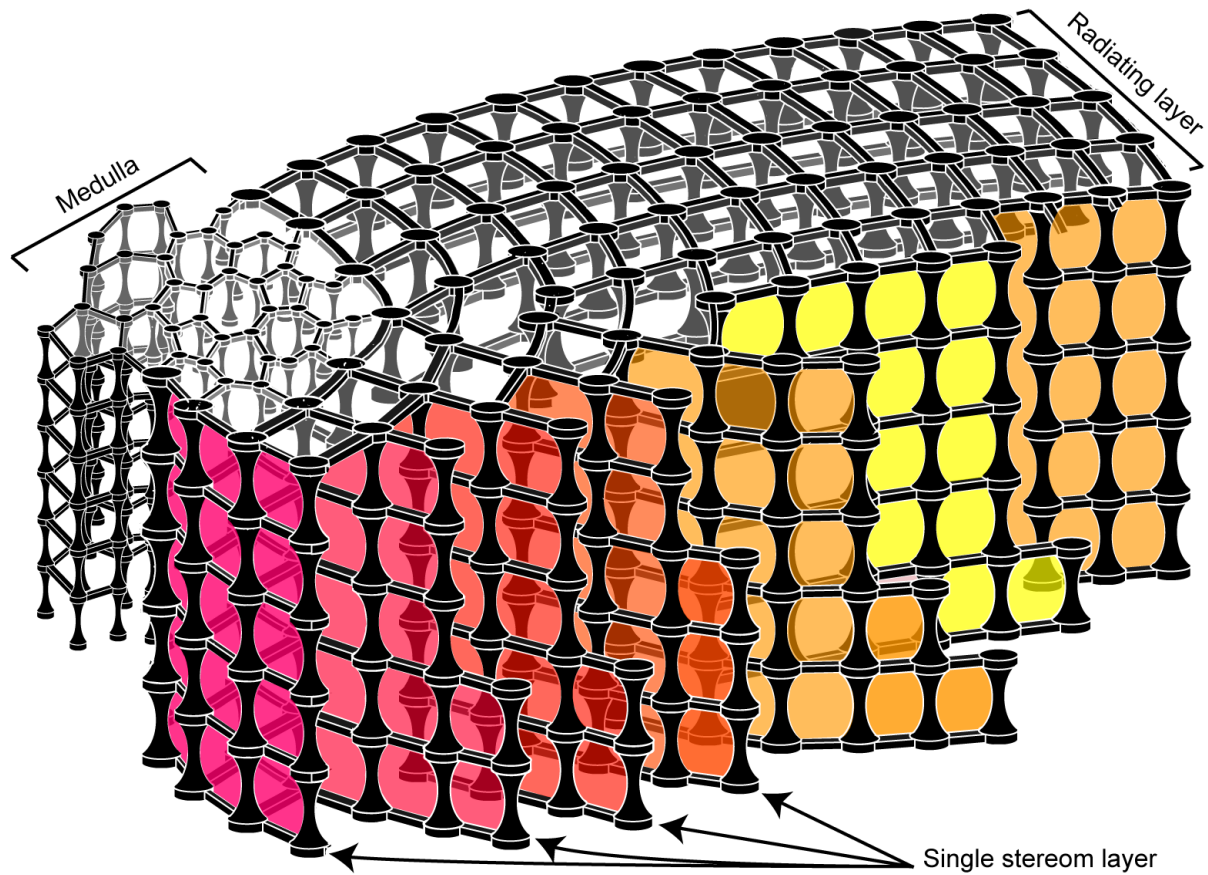


Fig. 4.3: First CAD model of the wedge of the spine of *Phyllacanthus imperialis*.

In order to create equal-sized trabecular rods and cross struts within a wedge-like configuration, a repeating unit volume extracted from the  $\mu$ CT reconstructions can be used to create an idealized representative volume element (RVE) of the wedge-like structure (Chen 2011). A macroscopic model of the entire aboral spine can be created by repeating the idealized RVE of the wedge-like structure.

## 5. Outlook

### 5.1 Transfer into a concrete-based column

Since the spine structure was described numerically (strut- and pore sizes, volume fraction of the stereom units) and morphologically (superstructures), a scalable CAD model could be developed in the future, which includes the whole microstructural characteristics of the spine of *Phyllacanthus imperialis*. It was demonstrated that the layered and columnar stereom structures can be transferred into a CAD model. But the basic building blocks of the trabecular rods have to be refined in order to come closer to the actual spine microstructure. On the basis of a CAD model, the finite element (FE) method could be utilized in order to gain a better understanding about the stress distribution and failure mechanism of the whole spine structure. So far, the FE method was applied to an individual section of the galleried stereom in Presser et al. (2009b) to determine the stress distribution. They have demonstrated that high stress accumulates at the tapered sides of the trabecular rods. Qualitative FE method simulations of the stress distribution of the whole microstructure including the superstructures of the spine do not yet exist. New findings of the FE method simulations could be utilized to optimize the CAD model.

An optimized CAD model can be used to transfer the spine microstructure into a concrete-based column on a construction-scale under the utilization of the frozen sand formwork technique developed by ILEK (Institut für Leichtbau und Entwerfen) at the University of Stuttgart. With this formwork method, it is possible to fabricate complex three-dimensional moulds by milling a frozen mixture of water and sand (Gericke et al. 2015). Recently, shell segments with a two-dimensional graded porosity inspired by the spine of *Heterocentrotus mammilatus* were manufactured with the frozen sand formwork technique (Fig. 5.1 (A)) and were assembled to a pavilion representing a prototype of weight-optimized load bearing system (Kovaleva et al. 2018). A section of the three-dimensional stereom structure based on concrete was manufactured by utilizing the frozen sand formwork technique as well (Fig. 5.1 (B): manufactured by Daria Kovaleva, ILEK).

It demonstrates that complex spatial moulds may be developed and fabricated with the frozen sand formwork technique, since it has no constraints, such as undercuts and bottleneck problems (Coupek et al. 2016). This fabrication technique for complex spatial negative moulds offers a way to manufacture a concrete-based column inspired by the spine structure of *Phyllacanthus imperialis*. In this case, the optimized CAD model comprising the total spine microstructure of *Phyllacanthus imperialis* can be exploited to fabricate the spatial negative mould (= pore network of the spine structure) for the concrete column. The frozen sand formwork technique is advantageous, since the fabrication of the moulds is waste-free and can be reused for further concrete casting. In view of the increasing scarcity of natural resources in contrast to a steadily growing population, manufacturing of concrete components combining high mechanical resilience with a lightweight design is of paramount importance for our society today.

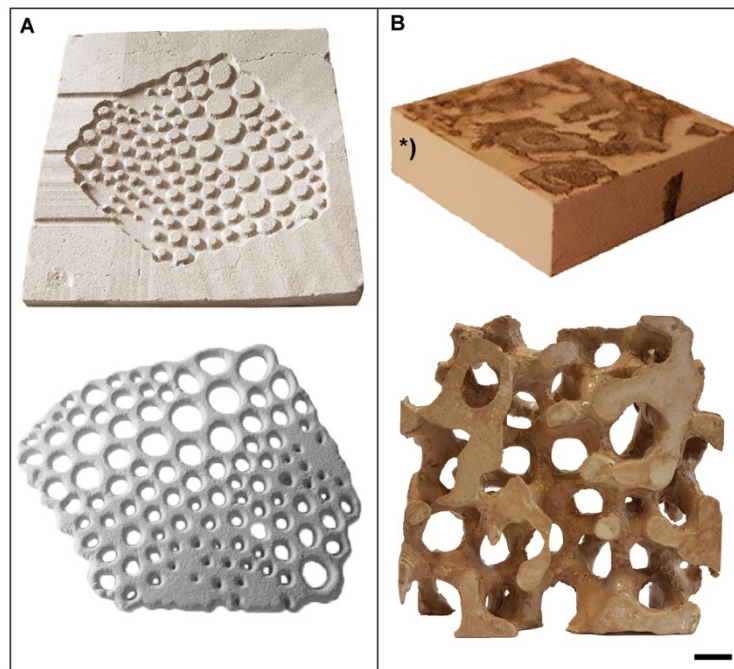


**Fig. 5.1:** Fabrication of concrete-based porous work pieces. In (A) is displayed a frozen sand form and the manufactured product, which contains a graded two-dimensional porosity (modified after Kovaleva et al. 2018). In (B) is displayed a frozen sand form, which creates three-dimensional structures (modified after Kovaleva et al. 2018). \*) Modified after Wulle et al. (2017). Scale bar = 1 cm.

## 5.2 Three-dimensional printing technique for porous ceramics

### 5.2.1 Bioinspired ceramic component

To transfer the spine microstructure with its integrated superstructures into a technical ceramic, freeze-casting is not suitable as manufacturing method. Freeze-casting is particularly suitable to manufacture one pore system containing a specific cell geometry and size in one specimen. The manufacturing of a graded pore structure is feasible, but the gradation is only limited to a specific height in one specimen. Manufacturing of the differentiated spine structure with its wedge-like interlocking with the side branches of the medulla and the cortex intersected by channels as well is not realizable with the freeze-casting technique (Fig. 5.2 (A), (B)). Alternatively, the three-dimensional printing technique can also be utilized to manufacture a ceramic component inspired by the microstructure of the spine of *Phyllacanthus imperialis*. The same optimized CAD model would be utilized in the process of manufacturing of the concrete-based column as well.

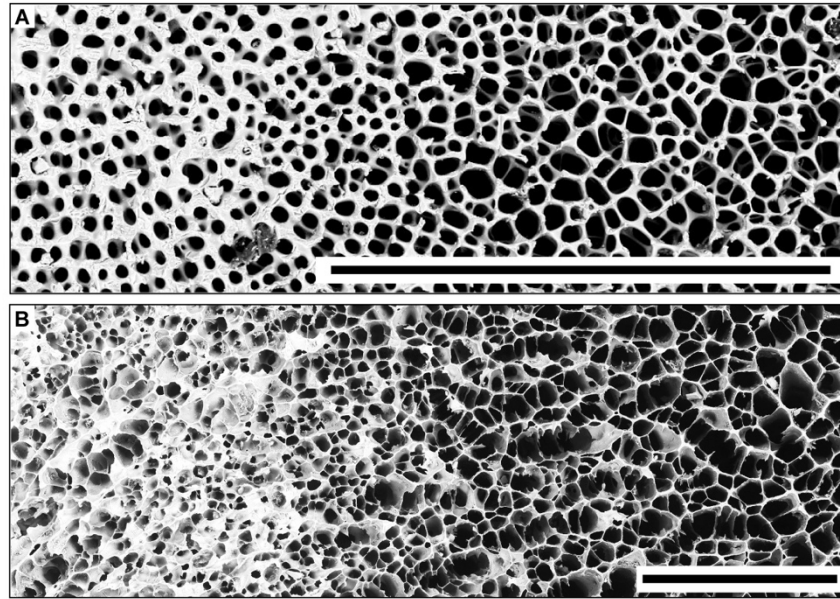


**Fig. 5.2:** Comparable display of BSE images of the spine microstructure of *Phyllacanthus imperialis* and of a graded freeze-casted alumina ceramic. The cross section (perpendicular to the c-axis) of the spine microstructure is displayed in (A). The graded freeze-cast alumina ceramic with its cross section is presented in (B). Scale bars: (A) = 500  $\mu\text{m}$ , (B) = 500  $\mu\text{m}$ .

### 5.2.2 Systematical investigation of the pore model by Pabst and Gregorová (2014)

Three-dimensional printed ceramic species could also be utilized to test systematically the spheroidal pore model by Pabst and Gregorová (2014). The influence of the composite material and varying structural units, which are prevailing in many biological materials, on the strength and stiffness might be removed in this way. Freeze-casted ceramics are not suitable for this systematical analysis of the pore model prediction by Pabst and Gregorová (2014) due to occurrence of varying strut thicknesses, a broad pore distribution and slightly tilted and bent cell walls. Three-dimensional printing, by contrast, is a common way to manufacture ceramic structures with well-defined cell geometry. However, the cell geometries are in the mm-range and reach not yet a comparable size in the  $\mu\text{m}$ -range of the freeze-casted ceramics. Reaching low cell geometry sizes plays a subordinate role for the applicability of the pore model by Pabst and Gregorová (2014) on porous ceramics in this issue. A common three-dimensional printing technique for porous ceramics is the so-called direct ink writing (DIW) where the desired body is assembled by specifically depositing small amounts of an ink or a paste (Lewis 2006). This can be realized by a filamentary-based approach, like robocasting (Zocca et al. 2015, Deckers et al. 2014) and fused deposition modeling (Guo and Leu 2013) or by a droplet-based approach, such as ink-jet printing (Sachs et al. 1992, Song et al. 1999). Each approach bases on CAD models, which is advantageous in order to ascertain the limitations of the pore model prediction for porous ceramics with regard to cell geometries. A basic CAD model, for instance with a prolate pore system, could be exploited to change systematically and step-wise the degree of interconnectivity of the cell walls, the cell sizes and geometries as well.

## 6. Literature

- Arabi N, Zamanian A (2013)** Effect of cooling rate and gelatin concentration on the microstructural and mechanical properties of ice template gelatin scaffolds. *Biotechnology and Applied Biochemistry* 60:573–9.
- Ashby MF, RF Mehl Medalist (1983)** The mechanical properties of cellular solids. *Metallurgical and Materials Transactions A* 14:1755-1769.
- Ashby MF (2006)** The properties of foams and lattices. *Philosophical Transactions of The Royal Society A Mathematical Physical and Engineering Sciences* 364(1838):15-30.
- Ashby MF, Shercliff HR, Cebon D (2007)** Materials: engineering, science, processing and design. *Elsevier Butterworth-Heinemann*.
- Bargel HJ, Schulze G (2008)** Werkstoffkunde. *Springer*, Berlin, Heidelberg, New York.
- Barthlott W (1990)** Scanning electron microscopy of the epidermal surface in plants. In: D Claugher (eds) Application of the scanning EM in taxonomy and functional morphology. Systematics Association's Special Volume. *Clarendon Press*, Oxford, 69-94.
- Barthlott W, Schimmel T (2010)** The Salvinia paradox: Superhydrophobic surfaces with hydrophilic pins for air-retention under water. *Advanced Materials* 22:2325–2328.
- Brezny R, Green DJ (1990)** Characterization of edge effects in cellular materials. *Journal of Material Sciences* 25:4571-8.
- Brook RJ (1991)** Concise encyclopedia of advanced ceramic materials. *Pergamon Press*, Oxford.
- Burkhardt A, Hansmann W, Märkel K, Niemann, HJ (1983)** Mechanical design in spines of diadematoïd echinoids (Echinodermata, Echinoidea). *Zoology* 102:189–203.
- Born L, Körner A, Schieber G, Westermeier AS, Poppinga S, Sachse R, Bergmann P, Betz O, Bischoff M, Speck T, Knippers J, Milwich M, Gresser GT (2017)** Fiber-reinforced plastics with locally adapted stiffness for bio-inspired hingeless, deployable architectural systems. In: A Herrmann (eds) 21st Symposium on Composites. *Key Engineering Materials* 742, 689–696.
- Bouville F, Portuguez E, Chang Y, Messing GL, Stevenson AJ, Maire E, Courtois L, Deville S (2014)** Templated grain growth in microporous materials. *Journal of the American Ceramic Society* 97(6):1736-1742.
- Boylell C, Kim Y (2011)** Three-dimensional micro-level computational study of Wolff's law via trabecular bone remodeling in the human proximal femur using design space topology optimization. *Journal of Biomechanics* 44:935-942.
- Carpentier G (2012)** Contribution: Angiogenesis Analyzer. ImageJ News.
- Chavez-Valdez A, Shaffer MSP, Boccaccini AR (2013)** Applications of Graphene Electrophoretic Deposition. A Review. *Journal of Physical Chemistry B* 117:1502-1515.
- Chen TT (2011)** Microstructure and micromechanics of the sea urchin, *Colobocentrotus atratus*. Doctoral dissertation, Massachusetts Institute of Technology.
- Cheng Q, Wu M, Li M, Jiang L, Tang Z (2013)** Ultratough artificial nacre based on conjugated cross-linked graphene oxide. *Angewandte Chemie International Edition* 52:3750-5.

- Coupek D, Kovaleva D, Christof H, Wurst KH, Verl A, Sobek W, Haase W, Gresser GT, Lechler A (2016)** Fabrication of Biomimetic and Biologically Inspired (Modular) Structures for Use in the Construction Industry. In: J Knippers, T Speck, K Nickel (eds) *Biomimetic Research for Architecture and Building Construction: Biological Design and Integrative Structures*, Springer, Cham, 319-339.
- Currey JD (2005)** Materials science—hierarchies in biomineral structures. *Science* 309:253–254.
- Cölfen H, Antonietti M (2008)** Mesocrystals and nonclassical crystallization. *John Wiley & Sons*, Chichester.
- Da Silva L, Galembeck F (2015)** Morphology of latex and nanocomposite adsorbents prepared by freeze-casting. *Journal of Materials Chemistry A* 3:7263–72.
- David B, Stock S, De Carlo F, Hétérier V, De Ridder C (2009)** Microstructures of Antarctic cidaroid spines: diversity of shapes and ectosymbiont attachments. *Marine Biology* 156:1559–1572.
- Dawson MA, LJ Gibson (2007)** Optimization of cylindrical shells with compliant cores. *International Journal of Solids and Structures* 44:1145-1160.
- Deckers J, Jef V, Kruth JP (2014)** Additive manufacturing of ceramics: a review. *Journal of Ceramic Science and Technology* 5:245-260.
- DeFoe OK, Compton AH (1925)** The density of rock salt and calcite. *Physical Review* 25:618-620.
- Dery A, Guibourt V, Catarino AI, Compere P, Dubois P (2014)** Properties, morphogenesis, and effect of acidification on spines of the cidaroid sea urchin *Phyllacanthus imperialis*. *Invertebrate Biology* 133:188–199.
- Deville S (2008)** Freeze-casting of porous ceramics: a review of current achievements and issues. *Advanced Engineering Materials* 10:155-169.
- Deville S (2010)** Freeze-casting of porous biomaterials: structure, properties and opportunities. *Materials* 3:1913-1927.
- Deville S, Viazzi C, Leloup J, Lasalle A, Guizard C, Maire E, Adrien J, Gremillard L (2011)** Ice shaping properties, similar to that of antifreeze proteins, of a zirconium acetate complex. *PlosOne* 6:e26474.
- Deville S, Meille S, Seuba J (2016)** A meta-analysis of the mechanical properties of ice-templated ceramics and metals. *Science and Technology of Advanced Materials* 16:043501.
- Doube M, Klosowski MM, Arganda-Carreras I, Cordelières FP, Dougherty RP, Jackson JS, Schmid B, Hutchinson JR, Shefelbine SJ (2010)** BoneJ: Free and extensible bone image analysis in ImageJ. *Bone* 47:1076-9.
- Dubois P, Chen CP (1989)** Calcification in echinoderms. In: M Jangoux, JM Lawrence (eds) *Echinoderm Studies*, A.A. Balkema, Rotterdam, 109–178.
- Eshelby JD (1957)** The determination of the elastic field of an ellipsoidal inclusion and related problems. *Proceedings of the Royal Society A* 241:376-96.
- Ferraro C, Garcia-Tunon E, Barg S, Miranda M, Ni N, Bell R, Saiz E (2018)** SiC porous structures obtained with innovative shaping technologies. *Journal of the European Ceramic Society* 38:823-835.
- Guo N, Leu MC (2013)** Additive manufacturing: technology, applications and research needs. *Frontiers of Mechanical Engineering* 8:215-243.

- Fukasawa T, Ando M, Ohji T, Kanzaki S, (2001)** Synthesis of porous ceramics with complex pore structure by freeze-dry processing. *Journal of the American Ceramic Society* 84:230–2.
- Fukushima M, Yoshizawa YI, Ohji T (2014)** Macroporous ceramics by gelation-freezing route using gelatin. *Advanced Engineering Materials* 16:607-621.
- Gericke O, Haase W, Sobek W (2015)** Herstellung von Freiform-Betonformen mittels einer gefrorenen Schalung aus Wasser und Sand. *DAfStb-Jahrestagung mit 56. Forschungskolloquium, Stuttgart, 23-30.*
- Gao L, Hong JS, Miyamoto H, Torre SDDL (2000)** Bending strength and microstructure of Al<sub>2</sub>O<sub>3</sub> ceramics densified by spark plasma sintering. *Journal of the European Ceramic Society* 20:2149-2152.
- Gibson LJ (2005)** Biomechanics of cellular solids. *Journal of Biomechanics* 38:377-399.
- Gibson LJ, Ashby MF (1997)** Cellular solids: Structure and Properties, *Cambridge University Press, Cambridge.*
- Gibson LJ, Ashby MF, Harley BA (2010)** Cellular materials in nature and medicine. *University Press, Cambridge.*
- Grun TB, Von Scheven M, Bischoff M, Nebelsick JH (2018)** Structural stress response of segmented natural shells: a numerical case study on the clypeasteroid echinoid *Echinocyamus pusillus*. *Royal Society Interface* 15(143):pii 20180164.
- Gross D, Seelig T (2006)** Bruchmechanik: Mit einer Einführung in die Mikromechanik. *Springer, Berlin, New York, Heidelberg.*
- Grossmann, JN, Nebelsick, JH (2013)** Comparative morphological and structural analysis of selected cidaroid and camarodont sea urchin spines. *Zoomorphology* 132:301–315.
- Han J, Hu L, Zhang Y, Zhou Y (2009)** Fabrication of ceramics with complex porous structures by the impregnate–freeze-casting process. *Journal of the American Ceramic Society* 92:2165-2167.
- Hasan MI, Rageb A, Yaghoubi M, Homayoni H (2009)** Influence of channel geometry on the performance of a counter flow microchannel heat exchanger. *International Journal of Thermophysics* 48(8):1607-1618.
- Hautcoeur D, Gonon M, Lardot V, Leriche A, Cambier F. (2018)** Alumina porous ceramics obtained by freeze casting: Structure and mechanical behaviour under compression. *Ceramics* 1:83-97.
- Heatfield, BM (1971)** Growth of the calcareous skeleton during regeneration of spines of the sea urchin, *Strongylocentrotus purpuratus* (Stimpson): a light and scanning electron microscopic study. *Journal of Morphology* 134:57–90.
- Hou B, Zhao H, Pattofatto S, Liu JG, Li Y (2012)** Inertia effects on the progressive crushing of aluminum honeycombs under impact loading. *International Journal of Solids and Structures* 49:2754-2762.
- Hulbert SF (1993)** The use of alumina and zirconia in surgical implants. In: LL Hench, J Wilson (eds) *An Introduction to Bioceramics. World Scientific, Singapore, 25-40.*
- Hunger P, Donius A, Wegst U (2013)** Structure-property-processing correlations in freeze-cast composite scaffolds. *Acta Biomaterialia* 9:6338–48.
- Husmann A, Pawelec K, Burdett C, Best S, Cameron R (2015)** Numerical simulations to determine the influence of mould design on ice-templated scaffold structures. *Journal of Biomedical Engineering and Informatics* 1:47-58.

- ISO 18458 2015** Biomimetics—Terminology, Concepts and Methodology ISO 18458:2015-05 2015 (Berlin: Beuth).
- ISO 18459 2015** Biomimetics—Biomimetic Structural Optimization ISO 18459:2015-05 2015 (Berlin: Beuth).
- Ito J, Matsushima Y, Unuma H, Horiuchi N, Yamashita K, Tajika M (2017)** Preparation and properties of pressureless-sintered dense calcite ceramics. *Materials Chemistry and Physics* 192:304-310.
- Jeronimidis G, Atkins AG (1995)** Mechanics of biological materials and structures—Nature's lessons for the engineer. *Journal of Mechanical Engineering Science* 209:221–235.
- Karam GN, LJ Gibson (1995a)** Elastic buckling of cylindrical shells with elastic cores – I. Analysis. *International Journal of Solids and Structures* 32:1259-1283.
- Karam GN, LJ Gibson (1995b)** Elastic buckling of cylindrical shells with elastic cores—II. Experiments. *International Journal of Solids and Structures* 32:1285-1306.
- Kelley A (1973)** Werkstoffe hoher Festigkeit. *Friedrich Vieweg + Sohn GmbH, Verlag, Braunschweig*.
- Kingery WD, Coble RL (1956)** Effect of porosity on physical properties of sintered alumina. *Journal of the American Ceramic Society* 39:377-385.
- Klang K, Bauer G, Toader N, Lauer C, Termin K, Schmier S, Kovaleva D, Haase W, Berthold C, Nickel KG, Speck T, Sobek W (2016)** Plants and animals as source of inspiration for energy dissipation in load bearing systems and facades. In: J Knippers, T Speck, KG Nickel (eds) *Biomimetic Research for Architecture and Building Construction: Biological Design and Integrative Structures*. Springer, Springer, Cham, 103–127.
- Kowalewski M, Nebelsick JH (2003)** Predation on recent and fossil echinoids. In: PH Kelley, M Kowalewski, TA Hansen (eds) *Predatory–prey Interactions in the Fossil Record: Topics in Geobiology*. *Plenum Press/Kluwer*, New York, 279–302.
- Kovaleva D, Gericke O, Kappes J, Haase W (2018)** Rosenstein-Pavillon: Auf dem Weg zur Ressourceneffizienz durch Design. *Beton- und Stahlbetonbau* 113:433-442.
- Kurz RC (1995)** Predator–prey interactions between gray triggerfish (*Balistes capriscus* Gmelin) and a guild of sand dollars around artificial reefs in the Northeastern Gulf of Mexico. *Bulletin of Marine Science* 56:150–160.
- Kyriakides S, Shaw PK (1982)** Response and stability of elastoplastic circular pipes under combined bending and external pressure. *International Journal of Solids and Structures* 18:957-973.
- Lamarck JBM de (1816)** Histoire naturelle des animaux sans vertèbres. Tome deuxième. *Verdière, Paris*.
- Lewis JA (2006)** Direct ink writing of 3D functional materials. *Advanced Functional Materials* 16:2193–2204.
- Li D, Li M (2012)** Preparation of porous alumina ceramic with ultra-high porosity and long straight pores by freeze casting. *Journal of Porous Materials* 19:345–349.
- Lichtner A, Roussel D, Jauffrès D, Martin C, Bordia R (2015)** Effect of macropore anisotropy on the mechanical response of hierarchically porous ceramics. *Journal of the American Ceramic Society* 99:1-9.
- Liu X, Rahaman M, Fu Q, Tomsia A (2018)** Porous and strong bioactive glass (13–93) scaffolds prepared by unidirectional freezing of camphene-based suspensions. *Acta Biomaterialia* 8:415–23.

- Magdans U, Gies H (2004)** Single crystal structure analysis of sea urchin spine calcites: Systematic investigations of the Ca/Mg distribution as a function of habitat of the sea urchin and the sample location in the spine. *European Journal of Mineralogy* 16:261–268.
- Märkel K, Röser U (1983)** The spine tissues in the Echinoid *Eucidaris tribuloides*. *Zoomorphology* 103:25–41.
- Märkel K, Kubanek F, Willgallis A (1971)** Polykristalliner Calcit bei Seeigeln (Echinodermata, Echinoidea). *Zeitschrift für Zellforschung* 119:355–377.
- Munch E, Saiz E, Tomsia AP, Deville S (2009)** Architectural control of freeze-cast ceramics through additives and templating. *Journal of the American Ceramic Society* 92(7):1534–1539.
- Nebelsick JH (1992a)** Echinoid distribution by fragment identification in the Northern Bay of Safaga, Red Sea. *Palaios* 7:316–328.
- Nebelsick JH (1992b)** The Northern Bay of Safaga (Red Sea, Egypt): an actual palaeontological approach. III. Distribution of echinoids. *Beiträge zur Paläontologie von Österreich* 17:5–79.
- Nebelsick JH (1996)** Biodiversity of shallow-water red sea echinoids implications for the fossil record. *Journal of the Marine Biological Association of the UK* 76:185–194.
- Naviroj M, Voorhees P, Faber K (2017)** Suspension- and solution-based freeze casting for porous ceramics. *Journal of Materials Research* 32:1–11.
- Pabst W, Gregorová E (2014)** Young's modulus of isotropic porous materials with spheroidal pores. *Journal of the European Ceramic Society* 34:3195–3207.
- Pan WF, Hsu CM (1999)** Viscoplastic analysis of thin-walled tubes under cyclic bending. *Structural Engineering and Mechanics* 7:457–471.
- Pawelec K, Husmann A, Best S, Cameron R (2015)** Altering crystal growth and annealing in ice-templated scaffolds. *Journal of Materials Science* 451:1–7.
- Pawson DL (2007)** *Phyllum Echinodermata*. *Zootaxa* 1668:749–764.
- Peppin S, Elliott J, Worster M (2006)** Solidification of colloidal suspensions. *Journal of Fluid Mechanics* 554:147–66.
- Peppin S, Worster M, Wettlaufer J (2007)** Morphological instability in freezing colloidal suspensions. *Proceedings: Mathematical, Physical and Engineering Sciences* 463:723–33.
- Peppin S, Wettlaufer J, Worster M (2008)** Experimental verification of morphological instability in freezing aqueous colloidal suspensions. *Physical Review Letters* 100:238301.
- Perry J, Kandlikar S (2006)** Review of fabrication of nanochannels for single phase liquid flow. *Microfluid Nanofluid* 2:185–93.
- Podsiadlo P, Kaushik AK, Arruda EM, Waas AM, Shim BS, Xu JD, Nandivada H, Pumphlin BG, Lahann J, Ramamoorthy A, Kotov NA (2007)** Ultrastrong and stiff layered polymer nanocomposites. *Science* 318:80–3.
- Porter M, Imperio R, Wen M, Meyers M, McKittrick J (2014)** Bioinspired scaffolds with varying pore architectures and mechanical properties. *Advanced Functional Materials* 24:1978–87.
- Presser V, Schultheiß S, Berthold C, Nickel KG (2009a)** Sea urchin spines as a model-system for permeable, light-weight ceramics with graceful failure behaviour. Part I. Mechanical behaviour of sea urchin spines under compression. *Journal of Bionic Engineering* 6:203–213.

- Presser V, Kohler C, Zivcova Z, Berthold C, Nickel KG, Schultheiß S, Gregorova E, Pabst W (2009b)** Sea urchin spines as a model system for permeable, light-weight ceramics with graceful failure behavior. Part II. Mechanical behavior of sea urchin spine inspired porous aluminum oxide ceramics under compression. *Journal of Bionic Engineering* 6:357–364.
- Presser V, Schultheiß S, Kohler C, Berthold C, Nickel KG, Vohrer A, Finckh H, Stegmaier T (2011)** Lessons from nature for the construction of ceramic cellular materials for superior energy absorption. *Advanced engineering materials* 13(11):1042–1049.
- Ridler TW, Calvard S (1978)** Picture thresholding using an iterative selection method. *IEEE transactions on systems, man, and cybernetics* 8:630–632.
- Roberts AP, Garboczi EJ (2001)** Elastic moduli of model random three-dimensional closed-cell cellular solids. *Acta Materialia* 49:189–197.
- Sachs E, Cima M, Williams P, Brancazio D, Cornie J (1992)** Three-dimensional printing: rapid tooling and prototypes directly from a CAD model. *Journal of Engineering for Industry* 114:481–488.
- Seuba J, Deville S, Guizard C, Stevenson AJ (2016)** Mechanical properties and failure behavior of unidirectional porous ceramics. *Scientific Reports* 6:24326.
- Seto J, Zhang Y, Hamilton P, Wilt F (2004)** The localization of occluded matrix proteins in calcareous spicules of sea urchin larvae. *Journal of Structural Biology* 148:123–130.
- Schmier S, Lauer C, Schäfer I, Klang K, Bauer G, Thielen M, Termin K, Berthold C, Schmauder S, Speck T, Nickel KG (2016)** Developing the experimental basis for an evaluation of scaling properties of brittle and ‘quasi-brittle’ biological materials. Plants and animals as source of inspiration for energy dissipation in load bearing systems and facades. In: J Knippers, T Speck, KG Nickel (eds) *Biomimetic Research for Architecture and Building Construction: Biological Design and Integrative Structures*. Springer, Cham, 277–294.
- Scotti K, Northard E, Plunk A, Tappan B, Dunand D (2017)** Directional solidification of aqueous TiO<sub>2</sub> suspensions under reduced gravity. *Acta Materialia* 124:608–19.
- Scotti K, Dunand DC (2018)** Freeze casting: A review of processing, microstructure and properties via the open data repository, FreezeCasting.net. *Progress in Materials Science* 94:243–305.
- Shimizu M, Yamada J (1976)** Light and electron microscope observation of the regenerating test in the sea urchin, *Strongylocentrotus intermedius*. In: N Watabe, KM Wilbur (eds) *The Mechanisms of Mineralization in the Invertebrates and Plants*. University of South Carolina Press, Columbia, 261–281.
- Smith AB (1980)** Stereom microstructure of the echinoid test. *The Palaeontological Association*, London.
- Smith AB (1990)** Biomineralization in echinoderms. In: JG Carter (eds) *Skeletal biomineralization: patterns, process and evolutionary trends*. Van Nostrand Reinhold, New York, 413–443.
- Speck O, Speck D, Horn R, Gantner J, Sedlbauer KP (2017)** Biomimetic bio-inspired biomorph sustainable? An attempt to classify and clarify biology-derived technical developments. *Bioinspiration & Biomimetics* 12(1):011004.

- Sofie SW, Dogan F (2001)** Freeze casting of aqueous alumina slurries with glycerol. *Journal of the American Ceramic Society* 84:1459–64.
- Song JH, Edirisinghe MJ, Evans JRG (1999)** Formulation and multilayer jet printing of ceramic inks. *Journal of the American Ceramic Society* 82:3374–80.
- Sun Z, Li B, Hu P, Ding F, Yuan F (2016)** Alumina ceramics with uniform grains prepared from Al<sub>2</sub>O<sub>3</sub> nanospheres. *Journal of Alloys and Compounds* 688:933–938.
- Tang Z, Kotov N, Magonov S, Ozturk B (2003)** Nanostructured artificial nacre. *Nature Materials* 2:413–8.
- Tang J, Chen YF, Wang H, Liu HL, Fan QS (2005)** Preparation of oriented porous silicon carbide bodies by freeze-casting process. *Key Engineering Materials* 280–283:1287–90.
- Theobald MD, Langdon GS, Nurick GN, Pillay S, Heyns A, Merrett RP (2010)** Large inelastic response of unbonded metallic foam and honeycomb core sandwich panels to blast loading. *Composite Structures* 92:2465–2475.
- Vajjhala S, Kraynik AM, Gibson LJ (2000)** A cellular spherulite model for modulus reduction due to resorption of trabeculae in bone. *Journal of Biomechanical Engineering* 122:511–5.
- Vijayan S, Narasimman R, Prabhakaran K (2015)** Freeze gelcasting of naphthalene-inaqueous alumina slurry emulsions for the preparation of macroporous alumina ceramics. *Ceramics International* 41:1487–1494.
- Vincent JFV, Bogatyreva OA, Bogatyrev NR, Bowyer A, Pahl AK (2006)** Biomimetics: its practice and theory. *Journal of The Royal Society Interface* 3:471–482.
- Weber JN (1969)** Incorporation of magnesium into the skeletal calcites of echinoderms. *American Journal of Science* 267:537–566.
- Wegst U, Schecter M, Donius P, Hunger P (2010)** Biomaterials by freeze casting. *Philosophical Transactions of the Royal Society* 368:2099–121.
- Wolff J (1986)** The law of bone remodeling. Springer, Berlin, Heidelberg, New York (translation of the German 1892 edition).
- Wu TT (1966)** The effect of inclusion shape on the elastic moduli of a two-phase material. *International Journal of Solids and Structures* 2:1–8.
- Wu X, Liu Y, Li X, Wen P, Zhang Y, Long Y, Wang X, Guo Y, Xing F, Gao J (2010)** Preparation of aligned porous gelatin scaffolds by unidirectional freeze-drying method. *Acta Biomaterialia* 6:1167–1177.
- Wulle F, Kovaleva D, Christof H, Wurst K-H, Lechler A, Verl A, Sobek W, Haase W, Gresser G (2017)** Die Natura als Ideengeber für moderne Fertigungstechniken. In: J Knippers, U Schmid, T Speck (eds) Baubionik Biologie beflügelt Architektur. *Staatliches Museum für Naturkunde Stuttgart*, 72–79.
- Xue W, Sun Y, Huan Y, Xie Z, Sun J (2011)** Preparation and properties of porous alumina with highly ordered and unidirectional oriented pores by a self-organization process. *Journal of the American Ceramic Society* 94:1987–1981.
- Yang J, Hu X, Sultana R, Day R, Ichim P (2015)** Structure design and manufacturing of layered bioceramic scaffolds for load-bearing bone reconstruction. *Biomedical Materials* 10:045006.
- Yao HB, Fang ZH, Tan ZH, Wu LH, Yu SH (2010)** Biologically inspired, strong, transparent, and functional layered organic-inorganic hybrid films. *Angewandte Chemie International Edition* 49:2140.

**Yoon BH, Choi WY, Kim HE, JH Kim, Koh YH (2008)** Aligned porous alumina ceramics with high compressive strength for bone tissue engineering. *Scripta Materialia* 58:537-540.

**Yu S, Liu J, Wei M, Luo Y, Zhu X, Liu Y (2009)** Compressive property and energy absorption characteristic of open-cell ZA22 foams. *Materials and Design* 30:87–90.

**Zeng J, Zhang Y, Zhou K, Zhang D (2014)** Effects of alcohol additives on pore structure and morphology of freeze-cast ceramics. *Transactions of Nonferrous Metals Society of China* 24:718-722.

**Zhang H, Fidelis CL, Serva ALT, Wilhelm M, Rezwani K (2017)** Water-based freeze casting: adjusting hydrophobic polymethylsiloxane for obtaining hierarchically ordered porous SiOC. *Journal of the American Ceramic Society* 100:1907–18.

**Zhang M, Wang Y, Huang L, Xu Z, Li C, Shi G (2015)** Multifunctional pristine chemically modified graphene films as strong as stainless steel. *Advanced Materials* 27:6708-13.

**Zhang J, Ashby MF (1992)** The Out-of-Plane Properties of Honeycombs. *International Journal of Mechanical Sciences* 34:475-489.

**Zhang Y, Hu L, Han J, Jiang Z (2010)** Freeze casting of aqueous alumina slurries with glycerol for porous ceramics. *Ceramics International* 36:617–21.

**Zocca A, Colombo P, Gomez CM, Günster J (2015)** Additive manufacturing of ceramics: issues, potentialities, and opportunities. *Journal of the American Ceramic Society* 98:1983–2001.

# Appendix

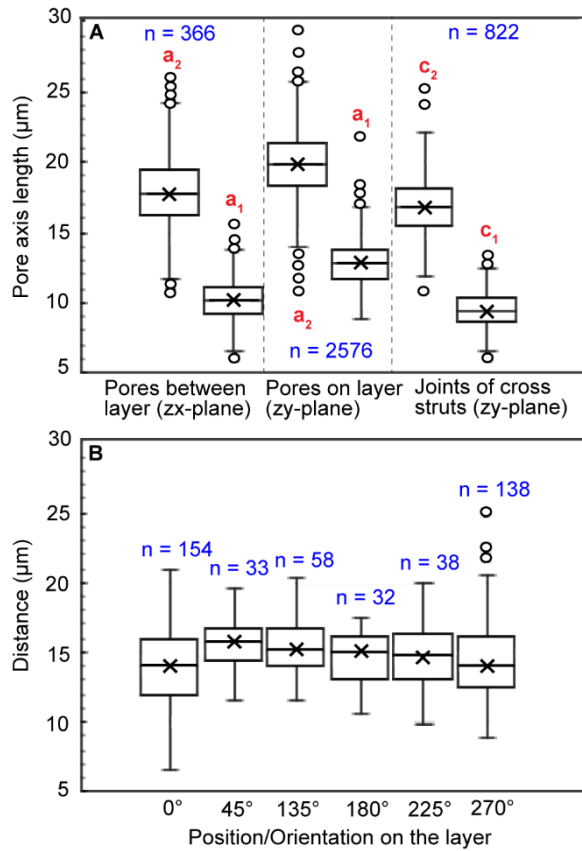


**Fig. A.1:** Boxplots of the analyzed  $\mu\text{CT}$  reconstruction of the radiating layer of the spine of *Phyllacanthus imperialis*. The boxplot in (A) gives the pore axis lengths of the pores between and on the stereom layer. The statistical distribution of the lengths of the cross struts is also plotted in (A). The numerical spacing between the pores is illustrated in (B) in form of a boxplot.

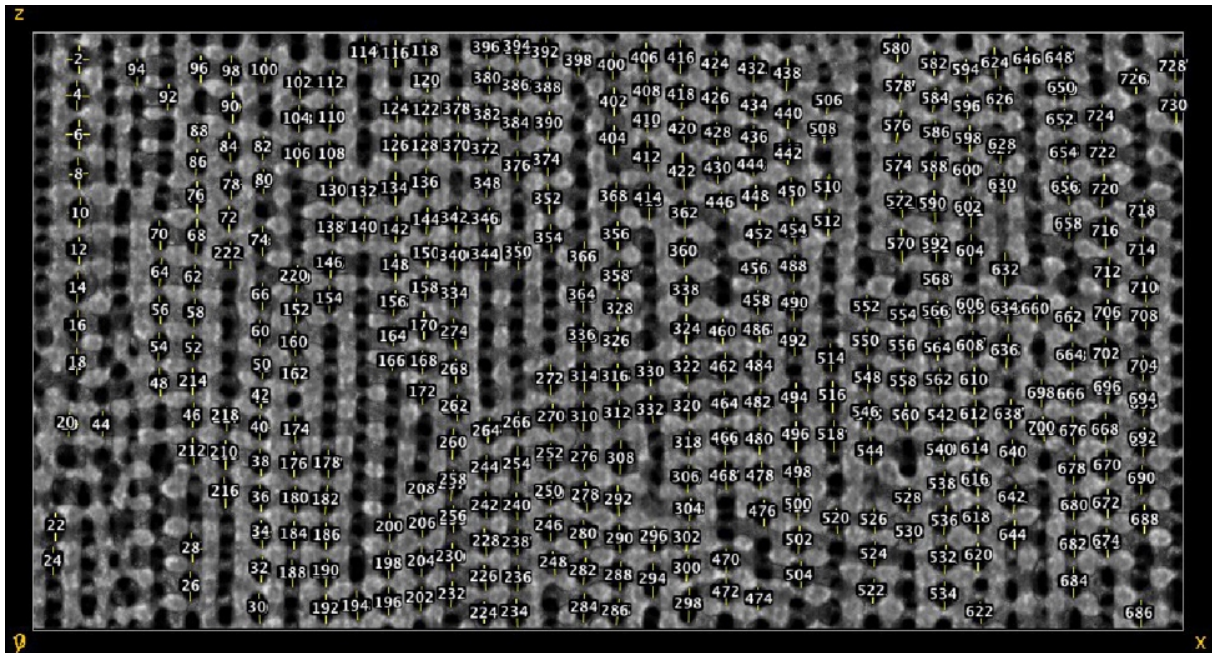


**Fig. A.2:**  $\mu\text{CT}$  scan of the radiating stereom layer of the spine of *Phyllacanthus imperialis*. The  $\mu\text{CT}$  reconstruction displays the position of the pore axis lengths between the stereom layers.

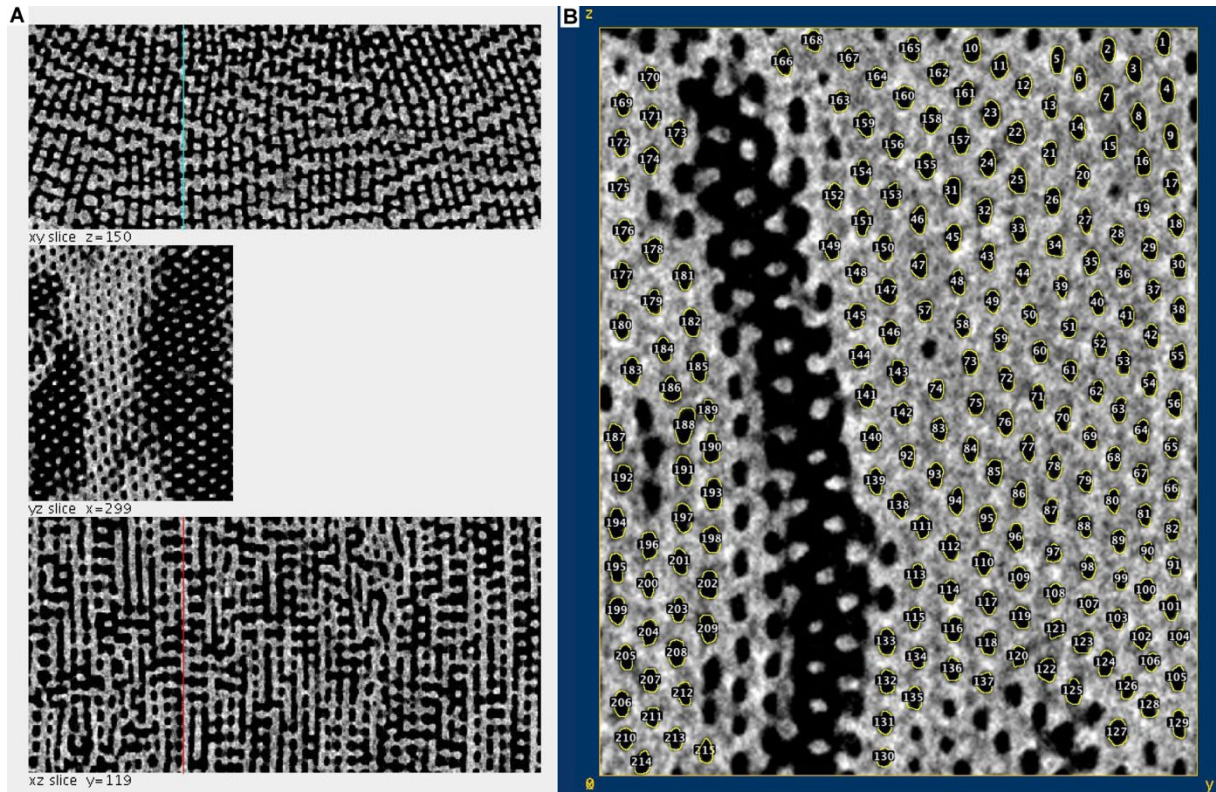


**Fig. A.3:**  $\mu$ CT scan of the radiating stereom layer of the spine of *Phyllacanthus imperialis*. The position of the selected slice plane is given in (A) as light blue and red line. The positions of the pore axis lengths are illustrated in (B).

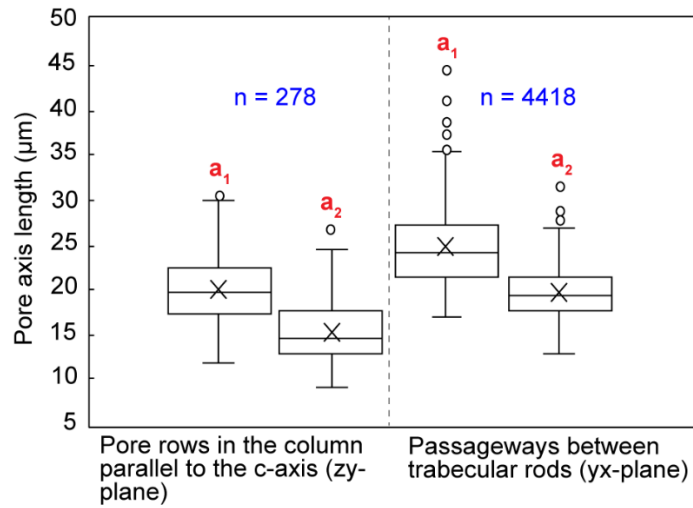


**Fig. A.4:** Boxplot gives the axis lengths of the pores belonging to the columnar stereom type of the spine *Phyllacanthus imperialis*.

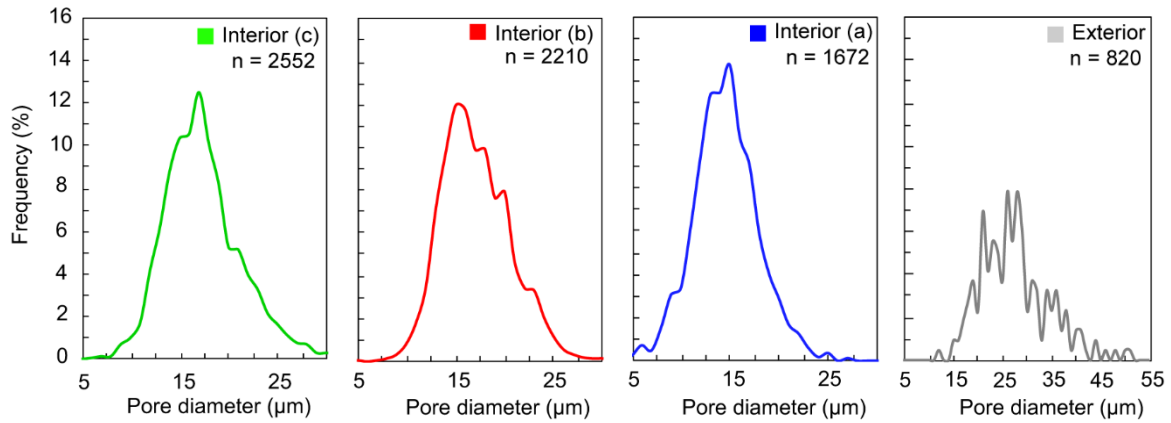


**Fig. A.5:** Pore size distribution of the  $\mu$ CT sections, which are displayed in Fig. 2.18 and belong to the stacked  $\mu$ CT section of the cortex (spine of *Phyllacanthus imperialis*).

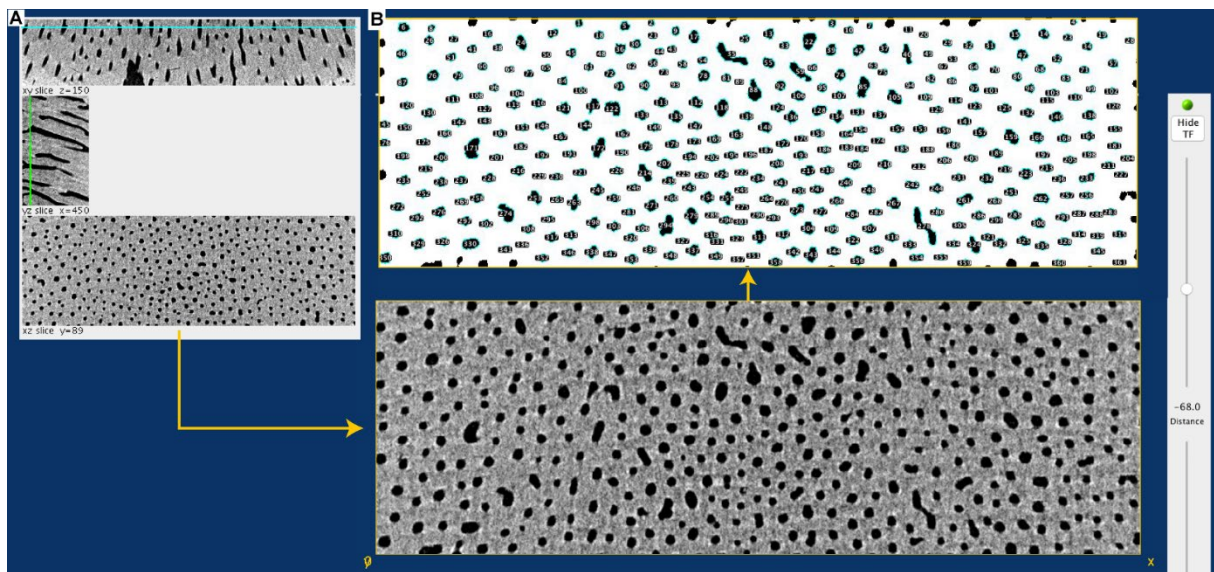


**Fig. A.6:** Stacked  $\mu$ CT section of the cortex belonging to the spine of *Phyllacanthus imperialis*. The position of the selected slice plane is given in (A) as turquoise and green line. The positions of the pore axis lengths are illustrated in (B).

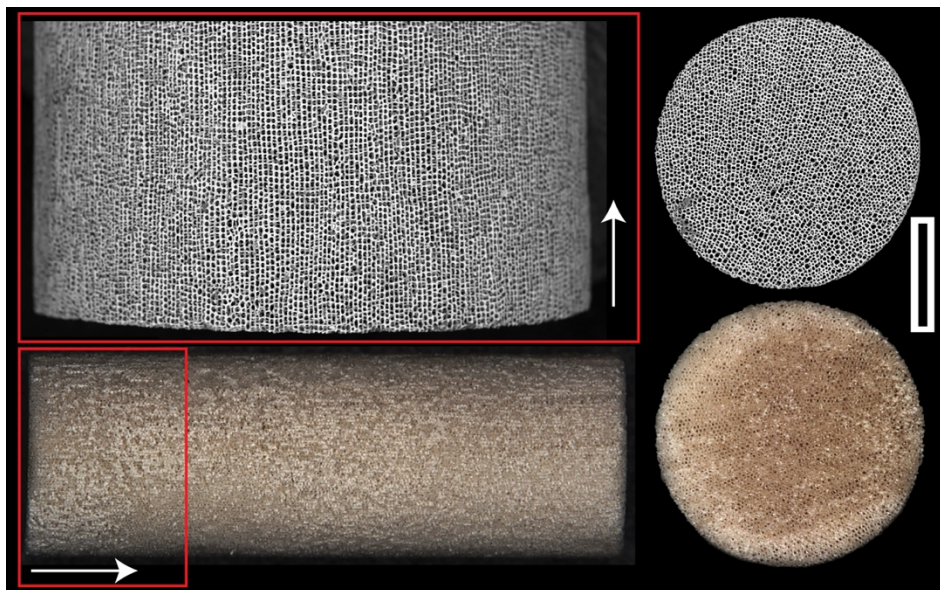


**Fig. A.7:** Display of a prepared radiating layer-cylinder of the spine of *Phyllacanthus imperialis*. Scale bar = 1 mm

# Danksagung

Zu allererst möchte ich mich bei Herrn Prof. Dr. Klaus G. Nickel für die Vergabe und engagierte fachliche Betreuung meiner Dissertation und Promotion bedanken. Die fachlichen Diskussionen und Anmerkungen waren immer sehr konstruktiv und haben mich wissenschaftlich immer sehr vorangetrieben.

Ich bedanke mich auch sehr bei der Deutschen Forschungsgemeinschaft (DFG) für die finanzielle Unterstützung meiner Dissertation.

Herrn Dr. Christoph Berthold danke ich für die Bereitschaft das Zweitgutachten für diese Arbeit zu erstellen.

Auf diesem Wege möchte ich mich auch bei der AG für die gute Aufnahme in Tübingen und stete Hilfsbereitschaft bedanken.

Ein ganz herzliches Dankeschön geht auch an Kathrin Stork (geb. Termin), die mir immer tatkräftig mit Geduld, Kompetenz und aufbauenden Worten zur Seite stand.

Ich möchte mich auch ganz herzlich bei Saskia Rughöft, Rima Ghanem und Elena Glökler (geb. Pylaeva) bedanken, die mir während der Promotionszeit in den vergangenen Jahren immer zur Seite gestanden haben.

Ein riesiges Dankeschön geht auch an Michael Bergler, Samuel Schmiedeke, Udo Eckstein, Kerstin Schopp, Marius Albiez, Jessica Steinbach (geb. Starke), Julia Otte, Florian Steinbach und Sara Ghanem. Eure emotionale Unterstützung und motivierenden Worte haben ebenfalls zur Fertigstellung dieser Dissertation beigetragen.

Simone Schafflick und Barbara Meier danke ich für die Unterstützung bei der Probenpräparation und Anfertigung von speziellen technischen Komponenten. Eure kreativen Lösungsvorschläge haben mein Promotionsprojekt stets vorangetrieben.

Ich bedanke mich auch bei meinen Projektpartner aus dem Sonderforschungsbereich (SFB) für die gute und produktive Zusammenarbeit.

Ein ganz besonderer und herzlicher Dank geht an meine Familie, die mich mein gesamtes Leben lang stets unterstützt hat.

## Gelatine hält rücksichtslose Eiskristalle klein ..

